# Relations entre vitesse d'ascension des magmas et explosivité

Guillaume Georgeais

Université Clermont Auvergne
Collégium des Sciences Fondamentales
Laboratoire Magmas et Volcans

École Doctorale des Sciences Fondamentales

# Thèse de Doctorat

Présentée pour obtenir le grade de :

## Docteur d'Université

Spécialités : Structure et évolution de la Terre et des autres planètes

Par

**Guillaume Georgeais**

Titulaire du Master Recherche Magmas et Volcans

# Relations entre vitesse d'ascension des magmas et explosivité

Soutenue publiquement le 24 mars 2023 devant le jury :

| | | |
|---|---|---|
| Fidel Costa | Institut de Physique du Globe de Paris | Rapporteur |
| Margaret Hartley | Manchester University | Rapporteur |
| Caroline Martel | Institut Sciences de la Terre d'Orléans | Examinatrice |
| Timothy Druitt | Université Clermont Auvergne | Examinateur |
| Nicole Métrich | Institut de Physique du Globe de Paris | Invitée |
| Estelle Rose-Koga | Institut Sciences de la Terre d'Orléans | Directrice de Thèse |
| Yves Moussallam | Columbia University | Directeur de Thèse |
| Kenneth Koga | Institut Sciences de la Terre d'Orléans | Directeur de Thèse |
| Andrew Harris | Université Clermont Auvergne | Directeur de Thèse |

# Remerciements

Un travail de thèse, constitue un effort important et de longue haleine. Mais c'est surtout un effort que personne ne peut ni ne devrait accomplir seul. Au crépuscule de mon parcours de doctorant, il me semble plus qu'essentiel de remercier toutes ces personnes qui ont eu la gentillesse et le courage de m'accompagner dans cette aventure.

Je voudrais dans un premier temps remercier la trinité sans laquelle ce sujet n'aurait pas vu le jour. Bien entendu, **Estelle Rose-Koga**, **Yves Moussallam** et **Ken Koga**, je ne peux qu'être reconnaissant du soutien dont vous avez fait preuve tout au long de ces presque 4 années, dans les bons comme les mauvais moments. Je remercie aussi **Andrew Harris** pour m'avoir permis de mener cette thèse à son terme. Je me suis souvent répété qu'au cours d'une thèse, soit l'étudiant apprenais la rigueur, soit les encadrants apprenaient la patience. Merci donc d'avoir été si patients et motivants. Comment ne pas donner le meilleur de moi-même lorsque mes encadrants se démènent pour me fournir le plus de chances possibles pour le futur ? Je pense avoir fait le bon choix d'encadrants de stage vers fin 2018 et j'espère vous avoir convaincu que, vous aussi, vous avez fait le bon choix.

Dans un second temps, il me semble essentiel de remercier les membres du jury, **Timothy Druitt**, **Margaret Hartley, Fidel Costa** et **Caroline Martel et Nicole Métrich** qui ont accepté de se déplacer et de juger les travaux effectués au cours de ces trois ans. Merci pour vos retours et vos conseils. Suite à nos discussions, je pense avoir de quoi occuper facilement quelques années pour la suite de ma carrière de chercheur.

Merci beaucoup à l'ensemble du personnel du Laboratoire Magmas et Volcans avec qui j'ai pu interagir dans la joie et la bonne humeur. Je voudrais remercier dans un premier temps les personnes qui m'ont formé et accompagné et ce depuis le début de la thèse. Merci beaucoup à

**Claire Fonquernie** pour l'aide apportée à la préparation des échantillons, à **Jean Luc Devidal** qui s'est donné à 100% pour trouver une solution à mes rares mais embêtants problèmes de microsonde, à **Federica Sciavi** pour m'avoir enlevé une belle épine du pied et aidé à caractériser mes embayments, à **Nicolas Cluzel**, notre grand chef de la salle inclusions, à **Emmy Voyer** pour avoir pris le meilleur profil de chacun de mes échantillons, à **Simon Falvard** pour m'avoir accompagné pour mes premiers pas avec les analyses 3D, à **Sylvaine Jouhannel** pour l'aide apportée avec les publications et à **Delphine Auclair** pour sa joie de vivre (et le pied de menthe !). Je remercie aussi grandement le personnel administratif, notamment **Audrey Chazal**, **Nathalie Elaydi**, **Isabelle Roche** et **Gilles Schweiger** pour leur efficacité et la qualité de vie qu'ils apportent au laboratoire au quotidien. Je dois aussi ce travail a quelques personnes qui m'ont permis d'en être là où je suis aujourd'hui. Je suis reconnaissant envers **Lucia Gurioli** pour le support et formation au monde merveilleux des textures magmatiques, à **Franck Donnadieu** qui a parrainé cette thèse et toujours gardé un œil sur mes progrès, à **Thierry Menand** pour les discussions scientifiques (et autres) autour d'un bon café, à **Etienne Médard** pour fournir un support quotidien avec le sourire et à **Marion Garçon** pour les rares mais sympathiques discussions que nous avons eues récemment.

Je tiens aussi à remercier les personnes qui ont accepté de me suivre dans ce projet de thèse et en particulier **Marco Pistolesi** et **Antonella Bertagnini** pour l'aide inestimable fournie avec les échantillons du capricieux Stromboli et les discussions plus que formatrices que nous avons pu avoir. Je souhaite remercier toute l'équipe de la nanoSIMS du muséum d'histoire naturelle de Paris et en particulier **Maximillien Verdier-Paoletti** qui nous produit des analyses exceptionnelles entre deux bouts de saint-nectaire, mais aussi **Laurent Remusat, Jérome Aléon** et **Smail Mostefaoui**. Une partie de nos résultats est aussi due à l'équipe de la SIMS du centre de recherches pétrographiques et géochimiques de Nancy et en particulier **Etienne Deloule**, **Nordine Bouden**, **Johan Villeneuve** et **Yves Marrocchi**. Enfin, je suis extrêmement

reconnaissant envers l'équipe du JAMSTEC Kochi Core Center et surtout **Kenji Shimizu** et **Takayuki Ushikubo** qui nous ont accueilli et nous ont permis de gagner un temps précieux avec la caractérisation de nos échantillons

Ce travail n'aurait été rien sans le temps passé au contact de mes camarades et les bons moments passés en leur compagnie. Il me semble donc essentiel de remercier mes amis qui ont influencé chaque jour de mon parcours. Merci à **Masataka Kawaguchi** de m'avoir fourni une excuse pour aller au Japon. Merci à **Sophie Pailot-Bonnetat** pour les touches de verdure dans le bureau et la cancoillotte. Merci à **Paul Tao** pour les fous rires au sommet du Vulcano, sans doute responsables de la perte de quelques neurones. Merci à **Lucas Maulny** pour cette année de M1 et les parties de Mario Kart. Merci **Cyril Aumar**, chef randonneur et collègue enseignant, ainsi que **Rémy Pierru**, poète invétéré et révolutionneur de science. Un grand merci aux anciens **Narouherallaman** et **Loïs Martinkek,** rôlistement vôtre. Merci **Freddy Vasconez** pour le petit rayon de soleil que tu apportes quotidiennement au bureau. Merci **Mr NootVigné** pour les bons moments de franche rigolade et pour tout le poisson. Merci **Quentin Aquila**, ou **Lukas Nicol**, je ne sais plus vraiment, bref l'un des deux pour les petites attentions, les petits cafés et les bonnes blagues toute la journée. Trugarez all mignon memes ma fall eo ar komz d'al vell-droad c'harr. Et enfin merci **RoxylightBusochou** pour ces 8 années passées en bonne compagnie, pour ces rires et ces pleurs, les rêves fous et les fous rires. Je ne regrette pas toutes les feuilles que je t'ai imprimées et toutes les salles que je t'ai réservées.

Parce que la vie ne se résume pas qu'à la vie au bureau, il me semble quand même important de remercier les piliers externes de ma santé mentale, j'ai nommé mes ptits zébus, et en particulier **Cédric Jadot** et **Clément Pétillot**, ainsi que les 7 autres des fantastiques 8 et particulièrement **Minou** et **Minette.**

Parce qu'on trouve aussi de la force chez des personnes qui ne le savent pas toujours, je remercie grandement **Soufiane** et **Stanley Stevenson Byrne**.

À mes parents, mes sœurs, mon chien et mon chat.

À mes grands-parents qui n'auront pu assister à la fin du spectacle.

*« Kimbé red pa moli »*

# Table des matières

# CHAPITRE 1

# INTRODUCTION GENERALE

## 1.1 Qualification de la taille et la violence d'une éruption

Les éruptions volcaniques correspondent à la hausse brutale de l'activité volcanique, résultant généralement en l'émission de matériel volcanique à la surface. Les éruptions volcaniques présentent une large variation de paramètres physico-chimiques à travers une gamme de styles éruptifs. Elles présentent aussi une grande variation de dangerosité, de potentiel destructeur et d'impact sur l'environnement plus ou moins proche du volcan. Ces éruptions sont généralement caractérisées et quantifiées par les phénomènes externes directement observables par l'homme. Suite aux études successives de Mercalli (1907), MacDonald (1973), ou encore Bonadonna et al. (2016), on peut distinguer différents types d'éruptions en fonction de la structure du volcan, la nature de l'activité (effusive ou explosive) et des produits, et des propriétés physiques du magma. La détermination de la taille et de la violence d'une éruption est néanmoins complexe et a résulté en l'élaboration de plusieurs catégorisations en fonction des paramètres considérés. Parmi ces paramètres, on peut distinguer la masse totale de matériel émis au cours d'une éruption. Ce paramètre est en général calculé à partir d'une estimation de volume. Pour les éruptions actuelles, le volume de matériel émis est calculé à partir des variations de topographie (e.g., Neal et al., 2019). Pour les éruptions plus anciennes, il est possible d'estimer le volume à partir d'une cartographie de l'épaisseur et des isopachs de dépôt (e.g., Wiesner et al., 2004). Ces volumes sont convertis en volume de roche uniquement (*dense rock equivalent* ; ne considère pas le volume des bulles), puis en masse à

partir d'une estimation de densité. Les variations de magnitude des volcans connus s'étendent sur plusieurs ordres de grandeur. Une échelle logarithmique est, de ce fait, communément utilisée pour représenter la masse d'une éruption : la magnitude.

Bien que représentatif de la taille d'une éruption, ce paramètre ne considère pas la durée de l'évènement et n'est donc pas représentatif de la violence de celle-ci, une éruption longue mais peu vigoureuse ayant une magnitude potentiellement plus grande qu'une éruption beaucoup plus courte mais intense (Pyle, 2015). Un autre paramètre, plus représentatif de la violence d'une éruption est le taux d'éruption massique (la masse de matériel éjecté par unité de temps). Ce paramètre est généralement calculé à la fin d'une éruption en divisant la masse de matériel émis par la durée de l'éruption (e.g., Rosi et al., 2006). Pour une éruption en cours, il est aussi possible d'effectuer une mesure directe via des installations radar par exemple (Freret-Lorgeril et al., 2018). Pour les éruptions non observées les plus vigoureuses, il est aussi possible de déterminer le flux massique à partir d'une estimation de la hauteur du panache (Sparks et al., 1997).

L'intensité d'une éruption reste difficile à directement estimer pour des éruptions plus anciennes dont la durée n'est pas connue. Un autre paramètre directement lié à la violence d'une éruption est l'énergie cinétique (Shimozuru, 1968) mais n'est déterminable que pour les éruptions observées. Plus général, l'index d'explosivité volcanique (VEI) est une échelle logarithmique discrète allant de 0 à 8. Le VEI

est représentatif de l'explosivité d'une éruption et est basé sur la multiplication des contraintes et la considération de plusieurs paramètres en même temps (magnitude, intensité, hauteur du panache, durée de l'éruption ; Newhall and Self, 1982). Cette échelle est particulièrement efficace pour les éruptions explosives mais difficile à utiliser pour les éruptions de longue durée ou intermittentes. Le VEI d'une éruption est communément calculé en utilisant sa magnitude et son intensité, qui ont l'avantage de constituer deux échelles continues, certes plus ou moins précises pour des éruptions récentes mais aussi plus anciennes (Pyle, 2015) et fournissent une donnée sur l'explosivité d'une éruption pour un grand nombre de systèmes volcaniques.

## 1.2 Introduction à la vitesse de remontée du magma

L'ascension du magma vers la surface a généralement lieu (1) à travers des fissures éruptives fracturées, nommés dykes, par le magma sous pression (Wilson et Head, 1981; Lister et Kerr, 1991) ou (2) à travers un conduit approximé à un cylindre (Gonnermann and Manga, 2012).

Les éléments volatils ont un rôle majeur dans la dynamique de remontée des magmas et sont à la base des phénomènes de formation des bulles par décompression et de la flottaison du magma (Sparks, 1978; Prousevitch et al., 1993; Ripepe and Gordeev, 1999). Le couplage des bulles avec le magma au cours de la remontée est due aux paramètres physico-chimiques du magma, en

particulier la viscosité, et est à l'origine des différents processus dans le conduit magmatique et dynamiques éruptives observables à la surface (Figure 1-1).

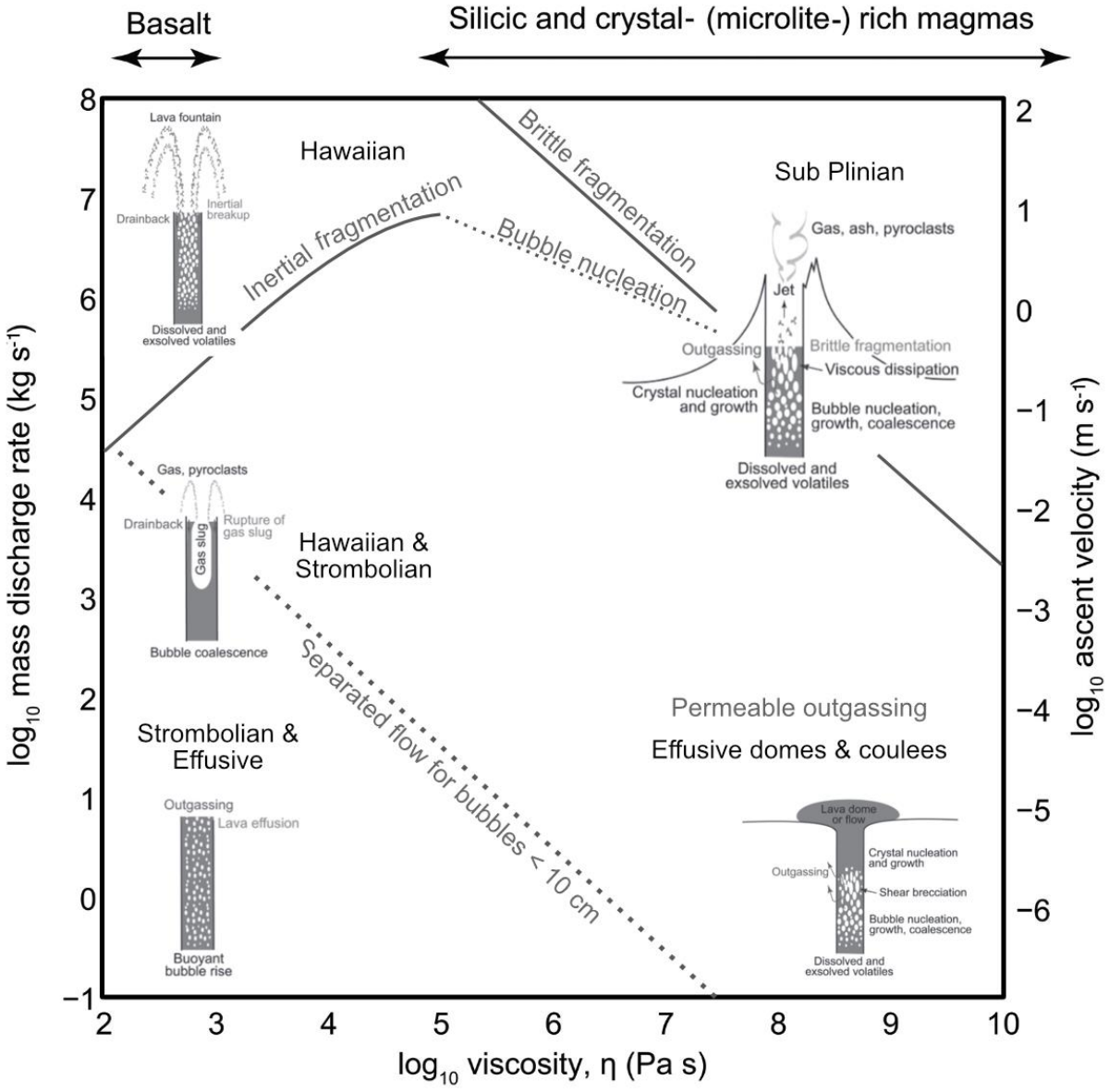


***Figure 1-1:*** *Représentation schématique de différents processus dans le conduit, la fragmentation et l'émission de produits volcaniques en fonction de la viscosité et de la vitesse de remontée du magma. Lors d'une remontée lente de magma, un magma visqueux produit un plug, piégeant les bulles plus en profondeur et limitant le dégazage aux émissions à travers les fractures dans le conduit. Un magma fluide mais pauvre en éléments volatils entraine un découplage entre bulles et liquide silicaté et un dégazage passif continu. Pour un magma fluide mais riche en éléments volatils, les nombreuses bulles coalescent en formant un « slug » caractéristique des éruptions stromboliennes. Lorsque les bulles remontent rapidement conjointement à un magma fluide, l'arrivée à la surface entraine la fragmentation fluide du magma et la formation de fontaines de lave. En revanche, lorsque cette remontée s'effectue avec un magma plus visqueux, la surpression dans les bulles entraine leur fragmentation à la surface et la transition d'un écoulement de liquide silicaté avec des bulles, à du gaz avec des pyroclastes en suspension. Tiré de l'étude de Gonnermann and Manga, (2012).*

Les interactions entre ces paramètres complexifient encore grandement notre compréhension des phénomènes se déroulant le long du conduit. Parmi tous ces paramètres, la vitesse d'ascension du magma est un paramètre physique fondamental pour déterminer le sort d'une éruption volcanique. La vitesse d'ascension à l'évent, par exemple, est directement lié au flux massique de matériel émis qui, à son tour, détermine si une colonne éruptive va se soulever, formant un panache, ou s'effondrer, générant des courants de densité pyroclastique (par exemple, Wilson et al., 1980). Pendant l'ascension du magma, la surpression et l'exsolution des matières volatiles entraînent la formation et la croissance de bulles de gaz. Le fait que ces bulles restent associées ou s'échappent du liquide silicaté, et donc le style de dégazage ouvert ou fermé est partiellement fonction de la vitesse d'ascension du magma qui, à son tour, est influencée par le comportement de la phase gazeuse (Cassidy et al., 2018; Barth et al., 2019b). Dans les magmas à ascension rapide, les bulles restent dans le liquide silicaté, ce qui renforce la flottabilité du mélange magmatique et sa vitesse d'ascension. En revanche, dans les magmas à ascension lente, le gaz s'échappe à travers la remontée des bulles, les réseaux de fractures ou les parois des conduits, ce qui prive le magma d'une grande partie de sa force motrice pour l'ascension (par exemple, Gonnermann and Manga, 2007; Browne and Szramek, 2015). Ces relations sont en réalité beaucoup plus complexes puisqu’elles font rapidement intervenir un troisième paramètre difficilement négligeable: la viscosité. Un magma visqueux se déplace en général plus lentement et difficilement. Cependant, une forte viscosité peut aussi bien

inhiber la nucléation et la croissance des bulles (e.g., Prousevitch et al., 1993; Bagdassakov et al., 2000) et donc diminuer la force motrice ascendante, que retenir celles déjà existantes et conserver la force motrice de flottaison en recouplant gas et magma (Brennen, 2005; Gonnermann and Manga, 2012). De façon similaire, un magma qui remonte vite génère beaucoup de bulles, ce qui, dans le cas où les bulles sont aptes à se déformer facilement, diminue drastiquement sa viscosité (Manga et al., 1998; Stein and Spera, 2002; Rust et al., 2003). Malgré ces complexités, il découle de ces relations qu'il existe une base théorique pour une corrélation positive entre la vitesse d'ascension du magma et l'explosivité. À travers ce travail de thèse, nous avançons l'idée de tester si une telle relation existe effectivement dans la nature pour les éruptions explosives, et si elle peut être utile pour prévoir l'explosivité et la magnitude des événements volcaniques futurs.

Le premier grand défi de la volcanologie est de prévoir le début, la taille, la durée et le danger des éruptions volcaniques. La prévision de la taille d'une éruption imminente est sans doute l'un des défis les plus difficiles à relever, mais aussi l'un des plus importants, car il a un impact direct sur les dangers et les risques qui en découlent pour les vies humaines et l'environnement. Dans une situation de crise volcanique, le fait de disposer de certaines contraintes sur l'ampleur d'une éruption imminente permet aux observatoires d'exécuter des modèles de prédiction réalistes de l'étendue attendue des chutes de cendres, des coulées de lave, des courants de densité pyroclastique ou des lahars (par exemple, Suzuki, 1983;

Schilling, 1998; Bonadonna, 2005; Macedonio et al., 2005; Kelfoun and Vargas, 2016; Kelfoun, 2017). Ces simulations sont à leur tour utilisées par les autorités de défense civile pour déterminer si et où une évacuation est nécessaire. Cependant, à l'heure actuelle, il n'existe aucune méthode standard pour prévoir l'ampleur d'une éruption à venir, ce qui entraîne des niveaux d'incertitude élevés et inquiétants lors de la gestion des crises volcaniques.

## 1.3 État de l'art des méthodes de calculs de la vitesse de remontée

Ces dernières années, un nombre croissant d'études ont déterminé la vitesse d'ascension des magmas pendant les éruptions volcaniques. Une compilation globale par Cassidy et al. (2018) montre clairement que la transition entre les activités effusives et le style explosif est fortement corrélée avec la vitesse d'ascension du magma et la transition d'un style de dégazage ouvert vers fermé. Une vitesse d'ascension inférieure à ~0,1 m/s correspond presque systématiquement à des éruptions effusives, tandis que des vitesses d'ascension plus élevées sont presque toujours associées à des éruptions explosives (Fig. 1-2), sauf quelques exceptions (par exemple, la chaîne volcanique de l'Inyo, Castro and Gardner, 2008). La vitesse d'ascension du magma peut donc être un bon indicateur pour savoir si une éruption à venir est susceptible d'être de style effusif ou explosif, mais pour les éruptions explosives, peut-elle nous dire quoi que ce soit sur sa magnitude et son explosivité probables ?

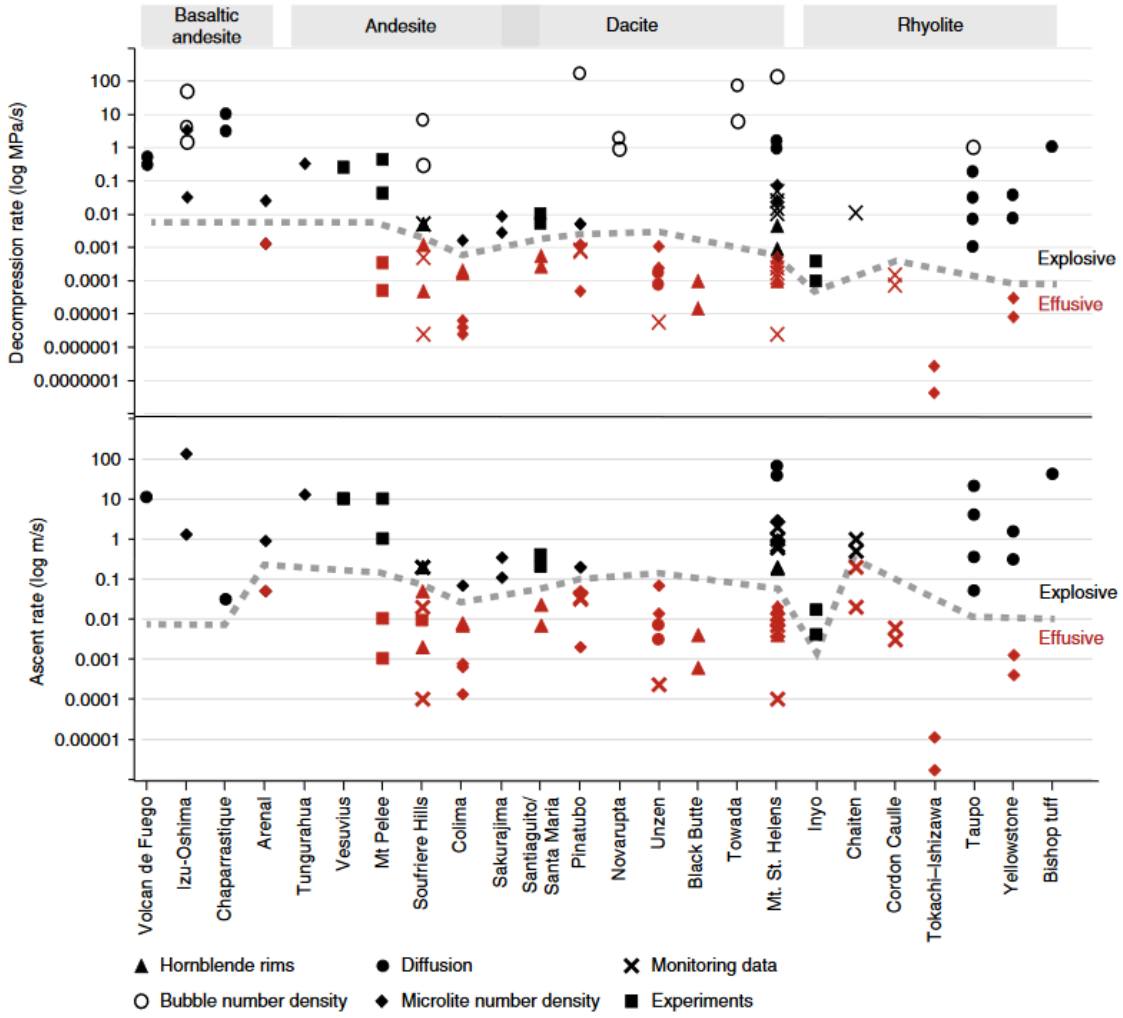


***Figure 1-2:*** *Représentation de la vitesse de décompression et de remontée de magma dans différents contextes volcaniques. La vitesse de remontée mesurée pour des éruptions de style explosif est significativement supérieure à celle mesurée pour les éruptions de style effusif. Figure issue de Cassidy et al. (2018)*

C'est à cette question que mon travail de thèse tente de répondre. La vitesse d'ascension de tout magma varie considérablement au cours de l'ascension (lorsque la pression diminue, la fraction volumique de gaz par rapport au liquide silicaté augmente nécessairement, d'où une augmentation de la flottabilité et donc de la vitesse d'ascension), de sorte que les estimations des vitesses d'ascension basées sur les taux d'éruption en surface, par exemple, ne sont pas directement comparables aux estimations pétrologiques des vitesses d'ascension du réservoir

magmatique vers la surface. Avant d'examiner plus en détail les compilations mondiales d'estimations pétrologiques, nous passons en revue les différentes méthodes disponibles pour déterminer la vitesse de remontée du magma.

Une grande diversité de méthodes pour déterminer la vitesse d'ascension du magma a été proposée au fil des années (voir les revues de Rutherford, 2008; Browne and Szramek, 2015). Elles peuvent être regroupées en deux grandes catégories, géophysiques et géochimiques. La méthode géophysique la plus couramment utilisée consiste à utiliser la vitesse de propagation de l'activité sismique vers la surface, en supposant que les séismes les moins profonds suivent la pointe de propagation du magma ascendant (par exemple, Aki and Koyanagi, 1981; Scandone and Malone, 1985; Klein et al., 1987; Endo and Murray, 1991; Tryggvason, 1994). Ces observations permettent d'obtenir des vitesses d'ascension variant entre 0.03 et 1.7 m/s pour l'activité éruptive se déroulant entre 1960 et 1983 du Kilauea (Klein et al., 1987). Une autre méthode utilise des mesures de déformation du sol (signaux GPS et d'inclinaison) pour suivre la pressurisation des conduits pendant l'ascension et l'expansion du magma (par exemple, Nishimura, 2006; Lyons et al., 2012; Cannavò et al., 2015). Enfin, une dernière méthode géophysique consiste à utiliser les flux massiques de magma mesurés, parfois en conjonction avec des analyses théoriques de l'écoulement dans les conduits pour dériver une vitesse d'ascension (par exemple, Carey and Sigurdsson, 1985; Geschwind and Rutherford, 1995; Rutherford et al., 2000). Cette méthode a, par exemple, été appliqué lors de l'éruption de 1980 du Mt. St.

Helens, avec des vitesses de remontée comprises entre 0.08 et 3 m/s. Le principal avantage des méthodes géophysiques est que la vitesse de remontée peut être déterminée en temps réel ou quasi réel. Cependant, le principal inconvénient est que les estimations ne peuvent être dérivées que pour les éruptions pour lesquelles des données de surveillance étaient disponibles.

Pour étudier les éruptions plus anciennes, ce sont les méthodes géochimiques (ou pétrologiques) qui sont utilisées. Elles utilisent l'éventail des réactions chimiques qui se produisent dans un magma pendant l'ascension, comme la cristallisation, la dissolution ou le dégazage, ainsi que la connaissance de la cinétique de ces réactions pour calculer la durée pendant laquelle la réaction a eu lieu et donc déduire un taux d'ascension. Une variété de méthodes géochimiques a été proposée, la plupart d'entre elles étant applicables à des types de magma spécifiques. Dans le magma andésitique, par exemple, l'épaisseur des bordures de décomposition autour des cristaux d'amphibole a été utilisée pour estimer une vitesse d'ascension basée sur des vitesses de déshydratation déterminées expérimentalement (par exemple, Carey and Sigurdsson, 1985; Rutherford and Hill, 1993; Geschwind and Rutherford, 1995; Browne and Gardner, 2006). Inconvénient majeur, la formation de cette bordure est lente, ne commence qu’après un certain délai de 4 jours selon les expérimentations effectuées sur des compositions du Mt. St. Helens (Rutherford et al., 1985; Rutherford, 2008). Au cours de ces expérimentations de calibrations, la méthode n’a permis d’enregistrer que des vitesses d’ascension comprises entre 0.004 et 0.015 m/s (Rutherford et al.,

1985). Un autre exemple est l'utilisation des profils de diffusion conservés naturellement (par exemple Fe-Mg ou $H_2O$) à travers les bords des xénolites du manteau lorsqu'ils se rééquilibrent avec le liquide silicaté ascendant vers la surface (par exemple, Mackwell and Kohlstedt, 1990; Klügel et al., 1997; Klügel, 1998; Kohlstedt and Mackwell, 1998; Le Voyer et al., 2014). Connaissant le coefficient de diffusion de l'espèce d'intérêt, on peut alors déduire une estimation de la vitesse d'ascension du magma pour ces éruptions (par exemple, Demouchy and Mackwell, 2006; Sparks et al., 2006; Rutherford, 2008). Appliquée aux xénolites remontés aux Iles Canaries, cette méthode fournis des vitesses de remontée supérieures à 0.06 m/s (Klügel et al., 1997), ce qui est consistent bien que légèrement inférieur aux vitesses minimales de remontée théorique de xénolites (au moins 0.2 m/s ; Spera, 1984) Une autre méthode, théoriquement applicable à toutes les éruptions explosives, est l'utilisation de la densité du nombre de bulles (Toramaru, 1989, 1995, 2006). Cette méthode, basée sur la théorie classique de la nucléation, relie la densité du nombre de bulles par unité de volume de matière fondue (mesurable à partir des observations 2D et 3D des produits éruptifs) à la vitesse de décompression qui peut ensuite être transformée en vitesse d'ascension. La relation calculée a été reproduite expérimentalement par un certain nombre d'études (voir la compilation de Shea, 2017), mais elle ne tient plus lorsque les bulles commencent à coalescer largement ou que la vitesse d'ascension lente provoque un effondrement de l’amas de vésicules (par exemple, Martel and Iacono-Marziano, 2015). Cette méthode est sensible aux variations de viscosité

exposées précédemment et enregistre principalement la dernière étape d'ascension où le dégazage est le plus important. L'association des données expérimentales et naturelles permet de déterminer une gamme de mesures possibles grâce à cette méthode. Cette gamme est comprise entre 1 m/s (Mourtada-Bonnefoi and Laporte, 2004) et 6500 m/s (calculée pour l'éruption de 1991 du Pinatubo ; Polacci et al., 2001; Toramaru, 2006), soit presque 20 fois la vitesse du son. Une autre méthode couramment utilisée consiste à comparer les textures des microlites d'un produit naturel émis suite à une éruption, à des expériences de décompression réalisées sur la même composition afin d'en déduire une vitesse de remontée (par exemple, Geschwind and Rutherford, 1995; Couch, 2003; Castro and Gardner, 2008; Castro and Dingwell, 2009; Andrews, 2014; Szramek, 2016). À l'exception de l'utilisation de la densité des bulles, ces méthodes sont grandement limitées pour de fortes vitesses d'ascension pour lesquelles les méthodes n'ont pas le temps d'enregistrer d'information (les microlites n'ont pas la possibilité de se former, l'amphibole n'as pas le temps de se déshydrater ou le Fe et Mg n'ont pas le temps de varier ou diffuser). Les différentes méthodes principales d'estimation de vitesse d'ascension du magma et la gamme des valeurs obtenues avec, sont résumées dans la Figure 1-3. Pour une même éruption (e.g., l'éruption de 1980 du Mt St Helens), il est possible de remarquer une différence dans l'estimation des vitesses de remontée de plusieurs ordres de grandeur entre les différentes méthodes, même au sein du même type d'éruption (effusif ou explosif). Cela est dû à la sensibilité des méthodes à

certaines portions du trajet (les méthodes utilisant la solubilité des éléments volatils sont plus sensibles aux derniers km de remontée comparé au suivi des séismes par exemple).

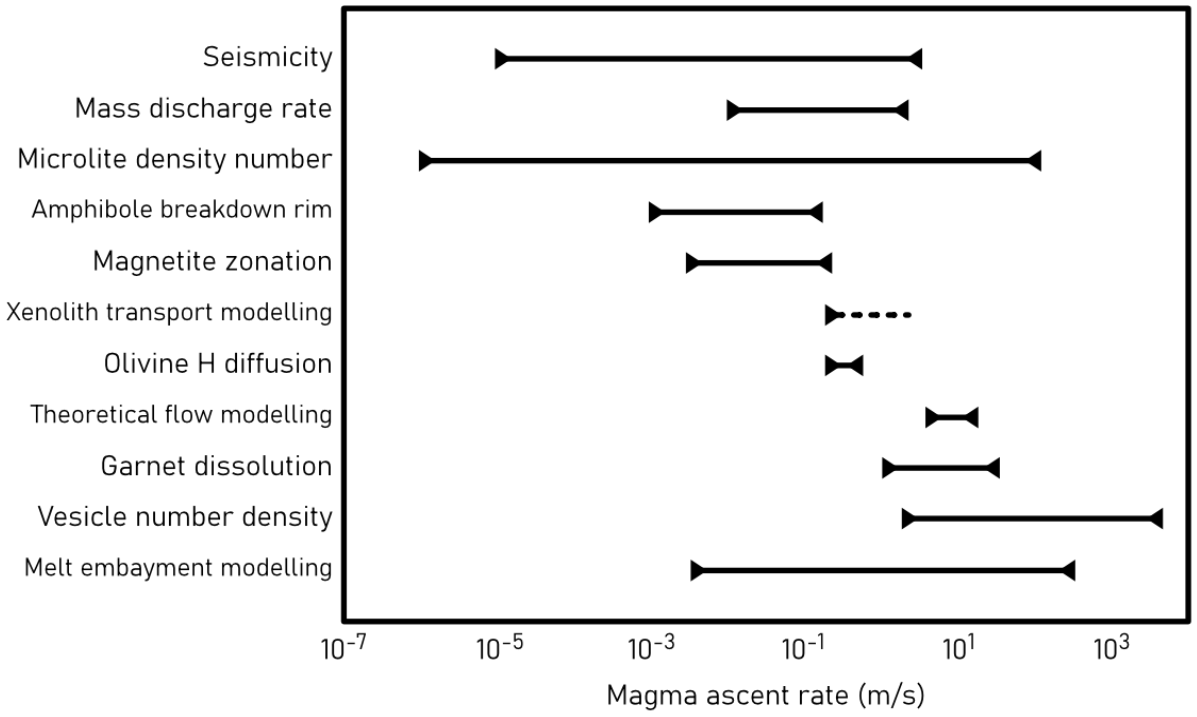


***Figure 1-3:*** *Compilation de la gamme de vitesse d'ascension de magma enregistrée par différents géochronomètres. Les données proviennent de plusieurs compilations (Rutherford, 2008; Cassidy et al., 2018). Les données de densité de vésicule et de modélisation de diffusion dans les embayments proviennent des études de Toramaru. (2006) et Georgeais et al. (2021), respectivement.*

## 1.4 Introduction à la méthode des embayments

L'analyse des profils de diffusion des éléments volatils le long du verre contenu dans des embayments est une méthode géochimique récente qui pourrait s'appliquer à une large gamme de compositions de magma et de taux de décompression. Elle dispose les avantages de fonctionner avec plusieurs espèces volatiles qui diffusent plus ou moins vite et donc d'enregistrer une ascension

comprise entre quelques secondes et plusieurs jours. Elle est aussi peu sensible à la température pour des systèmes rhyolitiques (deGraffenried and Shea, 2021) et n'est qu'indirectement sensible à la viscosité (sensibilité que l'on retrouve principalement dans le calcul du coefficient de diffusion). Les embayments - également appelés inclusions en sablier, golfes ouverts ou réentrants dans la littérature - sont des poches allongées à l'intérieur des cristaux, de formes et de tailles diverses, ouvertes sur le liquide silicaté extérieure (par exemple, Anderson, 1991). Leur mécanisme de formation est similaire à celui des inclusions vitreuses (par exemple, Faure and Schiano, 2005), par cristallisation autour d'un défaut ou par dissolution du cristal hôte, à l'exception du fait que dans le cas des embayments, le liquide silicaté n'est jamais complètement isolé/piégé dans le cristal. Au cours de l'ascension du magma, la teneur en éléments volatils du liquide silicaté entourant le cristal hôte diminue, maintenant l'équilibre avec la phase gazeuse exsolvée. Cependant, le volume limité des embayments empêche souvent la formation de bulles à l'intérieur, ce qui fait que le liquide silicaté contenue dans les embayments est sursaturé en volatils par rapport au liquide environnant (Fig. 1-4, voir aussi Fig. 6 dans Costa et al., 2020). Ce gradient de concentration entraîne un transport diffusif des espèces volatiles de la base à l'embouchure de l'embayment, ce qui donne lieu à un profil de diffusion. Si un tel profil est préservé dans les échantillons naturels, il peut alors être inversé pour dériver une vitesse d'ascension en supposant que la forme tubulaire allongée de l'embayment et la perméabilité relativement faible du cristal hôte conduisent à

une diffusion unidirectionnelle (c'est-à-dire 1D ; voir la comparaison avec la modélisation 3D dans deGraffenried and Shea, 2021) et empêche tout mouvement advectif du liquide silicaté dans l'embayment. La dépendance de la diffusion des éléments volatils dans les embayments à de multiples paramètres (composition du liquide silicaté, température, pression, trajet de dégazage, taux de décompression) fait que l'interprétation des profils de diffusion naturels n'est pas directe et qu'un modèle numérique est nécessaire pour générer de multiples profils de diffusion avec des paramètres connus et trouver le profil synthétique qui reproduit le plus fidèlement la mesure. Les embayments peuvent se produire dans n'importe quel cristal et la diffusion des substances volatiles à travers ces embayments a été étudiée dans le quartz (par exemple, Liu et al., 2007; Myers et al., 2018), le plagioclase (par exemple, Humphreys et al., 2008; Myers et al., 2021) et l'olivine (par exemple, Lloyd et al., 2014; Ferguson et al., 2016; Moussallam et al., 2019, 2021; Newcombe et al., 2020), pour des compositions de magmas allant de basaltique à rhyolitique. De par sa polyvalence d'application, la méthode des embayments dispose d'un potentiel unique de calcul des vitesses d'ascension dans le conduit vis-à-vis des autres géochronomètres. Cette méthode est développée plus en détail au cours du chapitre 2.

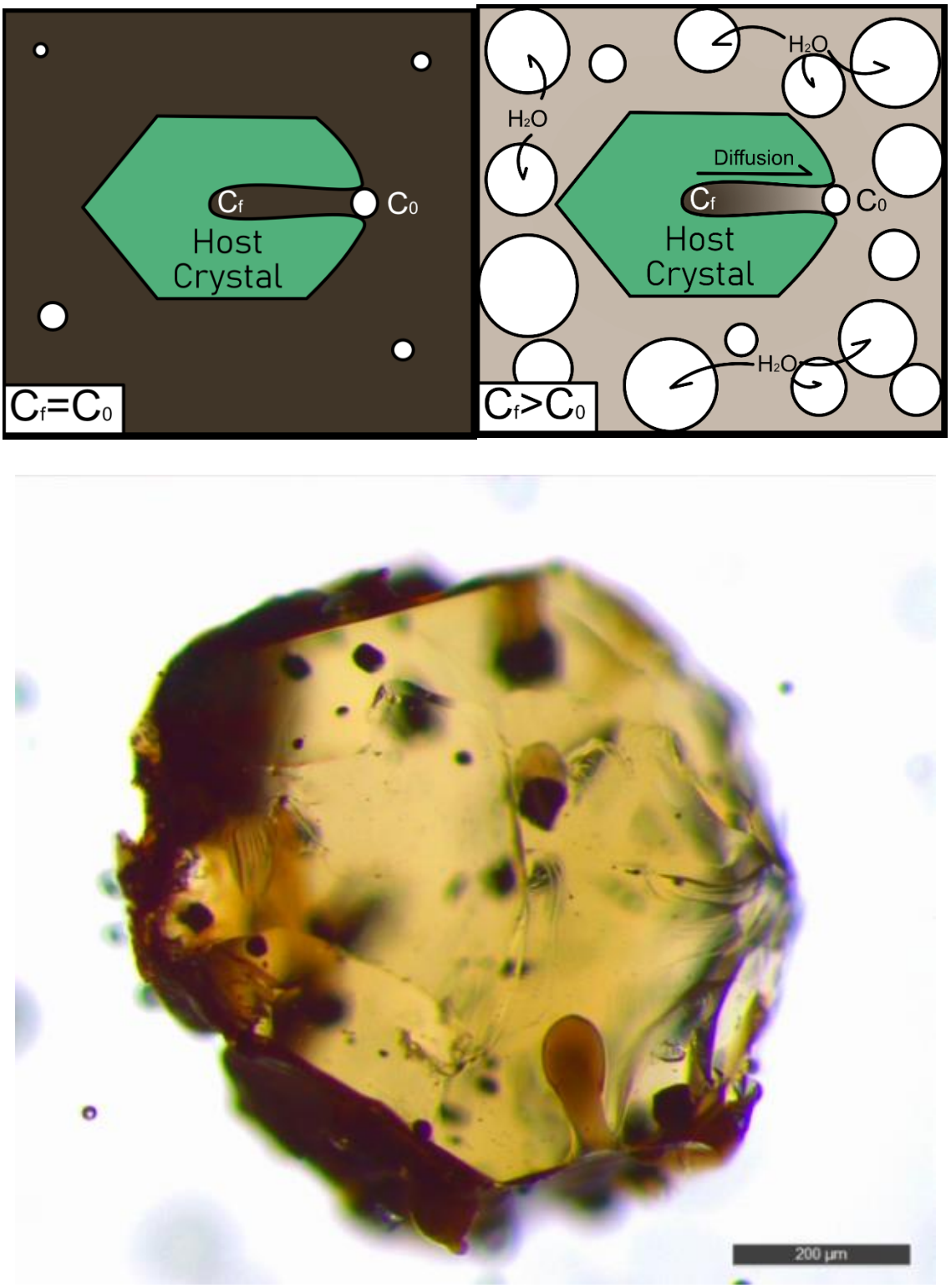


***Figure 1-4:*** *Représentation schématique des transferts d'éléments volatils au sein d'un embayment avant (haut gauche) et au cours (haut droite) de la remontée de magma syn-éruptif. La variation de pression entraîne l'exsolution des phases gazeuses contenues dans le liquide silicaté et la sursaturation du liquide contenu dans l'embayment en espèces volatiles. La différence de potentiel chimique à l'embouchure de l'embayment entraine le rééquilibrage des teneurs en éléments volatils via diffusion et la formation d'un profil de diffusion le long de l'embayment. Les phénomènes de diffusion stoppent quand l'échantillon est trempé. Photo d'un embayment naturel contenu dans une olivine (bas).*

L’essentiel de ce travail de thèse présente des vitesses de décompression en les assimilant au phénomène de remontée de magma, ce qui n’est pas forcément toujours le cas. La méthode des embayments enregistre le temps écoulé entre le début de la remontée du magma et sa fragmentation, lorsque le liquide silicaté refroidis et trempe. Ces deux limites sont contraintes par les pressions enregistrées via la solubilité des espèces volatiles, ce qui permet de convertir la durée de remontée en une vitesse de décompression constante. La vitesse de décompression est approximée à une vitesse d’ascension via une densité lithostatique (e.g., Liu et al., 2007; Ferguson et al., 2016), ce qui implique une interprétation supplémentaire. Les éruptions plus siliciques présentent une variation non linéaire de la pression avec la profondeur, en particulier sur les derniers kilomètres de remontée (Vergniolle and Jaupart, 1986; Dobran, 1992; Papale and Dobran, 1993; Proussevitch and Sahagian, 1998; Mastin, 2005). On peut alors distinguer 3 étapes. A forte profondeur, la faible quantité de bulles à un impact négligeable sur la densité de la colonne et la pression varie linéairement avec la profondeur selon le gradient lithostatique. En remontant et jusqu’à atteindre la profondeur de fragmentation, la forte viscosité associée à la nucléation des bulles entraine une diminution de la densité de la colonne ascendante et donc, de la pression en profondeur. Il est alors nécessaire d’employer d’un modèle de densité qui considère la croissance de bulles pour calculer un gradient magmastatique, plus représentatif de cette portion du trajet (e.g., Humphreys et al., 2008; Lloyd et al.,

2014). Finalement, la diminution de pression entre la profondeur de fragmentation et la surface est linéaire (Koyaguchi, 2005) mais est supposé de faible impact sur les vitesses enregistrées par les embayments car postérieur à la fragmentation et la trempe des embayments. Les résultats, relations et déductions présentés au long de cette thèse considèrent les vitesses de décompressions. Les vitesses d'ascension fournies tout au long de ce manuscrit sont issues d'approximations du premier ordre à partir de gradients lithostatiques et pas magmastatiques. Cette approximation peut entrainer une sous-estimations de la vitesse d'ascension allant jusqu'à 20% pour le Fuego par exemple (Lloyd et al., 2014).

## 1.5 Établissement du contexte de cette thèse

Au cours de cette thèse, je me suis concentré sur l'utilisation de la méthode des embayments pour déterminer les vitesses de remontée du magma et tenter d'établir de potentiels liens entre vitesse de remontée du magma et explosivité de l'éruption associée. Pour cela, l'essentiel de mon travail de thèse s'est organisé autour de 3 axes principaux.

Dans un premier temps, j'ai établi une base de donnée homogène et comparable sur les vitesses de remontée déterminée grâce aux embayments. La méthode est assez récente et s'est développée au cours des études, sur une gamme étendue de volcans et de compositions chimique de lave (par exemple, Liu et al., 2007; Humphreys et al., 2008; Lloyd et al., 2014; Ferguson et al., 2016; Myers et al.,

2018, 2021; Moussallam et al., 2019, 2021). La portée et le but de chaque étude est différent à chaque fois et le modèle numérique employé varie spécifiquement avec chaque étude, rendant les résultats incomparables. L'évolution des modèles a vu apparaitre la prise en considération de nouveaux paramètres d'étude tels que la fraction d'éléments volatils sous forme gazeuse, considérée dans les études de Liu et al., (2007) et Ferguson et al., (2016) par exemple, mais pas dans les études de Humphreys et al., (2008) ou Lloyd et al., (2014). Il existe par ailleurs d'autres distinctions plus ou moins significatives entre les modèles. Les relations de calcul de coefficients de diffusion utilisées ne sont pas forcément les mêmes et les coefficients de diffusivité utilisés peuvent être considérés constant (par exemple dans Moussallam et al., 2019) ou calculé tout au long de la remontée du magma (par exemple, Ferguson et al., 2016). Certaines différences font partie intégrante du déroulement du calcul du code. Le modèle développé dans l'étude de Humphreys et al. (2008) impose la valeur finale (au moment de la trempe) de concentration en élément volatile à l'embouchure de l'embayment, puis effectue le rééquilibrage par diffusion. D'autres modèles comme celui développé dans Myers et al. (2018) calculent les concentrations en éléments volatils à l'embouchure de l'embayment tout au long de la remontée grâce aux lois de solubilité et effectuent le rééquilibrage par diffusion en même temps. Enfin, il existe aussi des différences notables dans les stratégies de calcul. Par exemple, les vitesses calculées dans l'étude de Myers et al. (2021) considèrent un point de départ des embayments unique et définis par les inclusions vitreuses. D'autres

études comme celles de Moussallam et al. (2019) calculent des vitesses de remontée à partir d'un point de départ différent et définis selon les concentrations en éléments volatils dans le plateau du profil de diffusion, au fond de chaque embayment. Bien qu'anodines, ces simples différences cumulées peuvent entrainer des modifications de la vitesse d'ascension calculée allant jusqu'à un à deux ordres de grandeur, ce qui n'est pas négligeable. Ces différences et les variations qu'elles peuvent entrainer dans le calcul de vitesse d'ascension renforcent l'idée qu'il est nécessaire d'établir une base de comparaison pertinente avant de s'intéresser aux possibles relations avec d'autres paramètres éruptifs. Pour ceci, j'ai développé un programme gratuit et polyvalent pour déterminer une vitesse de remontée à partir des profils de diffusion en $H_2O$, $CO_2$ et S dans les embayments et quelques soit la composition du magma. Le traitement des données via le même modèle et le même outil permet d'obtenir des résultats comparables et de facto plus pertinents pour investiguer les liens entre vitesse d'ascension et explosivité des magmas. Cette base de donnée est globale et se base sur les travaux antérieurs effectués sur les magmas basaltiques à rhyolitiques pour des volcans de contexte de point chaud mais aussi d'arc volcanique. L'utilisation de cette base de données a permis de déterminer un potentiel lien entre vitesse maximale de remontée de magma et magnitude de l'éruption pour des compositions mafiques uniquement. Les données issues de compositions siliciques ou même la prise en compte de l'ensemble des compositions ne nous ont pas permis de déterminer de corrélations significatives. Ce travail fait l'objet

d'un article intitulé "*Magma ascent rate calculations with EMBER: A user-friendly software to model diffusion of $H_2O$, $CO_2$ and S in melt embayments",* publié en 2021 au journal *Geochemistry, Geophysics, Geosystems* (cf. Chapitre 2).

Dans une optique de suivi du risque éruptif, il me semble essentiel d'étudier s'il existe une telle relation pour un unique et même édifice. J'ai donc concentré, dans un second temps, mon étude sur un volcan mafique, densément étudié, très bien surveillé et source d'éruptions de différentes amplitudes : le Stromboli. J'ai étudié les échantillons issus de 8 éruptions d'intensité variables : 2 éruptions majeures, 4 éruptions paroxysmales et 2 éruptions paroxysmales de grande échelle. J'ai déterminé les vitesses moyenne de remontée de magma à travers 2 geochronomètres : la diffusion des éléments volatils le long des embayments et l'analyse texturale des populations de bulles (Toramaru, 2006; Shea et al., 2010). Les deux méthodes fournissent des vitesses d'ascension du même ordre de grandeur et très élevées (jusqu'à 280 m/s), correspondant à une remontée de magma depuis 1.6-5.9 km de profondeur en 10 s à 3 minutes. Les échantillons des éruptions majeures et des paroxysmes de faible échelle indiquent par ailleurs une forte corrélation entre vitesse d'ascension maximale du magma pour chaque éruption et la magnitude, l'intensité et la pression à laquelle les embayments commencent à remonter suffisamment vite pour enregistrer un déséquilibre en éléments volatils. Une forte corrélation positive entre vitesse de remontée des magma et magnitude et intensité indique donc qu'il existe une relation entre

vitesse d'ascension et explosivité du magma à l'échelle d'un volcan et plus précisément, à l'échelle du Stromboli. De plus, cette pression où le système commence à accélérer significativement et les hautes teneurs en éléments volatils associées sont potentiellement responsables des très fortes vitesses d'ascension enregistrées par les géochronomètres. L'essentiel de cette étude est synthétisé dans un article nommé *"Deeper, bigger, faster, stronger? Positive correlations between extreme magma ascent rate and explosive eruption parameters at Stromboli volcano (Italy).",* actuellement en revue au journal *Earth and Planetary Science Letters* (cf. Chapitre 3).

Le troisième axe développé au cour de ma thèse découle directement de l'étude sur le Stromboli et concerne l'élaboration d'un modèle prédictif destiné à estimer l'intensité d'une éruption en cours à partir des mesures via caméras thermiques, donc quasiment en temps réel. Cette relation repose sur une base théorique de calcul du flux massique de matériel volcanique à l'évent, mais aussi sur deux fortes corrélations entre la vitesse de remontée du magma déterminée par les embayments et (1) l'intensité de l'éruption, (2) la vitesse maximale d'éjection du gaz à l'évent. Ces deux corrélations impliquent qu'il existe aussi un lien fort entre la vitesse maximale d'éjection du gaz au cours d'une éruption et le pic d'intensité associée. Afin de quantifier cette relation pour Stromboli, j'ai estimé les paramètres éruptifs via des observations par caméra thermique et compilé les valeurs déjà existantes d'intensité d'une gamme d'éruptions Stromboliennes, Majeures et Paroxysmales. Une étude statistique approfondie via la méthode des

ordres de rangs met en avant une différence claire de processus entre les éruptions Stromboliennes classiques, d'un côté, et les éruptions majeures et paroxysmales, de l'autre côté. Il est alors possible de distinguer une tendance entre vitesse maximale d'éjection de gaz et intensité de l'éruption, dépendant de l'évent d'émission, pour les Stromboliennes classiques. Il est aussi possible de distinguer une seconde tendance, plus globale, pour les éruptions majeures et paroxysmales, qui constitue la base du modèle prédictif. Ce modèle corrèle bien avec les données du Stromboli et assez bien avec certaines éruptions d'autres volcans (Fuego, Mt St Helens, Pinatubo). Il s'avère prometteur pour établir un système de surveillance et de quantification de l'intensité volcanique globale basé sur l'imagerie thermique (i.e., une image en temps réel), une méthode de suivi simple et facilement applicable à travers le monde. Cette étude fait l'objet d'un article intitulé *" An empirical relation between velocity, mass discharge rate and vent area for normal through paroxysmal eruptions at Stromboli "*, actuellement en revue au journal *Bulletin of Volcanology* (cf. Chapitre 4).

La discussion et certains futurs axes de recherche sont développés dans le chapitre 5.

Les conclusions et un récapitulatif des bonnes pratiques nécessaires à la sélection d'embayments pertinents pour la méthode sont développés au cours du chapitre 6.

# CHAPITRE 2

# CALCUL DES VITESSES DE DÉCOMPRESSION DU MAGMA AVEC EMBER : UN LOGICIEL ERGONOMIQUE ET POLYVALENT POUR MODÉLISER LA DIFFUSION DE $H_2O$, $CO_2$ ET S DANS LES EMBAYMENTS

Le taux de décompression du magma est l'un des paramètres les plus importants pour contrôler la dynamique des éruptions et principalement le style éruptif d'un évènement volcanique. Une des différentes façons de déterminer le taux de décompression est d'ajuster un profil de diffusion d'éléments volatils à un gradient de concentration dans des embayments contenus dans des cristaux. Les études précédentes ont utilisé une grande variété de modèles de diffusion, ce qui limite la possibilité de comparaison entre les études. Nous présentons ici EMBER (*EMBayment-Estimated Rates*), un outil polyvalent et indépendant qui modélise la diffusion d'éléments volatils le long des embayments vitreux. Ce logiciel fonctionne à travers une interface graphique et est compatible avec les architectures Windows et Mac. Notre modèle s'appuie sur la fonction « pdepe » de MATLAB pour calculer les profils de diffusion de $H_2O$, $CO_2$ et S via la méthode des différences finies. EMBER utilise une grille de recherche pour trouver les valeurs les plus probables de taux de décompression, de la concentration en chaque élément volatil étudié dissout dans le magma au début de la remontée et la teneur initiale en élément volatile sous forme gazeuse, tout en fixant trois constantes : la température le long de la remontée et la pression au début et à la fin de la remontée. Notre modèle peut calculer le taux de décompression pour des compositions basaltiques, intermédiaires et rhyolitiques. Le modèle est très sensible à l'action de la teneur initiale en éléments volatils dégazés couplée à la pression de fin d'ascension/de trempe. Nous avons appliqué EMBER à des

études antérieures pour évaluer et valider notre modèle. Les vitesses de décompression recalculées varient dans le même ordre de grandeur que les vitesses obtenues dans la littérature. Certaines présentent quelques différences notables et systémiques comme pour l'étude de l'eruption de 1980 du Mt. St. Helens. Dans ce cas, nous avons obtenu une gamme de vitesses de décompression autour de 0.15-0.41 MPa/s soit la moitié de ce qui avait été calculé par Humphreys et al., (2008). Nous avons ensuite traité à nouveau, mais de manière "homogène", les données brutes de la littérature pour obtenir une base de comparaison. En d'autres termes, le même protocole a été utilisé pour chaque profil de diffusion en supprimant les stratégies spécifiques à la littérature utilisées pour contraindre les paramètres inconnus. Dans un premier temps, en considérant l'ensemble des données, aucune tendance globale ne dégage entre vitesse de décompression et magnitude. En revanche, nous avons trouvé une corrélation positive statistiquement significative entre les vitesses maximales de décompression des magma basaltiques et l'explosivité des éruptions correspondantes, avec un coefficient de Pearson de 0.93, une p-value de 0.01 et $R^2$=0.86. De façon analogue, aucune tendance globale n'apparait entre vitesse de décompression et hauteur du panache mais une tendance apparait pour les magmas basaltiques considérés séparément. Magnitude et hauteur du panache sont deux paramètres principaux constitutifs de l'échelle du VEI et mettre en avant une relation entre vitesse de décompression et magnitude et vitesse de décompression et hauteur du panache suggère qu'il existe une corrélation positive

entre vitesse de décompression et explosivité du magma pour les compositions basaltiques. L’utilité avec un logiciel intuitif et libre d’accès comme EMBER est de permettre d'augmenter le nombre d'études sur la diffusion de substances volatiles dans les embayments visant à déterminer les taux de décompression et d'ascension du magma et de faciliter les comparaisons entre les études.

# Magma decompression rate calculations with EMBER: A user-friendly software to model diffusion of $H_2O$, $CO_2$ and S in melt embayments

**Guillaume Georgeais[1], Kenneth T. Koga[1],Yves Moussallam[2,3], Estelle F. Rose-Koga[1]**

[1]*Université Clermont Auvergne, CNRS, IRD, OPGC, Laboratoire Magmas et Volcans, F-63000 Clermont-Ferrand, France*

[2]*Lamont-Doherty Earth Observatory, Columbia University, New York, NY 10027, USA*

[3] *Department of Earth and Planetary Sciences, American Museum of Natural History, New York, NY 10024, USA*

Corresponding author: Guillaume Georgeais; guillaume.georgeais@uca.fr

**Keywords**: volcanic eruption, magma degassing, conduit processes, volatile element exsolution, GUI

**Highlights:**

- EMBER is a new, freely available, GUI software that models magma ascent rates for basalt to rhyolite with $H_2O$, $CO_2$ and S diffusion profiles
- EMBER was validated by reproducing previous published literature data
- For mafic eruptions, we found a notable correlation between maximum recalculated decompression rates and eruption magnitude or plume height

Published in *Geochemistry Geophysics Geosystems*

## 2.1 Abstract

Magma decompression rate is one of the most important parameters in controlling eruption dynamics. One way to determine decompression rate is by fitting a volatile elements diffusion profile to a concentration gradient in crystal-hosted embayments. Previous studies have used a variety of diffusion models, limiting the possibility for inter-study comparison. Here, we introduce EMBER (EMBayment-Estimated Rates), a standalone versatile tool that models diffusion of volatile elements along melt embayments. Our model relies on the *pdepe* function of MATLAB to calculate diffusion profiles of $H_2O$, $CO_2$ and S through the finite difference method. EMBER uses a grid search seeking out the best fits for decompression rates, initial dissolved concentration of each studied volatile and initial exsolved gas content, while setting three constants: temperature along the ascent and pressure at the beginning and end of the ascent. Our model can compute the rate for basaltic, intermediate, and rhyolitic compositions. We applied EMBER to previous studies to evaluate and validate our model. We then re-processed ”homogeneously” the raw data from the literature for a comparison. In other words, the same protocol was used for each diffusion profiles removing the literature-specific strategies used to constrain unknown parameters. With this comparison, we found a statistically significant positive correlation between maximum magma decompression rates and explosivity of the related eruption. EMBER is expected to help increase the number of volatile diffusion in

embayments studies aiming at constraining magma decompression and ascent rates and to facilitate inter-study comparisons.

## 2.2 Introduction

Magma ascent rate is a fundamental physical parameter in determining the behavior of a volcanic eruption. Magma ascent rate can be estimated in several ways, during ascent and eruption by geophysical methods, or after the eruption using geochemical and petrological methods. One example of a geophysical method is the analysis of volcanic earthquakes, in which the progressive migration of tremors from a depth to the surface is interpreted as the upward migration of ascending magma [e.g., Aki and Koyanagi., 1981; Scandone and Malone., 1985; Klein et al., 1987; Tryggvason., 1994]. Geochemical methods to determine magma ascent rate are numerous but most of them are only applicable to limited melt compositions. In andesitic magma for instance, the thickness of amphibole breakdown rims has been used to determine ascent rates based on the experimentally determined rate of the break-down reaction [e.g., Carey and Sigurdsson., 1985; Rutherford and Hill., 1993; Geschwind and Rutherford., 1995; Browne and Gardner., 2006]. Another example is the use of diffusion profiles (e.g., Fe-Mg or $H_2O$) at the rims of minerals in mantle xenoliths as they re-equilibrate with their carrier melt on their way to the surface [e.g., Mackwell and Kohlstedt., 1990; Klügel et al., 1997; Klügel., 1998; Kohlstedt and Mackwell.,

1998; Le Voyer et al., 2014]. Knowing the diffusion coefficient of the species of interest, one can derive an estimate of the magma ascent rate for these eruptions [e.g., Demouchy and Mackwell., 2006; Sparks et al., 2006; Rutherford., 2008]. Another method, based on nucleation theory, links the bubble number density in erupted products (measurable from 2D and 3D observations) to the magma decompression rate [Toramaru., 1989, 1995, 2006]. This theoretical relationship has been reproduced experimentally but is not applicable to natural samples once bubbles start to coalesce [e.g., Martel and Iacono-Marziano., 2015].

One method, which holds the potential to be widely applicable for a wide range of magma compositions and decompression rates, is the analysis of the diffusion profiles of volatile elements along melt embayments (also called re-entrants). Embayments are crystal-hosted elongated melt pockets of various shapes and sizes, opened to the outside melt [e.g., Anderson., 1991]. Their formation mechanism is similar to that of melt inclusions [e.g., Faure and Schiano., 2005], through either crystallization around a defect or dissolution of the host crystal, with the exception that they remain connected to the surrounding bubbly melt. They have been studied in quartz [e.g., Liu et al., 2007; Myers et al., 2018], in plagioclases [e.g., Humphreys et al., 2008] and olivine crystals [e.g.,Lloyd et al., 2014; Ferguson et al., 2016; Moussallam et al., 2019], in quenched material ranging from basalt to rhyolite in composition. During magma ascent, the volatile content of the melt surrounding the embayment will decrease, maintaining equilibrium with the exsolved gas phase. The limited volume of melt embayments,

however, often prevents bubble formation inside, resulting in embayment melt being super-saturated in volatiles compared to the surrounding melt. This difference in chemical potential leads to a concentration gradient and to diffusive transport of volatile species from the interior to the mouth of the embayment resulting in a diffusion profile. If such a profile is preserved in natural samples, it can then be inverted to derive a decompression rate assuming that the elongated tubular shape of the embayment and the relative impermeability of the host crystal led to unidirectional (1D) diffusion and prevented any advective melt motion in the embayment. The dependency of volatile diffusion in embayments on multiple parameters (melt composition, temperature, pressure, degassing path, decompression rate) makes the interpretation of natural diffusion profiles a challenging endeavour. A numerical model adapted to a wide range of magma compositions is therefore needed to generate multiple diffusion profiles with known parameters and find the synthetic profile which most closely reproduces the measurement.

### 2.2.1 Existing embayment volatile diffusion models

Several such numerical models have been developed in the last decades (Table 2-1). The first published code was developed in FORTRAN 77 [Liu et al., 2007]. Assuming a certain temperature, pressure, initial volatile concentration, exsolved gas, degassing path and decompression rate, the code generated time-dependent profiles of $H_2O$ and $CO_2$ concentrations until the fragmentation pressure is reached.

The process was repeated several times with different decompression rates to find the best fit. A second model was presented by Humphreys et al. [2008] using the COMSOL multiphysics software to model only $H_2O$ profiles. Their model imposes the final concentration at the mouth of the embayment from the start of the calculation and allows the software to run the diffusion calculation. Lloyd et al. [2014] developed a model calculating simultaneously, for a range of decompression rates, three volatile element profiles at once: $H_2O$, $CO_2$ and S. In a following study, an improved development of a MATLAB code by Ferguson et al. [2016] took $H_2O$, $CO_2$ and S into account and considered not only a range of decompression rates but also the initial concentration of each volatile element as well as the exsolved gas content at the beginning of the ascent ($M_0$) for basaltic compositions. The addition of this new parameter, ($M_0$), the pre-existing (already exsolved) volatile content in equilibrium with magma at the onset of a magma ascent, proved to have a significant impact on the modelled profile and made the grid search more complex and the result better constrained [Ferguson et al., 2016]. Another study subsequently build the FORTRAN 77 model from Liu et al. [2007] in MATLAB with updated diffusion coefficients for rhyolitic compositions and a best fit search algorithm [Myers et al., 2018]. This code was later updated taking the pressure at which degassing stops as a free parameter [Myers et al., 2021]. Another code, written in RStudio and restricted to basaltic melts, took into account all the aforementioned parameters with fixed inputs and was made openly available [Moussallam et al., 2019]. One of the most recent models is tuned to

intermediate magma compositions, contains a specific S solubility relation and a general $H_2O$ diffusion coefficient relation for intermediate magma, and looks for the decompression rate and initial pressure [Newcombe et al., 2020]. The latest model to date is written in MATLAB and uses grid searches to find decompression rate, initial concentration of $H_2O$ and S and exsolved gas content [Moussallam et al., 2021].

At present, seven different data processing methods to model volatile diffusion profiles in embayments exist; each published study uses its specific model written on four different platforms (FORTRAN 77, COMSOL, MATLAB and RStudio). Other than the code of Moussallam et al. [2019], none are directly downloadable without a specific request to the authors. Each code considers different input parameters, different volatile species, and is tuned to a specific melt composition. This lack of consistency is an issue for inter-study comparison and the lack of open software access can be an impediment to a large number of new studies on natural products.

The aim of this article is to provide the community with a user-friendly and cross-operating system MATLAB code that is able to constrain decompression rates from volatile diffusion in melt embayments for rhyolitic to basaltic melt compositions, and for as wide a range of starting conditions as possible. We then retroactively analyze all volatile diffusion profiles from the literature using EMBER. Our results help identify potential discrepancies in published

decompression rates, notably for the Mt St Helens 1980 eruption, and provide an easily comparable, self-consistent summary of decompression rates obtained from volatile element diffusion in melt embayments published to date. Our software, EMBER, calculates results likely comparable to those by the DIPRA software [Girona and Costa., 2013], which can extract timescales from diffusion zoning in olivine crystals, and is also a widely distributed MATLAB program.

***Table 2-1:*** *Comparison of previously published codes. EMBER is a fully available complete software that covers a large spectrum of magma composition: dPdt = decompression rate, $C_i$ = initial concentration, $M_0$ = exsolved volatile content, $P_f$ = pressure of quench, gs stands for "grid search". Every study that models decompression rates from $CO_2$ and/or S uses the diffusion coefficients calculated from Zhang et al. [2007]. The only two exceptions are the $CO_2$ diffusivity from Liu et al. [2007] which is calculated from Behrens and Zhang [2001] and the S diffusivity from Ferguson et al. [2016], which is calculated from Freda et al. [2005].*

| *Article* | *Architecture* | *Volatiles studied* | *Magmatic composition* | *$H_2O$ diffusion coefficient* | *Input parameters* | *$M_0$ study* | *Availability* |
|---|---|---|---|---|---|---|---|
| *Liu et al, 2007* | FORTRAN 77 | $H_2O$ | Rhyolitic | a | dPdt, $C_i$, T, $M_0$, $P_f$, $P_0$ * | yes | On request |
| *Humphreys et al, 2008* | COMSOL | $H_2O$ | Rhyolitic | a ; b | dPdt, $C_i$ $P_f$, $P_0$, T * | | |
| *Lloyd et al, 2014* | n.d | $H_2O$,$CO_2$, S | Intermediate | Self-determined empiric law | dPdt, $P_f$, $P_0$, $C_i$, T * | | |
| *Ferguson et al, 2016* | MATLAB | $H_2O$,$CO_2$, S | Basaltic | c | gs(dPdt, $C_i$, $M_0$), $P_f$, $P_0$, T | yes | |
| *Myers et al, 2018* | MATLAB | $H_2O$,$CO_2$ | Rhyolitic | a | gs(dPdt, $P_f$, $M_0$), $C_i$, $P_0$, T | yes | On request |
| *Moussallam et al, 2019* | RStudio | $H_2O$ | Basaltic | Constant ( e ) | dPdt, $C_i$, $P_f$, $P_0$, T | yes | Publicly Available |
| *Newcombe et al, 2020* | MATLAB | $H_2O$,$CO_2$, S | Intermediate | d | dPdt, $M_0$, $P_f$, $P_0$, T * | yes | |
| *EMBER (this study)* | MATLAB | $H_2O$,$CO_2$, S | Basaltic, Intermediate and Rhyolitic | e ; d ; a | gs(dPdt, $C_i$, $M_0$), $P_f$, $P_0$, T | yes | Publicly Available |

a = Zhang and Behrens [2000]
b = Nowak and Behrens [1997]
c = Zhang et al. [2010]
d = Ni and Zhang [2018]
e = Freda et al. [2003]
*unconfirmed use of a grid search

## 2.3 **Code architecture**

### 2.3.1 Diffusion model

Volatile element diffusion in embayments can be regarded as a 1D process, because of their elongated, tube-like geometries and the incompatibility of the elements in their mineral host [Ferguson et al., 2016; Humphreys et al., 2008; Liu et al., 2007; Lloyd et al., 2014; Moussallam et al., 2019, 2021; Myers et al., 2018, 2021; Newcombe et al., 2020]. While this is a commonly accepted assumption, further studies are needed to assess the impacts of the three-dimensional shape of embayments to volatiles diffusion [deGraffenried and Shea., 2020]. If it proves to be relevant, EMBER will need to be updated accordingly to compute both 1D and 3D diffusion. The evolution of the concentration gradient is therefore described by Fick's Second Law (Eq.1):

$$\frac{\partial C}{\partial t} = \frac{\partial}{\partial x}\left(D(x,t)\frac{\partial \ C}{\partial x}\right) \quad (1)$$

$$C = C_i \ at \ x > 0, t = 0 \quad (2)$$

$$C = \ C_{sat}(t) \ at \ x = 0, t > 0 \ ; \ \frac{dC}{dx} = 0 \ at \ \ x = X, t > 0 \quad (3)$$

where $D$ is the diffusion coefficient of the studied volatile species; C, the concentration of studied species; x, the distance from the mouth of the embayment, X, the full length of the embayment; $C_{sat}$, the saturation concentration calculated at the mouth of the embayment by using a solubility model; $C_i$, the initial concentration along the embayment and t, the time. These diffusion equations

show that diffusion coefficients depend heavily on $H_2O$ concentration$(C_{H_2O})$, temperature and pressure. These three parameters, and therefore the diffusion coefficient, all change during ascent. Diffusion coefficients are hence calculated along every point of the embayment from the start to the end of the calculation.

The boundary condition at the interior is defined by an absence of mass flux (Neumann condition) (Eq.2) and the volatile concentration at the mouth of the embayment is fixed but varies with respect to time t (Dirichlet boundary condition). The initial volatile concentration $C_{init}$ along the embayment is constant, and the value should be the concentrations of volatile elements at the initiation of magma ascent. Volatile concentration at the mouth of the embayment is set by the solubility of each volatile species along a pressure related path of the magma ascent, and these constraints are entered into EMBER as a text file. For example, EMBER's default setup reads output files from SolEx [Witham et al., 2012], and VolatileCalc [Newman and Lowenstern., 2002] depending on magma types but can work with calculations made from any solubility model.

Solubility of gas species depends on T, P, magma composition and exsolved gas content ($M_0$). EMBER does not calculate the solubility of volatiles and uses an "external" solubility model like VolatileCalc [Newman and Lowenstern., 2002], Solex [Witham et al., 2012] or any other model that the user chooses to calculate the degassing paths. Since the value of $M_0$ is initially unknown, a typical calculation is done by choosing a "target exsolved gas content" thus by setting a

corresponding degassing path. EMBER works with seven solubility files accounting for $M_0$ values of 0, 0.1, 0.2, 0.4, 0.8, 1.6, 3.2 wt. %, which are supplied by the user. EMBER interpolates those seven degassing paths to find the degassing path associated with the targeted exsolved gas content. It should be noted that, when VolatileCalc-generated degassing paths are used, EMBER imposes the reference point concentrations of 0.01wt. % $H_2O$, 1 ppm $CO_2$ and 1 ppm S at P=1 bar because VolatileCalc does not model the degassing path down to one bar.

EMBER calculates all model diffusion profiles of the volatile elements following the grid search which range is defined by the user, before iteratively comparing measured and calculated profiles. First, profiles are calculated by varying three parameters for each calculation loop: constant decompression rate, initial volatile content and exsolved gas content, for each element. Parameters such as temperature, melt composition, initial pressure prior to ascent and pressure at which decompression stops are specified together with the volatile species of interest ($H_2O$, $CO_2$, S) and they are fixed for all calculations. The program calculates diffusion profiles using finite difference formulation solved with the *pdepe* function, an ordinary differential equation (ODE) solver from MATLAB.

Diffusion coefficients used in the model calculations are based on the following equations and calculated for each step of the ascent and at each point of a given

profile. Water diffusion coefficient ($D_{H_2O}$) in $m^2.s^{-1}$ for basaltic melt is given by

$$D_{H_2O} = \exp\left[-11.924 - 1.003\ln\left(C_{H_2O}\right)\right] * \exp\left[\frac{-\exp\left(11.836-0.139\ln\left(C_{H_2O}\right)\right)}{RT}\right] \quad (4)$$

where $C_{H_2O}$ is water concentration in wt. %; R, the gas constant in J.mol$^{-1}$.K$^{-1}$ and T, the temperature in Kelvin [Freda et al., 2003]. For melt with intermediate composition (55 < $SiO_2$ < 70 wt. %), the water diffusion coefficient ($D_{H_2O_t}$ in $m^2.s^{-1}$) is calculated using a combination of equations (5a-i), from Ni and Zhang [2018], as previously used by Newcombe et al. [2020]:

$$D_{H_2O_t} = D_{H_2O_m}\left(1 - \frac{dX_{OH}}{2dX}\right) + D_{OH}\frac{dX_{OH}}{2dX} \quad (5a)$$

$$D_{H_2O_m} = D_0\exp(aX) \quad (5b)$$

$$D_{OH} = const \quad (5c)$$

$$\frac{dX_{OH}}{2dX} = \frac{1-2X}{\sqrt{4X(X-1)\left(1-\frac{4}{K}\right)+1}} \quad (5d)$$

$$lnK = 2.6Y_{SI} - \frac{4339Y_{SI}}{T} \quad (5e)$$

$$a = -94.07 + 74.112Y_{SI} + \frac{198508-166674Y_{SI}}{T} \quad (5f)$$

$$lnD_{OH} = -16.78 - 37.428Y_{SI} - \frac{39250-27576Y_{SI}}{T} \quad (5g)$$

$$\ln\left(\frac{D_{OH}}{D_0}\right) = -56.09 - 115.93Y_{SI} + 160.54\sqrt{Y_{SI}} - \frac{3970\sqrt{Y_{SI}}}{T} \quad (5h)$$

$$lnD_0 = 8.02 - 31Y_{SI} + 2.348PY_{SI} + \frac{121824Y_{SI} - 118323\sqrt{Y_{SI}} - (10016Y_{SI} - 3648)P}{T} \quad (5i)$$

with $Y_{SI}$ the mole fraction of Si among all cations, $D_0$ a diffusion parameter in $m^2.s^{-1}$ , $K$ the equilibrium constant, $X$ the mole fraction of each species, P in GPa, T in Kelvin, $a$ is a dimensionless parameter, $D_{OH}$ the OH diffusivity in $m^2.s^{-1}$, $D_{H_2O_m}$ the molecular $H_2O$ diffusivity in $m^2.s^{-1}$, and $D_{H_2O_t}$ the total $H_2O$ diffusivity in $m^2.s^{-1}$.

For rhyolitic melt, the water diffusion coefficient (in $\mu m^2.s^{-1}$ ) is given by,

$$D_{H_2O} = C_{H_2O}\exp(10.49 - \frac{10.661}{T} - \frac{1.772P_t}{T}) \quad (6a)$$

for low (≤ 2 wt. %) water melt, where $P_t$ is the pressure in MPa at time $t$ [Zhang and Behrens., 2000]. However, if the water content is high (from 2 to 8 wt. %), diffusion coefficient is calculated by:

$$D_{H_2O} = X\exp(m)\left\{1 + \exp\left[56 + m + \mathrm{X}\left(-34.1 + \frac{44620}{\mathrm{T}} + \frac{57.3\mathrm{P_t}}{\mathrm{T}}\right) - \sqrt{\mathrm{X}}\left(0.091 + \frac{4.77*10^6}{\mathrm{T^2}}\right)\right]\right\} \quad (6b)$$

where $m = -20.79 - 5030/T - 1.4\,P_t/T$ , and $\mathrm{X} = \left(C_{H_2O}/18.015\right) / \left[C_{H_2O}/18.015 + \left(100 - C_{H_2O}\right)/32.49\right]$ [Zhang and Behrens., 2000]. The diffusion coefficient of $CO_2$ ($D_{CO_2}$), in $m^2.s^{-1}$ , is given by:

$$D_{CO_2} = \exp\left[-14.34 - \frac{17360 - 0.6527P_t}{T} + \left(-0.7171 + \frac{1436.8}{T}\right) C_{H_2O}\right] \quad (7)$$

for basalts to rhyolites [Nowak et al., 2004; Zhang et al., 2007]. The program also calculates diffusion coefficient of S ($D_S$), in $m^2.s^{-1}$ :

$$D_S(i) = \exp\left(-8.21 - \frac{27692 - 651.6\, C_{H_2O}}{T}\right) \quad (8)$$

[Zhang et al., 2007]. It is to be noted that the sulfur diffusivity determined by Zhang et al. [2007] is based on basaltic melts under reduced conditions (QFM-3; Freda et al., 2005).

### 2.3.2 Best fit determination

The second part of the code compares a measured concentration profile to a series of calculated ones (with N set of parameters) to find the best fit and its associated parameters (i.e. grid search). EMBER favours the grid search over other more efficient optimization methods (*e.g.* gradient search method), because with the mixture of diffusion of dissimilar species, it is not clear *a priori* if there will always exist a unique solution. While computationally intensive (and inefficient), we consider it is more suitable to take an approach of "calculate-all". The best fit is determined by comparing the dimensionless normalized residual square error ($NErr_j$) for each $j$ of N sets of parameters:

$$NErr_j = \sum_i \frac{1}{u_j{}^2}(C_{ij} - Cs_{ij})^2 \quad (9)$$

where $u_j$ is the analytical measurement uncertainty applied at the highest volatile concentration measured in the embayment, usually at the interior of the embayment (*i.e*: an uncertainty of 5% of $Cs_{ij}\_max$); $i$ denotes discrete points

along the distance to the embayment mouth, $C_{ij}$ is the calculated concentration and $Cs_{ij}$ is the measured concentration. Among the generated profiles, the one that gives the minimum $NErr_j$ is the best fit. EMBER calculates the parameters associated with the profiles of each volatile species separately and then constrained by all volatile species. One may calculate $NErr_j$ by considering the "weighting and scaling of the error" of each volatile (further details can be found in part 4.5). By doing so, the program first calculates $NErr_j$ values without dimensions thanks to $u_j$. The term $u_j$ effectively constrains the "weight" of three diffusion profiles ($H_2O$, $CO_2$, and S) as measurements with better uncertainty (in relative term) have a stronger influence to the sum total of three $NErr$. EMBER then scales the $NErr$ values between each volatiles before adding them. If one chooses not to weight and scale each volatile species' error, $u_j = 1$.

EMBER assesses statistical variations of $NErr$ by a Monte Carlo simulation accounting for the uncertainty of the measurement C $\pm \sigma$, using a Gaussian distribution random function to generate m iterations of possible profiles within measurement uncertainties. Therefore, for a parameter set (*i.e.* case j), there is m number of $NErr$ computed by comparing a calculated profile against m numbers of the randomly generated profiles $Cs_i + \varepsilon$ (Figure 2-1, Step 1). A similar approach is taken for the uncertainty of the distance of each measurement point: $x$. The result of this simulation is represented by a mean ($Nerr\_m$) and its related 1-σ confidence interval for a parameter set j (Figure 2-1, Step 2).

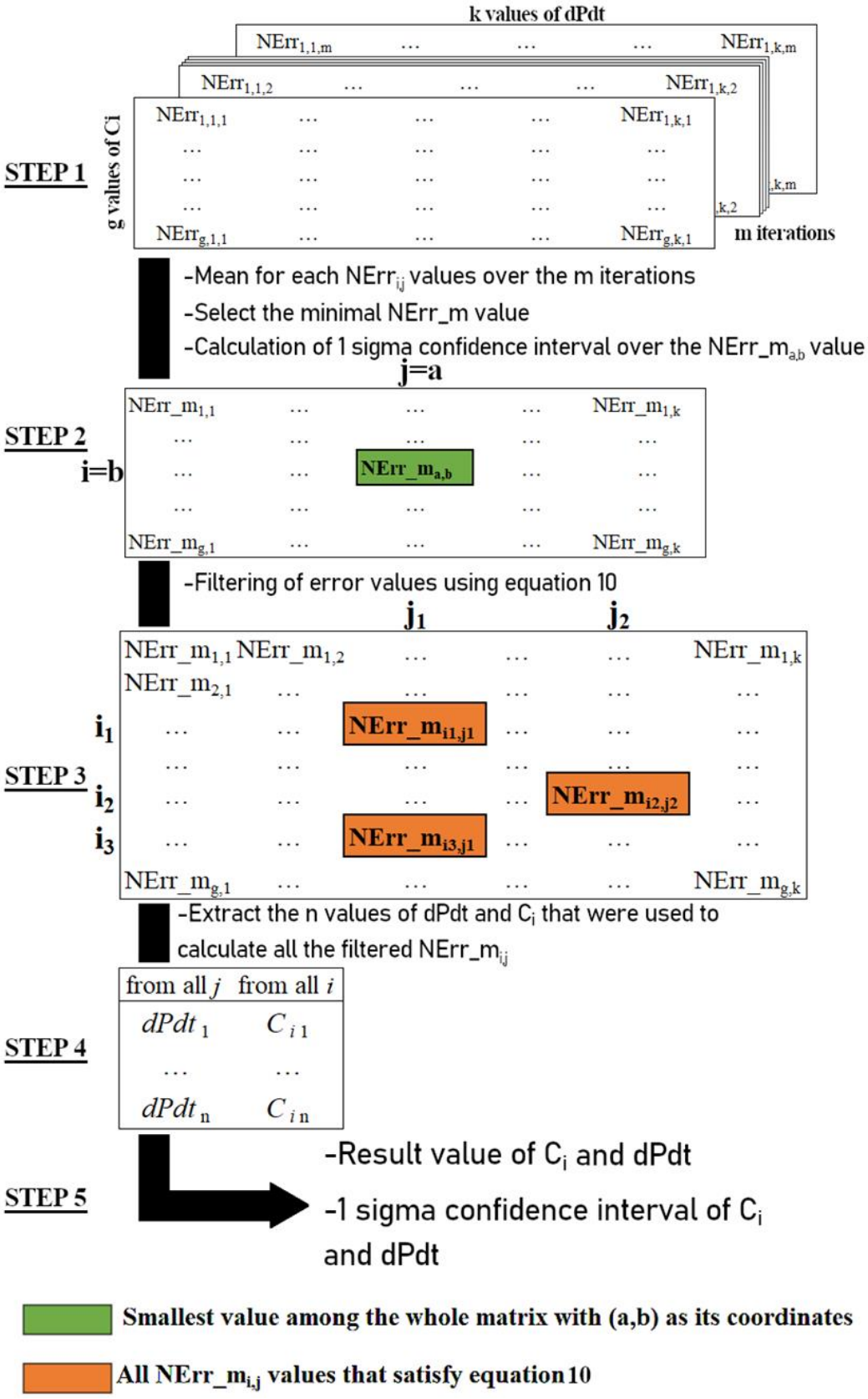


***Figure 2-1*** *: Flow chart showing the calculation steps used in EMBER to determine the parameters and associated errors resulting in the best fit of natural volatile diffusion profiles. The outputs are a decompression rate and an initial (dissolved) volatile concentration as well as their associated*

*confidence interval. This process of calculation is repeated for each value of exsolved volatile content ($M_0$). Estimation of the $M_0$ value and its related uncertainty is done in a similar manner but by considering the range of $M_0$ variation as the 4th dimension of the starting matrix.*

### 2.3.3 Propagation of errors

The uncertainties on the fit parameters $Ci,\ dPdt\ and\ M_0$ (to a lesser extent) are assessed by the statistical distributions of the parameters that are extracted from the calculated profiles $y$ that satisfy the following condition (Figure 2-1. Step 3):

$$\Pr(a - \sigma_1 \leq y \leq a + \sigma_2) = 68\% \quad (10)$$

Here, $a$ is the value for which $Nerr\_m$ is the smallest, and $\sigma_1\ and\ \sigma_2$ respectively the lower and upper boundaries of the confidence interval, calculated using the *prctile* MATLAB function. For every j calculated profiles (with a set of parameters), there is a corresponding $NErr$. Equation (10) states that there are cases of calculated profiles for which $NErr$ is within the expected uncertainty. EMBER extracts the corresponding parameters (dPdt and $C_i$) and reports the distribution of values as mean and 1-σ confidence interval, which are the best fit parameters and an associated uncertainty (Figure 2-1, Step 4 and 5). In consequence, measurement uncertainties must be entered by the user in EMBER because of the Monte Carlo error propagation. An uncertainty on the distance between two measurement spots is set by default at ±2 µm and can be changed to whichever value the user requires, down to 0 µm if needed.

## 2.4 **Examples of model outputs**

### 2.4.1 Organization of the graphical user interface

EMBER runs inside a user-friendly Graphical User Interface (GUI) upon execution of the application file. The GUI is separated in two parts: the input section, dedicated to generating the grid search and decompression conditions (left hand side Part 1, panels a, b, c; Fig.2-2), and the results section dedicated to displaying the results once calculation is terminated (Part 2, panels a, b; Fig. 2-2). Panel 2c displays a process log during the calculations. Figure 2-3 shows the result of a simulation using the volatile profiles measured in an embayment from the study of Ferguson et al. [2016] as an example. Unticking the "Weighting and scaling of error" checkbox will remove the scaling of NErr. The $u_j$ parameter from equation (8) is set to 1 in this case and NErr is not scaled before being added for the cumulative error calculation. In such cases, as all concentrations are treated as weight percent internally, the $H_2O$ profile will usually weight more than the others as it usually records much larger variations in absolute concentration.

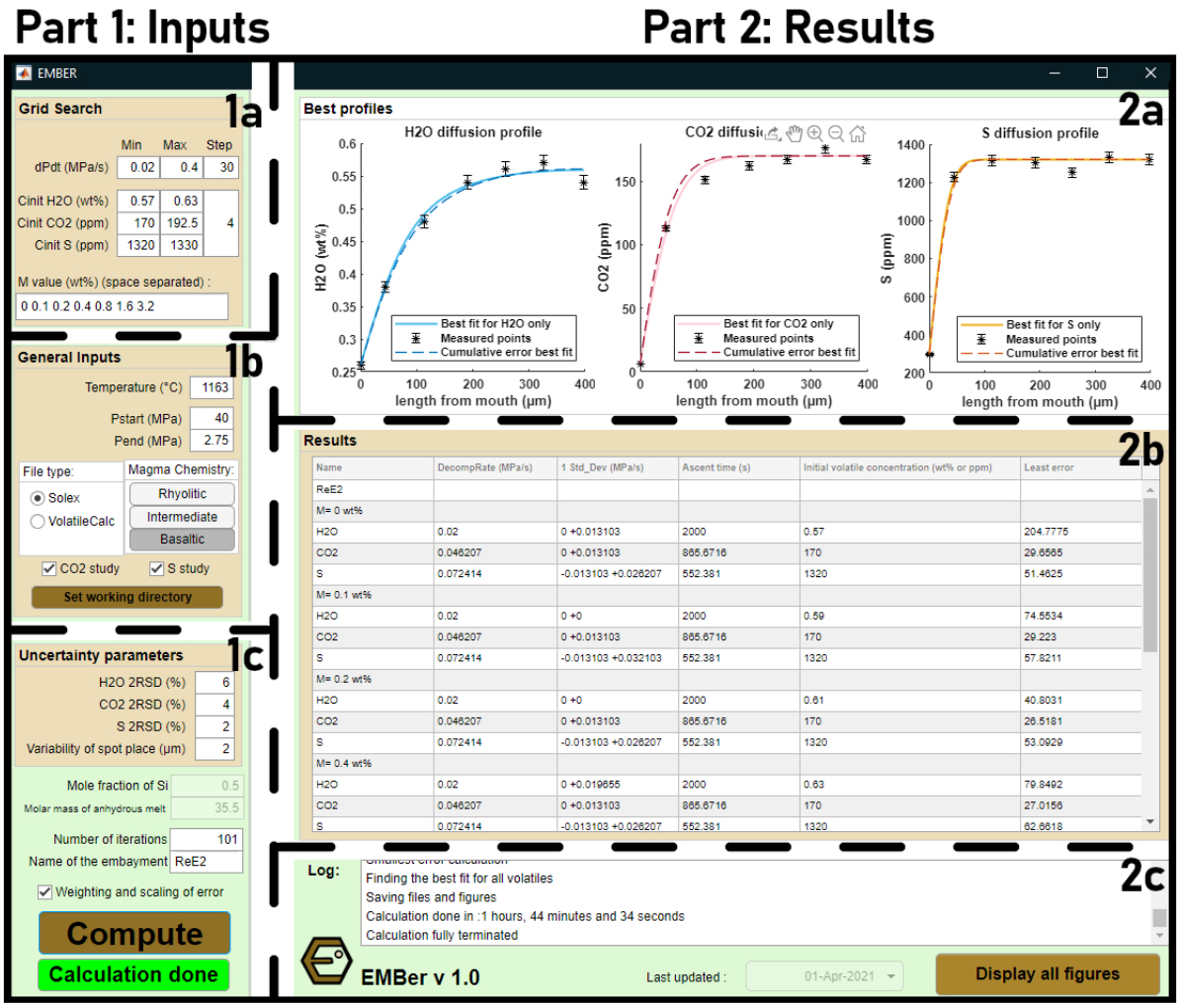


***Figure 2-2**: A display example of EMBER's GUI after a cycle of calculations. Input parameters are entered on the left panel (part 1) and results are displayed on the right (part 2). The input section is divided in three main parts, the grid search definition (1a), the main parameters and model selection (1b), and the parameters for the Monte-Carlo simulation (uncertainty and number of iterations) (1c). The result section is in three parts: comparison between best fit and natural diffusion profiles (2a), the result parameter of each best fit (2b) and the log section to follow the evolution of the calculation (2c). Clicking on the "Display all figures" once the program is done with the calculation will display best fits for each exsolved volatile content value and for each studied volatile species. It also displays three 3D-plots, of the evolution of the calculative error for each volatile (1) vs. the decompression rate and initial concentration, (2) the evolution of the decompression rate vs. exsolved volatile content and initial volatile concentration for each studied volatile species and (3) the evolution of the cumulative error vs. decompression rate and exsolved volatile content (Figure 2-3 ).*

### 2.4.2 Outputs of the calculation

Figures generated by EMBER have two purposes: (1) to display the results of the calculation and (2) to track the variation of the best-fit estimation with parameters from the grid search such as $M_0$ or $C_i$. Figure 2-3a shows the influence of the exsolved gas content to the resulting best-fit diffusion profile. Other parameters can be tested. For example, the number of volatile species fitted at once (single or up to three, solid line or dashed line, respectively; Fig. 2-3b) also influences the resulting best-fit profile. Figure 2-3c shows the sensitivity of the cumulative error over decompression rate and exsolved gas content ($M_0$). Figure 2-3d shows the influence of the initial concentration on each volatile best-fit error calculation.

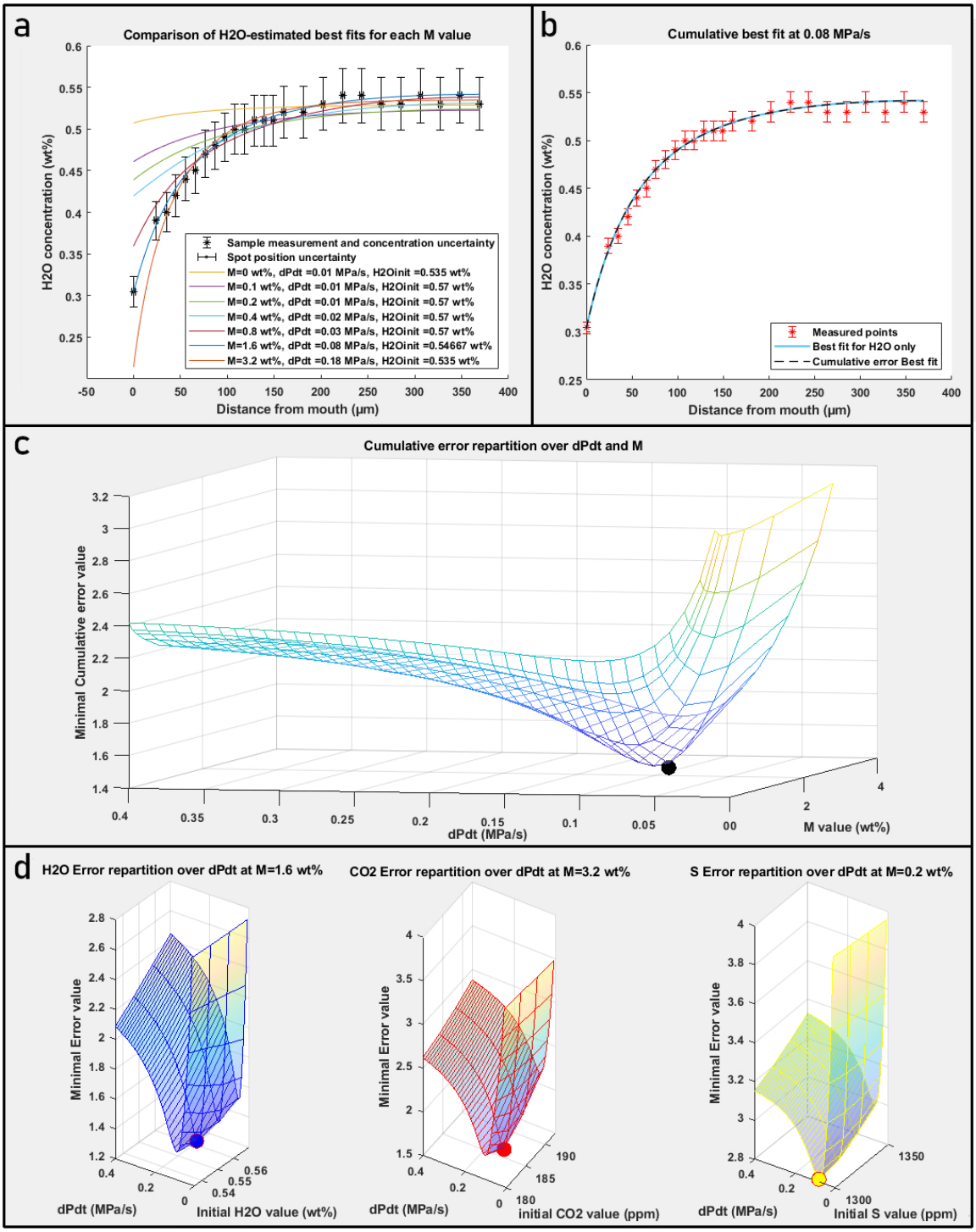


***Figure 2-3****: Subset of plots generated from a calculation on the 1500 CE Kīlauea reticulite ReaE1 studied previously by Ferguson et al. [2016]. (a) Influence of exsolved volatile content $M_0$ on best fit diffusion profiles of $H_2O$. Initial parameters from the grid search are listed in the caption. (b) Best fit diffusion profiles calculated by considering $H_2O$ only (solid line) or all studied species (dashed lines). (c) Evolution of the cumulated scaled $log_{10}$ (NErr_m) values over a range of decompression rates and exsolved volatile contents. (d) Evolution of the NErr_m value for each volatile over a range of decompression rates and initial volatile contents. The NErr_m values are in a $log_{10}$scale. The values of interest, linked to the smallest error value, are highlighted by a blue, red or yellow dot for $H_2O$, $CO_2$ and S respectively (d), and a black dot for the cumulative error (c).*

Each figure generated is saved in a unique file (.fig) directly openable with EMBER. Along with the figures, EMBER also produces four Excel (.xls) files (.csv for Mac). They contain the input parameters, the diffusion profiles of each best case, for every decompression rate with the best $C_i$ and $M_0$, and a copy of the results for each volatile with the respective exsolved gas content.

## 2.5 **Calculation and performance test**

### 2.5.1 *A priori* requirements

As with all computational software, meaningful results in EMBER will only be achieved with an appropriate dataset. Investigations should be limited to entirely glassy embayments, sampled from rapidly quenched deposits (e.g., <2 cm sized tephra), exhibiting a geometry that is close to that of a cylinder with constant radius. More complex geometries would void the core assumption of unidirectional diffusion and necessitate 3D diffusion modeling. [e.g., deGraffenried and Shea., 2020], which is not currently supported by EMBER. The longer the embayment, the more likely it is to display a concentration plateau in the diffusion profile indicative of $C_i$ and the starting pressure of ascent ($P_{Start}$). In absence of such condition, we recommend the user to determine $P_{Start}$, $C_i$ and T from melt inclusions and geo-thermobarometry studies. Finally, volatile

concentration measurements on surrounding glass are required to assess $P_{end}$, the pressure of quenching.

While we used VolatileCalc and SolEx as the main degassing path generators in the examples below, it should be noted that EMBER can also read degassing paths from any other software as long as the input files comply with the required format (see the tutorial in the additional instructions). Hence, the choice of degassing path software is ultimately up to the user's preference.

### 2.5.2 Comparison with previous studies

We re-analysed the natural volatile diffusion profiles in embayments from previous studies, to assess the quality of EMBER's decompression rate calculation: from the 1980 Mt St Helens [Humphreys et al., 2008], 1974 Fuego [Lloyd et al., 2014], 1500, 1650 and 1959 Kīlauea [Ferguson et al., 2016], 27 ka Taupo [Myers et al., 2018], 767 ka Long Valley [Myers et al., 2018], 2 Ma Yellowstone [Myers et al., 2018], 2017-2018 Ambae/Aoba [Moussallam et al., 2019], Late Bronze Age (LBA) Santorini [Myers et al., 2021] and December 2018 Ambrym [Moussallam et al., 2021] eruptions. We used the uncertainties reported in each study when provided. Also when provided, we directly used the specific grid search (e.g. Ferguson et al. [2016] provide a range of $M_0$). Otherwise, we estimated the possible range of grid search from the reported uncertainties for decompression rates and initial concentrations. Degassing paths were calculated

respecting P, T, and volatile contents used in the original studies (typically, we use SolEx or VolatileCalc when authors specified it). Similarly, the re-analysed results were calculated using the same set of values for $M_0$ as the original literature data to which they are compared. In detail this was $M_0$ = 0.1, 1.6, 1.6, 0.8 wt. % respectively for IkiE1, ReticE1, ReticE2 and KeaE1 [Ferguson et al., 2016], $M_0$ = 0.4, 0, 0, 3.2 wt. % respectively for AF2, AD5, AE38 and PG11 [Moussallam et al., 2021] and $M_0$ = 0 wt. % for all embayments from Ambae [Moussallam et al., 2019]. For all other studies of which the exsolved gas content was not specified we used $M_0$ = 0 wt. %. In some cases [Myers et al., 2018], we limited our tests to three samples from each investigated eruption, making sure to test the samples with the highest and lowest decompression rate estimation. All results except those from Ambrym were calculated with the weighting and scaling of the error. EMBER provides good fits for most diffusion profiles when volatile species are taken separately. However, when constraining eruption parameters with multiple volatile species, the software optimizes the result to show the lowest cumulative error despite worsening several fits. The comparison between literature data and EMBER calculated decompression rate is shown in Figure 2-4.

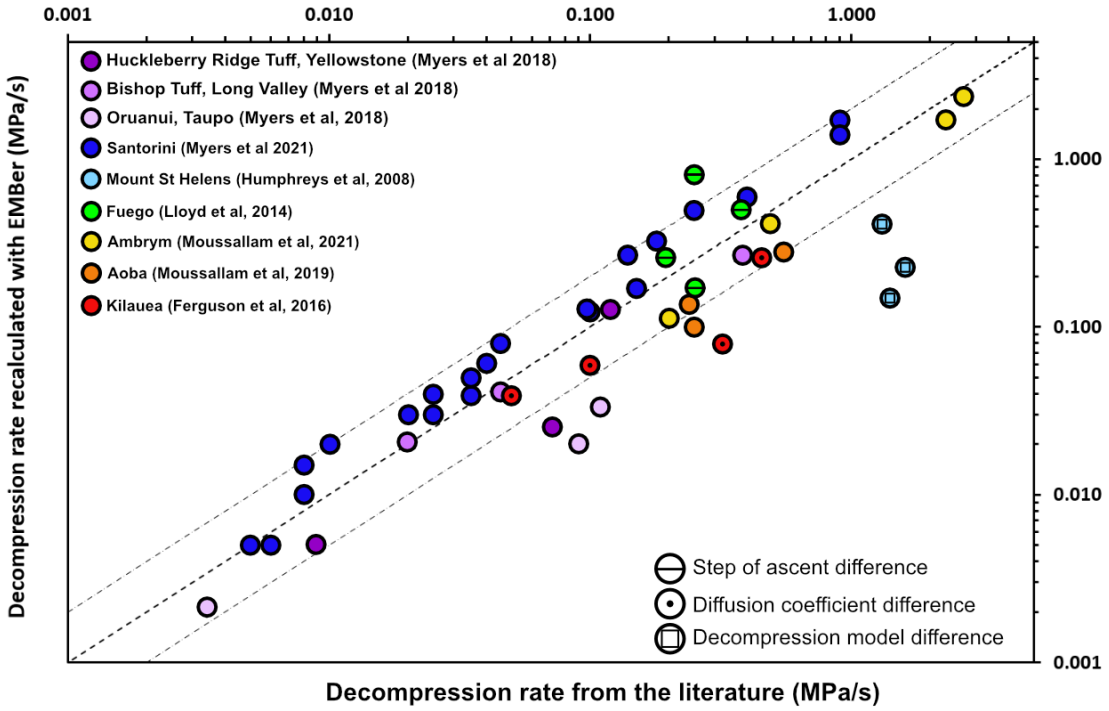


***Figure 2-4*** *: Comparison between recalculated data with EMBER using a combination of $H_2O$, $CO_2$ and S according to the each initial study, and previous estimation from the literature. EMBER estimations are comparable with literature estimates with a few systematic differences (see text for details). Dashed line indicates the 1:1 ratio and thin solid lines indicate 2:1 and 0.5:1 ratios. Results from EMBER were acquired taking the input conditions of the respective original studies. Calculations for samples from Lloyd et al. [2014] were made using their original $H_2O$ diffusion coefficient. All the results displayed are calculated for $M_0$=0 excepted when original studies provided a range of $M_0$ [Ferguson et al., 2016]. EMBER calculations were made using the "weighting and scaling of error" option which is a source of difference with previously reported literature decompression rate.*

There is a good agreement between EMBER results and most literature values. Data from the 1980 Mt St Helens eruption [Humphreys et al., 2008] show consistent disparity between the published decompression rates and EMBER's. This difference is due to significantly different boundary conditions of this study compared with the original. The model from the original study [Humphreys et al., 2008] fixed the final concentration at the mouth of the embayment, prior to the ascension. Since the diffusion phenomenon is gradient-dependent, imposing a

high concentration gradient at the beginning of the simulation should lead to faster volatile diffusion and a higher decompression rate estimation. This is a critical simplification leading to significant differences in the calculated decompression rate. Other minor differences observed between our re-analysis and earlier decompression rate estimates come from (1) the use of a different $H_2O$ diffusion coefficient as well as a single episode of ascent in all our calculation (as opposed to two-step ascent [Lloyd et al., 2014]), (2) the calculation of diffusion coefficient (e.g., taking into account the change of diffusivity due to $H_2O$ diffusion or choosing different equations of diffusivity) and (3) the weighting and scaling of error associated with each volatile diffusion profile in all our calculations (Fig. 2-4).

### 2.5.3 Monte Carlo simulation

We ran tests on three samples with variable number of Monte Carlo iterations (m=3, 11, 101, 501 and 1001) to determine the lowest number of the iterations to achieve stable assessment of uncertainties: BT251, a rhyolite from Long Valley, ReE2, a reticulite from 1500 CE Kīlauea lava fountain and AO02, a basalt from phase 2 of the 2017-2018 eruption of Ambae. For BT251, the representation gradually acquires the shape of a pseudo-gaussian distribution with increasing iteration counts. The median and mean values of all filtered decompression rate do not change significantly with increasing iterations (Fig 2-5) and a stability of the data distribution is quickly achieved (for m=11). For ReE1, the precision of

the nanoSIMS measurements and the low decompression rate leads to a stable calculation and a needle shaped histogram even for m=3, suggesting that the results are well constrained. For AO02 the shape of the histogram is pointy, unimodal and skewing right with a long tail. With higher dP/dt values (i.e., sharper diffusion profiles), modelled diffusion profiles become more and more similar, making it harder for the software to find the best solution. This results in a skewed solution histogram with a long tail and a more noticeable difference between mean and median value. For such cases, stability is reached for m = 101. We recommend 101 iterations (EMBER default iteration value) as it was enough to reach a stable solution for our most uncertain case.

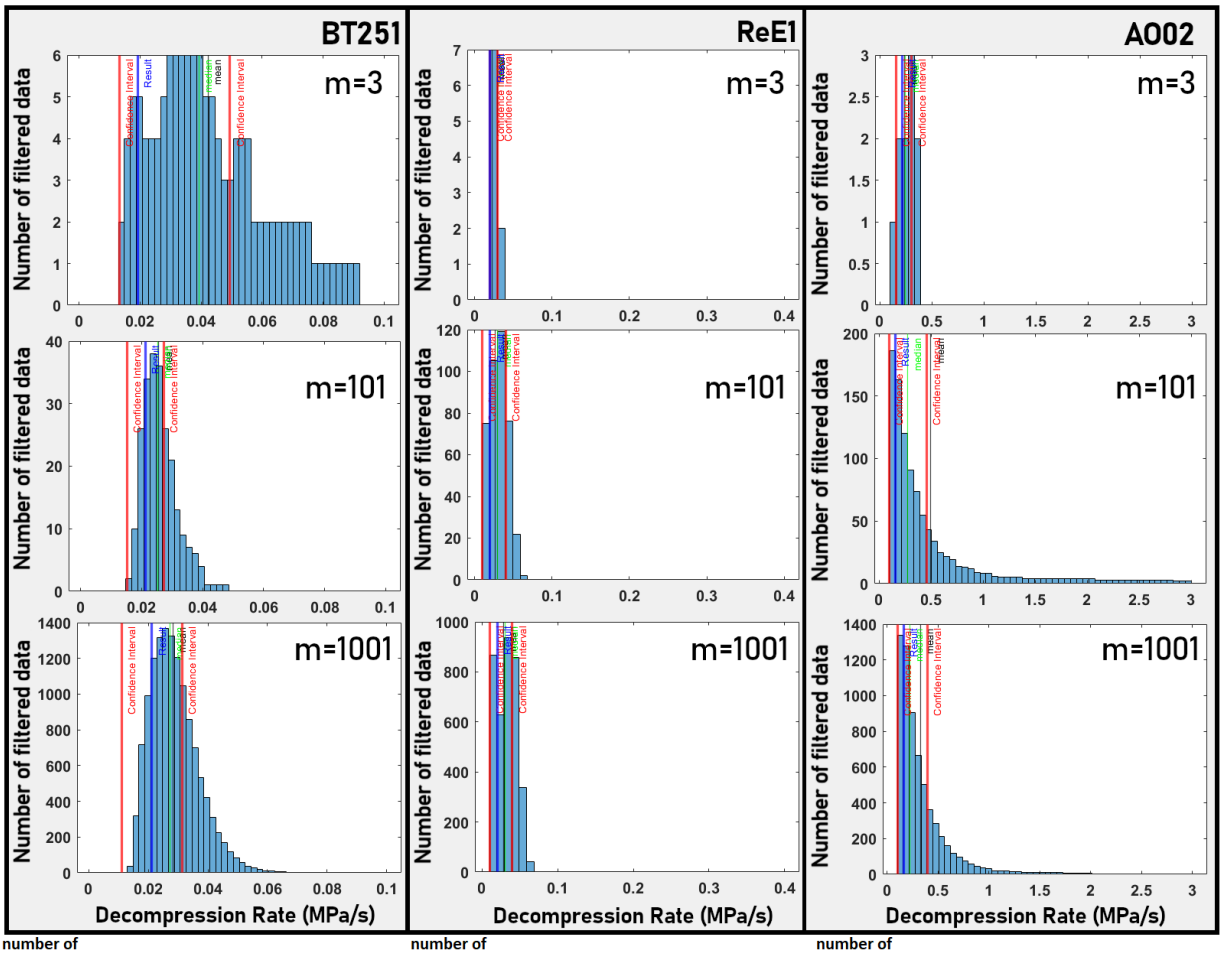


| number of iterations | 3 | 11 | 101 | 501 | 1001 |
|---|---|---|---|---|---|
| **BT251** | | | | | |
| Result | 0.019 | 0.021 | 0.021 | 0.021 | 0.021 |
| Median | 0.039 | 0.023 | 0.025 | 0.027 | 0.027 |
| Mean | 0.042 | 0.022 | 0.026 | 0.027 | 0.028 |
| Uncertainty | -0.006 | -0.004 | -0.006 | -0.008 | -0.01 |
| | +0.03 | +0.004 | +0.006 | +0.008 | +0.01 |

| number of iterations | 3 | 11 | 101 | 501 | 1001 |
|---|---|---|---|---|---|
| **ReE1** | | | | | |
| Result | 0.020 | 0.020 | 0.020 | 0.020 | 0.020 |
| Median | 0.020 | 0.020 | 0.030 | 0.020 | 0.030 |
| Mean | 0.022 | 0.023 | 0.027 | 0.023 | 0.028 |
| Uncertainty | -0 | -0 | -0.01 | -0 | -0.01 |
| | +0.01 | +0.02 | +0.02 | +0.03 | +0.02 |

| number of iterations | 3 | 11 | 101 | 501 | 1001 |
|---|---|---|---|---|---|
| **AO02** | | | | | |
| Result | 0.218 | 0.218 | 0.159 | 0.159 | 0.159 |
| Mean | 0.248 | 0.218 | 0.278 | 0.218 | 0.218 |
| Median | 0.236 | 0.250 | 0.498 | 0.287 | 0.326 |
| Uncertainty | -0.059 | -0.059 | -0.059 | -0.059 | -0.059 |
| | +0.089 | +0.202 | +0.296 | +0.178 | +0.237 |

***Figure* 2-5 :** *Statistical repartition of all filtered decompression rate values with increasing iteration count of the Monte Carlo approach, using $H_2O$ only (AO02), $H_2O$ and $CO_2$ (BT251) and all three volatile species (ReE1). The repartition gradually acquires a more pronounced shape. The red bars indicates the 1-σ confidence interval of those decompression rates while the blue, green and black ones respectively indicate the best-fit result, the median and the mean. Calculation is done with fixed initial concentration and exsolved volatile content. All displayed data are in MPa/s*

## 2.5.4 How well does EMBER constrain $M_0$?

Calculation of the exsolved gas content has been introduced within the embayment method with the calculations made by Ferguson et al. [2016]. They noted it had a significant influence on their calculation of decompression rate,

which was confirmed by later studies and by EMBER (Fig 2-3a and Fig 2-6a). The effect is mostly a result of the exsolved gas content having a large influence on the degassing trend. From our investigation of literature data, we see that a change of $M_0$ from 0 to 3.2 wt. % can cause the decompression rate estimation to increase 10-fold (Fig 2-6 (a)). This variation is most pronounced on $H_2O$ profiles in embayments of basaltic composition (Fig 2-6 (a), (b), (c)). Except for these few cases, the impact of $M_0$ is hardly significant enough for it to be accurately determined using only diffusion profiles (the associated error frequently covering the entire range studied).

The change of decompression rate in response to variable $M_0$ illustrates the importance of $P_{end}$ (Fig. 2-6 (d)) (which must be determined from measured data) and the critical influence of the modelled degassing path.

The best fit $M_0$ values are directly affected by the choice of $P_{end}$ (Fig. 2-6 (d)) which must be determined from measured data. Taking as an example, the calculation of one profile from Ferguson et al. [2016] which ends at a specified quenching pressure $P_{end}$ = 2.75 MPa. Using the decompression path (from SolEx) for $M_0$<1.6 wt. %, the resulting $H_2O$ concentration at P=2.75 MPa would be higher than $C_S(x = 0)$, the measured concentration at the mouth of the embayment approximated with the glass measurement, by up to 0.20 wt. %. Synthesized diffusion profiles in this case cannot reproduce the concentration at the mouth of the embayment for $M_0$<1.6 wt. %. Because of this limitation, as shown in figure

2-3a, only a degassing paths associated with at the best fit $M_0$ value could match the whole diffusion profile by fitting the concentration at the mouth. It should be noted that if a different $P_{end}$ is chosen, it is possible that EMBER finds another best-fit $M_0$ (Fig 2-6 (d)). Therefore, we advise the user to be cautious when choosing $P_{end}$ for decompression rate modelling, especially in case constrained by one volatile species (Fig 2-6 (e), (f)).

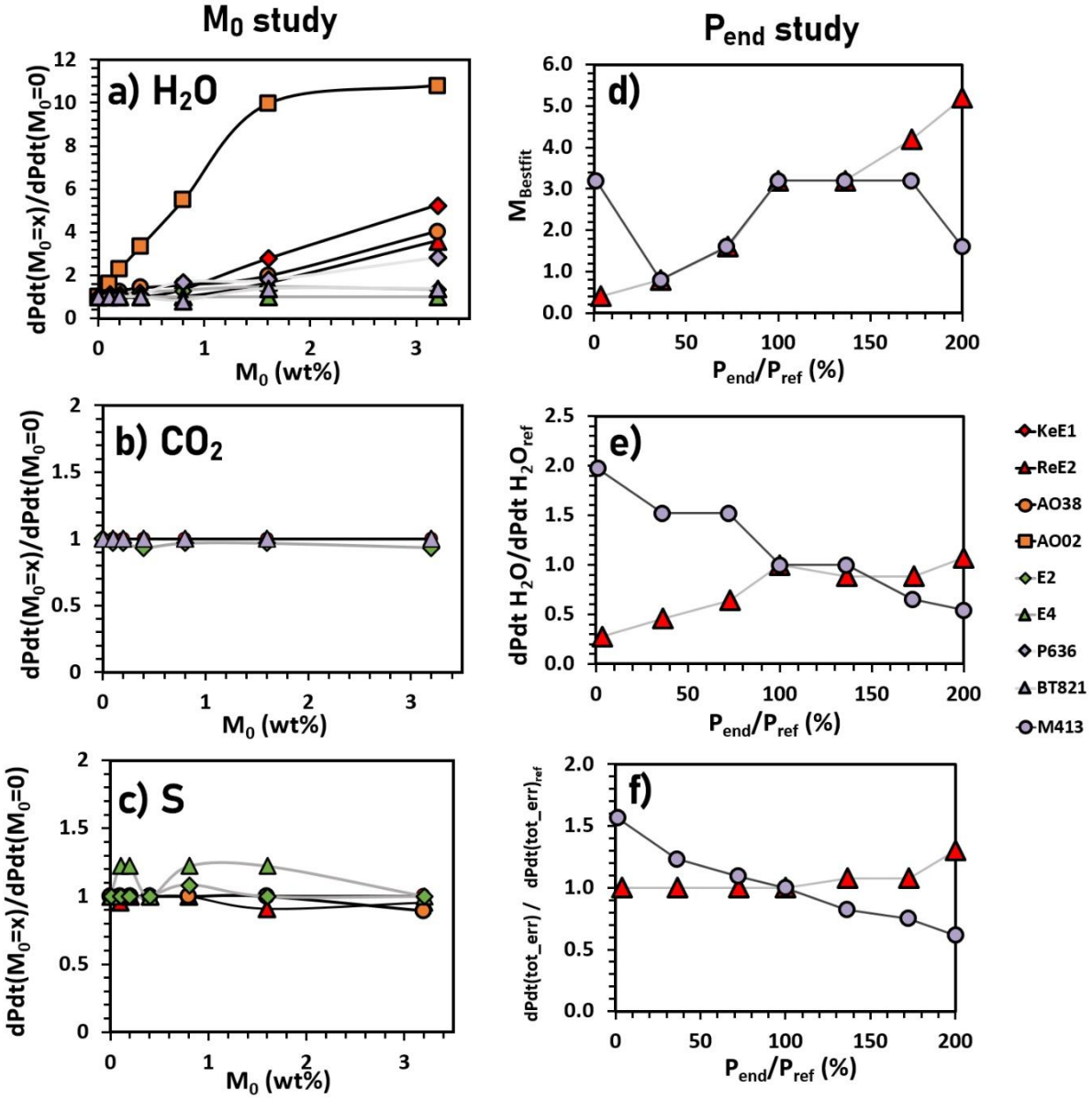


***Figure 2-6**: Evolution of modeled relative decompression rates from $H_2O$ (a), $CO_2$ (b) and S (c) as a function of the exsolved volatile content for a selection of embayments. Each case in a), b) or c) is*

*calculated with a fixed $P_{end}$, reported in Table 2-2. For figures (d), (e) and (f), $P_{ref}$ is the $P_{end}$ value displayed in Table 2-2 for ReE2 and BT251. (d) The initial exsolved volatile content needed to generate the best fit ($M_{Bestfit}$) increases for ReE2 when changing $P_{end}$ but not systematically for M413. (e) Variation of relative decompression rate modeled from the $H_2O$ diffusion profile only with $P_{end}$. (f) Variation of relative decompression rate modeled from all studied species ($H_2O$, $CO_2$ and S for ReE2, and $H_2O$ and $CO_2$ for M413) with $P_{end}$.*

### 2.5.5 Weighting and scaling of error

EMBER leaves the user the choice to, or not to, equally weigh and scale the relative contribution of each volatile profile equally, when calculating the cumulative error. For example, the study from Ferguson et al. [2016] gives equal weight ($u_j = 1$) to all three volatile species, except on a few cases. By doing so, the best fit $NErr_j$ calculated from $H_2O$ profiles is several orders of magnitude higher than the best fit $NErr_j$ calculated for $CO_2$ or S profiles. That difference is due to the range of concentration variation, as $H_2O$ usually varies within a few wt. % and $CO_2$ and S usually vary within thousands of ppm at best. Cumulative error calculation, and subsequently the best fit determination, becomes heavily dependent on the $H_2O$ $NErr_j$ value, making the constraints brought by $CO_2$ or S profiles almost negligible. Another approach is to weight the $NErr_j$ values either with analytical uncertainty [Myers et al., 2018] or maximum measured concentration in the embayment [Newcombe et al., 2020] of volatile species. Weighting the concentration with the error value nondimensionalizes the profile and gives equal weight to the quality of fit of each volatile specie. In EMBER, the $NErr_j$ values are weighted by the analytical uncertainty on each volatile

concentration. It results in an even consideration of the constraints brought by each volatile species. There are pros and cons for this choice; if one thinks the S degassing model to not be as accurate as the $H_2O$ degassing model for instance, one may choose not to weigh and scale the errors. The user ultimately must make the choice and it should be reported. As previously noted, constraining decompression rates with multiple volatile species tend to provide less accurate fits in some cases. We also stress that decompression rates obtained from $CO_2$ for instance can be one to two order of magnitude lower compared to $H_2O$. This brings forth the interrogation whether the different volatile species record the same constant decompression rate from a unique embayment or not.

### 2.5.6 Recalculation of decompression rates

In the previous section, we presented EMBER calculation results using initial conditions ($C_i$, $M_0$ if studied, range of dPdt, $P_{end}$, $P_{start}$) directly from the original literature studies to demonstrate the quality of EMBER and its ability to reproduce the former literature results. Now, we use EMBER to reprocess the raw data from the literature, but this time using a uniform protocol that takes into account the following parameters: the presence of exsolved gas, the same set of formulas for diffusion coefficient calculation, a model with a single step ascent and an initial volatile element concentration, determined from the concentration plateau (Table 2-2). Detailed modelled profiles of each embayments can be found in the supplementary materials. We restricted the calculations to 3 profiles per eruption

for Myers et al. [2018], including the ones associated with the highest and lowest decompression rate recorded, and to 5 profiles for Myers et al. [2021].

***Table 2-2*** *: Re-calculated decompression rates with initial conditions and related eruption parameters. Ascent rates were calculated with density values from each original studies using the equation* $Asc\_rate = (Decomp\_rate/9.81 \times Crustal\_density) \times 10\text{^}6$ *with Decomp_rate in MPa/s, Asc_rate in m/s and the crustal density in kg/m*$^3$

| | Decompression rate (Mpa/s) | | | | Ascent rate (m/s) | Initial concentration | | | $M_0$ (wt%) | Time of ascension (s) | Pstart (MPa) | Pend (MPa) | T(°C) | Magnitude |
|---|---|---|---|---|---|---|---|---|---|---|---|---|---|---|
| | $H_2O$ based | $CO_2$ based | S based | all species | | $H_2O$ (wt%) | $CO_2$ (ppm) | S (ppm) | | | | | | |
| ***Ferguson et al. (2016)*** | | | | | | | | | | | | | | |
| IkiE1 | 0.03 $^{+0.01}_{-0.00}$ | 0.02 $^{+0.00}_{-0.00}$ | 0.04 $^{+0.01}_{-0.00}$ | **0.04** $^{+0.00}_{-0.00}$ | 1.4 | 0.60 $^{+0.00}_{-0.00}$ | 300 $^{+0}_{-0}$ | 1390 $^{+0}_{-0}$ | 0.1 $^{+0.1}_{-0.0}$ | 2755 | 107 | 0.1 | 1192 | 1.5 |
| ReticE1 | 0.08 $^{+0.03}_{-0.01}$ | 0.09 $^{+0.02}_{-0.01}$ | 0.08 $^{+0.04}_{-0.02}$ | **0.08** $^{+0.02}_{-0.01}$ | 2.9 | 0.55 $^{+0.00}_{-0.00}$ | 184 $^{+0}_{-0}$ | 1316 $^{+0}_{-0}$ | 1.6 $^{+0.0}_{-0.0}$ | 553 | 47 | 2.75 | 1163 | 2.5 |
| ReticE2 | 0.07 $^{+0.03}_{-0.01}$ | 0.03 $^{+0.01}_{-0.00}$ | 0.40 $^{+0.00}_{-0.03}$ | **0.06** $^{+0.02}_{-0.00}$ | 2.1 | 0.57 $^{+0.00}_{-0.00}$ | 170 $^{+0}_{-0}$ | 1320 $^{+0}_{-0}$ | 3.2 $^{+0.0}_{-0.0}$ | 676 | 40 | 0.1 | 1163 | 2.5 |
| KeaE1 | 0.28 $^{+0.10}_{-0.05}$ | 0.11 $^{+0.04}_{-0.01}$ | 0.35 $^{+0.25}_{-0.16}$ | **0.26** $^{+0.05}_{-0.04}$ | 9.3 | 0.52 $^{+0.03}_{-0.00}$ | 265 $^{+5}_{-0}$ | 1415 $^{+5}_{-0}$ | 1.6 $^{+0.0}_{-0.0}$ | 185 | 50 | 2 | 1160 | 2.6 |
| ***Moussallam et al. (2019)*** | | | | | | | | | | | | | | |
| AO2 | **0.46** $^{+0.27}_{-0.18}$ | | | | 16.0 | 1.32 $^{+0.00}_{-0.00}$ | | | 0.1 $^{+0.1}_{-0.0}$ | 110 | 50 | 0.1 | 1150 | 3.3 |
| AO13 | **0.12** $^{+0.03}_{-0.01}$ | | | | 4.2 | 1.15 $^{+0.00}_{-0.00}$ | | | 1.6 $^{+1.6}_{-1.4}$ | 253 | 30 | 0.1 | 1150 | 3.3 |
| AO38 | 0.17 $^{+0.05}_{-0.03}$ | | 0.39 $^{+0.01}_{-0.16}$ | **0.19** $^{+0.08}_{-0.07}$ | 6.7 | 1.15 $^{+0.00}_{-0.00}$ | | 403 $^{+0}_{-0}$ | 0.8 $^{+0.8}_{-0.5}$ | 237 | 45 | 0.1 | 1150 | 3.3 |
| ***Lloyd et al. (2014)*** | | | | | | | | | | | | | | |
| E1 | 0.24 $^{+0.01}_{-0.04}$ | 0.03 $^{+0.00}_{-0.00}$ | 0.01 $^{+0.00}_{-0.00}$ | **0.06** $^{+0.03}_{-0.02}$ | 2.2 | 4.00 $^{+0.00}_{-0.00}$ | 100 $^{+0}_{-0}$ | 1500 $^{+0}_{-0}$ | 0.1 $^{+0.3}_{-0.1}$ | 3333 | 202 | 2 | 1030 | 4.4 |
| E2 | 1.07 $^{+0.29}_{-0.26}$ | 0.10 $^{+0.00}_{-0.00}$ | 0.13 $^{+0.34}_{-0.03}$ | **0.30** $^{+0.03}_{-0.09}$ | 11.1 | 2.20 $^{+0.10}_{-0.00}$ | 150 $^{+3}_{-0}$ | 1900 $^{+33}_{-0}$ | 0 $^{+0.2}_{-0.0}$ | 175 | 54.6 | 2 | 1030 | 4.4 |
| E3 | 0.92 $^{+0.47}_{-0.21}$ | 1.47 $^{+0.03}_{-0.59}$ | | **1.10** $^{+0.32}_{-0.29}$ | 40.9 | 2.80 $^{+0.00}_{-0.00}$ | 160 $^{+0}_{-0}$ | | 1.6 $^{+1.6}_{-1.2}$ | 69 | 78 | 2 | 1030 | 4.4 |
| E4 | 0.35 $^{+0.08}_{-0.05}$ | 0.28 $^{+0.13}_{-0.08}$ | 0.46 $^{+0.01}_{-0.27}$ | **0.44** $^{+0.01}_{-0.10}$ | 16.3 | 2.80 $^{+0.00}_{-0.00}$ | 170 $^{+0}_{-0}$ | 2070 $^{+0}_{-0}$ | 0.1 $^{+0.1}_{-0.0}$ | 498 | 221 | 2 | 1030 | 4.4 |
| ***Myers et al. (2018)*** | | | | | | | | | | | | | | |
| BTF7-1_RE_no_2 | **0.021** $^{+0.002}_{-0.003}$ | | | | 0.8 | 3.70 $^{+0.10}_{-0.05}$ | | | 0.4 $^{+2.8}_{-0.2}$ | 3238 | 78 | 10 | 740 | 8.5 |
| BT_F2-5_RE_no_1 | **0.041** $^{+0.011}_{-0.010}$ | | | | 1.6 | 3.80 $^{+0.00}_{-0.00}$ | | | 1.6 $^{+1.6}_{-1.4}$ | 1014 | 77 | 35 | 740 | 8.5 |
| BTF8-2_RE_no_1 | **0.273** $^{+0.061}_{-0.061}$ | | | | 10.7 | 5.00 $^{+0.00}_{-0.00}$ | | | 0.1 $^{+1.5}_{-0.1}$ | 264 | 131 | 59 | 740 | 8.5 |
| P1963-6_RE_no_1 | 0.007 $^{+0.002}_{-0.002}$ | 0.0001 $^{+0.0004}_{-0.000}$ | | **0.002** $^{+0.002}_{-0.001}$ | 0.1 | 1.80 $^{+0.00}_{-0.00}$ | 90 $^{+0}_{-0}$ | | 0 $^{+0.8}_{-0.0}$ | 3846 | 38 | 13 | 780 | 8 |
| P2305-F_RE_no_1 | **0.020** $^{+0.018}_{-0.000}$ | | | | 0.8 | 3.40 $^{+0.00}_{-0.10}$ | | | 3.2 $^{+0.0}_{-0.3}$ | 900 | 68 | 50 | 780 | 8 |
| P1970-A_RE_no_6 | 0.068 $^{+0.058}_{-0.035}$ | 0.010 $^{+0.004}_{-0.000}$ | | **0.033** $^{+0.072}_{-0.019}$ | 1.3 | 3.40 $^{+0.10}_{-0.00}$ | 90 $^{+10}_{-0}$ | | 0.1 $^{+0.7}_{-0.1}$ | 515 | 89 | 54 | 780 | 8 |
| MM4_RE_no_12 | 0.009 $^{+0.014}_{-0.004}$ | 0.001 $^{+0.000}_{-0.000}$ | | **0.005** $^{+0.000}_{-0.000}$ | 0.2 | 2.00 $^{+0.00}_{-0.00}$ | 390 $^{+0}_{-0}$ | | 0 $^{+0.1}_{-0.0}$ | 4934 | 85 | 40 | 800 | 9 |
| MM7_RE_no_10 | 0.099 $^{+0.065}_{-0.058}$ | 0.007 $^{+0.000}_{-0.000}$ | | **0.013** $^{+0.006}_{-0.006}$ | 0.5 | 2.50 $^{+0.56}_{-0.00}$ | 170 $^{+8}_{-0}$ | | 3.2 $^{+0.0}_{-0.2}$ | 467 | 71 | 25 | 800 | 9 |
| MM4_RE_no_13 | 0.069 $^{+0.045}_{-0.018}$ | 0.152 $^{+0.086}_{-0.080}$ | | **0.105** $^{+0.081}_{-0.047}$ | 4.1 | 2.80 $^{+0.00}_{-0.00}$ | 290 $^{+0}_{-0}$ | | 1.6 $^{+1.6}_{-1.4}$ | 1272 | 98 | 10 | 800 | 9 |
| ***Humphreys et al. (2008)*** | | | | | | | | | | | | | | |
| KV518b-1 | **0.16** $^{+0.00}_{-0.00}$ | | | | 6.4 | 4.60 $^{+1.66}_{-0.00}$ | | | 0 | 662 | 137 | 33 | 880 | 4.9 |
| MSH1-3 | **0.23** $^{+0.00}_{-0.00}$ | | | | 9.3 | 6.50 $^{+0.00}_{-0.52}$ | | | 0 | 481 | 137 | 27 | 880 | 4.9 |
| MSH1-6 | **0.82** $^{+0.04}_{-0.02}$ | | | | 33.3 | 6.50 $^{+0.00}_{-0.48}$ | | | 0 | 157 | 137 | 9 | 880 | 4.9 |
| ***Moussallam et al. (2021)*** | | | | | | | | | | | | | | |
| AF2 | 2.64 $^{+1.55}_{-1.27}$ | | 5.87 $^{+0.14}_{-2.96}$ | **2.64** $^{+2.41}_{-1.55}$ | 99.5 | 1.48 $^{+0.03}_{-0.03}$ | | 220 $^{+10}_{-10}$ | 3.2 $^{+0.0}_{-0.4}$ | 26 | 68 | 0.1 | 1110 | 4 |
| AD5 | 0.49 $^{+0.12}_{-0.08}$ | | 0.14 $^{+0.96}_{-0.04}$ | **0.53** $^{+0.19}_{-0.14}$ | 19.9 | 1.05 $^{+0.05}_{-0.10}$ | | 950 $^{+50}_{-100}$ | 0.1 $^{+0.3}_{-0.1}$ | 64 | 34 | 0.1 | 1110 | 4 |
| AE38 | 0.11 $^{+0.03}_{-0.02}$ | | 0.01 $^{+0.00}_{-0.00}$ | **0.11** $^{+0.04}_{-0.03}$ | 4.2 | 1.05 $^{+0.10}_{-0.00}$ | | 950 $^{+233}_{-0}$ | 0 $^{+0.2}_{-0.0}$ | 335 | 37 | 0.1 | 1110 | 4 |
| PG11 | 1.70 $^{+0.87}_{-0.59}$ | | 0.10 $^{+0.06}_{-0.00}$ | **1.70** $^{+0.86}_{-0.59}$ | 64.1 | 1.80 $^{+0.20}_{-0.10}$ | | 797 $^{+33}_{-17}$ | 1.6 $^{+1.6}_{-1.4}$ | 68 | 115 | 0.1 | 1110 | 4 |
| ***Myers et al. (2021)*** | | | | | | | | | | | | | | |
| 18R1F | **1.70** $^{+0.86}_{-0.75}$ | | | | 66.7 | 4.70 $^{+0.10}_{-0.00}$ | | | 0 | 49 | 143 | 60 | 850 | 7.4 |
| 18R1O | **1.70** $^{+0.56}_{-0.40}$ | | | | 66.7 | 4.30 $^{+0.08}_{-0.00}$ | | | 0 | 55 | 119 | 26 | 850 | 7.4 |
| 18R2O | **0.43** $^{+0.05}_{-0.05}$ | | | | 16.9 | 4.60 $^{+0.00}_{-0.00}$ | | | 0 | 274 | 120 | 2 | 850 | 7.4 |
| 20R1O | **0.47** $^{+0.01}_{-0.08}$ | | | | 18.4 | 3.35 $^{+0.05}_{-0.03}$ | | | 0 | 153 | 77 | 5 | 850 | 7.4 |
| 11R6O | **2.93** $^{+1.32}_{-1.31}$ | | | | 114.8 | 4.30 $^{+0.10}_{-0.00}$ | | | 0 | 26 | 116 | 40 | 850 | 7.4 |

### 2.5.7 The impact of calculation strategies

Our hope with developing EMBER is to minimize differences in modelling parameters (e.g., diffusion coefficients, error treatment, minimization strategy…) in future studies. It is important to realize however that differences in strategies will persist. For instance, whilst EMBER allows the user to set the exsolved gas content ($M_0$) as a free parameter to be determined by a gridsearch, some users might prefer to impose an exsolved gas content based on independent constraint. This is the case for instance of the Moussallam et al. [2019] study of the 2017-2018 Ambae eruption where, in a second set of calculations, the authors used the difference between the volatile content of the melt inclusions and the starting volatile content of the embayments to estimate the likely amount of exsolved volatiles in the system at the initiation of ascent.

Another strategy is to use the volatile content of melt inclusions as starting conditions for the diffusion model instead of the measured plateau values in the embayment interior. This was the strategy adopted by Myers et al., [2021] for the Minoan eruption of Santorini, where a fixed initial concentration of 5.2 wt. % $H_2O$ (except for one embayment at 5.6 wt. % $H_2O$) was used for all model calculations. Such strategy was also used by Humphreys et al. [2008] for Mt St Helens calculations.

In this study, we recalculated all embayment profiles using the same strategy throughout, but we do not pass judgement on the validity of one strategy over

another. Our aim is to present a dataset which is as comparable as possible. The data presented in Fig. 2-7 and Table 2-2 are hence all calculated leaving the exsolved volatile content ($M_0$) as unconstrained (i.e., as a part of the grid search) and using the plateau values in volatile content recorded in embayment interiors as the model starting conditions ($C_i$).

This difference in starting assumptions can lead to significant differences in the resulting decompression rate. Recalculating the embayment data from Myers et al., [2021] with our protocol leads to decompression rates 3 to 20 times higher. It is therefore of paramount importance that users of EMBER explicitly report their assumptions and starting conditions. We recommend that future compilations continue to reprocess original data in a consistent manner (as done here) in order to render inter-study comparison as coherent as possible.

## 2.6 Decompression rates vs eruption parameters

A recent literature compilation showed a clear relationship between magma decompression rate and whether an eruption is explosive or effusive in character [Cassidy et al., 2018]. This relationship deserves more scrutiny to establish if finer relationships between magma decompression rates and explosivity exists in nature. The VEI (Volcanic Explosivity Index), as an approximation of eruption explosivity, is related to eruption magnitude and/or plume height [Newhall and Self., 1982]. To show the utility of EMBER for the studies of volcanic explosivity,

we tested the presence (or absence) of a correlation between decompression rate and both eruption magnitude and plume height, with our reprocessed data. Previous studies have found that the eruption magnitude is positively correlated with decompression rate [Ferguson et al., 2016; Moussallam et al., 2019]. However, our compilation shows no clear global correlation between decompression rate and eruption magnitude (Fig. 2-7a).

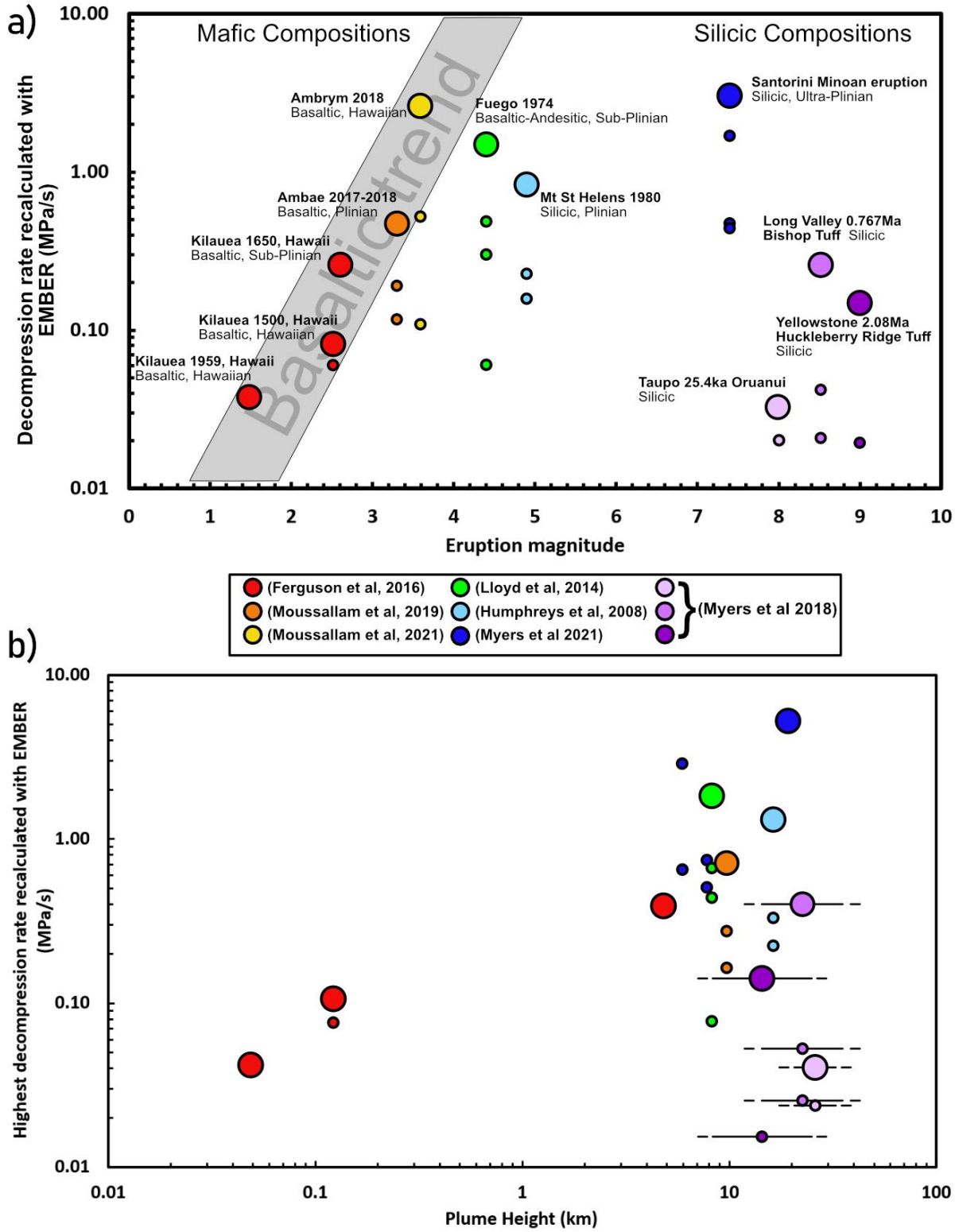


***Figure 2-7*** *: (a) Compilation of EMBER-recalculated decompression rates as a function of eruption magnitude. The bigger mark indicates the highest decompression rate estimate for each eruption. For basaltic magmas, there is a trend of increasing decompression rate related to increasing magnitude only when considering the maximum decompression rate values. The trend does not apply to rhyolitic magmas. (b) Compilation of EMBER-recalculated decompression rates as a function of eruption plume height. The bigger mark indicates the highest decompression rate estimate for each eruption. With the exception of Ambrym, which plume maximal height is unknown and assessed by lava fountain height,*

*there is a notable correlation between maximal decompression rate and plume height for basaltic magmas. The same legend applies for both figures. Magnitude estimates were calculated from either orginal article or respectively Shreve et al. [2019], Johnston et al. [2014], Self [2006] and Mason et al. [2004] for Ambrym's 2018 eruption, Santorini's Minoan eruption, Taupo's Oruanui eruption and both Long Valley's Bishop Tuff and Yellowstone's Huckleberry Ridge Tuff. Plume height estimation comes from models from Gardner et al. [1991], Mastin et al. [2014] and Van Eaton et al. [2012] respectively for Long Valley's Bishop Tuff, Yellowstone's Huckleberry Ridge Tuff and Taupo's Oruanui eruptions.*

We notice that an increase in decompression rate with eruption magnitude is noticeable for basaltic magmas (Kīlauea, Ambae and Ambrym) but the correlation is weakly significant (Pearson coefficient of 0.24 with a p-value of 0.35 and $R^2$=0.47, which corresponds to a weak positive correlation). In a single eruption, there can be varying flow regime creating a range of decompression rates within the conduit; a batch of magma may potentially ascend faster than others (e.g., [Martel et al., 1998; Gonnermann and Manga., 2007; Cassidy et al., 2015]). If we only consider the highest decompression rate of any given eruption however, the aforementioned weak correlation between decompression rate and magnitude becomes more significant for mafic eruptions (Figure 2-7a) (Pearson coefficient of 0.93 with a p-value of 0.01 and $R^2$=0.86). The calculated decompression rates for rhyolitic eruptions on the other hand show no correlation with eruption magnitude.

The eruption intensity is also assessed with the plume height, which is directly observed or calculated through several empirically determined relations involving isopachs for explosive eruptions (e.g., Woods and Wohletz. [1991], Mastin et al. [2009], Pyle. [2015]). The eruption intensity, estimated from the mass eruption

rate, has been shown to be positively correlated with decompression rate [Barth et al., 2019b; Ferguson et al., 2016; Newcombe et al., 2020]. Thus, the plume height is expected to correlate with the decompression rate. We used EMBER-recalculated decompression rates to test this hypothesis. For the two eruptions of Kīlauea for which the plume height is not constrained, we used the maximal height of the lava fountain instead. Ambrym's plume height data for the 2018 eruption is undetermined and therefore not added to Figure 2-7b. Results show no global correlation between these two parameters (Figure 2-7b). However, considering again the highest decompression rate recorded for each eruption, a strong positive correlation emerges for basaltic eruptions (with a Person coefficient of 0.76, a p-value of 0.005 and $R^2$=0.88). Again, the calculated decompression rate for rhyolitic eruptions shows no correlation with eruption plume height. The maximum decompression rate for basaltic eruption therefore shows a statistically significant positive correlation with both eruption magnitude and plume height. A first order positive correlation therefore exists between the maximal magma decompression rate and the explosivity of an eruption for basaltic eruptions.

## 2.7 Conclusion

We present EMBER, a user-friendly GUI program that calculates decompression rates from $H_2O$, $CO_2$ and S concentration profiles along embayments of basaltic to rhyolitic compositions.

We found that decompression rate calculations are particularly sensitive to variations of $M_0$ especially for the $H_2O$ diffusion profile. Variations of $P_{end}$ are also accompanied by a variation of the best fit exsolved gas content, but not necessarily by a variation of associated decompression rate.

We recalculated decompression rates from previous studies twice: first, to validate and test how well EMBER reproduced existing results using the parameters from the original studies, and secondly, to homogenize determined decompression rates applying the same protocol to the existing raw data from previous studies, in order to improve inter-study comparison.

In the first case, recalculated decompression rates are in the same order of magnitude as original calculations but notable differences do occur such as for the 1980 Mt St Helens eruption where recalculated decompression rate are at 0.15-0.41 MPa/s, half of the previously reported values [Humphreys et al., 2008].

In the second case, the recalculated dataset shows no significant correlation between magma decompression rate and eruption magnitude when considering the entire dataset and shows a weak correlation when considering the subset of decompression rates of basaltic magma (Pearson coefficient of 0.24 with a p-value of 0.35 and $R^2$=0.47.) The correlation is significant when considering only the maximum decompression rates of each basaltic eruption (Pearson coefficient of 0.93 with a p-value of 0.01 and $R^2$=0.86). Additionally, there is no significant correlation between decompression rate and plume height when considering the entire dataset. However, once again, a statistically significant trend appears when considering only the maximum decompression rate of the basaltic eruptions (with a Pearson coefficient of 0.84, a p-value of 0.007 and $R^2$=0.88).

Our results suggest for the first time a significant positive correlation between embayment-calculated maximum decompression rate and eruption explosivity parameters such as magnitude and plume height, for basaltic eruptions.

## 2.8 Computer code availability

Title of the software: EMBER

Developers: Guillaume Georgeais, Kenneth T. Koga, Yves Moussallam, Estelle F. Rose-Koga

Hardware used: EMBER was run on a computer with 4 core (4.5GHz) and 16 GB of RAM

Link to the software, tutorial and test using data from Ferguson et al. [2016] DOI: 10.6084/m9.figshare.13663811

Software required: MATLAB Runtime Environment 2019b and up https://www.mathworks.com/products/compiler/matlab-runtime.html

## 2.9 Acknowledgement

We would like to thank M Humphreys for providing the raw data of the Mt St Helens embayments. GG was supported by a PhD fellowship from the French Government “Ministère de l’Enseignement Supérieur, de la Recherche et de l’Innovation”. ERK acknowledges partial funding from Laboratory of Excellence initiative n°ANR-10-LABX-0006, the Région Auvergne and the European Regional Development Funds. Y M acknowledges funding from INSU and the Région Auvergne Rhone Alpes. This is Laboratory of Excellence ClerVolc contribution number 463. We thank Madison Myers for

sharing her code during the review process of our manuscript. We would like to thank Madison Myers and an anonymous reviewer for their comments on the original manuscript and Marie Edmonds for editorial handling.

## 2.10 Appendices

The following figures represent the comparison between literature and EMBER derived decompression rates and calculated best fits. Diffusion profiles are usually well fitted when volatile species are considered separately but worsen when constraining decompression rate with multiple volatile species. In addition, several volatile profiles are badly fitted near the mouth (usually for S) due to the degassing paths (Solex) not providing a pressure fitting all three volatile concentration at the mouth.

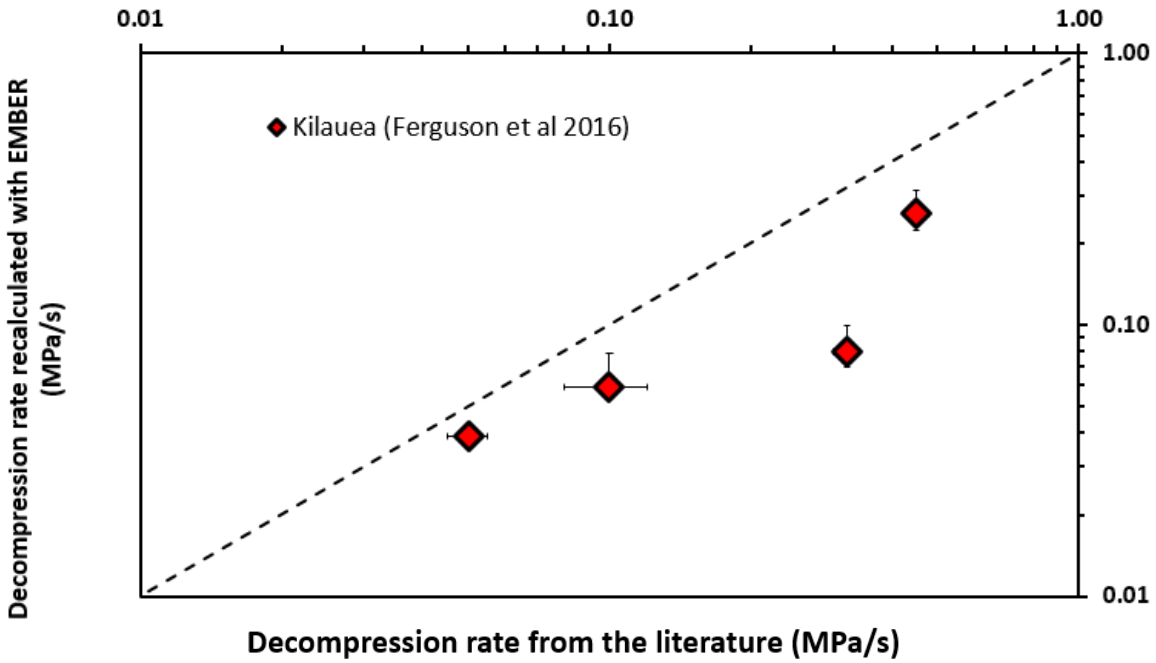


***Figure s2-1:*** *Comparison between decompression rate from original study and those recalculated by EMBER*

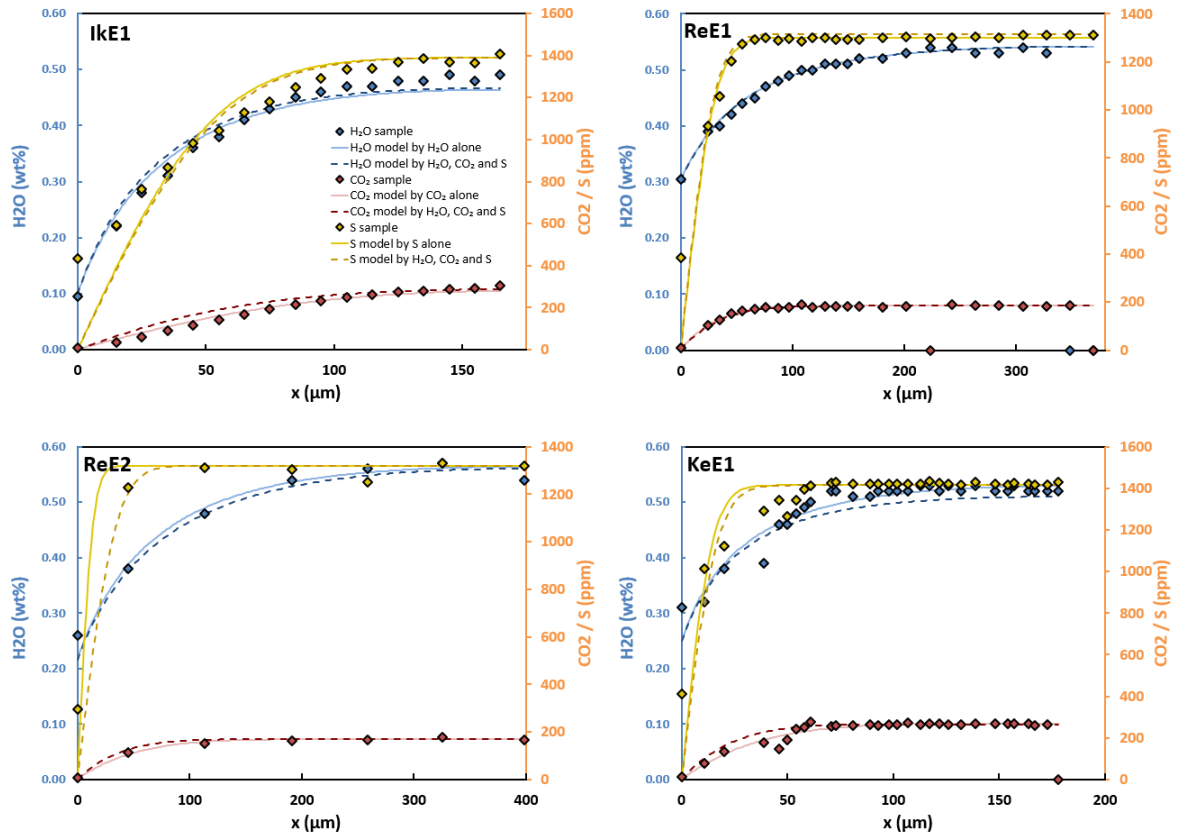


***Figure s2-2:*** *Best fit diffusion profiles calculated from EMBER on Kilauea data from Ferguson et al. [2016]*

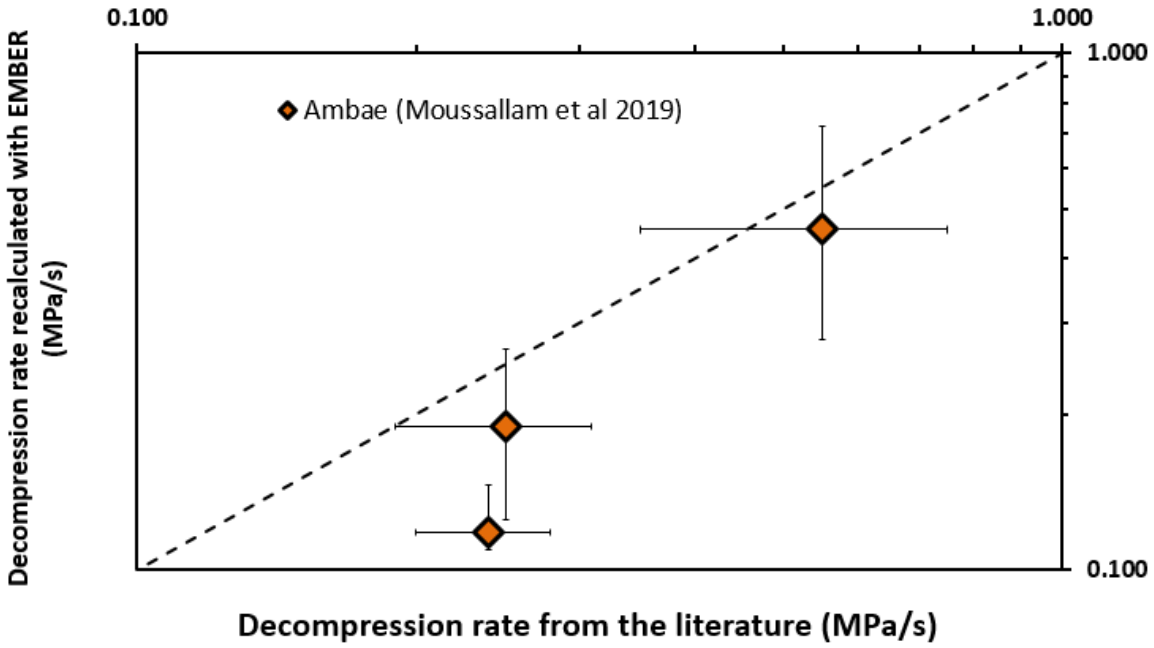


***Figure s2-3:*** *Comparison between decompression rate from original study and those recalculated by EMBER*

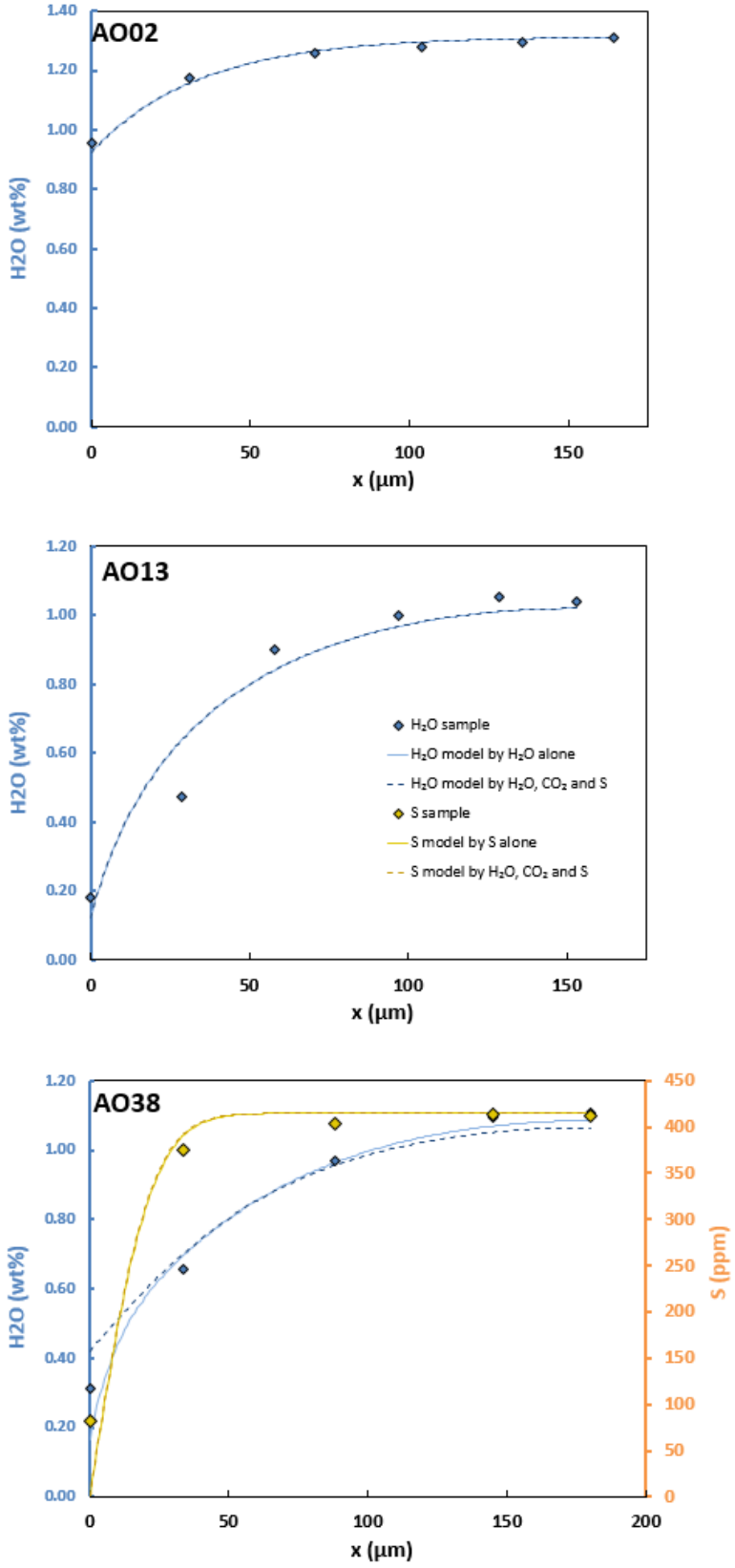


***Figure s2-4:*** *Best fit diffusion profiles calculated from EMBER on Ambae data from Moussallam et al. [2019]*

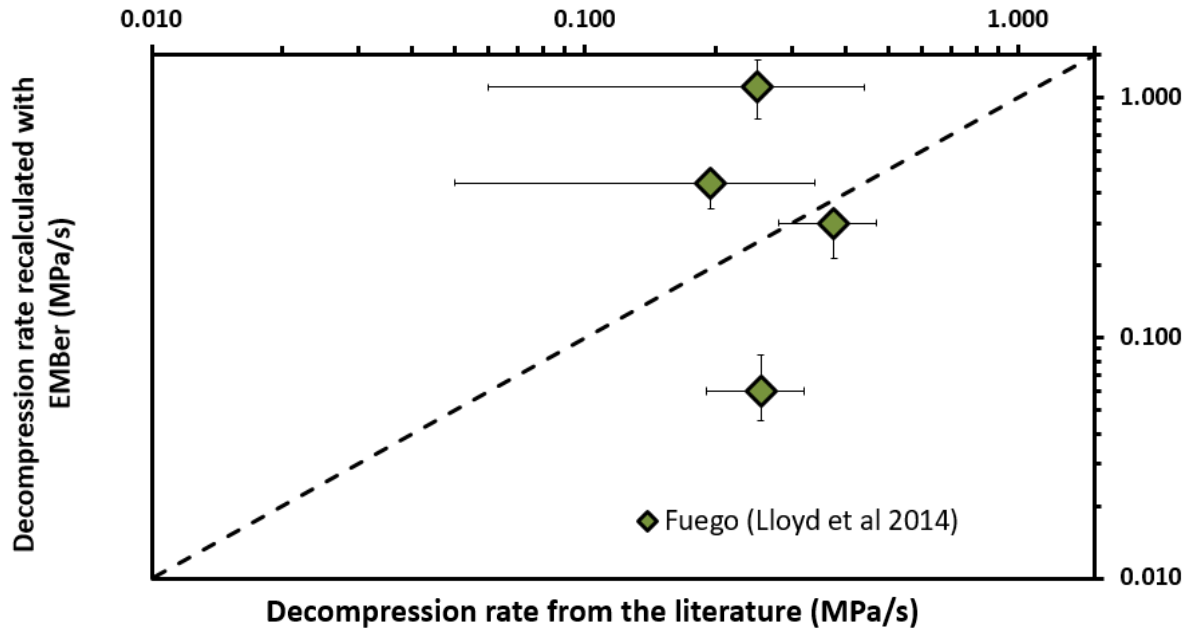


***Figure s2-5:*** *Comparison between decompression rate from original study and those recalculated by EMBER*

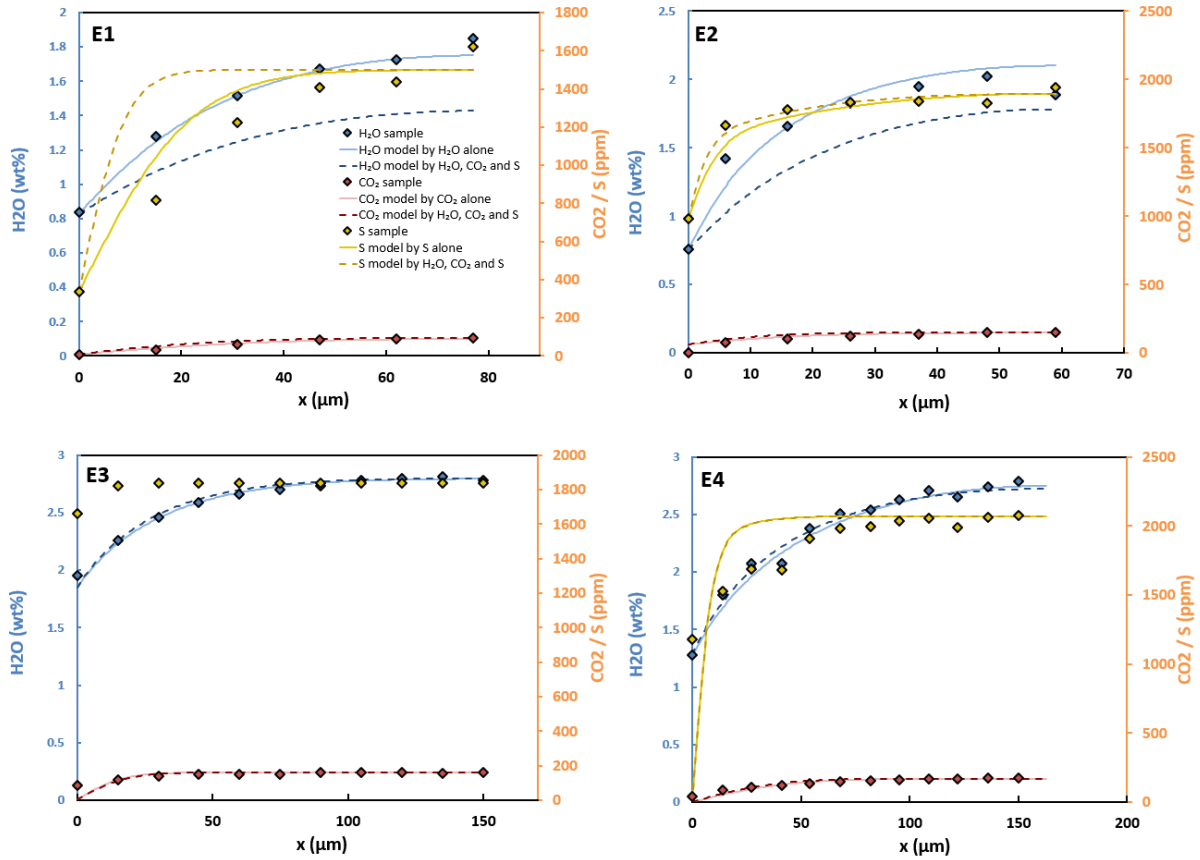


***Figure s2-6:*** *Best fit diffusion profiles calculated from EMBER on Fuego's data from Lloyd et al. [2014]. The S profile was not calculated for E3 as the measurement uncertainty is big enough to fit almost any diffusion profile and thus bring no constrain on decompression rate.*

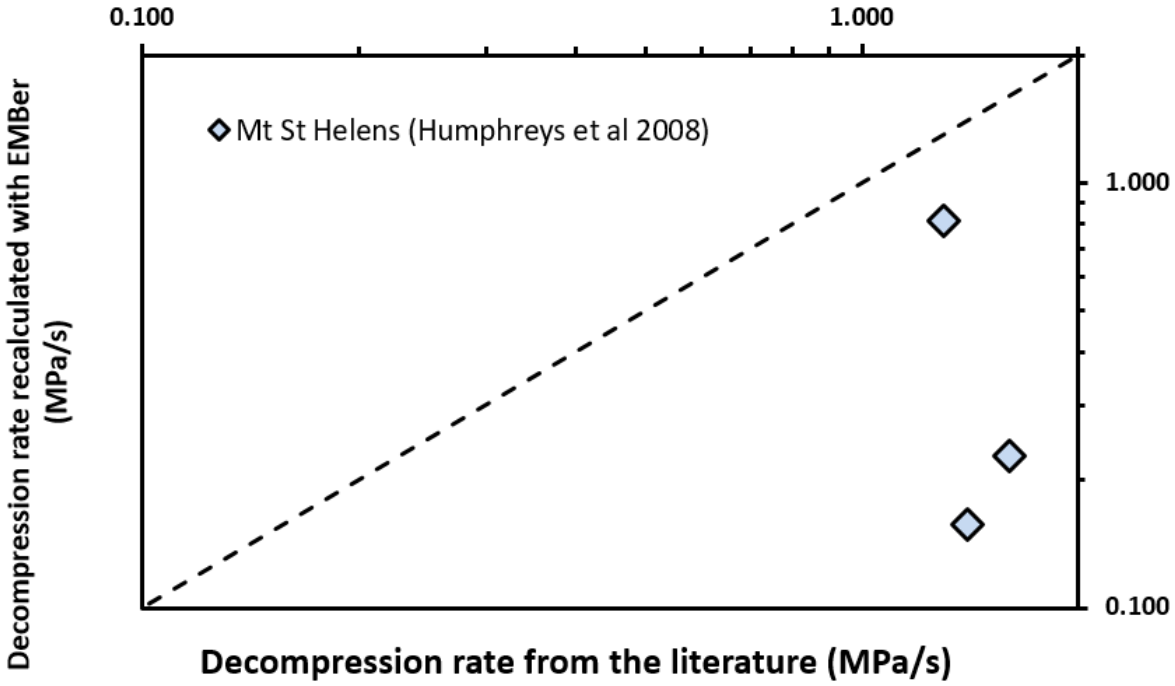


***Figure s2-7:*** *Comparison between decompression rate from original study and those recalculated by EMBER*

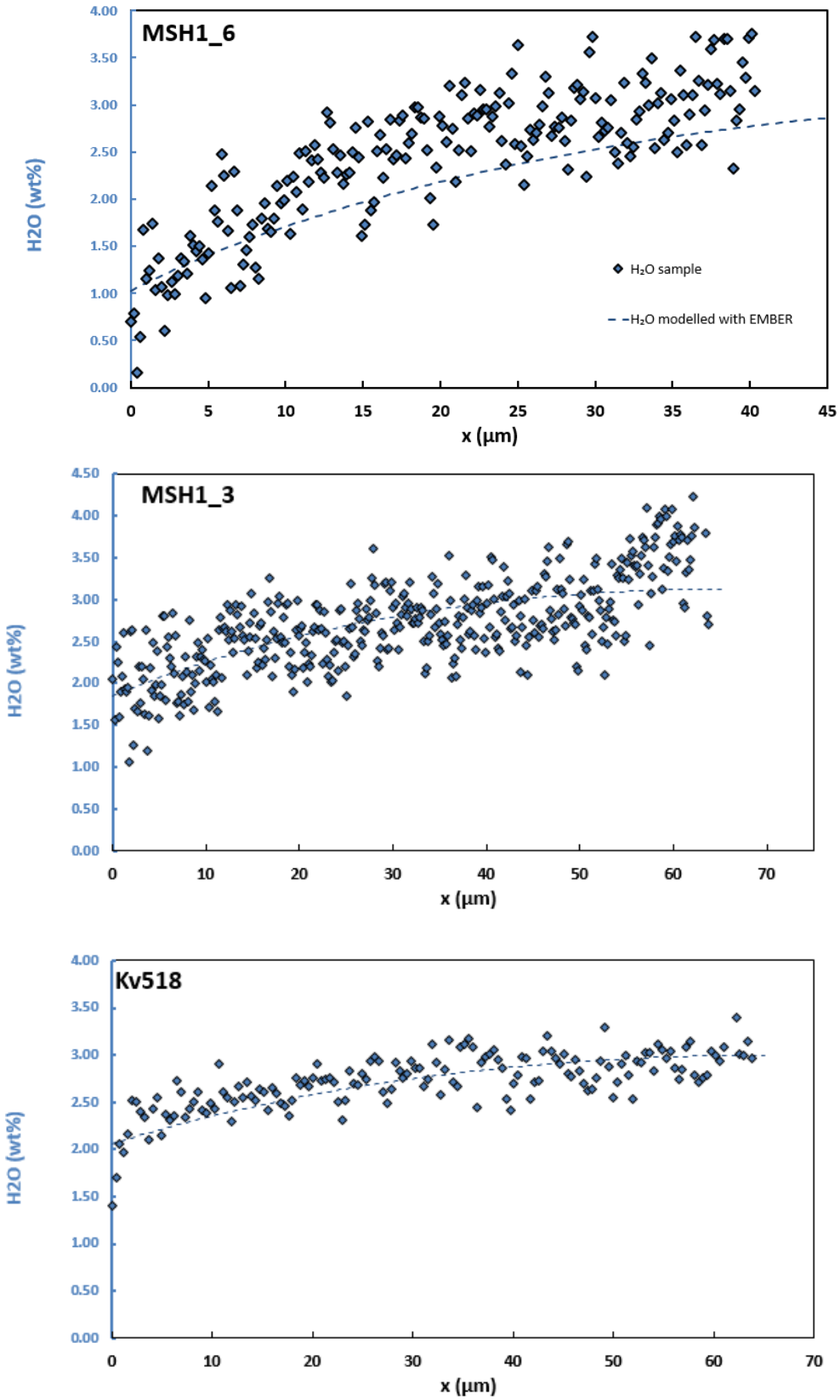


***Figure s2-8:*** *Best fit diffusion profiles calculated from EMBER on Mt St Helens data from Humphreys et al., [2008]*

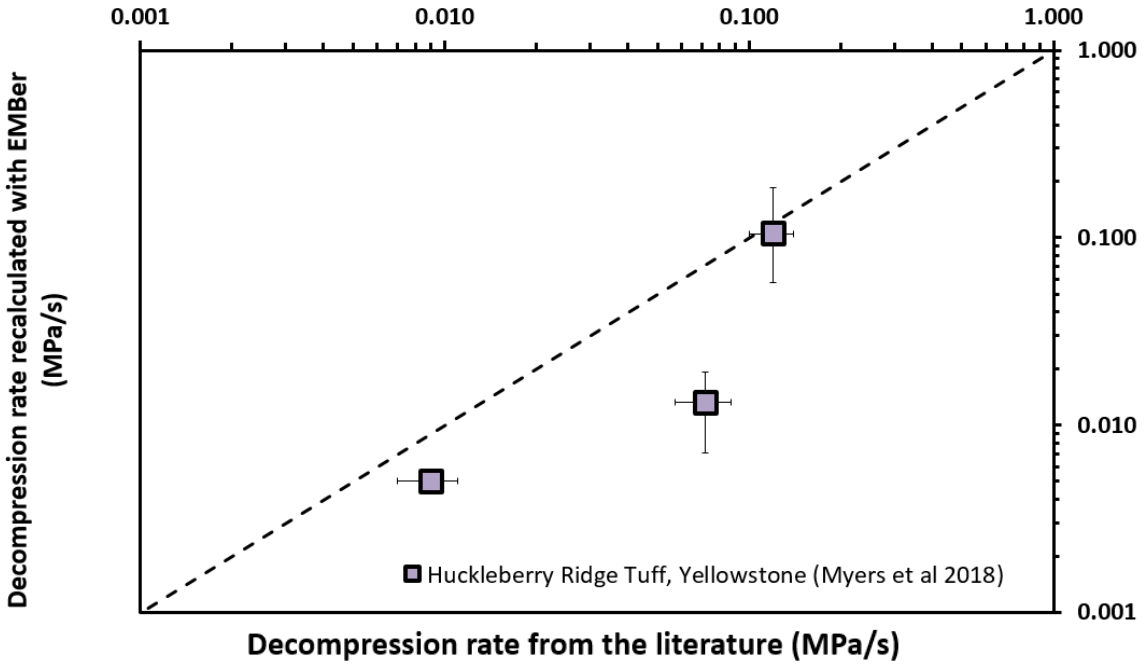


***Figure s2-9:*** *Comparison between decompression rate from original study and those recalculated by EMBER*

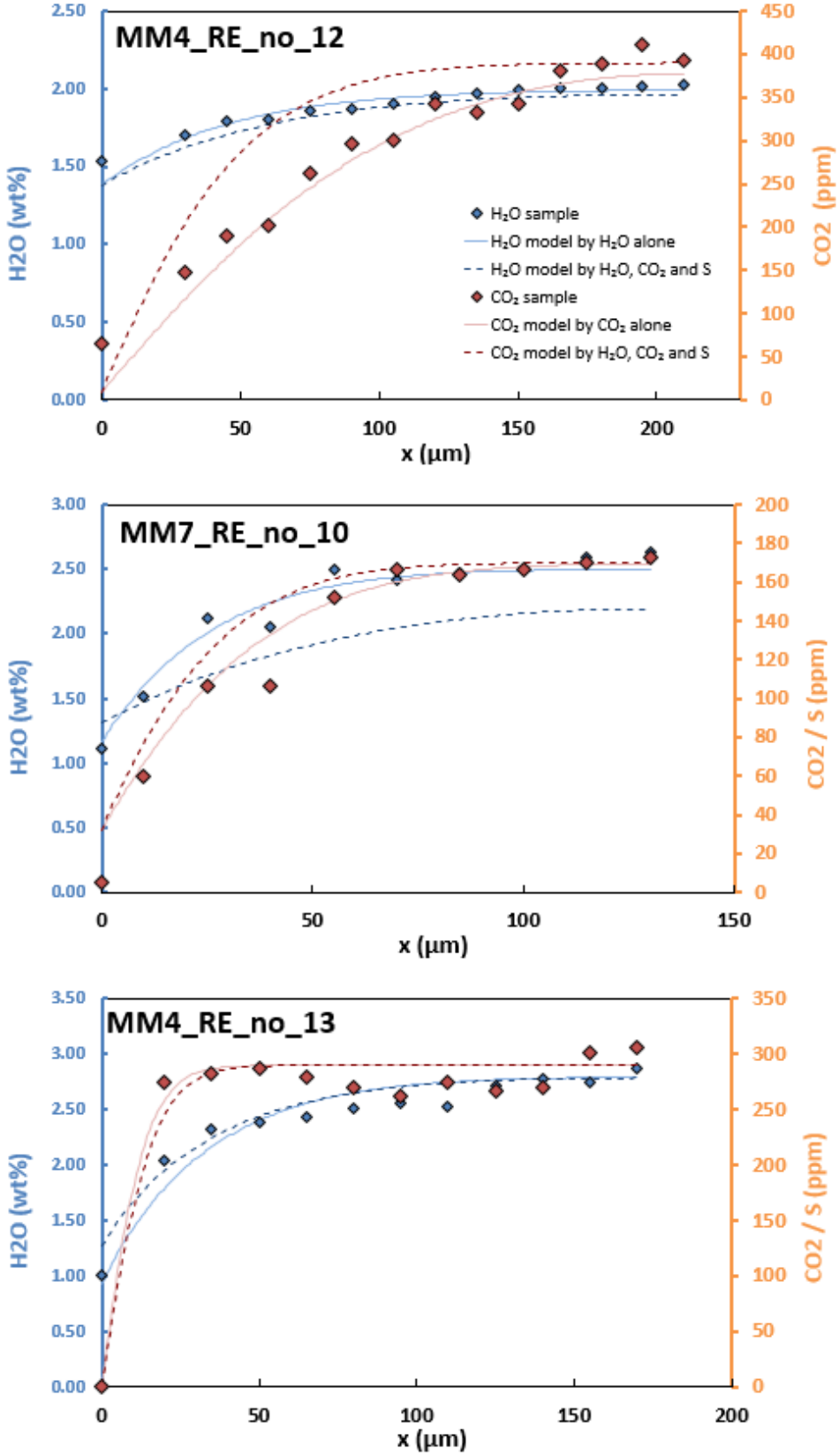


***Figure s2-10:*** *Best fit diffusion profiles calculated from EMBER on Yellowstone data from Myers et al. [2018]*

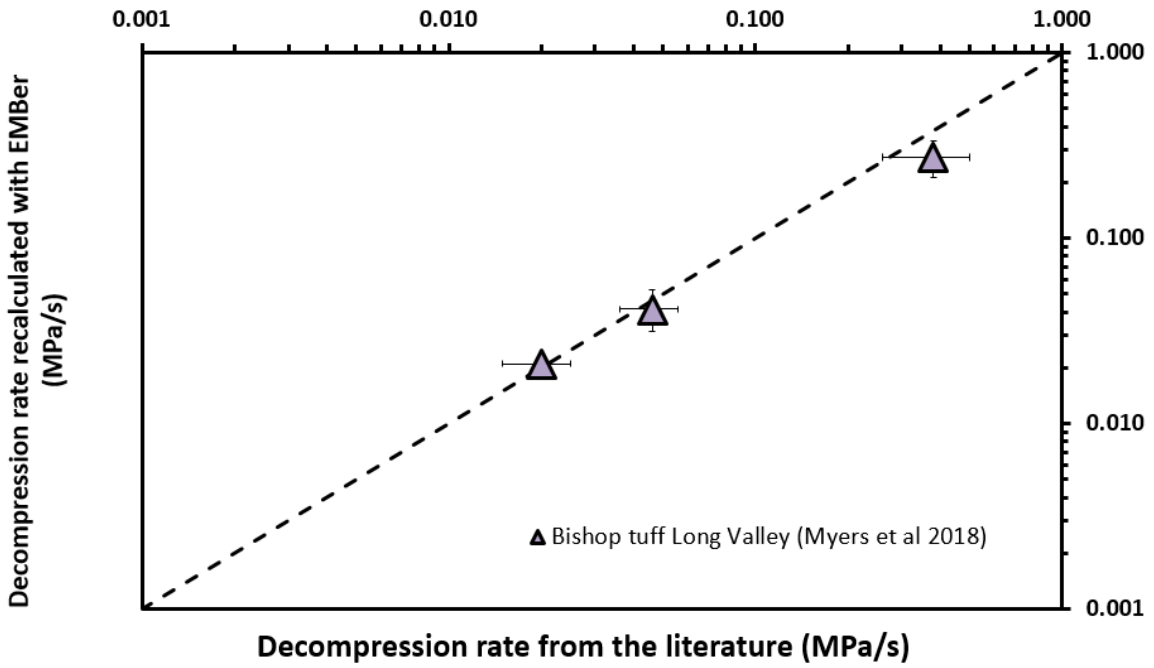


***Figure s2-11:*** *Comparison between decompression rate from original study and those recalculated by EMBER*

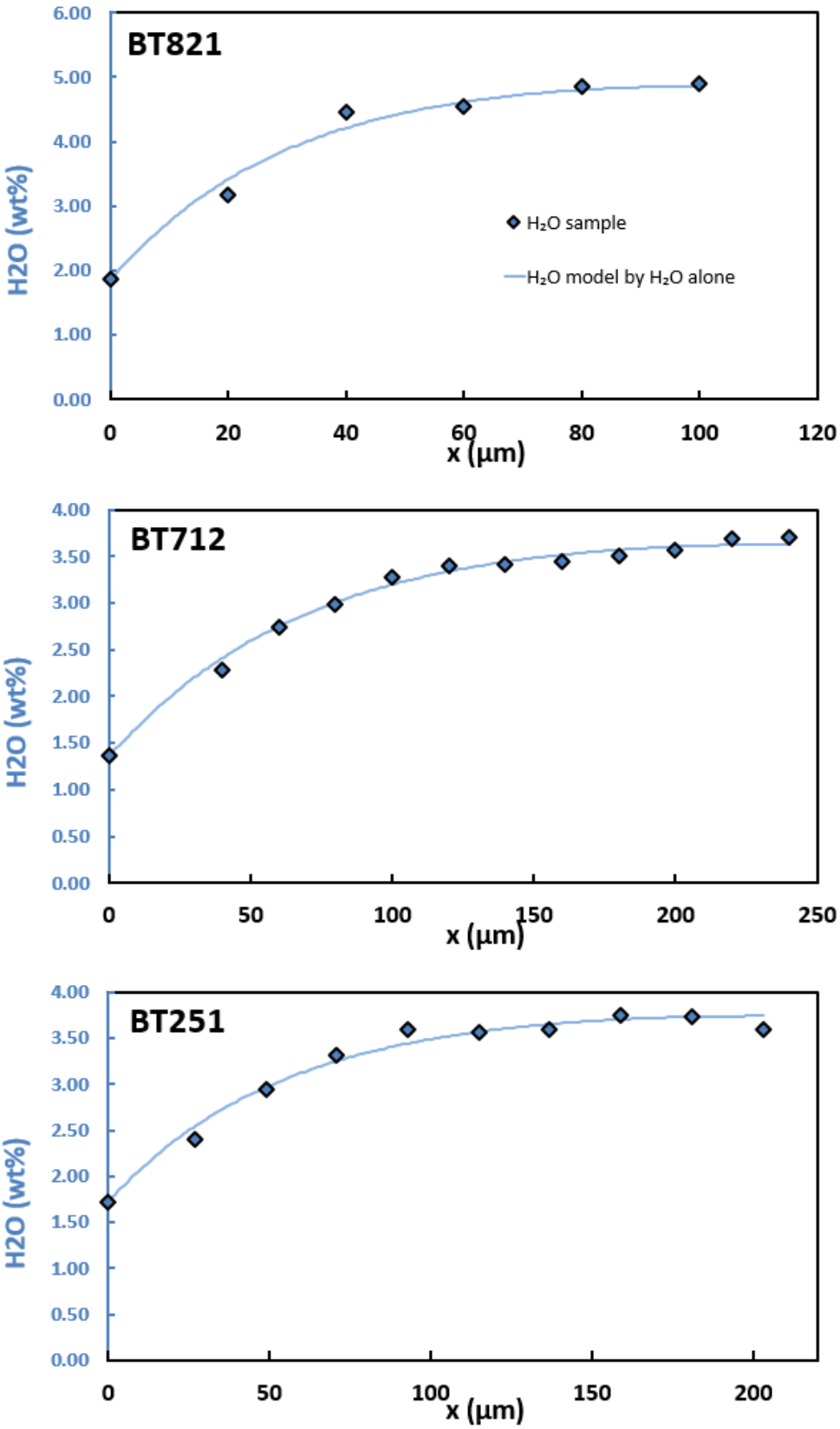


***Figure s2-12:*** *Best fit diffusion profiles calculated from EMBER on Long Valley data from Myers et al. [2018]*

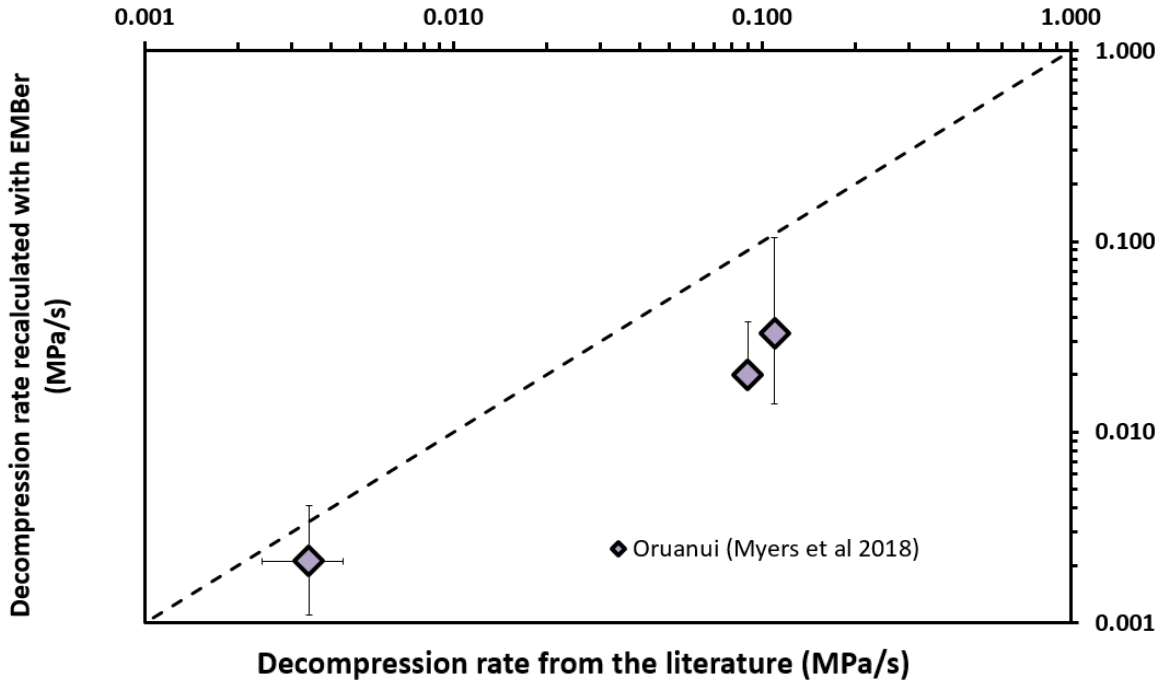


***Figure s2-13:*** *Comparison between decompression rate from original study and those recalculated by EMBER*

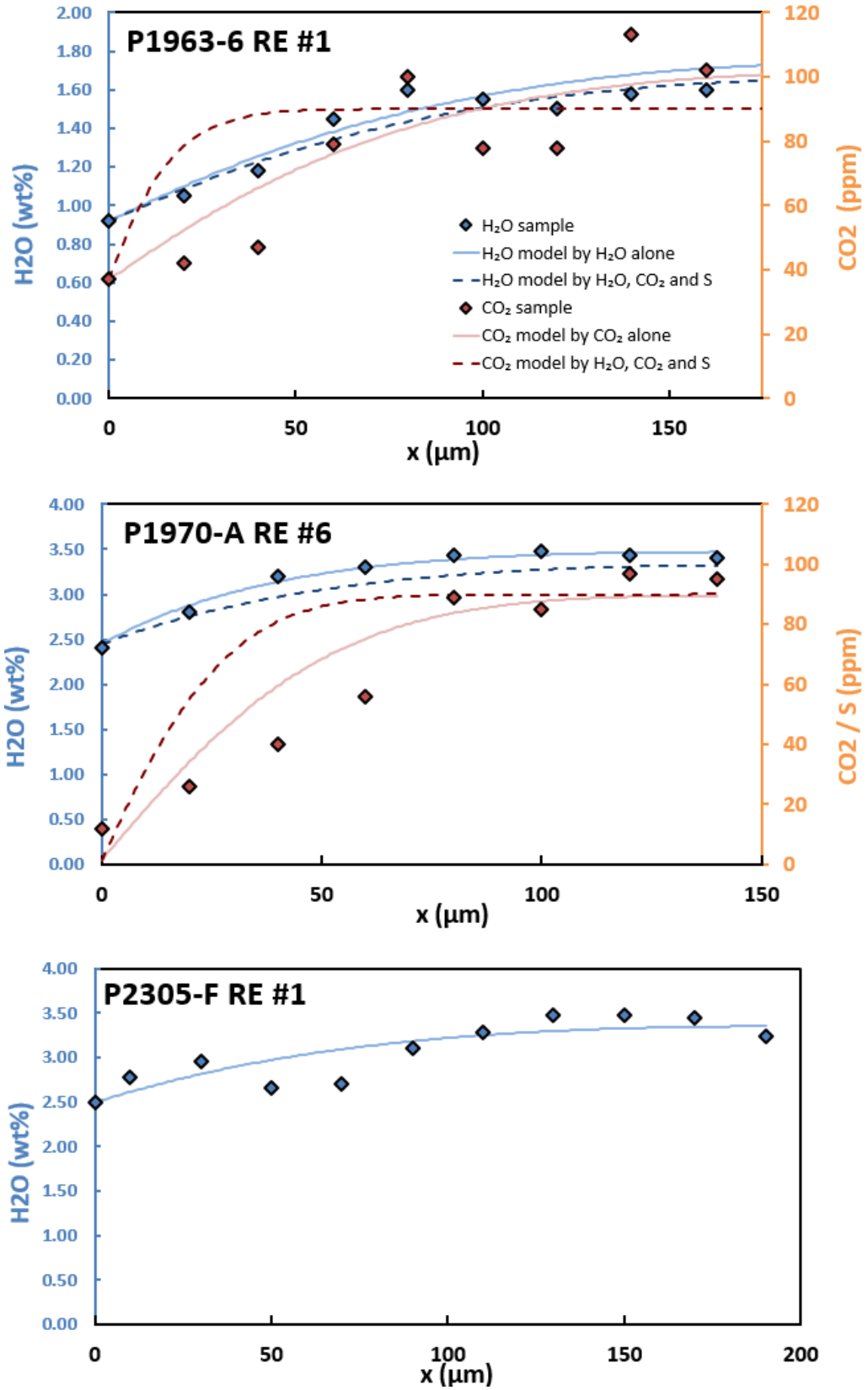


***Figure s2-14:*** *Best fit diffusion profiles calculated from EMBER on Taupo Oruanui data from Myers et al., [2018]*

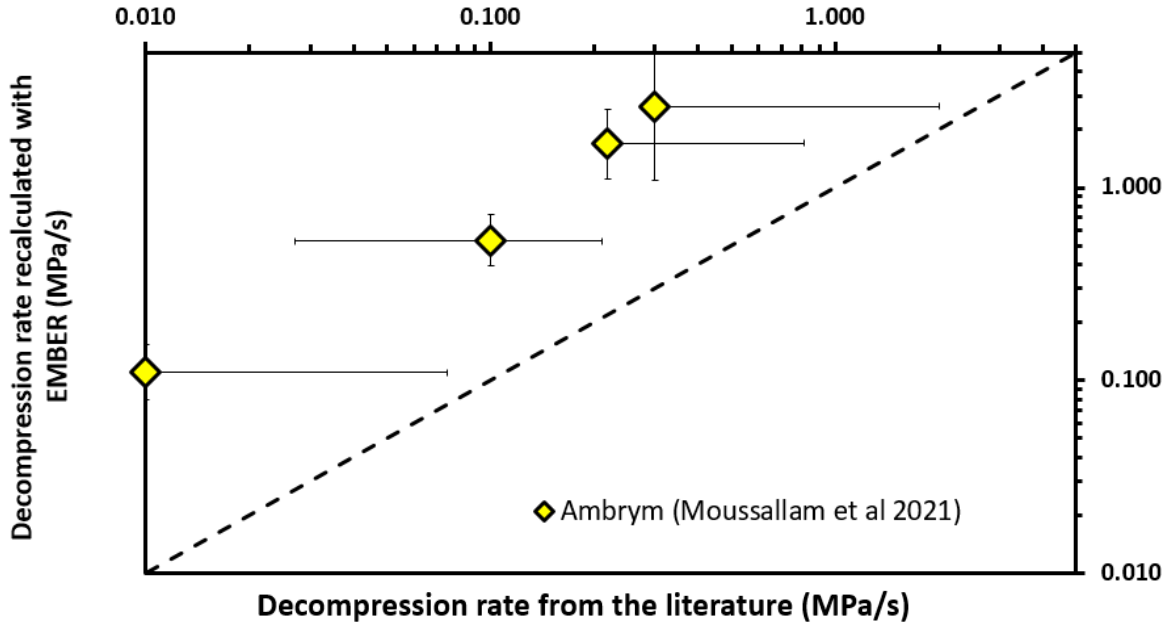


***Figure s2-15:*** *Comparison between decompression rate from original study and those recalculated by EMBER*

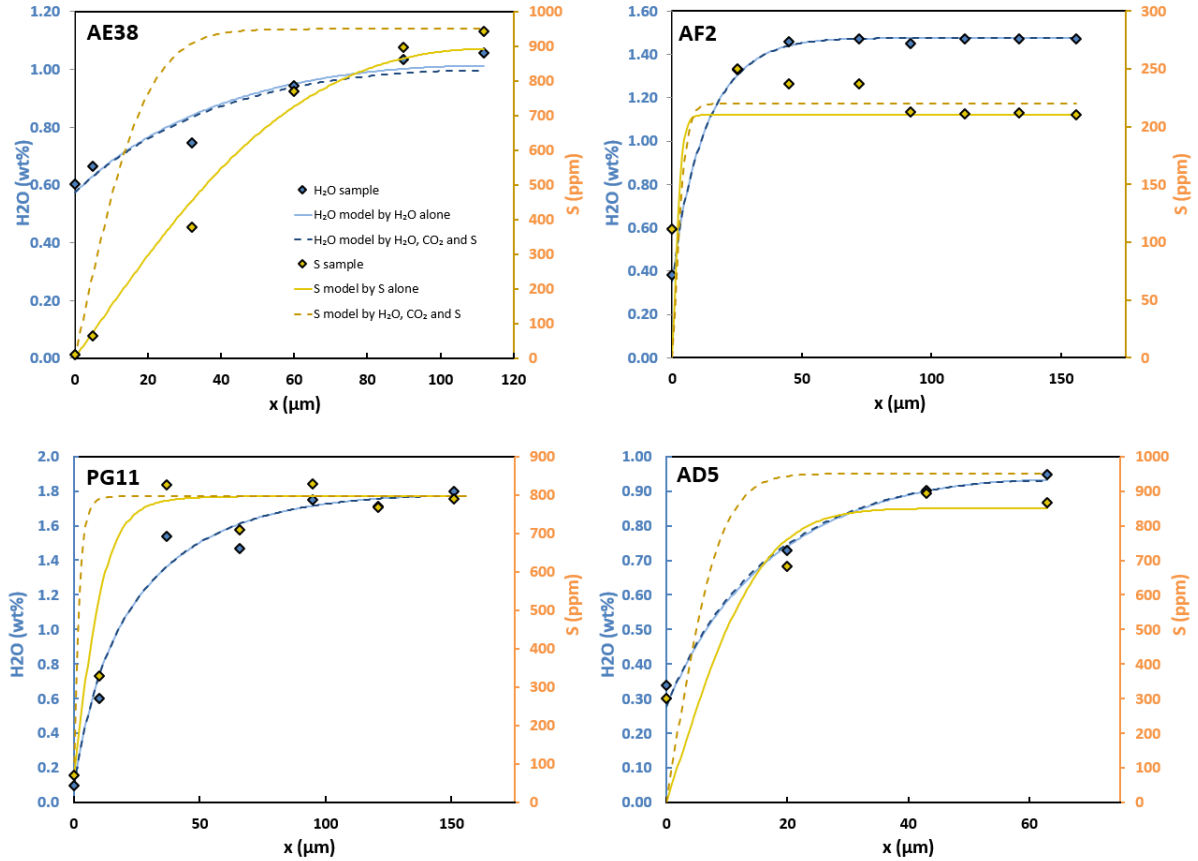


***Figure s2-16:*** *Best fit diffusion profiles calculated from EMBER on Ambrym data from Moussallam et al. [2021]*

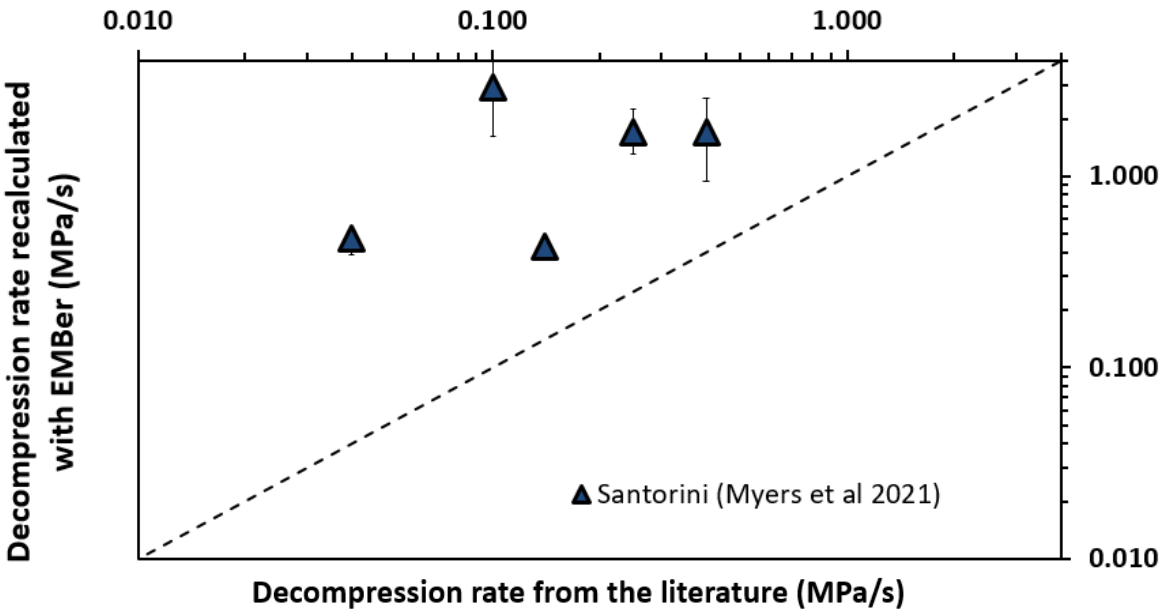


***Figure s2-17:*** *Comparison between decompression rate from original study and those recalculated by EMBER*

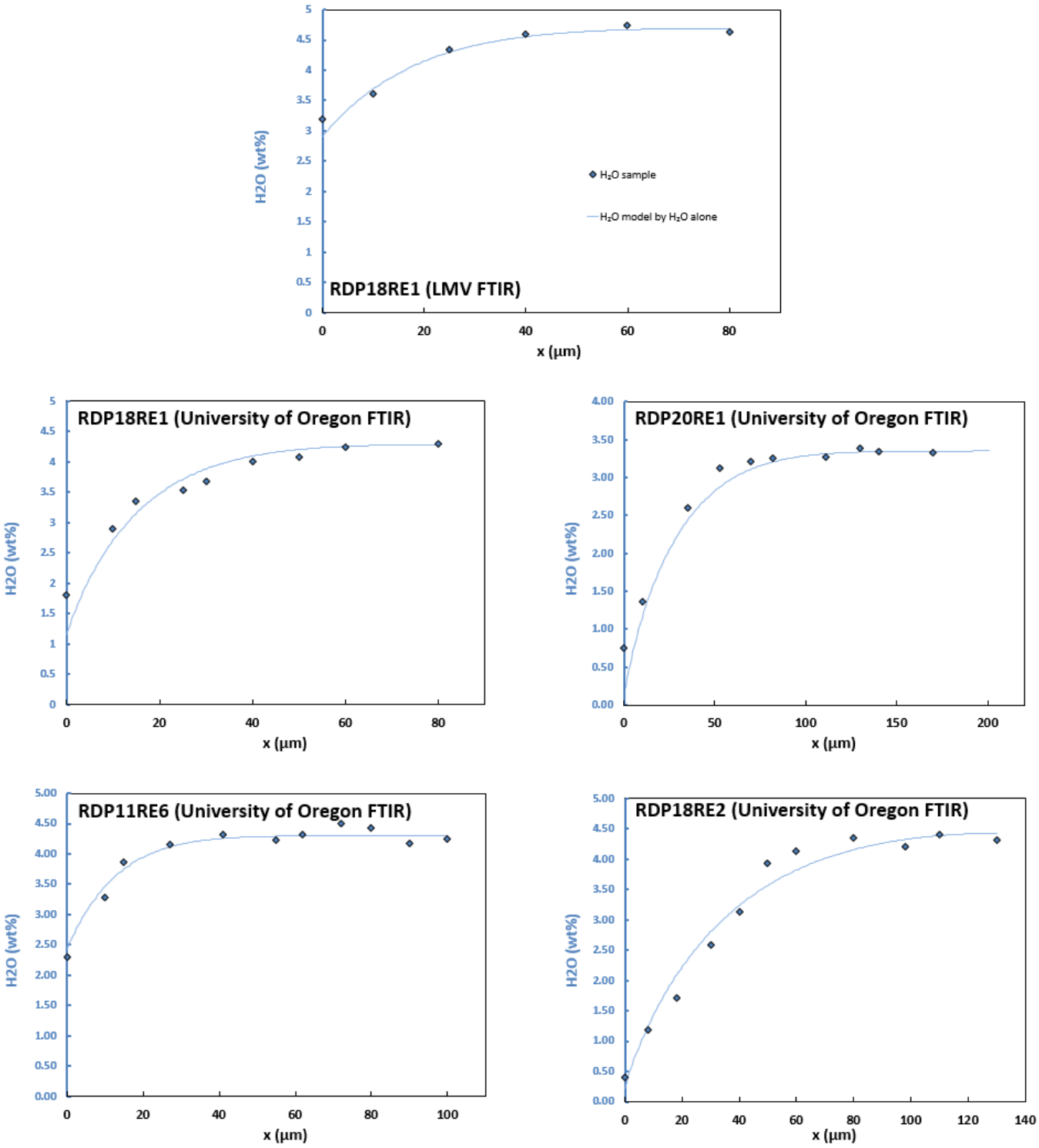


***Figure s2-18:*** *Best fit diffusion profiles calculated from EMBER on Santorini data from Myers et al. [2021]*

# CHAPITRE 3

# CORRELATIONS POSITIVES ENTRE VITESSES EXTREMES D'ASCENSION DES MAGMA ET PARAMETRES ERUPTIFS A L'ECHELLE D'UN UNIQUE VOLCAN : LE STROMBOLI (ITALIE)

La vitesse de remontée d'un magma vers la surface est un paramètre complexe et difficile à déterminer, mais fortement lié au style explosif ou effusif d'une éruption volcanique. Il a été suggéré, principalement à travers la modélisation des volatiles dissous dans les embayments, que cette relation va plus loin et que l'ascension est positivement corrélée à la magnitude de l'éruption et potentiellement la hauteur du panache pour les volcans basaltiques. Nous avons testé cette hypothèse sur le volcan Stromboli (Italie) qui est caractérisé par des styles éruptifs variables alimentés par le même système. Les vitesses d'ascension du magma de 8 éruptions historiques (2 éruptions majeures, 4 éruptions paroxysmales et 2 éruptions paroxysmales de grande ampleur) ont été calculées en utilisant (1) la diffusion d'éléments volatils dans les embayments trouvées dans les cristaux d'olivine et (2) la densité de vésicules et l'analyse texturale. La méthode des embayments, appliquée à 22 embayments, nous a permis d'obtenir des taux moyens de décompression de 0,39-7,21 MPa/s (16-283 m/s) avec une ascension enregistrée à partir de 1,6-5,9 km de profondeur correspondant à un temps de déplacement du magma de 10 s à 3 minutes jusqu'à la surface, en accord avec les signaux sismiques et la déformation du sol. La densité du nombre de bulles fournit des taux de décompression du même ordre de grandeur (1,57-4 MPa/s), confirmant ces taux d'ascension très rapides. Ces vitesses de remontée extrêmes sont potentiellement dues aux teneurs élevées en éléments volatils qui génèrent beaucoup de bulles et une forte poussée ascendante tôt pendant la remontée du magma Nous avons identifié une forte corrélation positive entre les taux de

décompression et la magnitude de l'éruption, son taux massique d’éjection de matériel et la profondeur de stockage des embayments pour les éruptions majeures et paroxysmales de plus petite échelle. Par ailleurs, les vitesses de remontée maximale obtenues pour chaque éruption grâce aux embayments corrèlent bien avec les vitesses d’éjection maximales de gaz et de balistiques à la sortie de l’évent mais restent environ 60m/s plus faibles. Dans ce cas, à Stromboli au moins, mais potentiellement plus généralement pour les éruptions basaltiques, des vitesses de décompression plus élevées signifient une intensité et une magnitude plus élevées. Une éruption qui commence depuis un point plus profond, remonte plus rapidement et est plus grosse et intense.

# Deeper, bigger, faster, stronger? Positive correlations between extreme magma ascent rate and explosive eruption parameters at Stromboli volcano (Italy).

**Guillaume Georgeais [1], Yves Moussallam[2,3], Estelle F. Rose-Koga[1,4], Kenneth T. Koga[4], Lucia Gurioli[1], Andrew Harris[1], Nicole Métrich[5] Antonella Bertagnini[6], Maximilien Verdier-Paoletti[7], Marco Pistolesi[8]**

[1] *Université Clermont Auvergne, CNRS, IRD, OPGC, Laboratoire Magmas et Volcans, F-63000 Clermont-Ferrand, France*

[2] *Lamont-Doherty Earth Observatory, Columbia University, New York, NY 10027, USA*

[3] *Department of Earth and Planetary Sciences, American Museum of Natural History, New York, NY 10024, USA*

[4] *Institut des Sciences de la Terre d'Orléans (ISTO), UO/CNRS/BRGM, 1A rue de la Férollerie, 45071, Orléans, France*

[5] *Université de Paris, Institut de Physique du Globe de Paris, CNRS, Paris, France,*

[6] *Instituto Nazionale di Geofisica e Vulcanologia, Sezione di Pisa, Pisa, Italy*

[7] *Institut de Mineralogie, Physique des Materiaux et de Cosmochimie, Museum National d'Histoire Naturelle, CNRS, Sorbonne Université, Paris, F-75231, France*

[8] *Dipartimento di Scienze della Terra, Università di Pisa, Pisa, Italy*

Corresponding author: Guillaume Georgeais; guillaume.georgeais@uca.fr

**Keywords:** Conduit processes, magma degassing, embayments, pyroclastic texture, volatile diffusion

Submitted to *Earth and Planetary Science Letters*

## 3.1 Abstract

The ascent rate of a magma rising toward the surface is a complex and challenging parameter to determine yet strongly related to the explosive or effusive style of a volcanic eruption. It has been suggested mainly through modelling of volatiles dissolved in melt embayment that this relationship goes further and that ascent is positively correlated with eruption magnitude for basaltic volcanoes. We tested this hypothesis at Stromboli volcano (Italy) that is characterized by variable eruptive styles fed by the same system. Magma ascent rates of 8 historical eruptions were calculated using (1) the diffusion of volatile elements in embayments found in olivine crystals and (2) bubble population and textural analysis. We obtained average decompression rates of 0.39-7.21 MPa/s (20-283 m/s) for melt embayment modelling with an ascent from 1.6-5.9 km deep corresponding to a 10 s to 3 minutes magma travel time to the surface, in agreement with seismic signals and ground deformation. Bubble number density provides decompression rates within the same order of magnitude (1.57-4 MPa/s), confirming these very fast ascent rates. We identified a strong positive correlation between decompression rates and eruption magnitude, mass eruption rate and embayment storage depth for major and small-scale paroxysmal eruptions. In this case, at Stromboli at least, but potentially more generally for basaltic eruptions, higher decompression rates mean higher intensity and magnitude (i.e., deeper = bigger = faster = stronger).

## 3.2 Introduction

Magma ascent rate is one of the most complex yet crucial parameters impacting eruption dynamics. Slowly ascending magmas are prone to volatile decoupling from the melt in an open system, which decreases the buoyancy force and therefore decompression rate (i.e., ascent velocity within the conduit). In fast-ascending magmas, bubbles remain in the melt and ascend with it in a closed system, increasing the buoyancy force and concomitantly decompression rate (e.g., Gonnermann and Manga, 2007). Therefore, ascent rate controls eruption dynamics and can lead to effusive or eruptive activity (e.g., Cassidy et al., 2018).

Recent studies have established preliminary correlations between ascent rate and: plume height during a single silicic eruption (e.g., Myers et al., 2021), eruption intensity for two eruptions at a single volcano (e.g., Barth et al., 2019a; Newcombe et al., 2020), eruption magnitude for two eruptions at a single volcano (e.g., Ferguson et al., 2016) and eruption magnitude for basaltic volcanoes at large (e.g., Moussallam et al., 2019; Georgeais et al., 2021). So far, most of these works, albeit providing key findings in magma dynamics, rely either on past eruptions (i.e., with no monitoring or eyewitness accounts) or recent but poorly monitored events.

A well-studied volcano such as Stromboli (Italy) represents the perfect natural laboratory to investigate the relation between eruption parameters and ascent rates. Active for the last 1400 years (Rosi et al., 2013), Stromboli displays a range of

explosive activity inversely proportional to its frequency with regular (every 10–20 min on average) Strombolian eruptions, rare ‘major’ explosions that happen about twice a year on average (e.g., Bertagnini et al., 2008; Bevilacqua et al., 2020) and much rarer ‘paroxysmal’ blasts (e.g., 1919, 1930, 1936, 1944, 1959, 1998, 2003, 2007 and 2019; Rosi et al., 2006, 2013; Giudicepietro et al., 2020). Strombolian eruptions are thought to be related to slug flow through a resident magma column (e.g., Gonnermann and Manga, 2012; Leduc et al., 2015) during which degassed, high porphyritic (HP) magma is commonly ejected. This results in the emplacement of scoriaceous black scoria and ash around the crater area. Major and paroxysmal eruptions, by contrast, eject significant amounts of material and involve the so-called low-porphyritic (LP) magma (e.g., Pioli et al., 2014) ascending together with the gas phase from depths of 7-10 km (e.g., Bertagnini et al., 1999; Métrich et al., 2005, 2010, 2021) and which materials are known as golden pumice. Both LP and HP magma contain three mineral species (olivines, clinopyroxenes and plagioclases). LP magma carry olivines with compositions ranging from $Fo_{90}$ to $Fo_{65}$ following the scarce to extensive transformation into HP magma (e.g., Bertagnini et al., 2013). Thus, the crystals are likely heterogeneous with reverse (decreasing magnesium concentration from core to rim) and direct (increasing magnesium concentration from core to rim) zoning, representative of the complex feeding system of the Stromboli volcano. The magma ascent rate during Stromboli’s paroxysms remains unconstrained and debated. A slow ascent rate of 3 mm/s was proposed by Calvari et al. (2011) for

the 2003 and 2007 paroxysms despite the lack of microlites observed in the golden pumice clasts, which suggests ascent rate of at least 0.2 m/s from experimental petrology constraints (e.g., Pichavant et al., 2011). At the other extreme, an ascent rate of 32 m/s was proposed for the 2003 paroxysm based on viscosity measurements and conduit flow modelling (Misiti et al., 2009). In this study, we investigate 8 of Stromboli's most studied eruptions covering eruption styles going from major to paroxysmal activity. We perform volatile diffusion measurements in embayments from olivine crystals of two major eruptions and six paroxysms in order to determine their ascent rate and compare these to measured eruption parameters such as plume height or eruption magnitude. We also compare best-fit decompression rates from the embayment method with texture-determined decompression rates from bubble number density measurements. We show that a strong positive correlation exists between the maximum decompression rate of an eruption and: (1) its magnitude, (2) its mass discharge, and (3) the pressure at which the host crystal is picked up by the ascending magma.

## 3.3 **Method**

### 3.3.1 Sample description

This study focuses on eight eruptions: two major eruptions from the 8$^{th}$ (STN-9) and 21$^{st}$ (STN-8) of November 2009 and six paroxysmal eruptions of varying intensity: 1456 CE (ST207), 11 September 1930 (PST205), 5 April 2003 (ST345),

15 March 2007 (07PRX), 3 July 2019 (STG) and 28 August 2019 (SHE750). These eruptions provide a wide range of eruptive parameters (e.g., erupted mass between $10^5$-$10^9$ kg , mass discharge rate from $10^4$-$10^7$ kg/s, plume height from 150 to 8400 m; Métrich et al., 2021; Table 3-1). Figure S3-1 shows the age and location of the different samples. Tephra collected are multi-centimetric fragments with visible mingling patches of a few mm size between the degassed, shallow, (HP) black scoria and the gas-rich, deep, (LP) golden pumice magma. Highly porphyritic material is characterized by higher $SiO_2$ and $K_2O$ concentrations (48.5 wt.% < $SiO_2$ <53 wt.%, 2 wt.% < $K_2O$) compared to LP materials. HP magma also records increased number of crystals with bigger (up to a few millimeters) and usually euhedral plagioclase, clinopyroxene and olivine phases. These crystals, mostly the plagioclase, are concentrically zoned in accordance with crystallization/dissolution processes (Bertagnini et al., 2013) occurring in the shallow part of the magmatic conduit. HP melts contains low-Fo olivines (< $Fo_{75}$) in low quantities. LP material is instead characteristic of less evolved melt (e.g., lower $SiO_2$ and $K_2O$, $Fo_{88+}$ olivines) with smaller olivines and lower crystallinity.

The embayment method usually requires a large quantity of sample to find a reasonable number of the straight cylindrical glassy embayments (also called re-entrants). We decided to crush the HP-LP mingled tephras first and extract the crystals that range between 400 µm and 2 mm either manually or with an

isodynamic Frantz L-1 magnetic separator. We split the crystals between LP and HP phases, on the basis of surrounding glass texture: golden bubble-rich glass indicates usually intense exsolution from a volatile-rich melt, hence a LP phase from a deeper reservoir (Métrich et al., 2010; Andronico et al., 2021), while HP crystals are commonly characterized by honey-colored, less vesicular glass. Embayments were polished according to the method described in Moussallam et al. (2019). Selected embayments were tested with secondary ion spectrometry (SIMS and nanoSIMS), Raman spectroscopy and microprobe analysis and characterized using glass major element analysis (e.g., $K_2O$ vs $SiO_2$ plot according to Bertagnini et al., 2013).

***Table 3-1:*** *Eruptive parameters of the studied 8 eruptions.*

| Name of the sample | ST207 | PST205 | ST320/ST345 | 07PRX | STN_9 | STN_8 | STG | SHE750 |
|---|---|---|---|---|---|---|---|---|
| **Date of eruption** | 1456 | 11/9/1930 | 5/4/2003 | 15/3/2007 | 8/11/2009 | 24/11/2009 | 3/7/2019 | 28/8/2019 |
| **Type of eruption** | Large scale Paroxysm | Large scale Paroxysm | Paroxysm | Paroxysm | Major | Major | Paroxysm | Paroxysm |
| **Fallout total volume ($m^3$)** | 5.00E+06 *a,e* | 2.50E+06 *a,e* | 2.30E+05 *d,f* | 1.85E+04 *d,f* | 107 *c,f* | 1070 *c,f* | 353000 *e* | 92800 *e* |
| **Fallout Low Porphyric volume ($m^3$)** | 3.50E+06 *e* | 1.75E+06 *e* | 8.05E+04 *e* | 1.28E+04 *e* | 58 *e* | 835 *e* | 247100 *e* | 55680 *e* |
| **Fallout Mass (kg)** | **2.1E+09** *i* | **1.1E+09** *i* | 1.1-1.4E+8 *h* | 2.2-2.7E+7 *g* | 0.9-1.1E+5 *f* | 0.9-1.1E+6 *f* | 1.4E+8 *b* | **5.4E+08** *i* |
| **Magnitude** | **2.32** | **2.02** | **1.08** | **0.40** | **-2.00** | **-1.00** | **1.15** | **1.73** |
| **Mass discharge rate (kg/s)** | | | 1.0-1.2E+7 *h* | 1.9-2.3E+6 *g* | 1.1-1.4E+4 *f* | 5-6.1E+4 *f* | 1.1E+6 *b* | 3.6E+5 *b* |
| **Intensity** | | | **10.04** | **9.32** | **7.10** | **7.75** | **9.04** | **8.56** |
| **Plume Height (m)** | **10621** *n* | **8622** *n* | 4000 *h* | 2980 *h* | 200 *f* | 150 *f* | 8400 *b* | 6400 *b* |
| **Maximum ballistic exit velocity (m/s)** | | | 200 *h* | 150 *o* | 130 *m* | 90 *m* | 120-160 *b* | 90-130 *b* |
| **Maximum gas exit velocity (m/s)** | | | 324 *h* | 210 *g,o* | **146** *p* | **106** p | >200 *b* | >200 *b* |
| **Volume of magma ($m^3$)** | >1E+6 *a* | >1E+6 *a* | 2.2-2.4E+5 *a* | | | | | |
| **Volumic flux ($m^3/s$)** | | | | | | | 385 *b* | 125 *b* |
| **BND Golden pumice Nv ($mm^{-3}$)** | 1838 k | 8075 k | 643 *j* | 860 *j* | | | 4096 *l*<br>3503 *k* | 5540 *l*<br>*8196* *k* |
| **BND Golden pumice Na ($mm^{-2}$)** | | | | | | | 280-521 *l* | 342-685 *l* |

*a* (Bertagnini et al., 2003)
*b* (Giordano and De Astis, 2020)
*c* (La Felice and Landi, 2011)
*d* (Métrich et al., 2010)
*e* (Métrich et al., 2021)
*f* (Pioli et al., 2014)
*g* (Pistolesi et al., 2011)
*h* (Rosi et al., 2006)
*i* Calc. similarly to Métrich et al. (2021)
*j* (Polacci et al., 2009)
*k* (Pichavant et al., 2022)
*l* (Andronico et al., 2021)
*m* (L. Gurioli et al., 2013)
*n* Calc. with Mastin et al. (2009)
o (Andronico et al., 2013)
p Calc. with Steinberg and Babenko, (1978)

*Values calculated using cited literature are displayed in bold.*

### 3.3.2 Melt embayments

Embayments – also called hourglass inclusions or melt re-entrants in the literature – are crystal-hosted elongated melt pockets of various shapes and sizes, opened to the outside melt. Their formation mechanism is similar to that of melt inclusions (e.g., Faure and Schiano, 2005), through either crystallization around a defect or dissolution of the host crystal, with the difference that in the case of embayments the melt is never completely entrapped by the crystal as occurs for melt inclusions. During magma ascent, the volatile content of the melt surrounding the embayment will decrease, maintaining equilibrium with the exsolved gas phase. The limited volume of melt embayments, often prevents bubbles formation inside, resulting in an embayment melt being super-saturated in volatiles compared to the surrounding melt (e.g., Fig. 6 in Costa et al., 2020). This concentration gradient leads to diffusive transport of volatile species from the base to the mouth of the embayment resulting in a diffusion profile. If such a profile is preserved in natural samples, it can then be inverted to derive an ascent rate assuming that the elongated tubular shape of the embayment and the negligible permeability of the host crystal leads to diffusion being unidirectional (i.e., 1D; see comparison with 3D modelling, highlighting when 1D modelling is appropriate in deGraffenried and Shea, 2021) and prevents any advective melt motion in the embayment itself. Embayments can occur in any crystal and volatile diffusion through embayments has been studied in quartz (e.g., Liu et al., 2007; Myers et al., 2018), plagioclase (e.g., Humphreys et al., 2008; Myers et al., 2021) and olivine (e.g., Lloyd et al., 2014; Ferguson et al., 2016; Moussallam et al., 2019,

2021; Newcombe et al., 2020), in melt compositions ranging from basaltic to rhyolitic. The diffusion of volatile elements in an embayment depends on multiple parameters (melt composition, temperature, pressure, degassing path, decompression rate, amount of pre-exsolved volatiles, oxygen fugacity), some of which change with time. Therefore the regression of natural diffusion profiles must be solved numerically, as an analytical solution is not available.

Here we use EMBER (Georgeais et al., 2021) to model the diffusion profiles of $H_2O$ in olivine-hosted embayments. EMBER produces time dependent diffusion profiles considering a grid search of input parameters such as initial dissolved concentrations and exsolved volatile mass fractions and constant ascent rates. The software reads model-generated degassing paths (e.g., Solex; Witham et al., 2012) to simulate equilibrium degassing upon ascent. The quenching pressure is determined by coupling the Iacono-Marziano et al. (2012) volatile solubility model with $H_2O$, $CO_2$ and major elements concentrations measured in the glass at the mouth of the embayment. Both the initial volatile concentration and initial storage pressure ($P_{pick\text{-}up}$) are calculated using the volatile concentration plateau within the embayments. We selected embayment at least twice as long as their width, and the most tubular. We also selected embayments with a diameter variation less than 60% to avoid bias of decompression rates due to embayment geometry (deGraffenried and Shea, 2021). The majority of selected embayments exhibit a bubble at their mouth. This bubble is assumed to remain close to ambient pressure during the ascent and therefore the volatile concentration at the volatile/melt boundary is dictated by the equilibrium solubility. In this study, we

use EMBER to fit $H_2O$ diffusion profiles as it is the fastest diffusing volatile specie, retaining gas-melt equilibrium even under high decompression rates (Pichavant et al., 2013).

The EMBER software tests several input parameters: an initial dissolved volatile element concentration ($C_i$), an initial exsolved volatile mass ($M_0$) and a constant decompression rate (dP/dt). Parameters such as temperature (T), melt composition and the pressures at which the embayment-bearing crystals are picked up by ascending magma and quenched (respectively $P_{pick\ up}$ and $P_{end}$) are set at constant values. The values used for the calculations are listed in Table A3.1. The temperature is set to 1100°C (La Spina et al., 2015). Starting and quenching pressure were calculated with the maximal $H_2O$ and $CO_2$ concentration within each embayment's plateau, combined with the model of Iacono-Marziano et al., (2012). Embayments that we measured only with Raman do not provide any $CO_2$ concentration to be used for pressure determination (ST207_2, ST207_3 and SHE750_C). Using embayments with both $H_2O$ and $CO_2$ measurement and their associated $P_{pick\text{-}up}$, we estimated a relationship to calculate the approximate starting pressure only with $H_2O$ (Figure S3-2). Volatile concentration at the mouth and at the concentration plateau are therefore representative of the conditions when the melt was quenched and prior to ascent, respectively. Quenching pressure is determined, when possible, with the closest volatile measurement to the outlet bubble. Otherwise, we repeat the fit calculation with different $P_{end}$ and we select the value associated with the best fit. The initial pressures are relatively well constrained with the volatile concentration measured at the concentration plateau.

In this study, we used the Iacono-Marziano et al. (2012) model to generate degassing path files. Modelling conditions are similar to those described in the EMBER original study (e.g., 101 Monte-Carlo iterations, 2 µm spatial uncertainty; Georgeais et al., 2021).

### 3.3.3 Analytical measurements

#### *3.3.3.1 SIMS and NanoSIMS*

We measured the concentrations of five volatile species ($H_2O$, $CO_2$, S, Cl and F) along large (>25 µm wide), glassy melt embayments with a Cameca IMS 1280 HR2 ion microprobe at CRPG-CNRS-Nancy. Analytical conditions followed the settings used in other volatile studies (e.g., Hauri et al., 2002; Shimizu et al., 2019; Rose-Koga et al., 2020; Moussallam et al., 2021). In brief, we used a 20 keV Cs+ primary ion beam of 0.5 nA defocused to be 15 – 20 µm in diameter and an electron gun to compensate for charge build-up at the sample surface. Secondary ions were accelerated at 10 kV. A 5-minute pre-sputter with a 30 × 30 µm square raster was applied, then analyses were performed on the 15 to 20 µm spot in the center of the rastered-clean area by a mechanical aperture placed at the secondary ion image plane. Mass resolving power was set at ~7000 to separate mass interferences. Negative secondary ions of $^{12}C$, $^{16.5}O$, $^{17}O$, $^{16}OH$, $^{18}O$, $^{19}F$, $^{27}Al$, $^{30}Si$, $^{32}S$, and $^{35}Cl$ and the mass position of 11.8 amu were measured by an axial electron multiplier and faraday cups, using the peak switching method. Each analysis consisted of 10 cycles, and the total measurement time was ~15 min. Calibrations were made using experimental glasses (Shishkina et al., 2010) for $H_2O$ and $CO_2$

and reference glass standards (KL2G, 40428, 47963 and VG2; Jarosewich et al., 1980; Jochum et al., 2000; Kamenetsky et al., 2000) for F, S and Cl. Typical relative standard deviations (1σ) obtained from repeated analysis of a secondary basaltic glass standard, were 4, 9, 6, 7 and 7% for $H_2O$, $CO_2$, S, Cl and F, respectively.

For thinner embayments (<20 µm wide), we used the Cameca N50 NanoSIMS installed at MNHN-INSU-IMPMC in Paris to measure the concentration of $H_2O$, $CO_2$, S and Cl. Each measurement point was pre-sputtered for 2 minutes on a 5×5 $\mu m^2$ raster to remove potential contaminants and reach steady-state sputtering, then analyzed for 5 minutes on a 3×3 $\mu m^2$ raster. Analyses were performed with a 16 keV Cs + primary ion beam (≈20 pA), with an AS2 (200×200 µm) aperture diaphragm, rastering the surface of the sample. An electron flood gun (–8 keV) was applied for electrostatic charge compensation of the analyzed area. Secondary ions of $^{12}C$, $^{16}O^1H^-$, $^{28}Si^-$, $^{32}S$ and $^{35}Cl$ were collected in multidetection mode with five electron multipliers at a mass resolving power of ~8000. Typical relative standard deviations (1σ) calculated by repeating the measurements of glass standards were 4, 6, 4 and 9% for $H_2O$, $CO_2$, S and Cl, respectively. Details of the calibration for both instruments and associated error assessment can be found in the appendix (Tables A1.1 to A1.4). Samples are pressed in indium to limit degassing within the controlled void.

#### *3.3.3.2 Microprobe*

Major and volatile (S, Cl and F) elements for the glassy embayment and host crystals were measured by electron microprobe at the Laboratoire Magmas et Volcans with a Cameca SxFiveTactis microprobe. Major element analyses on glass were achieved using a 15 kV accelerating voltage, an 8 nA beam current and a 20 µm beam spot. Major elements were measured twice, at the mouth and at the interior of the embayment in order to check any variation in composition due to crystallization (e.g., Lloyd et al., 2014). Relative analytical uncertainties (1σ) obtained from repeated measurements of the basaltic glass standard VG-2 (Juan de Fuca ridge basalt, Dixon, 1997; Jarosewich et al., 1980) were less than 0.6% for $SiO_2$, 1% for $Al_2O_3$, FeO and CaO, 3.5% for $TiO_2$ and $Na_2O$, 10% for MnO, 1.5% for MgO, 4.5% for $K_2O$, 17% for $P_2O_5$. Sulfur, chlorine and fluorine were analyzed at 40 nA with a 5 µm spot and with counting times of 50 s for S and Cl, and 200 s for F. The internal precision of the microprobe is calculated by repeating the measurements 5 times on each spot and expressed as 3 standard deviations. The standard deviations (1σ) for S, Cl, and F were less than 5%, 4%, and 30%, respectively. Further details and precautions on the method can be found in Rose-Koga et al. (2020).

#### *3.3.3.3 Raman*

Embayments hosted in crystals too fragile to be pressed in indium were analysed for $H_2O$ with Raman spectrometry. Raman spectra were collected using an InVia

confocal Raman micro-spectrometer from Renishaw, equipped with a 532 nm laser diode set at 200 mW during the analysis. Analytical conditions are similar to those described in the study of Schiavi et al. (2018). Linear baselines were anchored between ~2980 and 3750 $cm^{-1}$ to better constrain stability between the successive measurements along embayments. Calibrations were established on Stromboli melt inclusions and synthetic basaltic glasses from Médard and Grove (2008), every three hours, and we report a clear increase of the slope of the calibration curve in the morning and then a stabilization of the calibration in the afternoon (Table A1.5).

#### *3.3.3.4 BSE microphotograph*

Back-Scattered Electrons (BSE) imaging of the LP glass texture were made with a Helios 5 PFIB CXe scanning electron microscope from ThermoScientific installed at Laboratoire Magmas et Volcans (Aubière, France). LP samples from eruptions from the 15$^{th}$ century, 1930, 2007, 8 and 24 November 2009 and the August 2019 eruptions (ST207, L1930, 07PRX, STN_9, STN_8 and L2019, respectively) were analyzed in 2D. Bubble parameters (e.g., number, size, density) were determined through the use of the program FOAMS (Shea et al., 2010). Only objects with a diameter larger than seven pixel (16 µm and 4 µm respectively for ×25 and ×100 magnitude pictures) were counted. Plots and statistic generated by FOAMS for each sample can be found in the appendices (Figure S3-3). Decompression rate calculation are reported on Table 3-3 and

results from the combination of the vesicle number density obtained from FOAMS and from Toramaru, (2006)

## 3.4 **Results**

### 3.4.1 Melt embayment modelling:

#### *3.4.1.1 Embayment structural features*

We report $H_2O$ analyses of 22 embayments from eight eruptions: three from the 1456 paroxysm (ST207), three from the 1930 paroxysm (PST205), two from the 2003 paroxysm (ST345), four from the 2007 paroxysm (07PRX), one from the 8 November 2009 major eruption (STN9), two from the 24 November 2009 major eruption (STN8), four from the 3 July 2019 paroxysm (STG) and three from the 28 August 2019 paroxysm (SHE750). Embayments are entirely glassy due to rapid quench, cylindrical and range between 34 and 190 microns in length, and 6 to 86 microns in width. They exhibit close to no bottleneck (<40% constriction) except for a few embayments with up to 60% constriction near the outlet bubble. Detailed structural information can be found in Table A3.2. The vast majority of the embayments (19 out of 22) retain a bubble at their mouth.

#### *3.4.1.2 Major composition and volatile concentration*

Microprobe measurements yield uniform major elements concentrations (within error) through the entire length of all embayments. Major element composition in the inner region of the embayments (Table A3.3) is also uniform across the different eruptions with nonsystematic variations of $SiO_2$ (47.9-50.8 wt.%), $Al_2O_3$ (17.4-19.2 wt.%), CaO (10.8-12.9 wt.%), FeO (7.4-9 wt.%) MgO (3.8-5.2 wt.%).

$SiO_2$ and $K_2O$ concentrations show that all the embayments of our study belong to the LP basaltic magma of shoshonitic series (Figure 3-1).

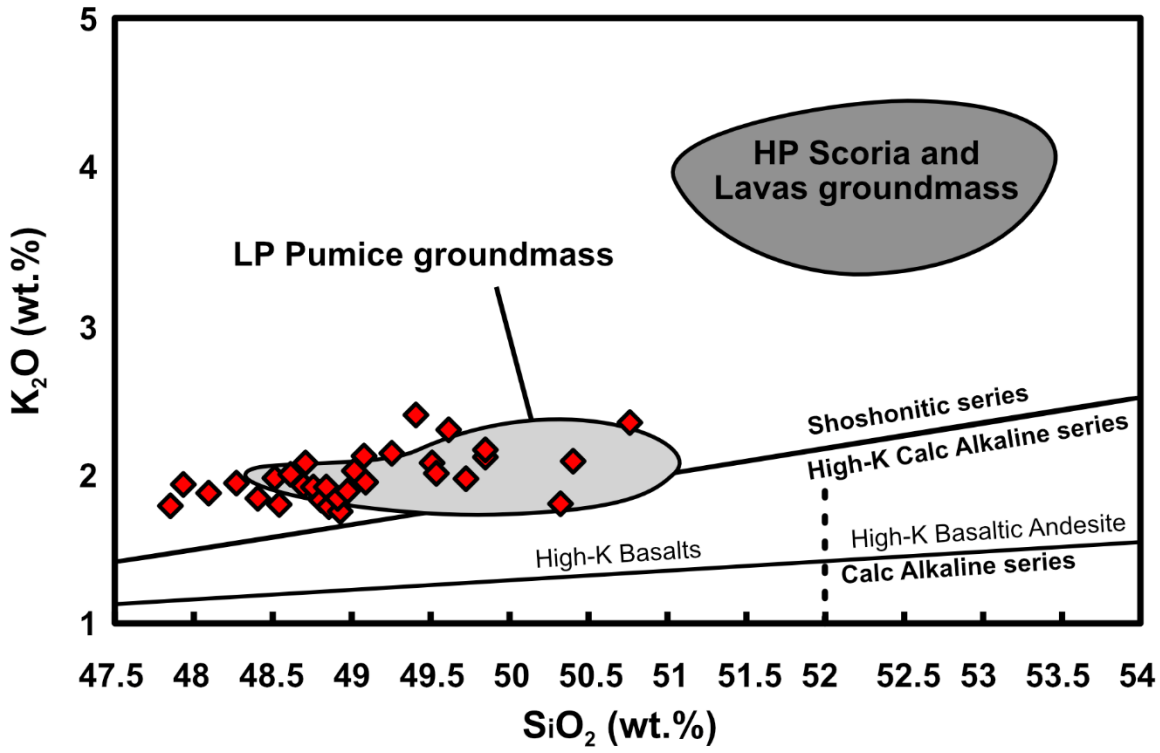


***Figure 3-1**: $K_2O$ vs $SiO_2$. All of our samples (in red diamonds) either fall within or close to the LP Pumice groundmass domain. Our data are placed within the framework of Bertagnini et al., (2013)*

All $H_2O$ profiles exhibit the same trend with an increasing volatile concentration inward, away from the bubble, eventually reaching a concentration plateau at the bottom of the embayment (Fig. 3-2). The L1930 embayment is the only exception, as in this case the concentration plateau was not reached by our analysis as only half of the embayment was exposed (polished). The variability and plateau of $H_2O$ concentration in major eruptions (0.63-1.27 wt.% and 0.6-1.9 wt.% respectively for the 8$^{th}$ and 24$^{th}$ November 2009) tend to be lower than in paroxysmal eruptions (0.2-1.9 wt.%, 0.43-1.74 wt.%, 0.58-2.70 wt.%, 0.63-2.25 wt.%, 0.31-2.64 wt.% and 0.35-2.26 wt.% respectively for the 15$^{th}$ century, 1930, 2003, 2007, July 2019 and August 2019 eruptions). The $H_2O$ concentration near the outlet bubble range

from 0.2 to 2.01 wt.%, which is sometimes significantly higher than the values in the glass rims. Additionally, with both SIMS and nanoSIMS, we measured the variation of $CO_2$, S, Cl and F along these embayments (Table A2.1 to A2.20).

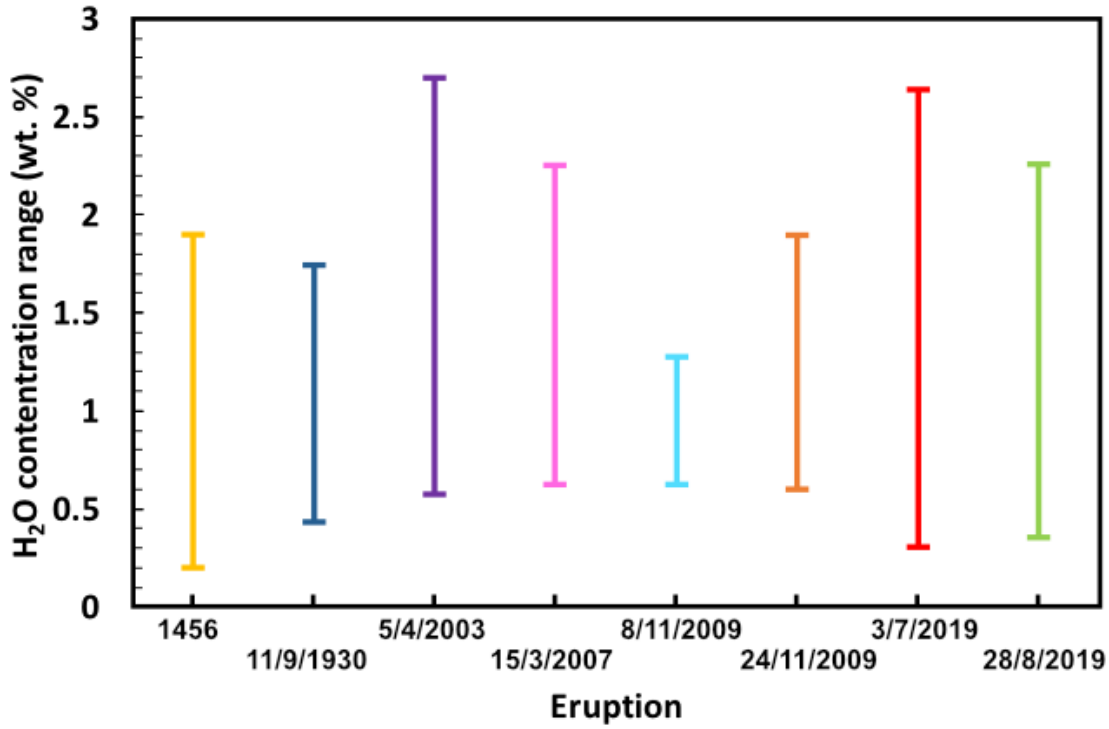


***Figure 3-2**: Range of $H_2O$ concentration recorded within embayments for each eruption. Embayments from major eruption cover a smaller range of $H_2O$ concentration with $H_2O$ variation under 1.5 wt.%.*

### *3.4.1.3 Decompression rate from embayment modelling*

The embayments record decompression rates between 0.5 and 7.2 MPa/s (20 to 283 m/s) which translates into ascents lasting between 10 seconds and 3 minutes from 46 to 177 MPa (around 1.6 to 5.8 km depth). By looking at the different eruptions, embayments from major eruptions record decompression rates between 0.5 and 2.2 MPa/s, while embayments from paroxysms record higher rates, up to 7.2 MPa/s. Seven embayments show a very good agreement between Raman, nanoSIMS and SIMS profiles (e.g., 07PRX2_5 from the 2007 eruption, Figure 3-3). We noticed that Raman spectrometry measurements however had poorer

reproducibility with overestimations of up to 1 wt.% $H_2O$. We preferred therefore SIMS and nanoSIMS profiles over Raman profiles in cases where differences were observed, although five embayments out of 22 were measured solely with Raman spectrometry (ST207_2, ST207_3, L1930, STN8v2_1_2a, STN8v2_1_2b). $H_2O$-modelled decompression rates for Stromboli are the highest ever recorded with the embayment method to date. Some diffusion profiles are not well fit by our models but are still kept within our results since they usually record intermediate decompression rates. In addition, we fit the whole dataset for each embayment even if measurements come from different methods (for instance, we modeled the best fit using both raman and nanoSIMS measurements for the profile displayed in Figure 3-3).

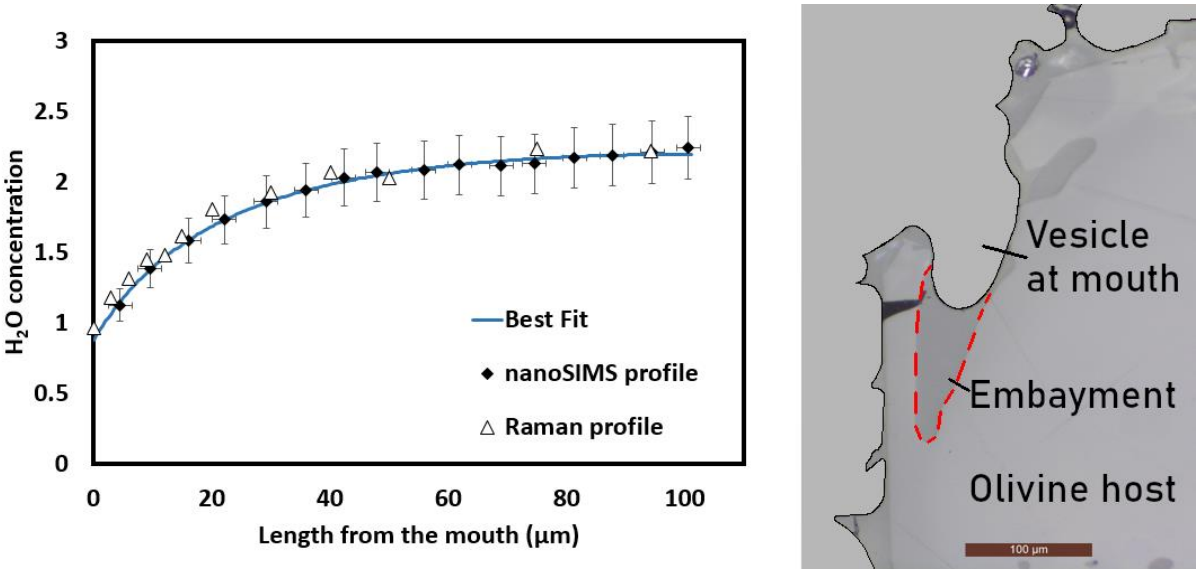


***Figure 3-3:*** *(Left) $H_2O$ diffusion profile measured with Raman and nanoSIMS, compared with the EMBER-generated best fit. Both measurements are in total agreement and well fitted. (Right) Picture of the corresponding olivine hosted melt embayment (07PRXv2_5) from the 2007 paroxysm.*

#### *3.4.1.4 Bottleneck correction factor*

Thirteen out of the twenty-two embayments (particularly STN9_4 and 07PRX2_4) show a noticeable bottleneck near the outlet bubble, where the embayment diameter is narrowed. This shape can limit volatile diffusion and artificially raise the recorded decompression rate. For the profile of 07PRX2_4, the $H_2O$ diffusion front is located within the bottleneck which, according to deGraffenried and Shea (2021), correspond to cases where the impact of the bottleneck on melt embayment modelling is almost negligible. For the others, we applied a correction following deGraffenried and Shea, (2021). This correction results from the comparison of 1D and 3D forward modelling for different bottleneck size and different decompression rates. Corrected decompression rates are usually within the direct measurement uncertainty range except for STN9_4 (Figure S3-4). Best-fit results and the associated corrected decompression rates are given in Table 3-2.

***Table 3-2:*** *EMBER's results of the 22 embayments following the aforementioned gridsearch (Table A3.1). The decompression rate and related error for each embayment, and the relative bottleneck-corrected values are displayed in bold. Ascent rate is calculated using a density of 2600 kg/m$^3$.*

| | dPdt (MPa/s) | | Ascent rate (m/s) | $C^{o}_{H2O}$ (wt%) | | $M_0$ (wt%) | | Time of ascension (s) | $P_{end}$ (MPa) | Bottleneck (%) | Bottleneck corrected dPdt (MPa/s) |
|---|---|---|---|---|---|---|---|---|---|---|---|
| **15th century** | | | | | | | | | | | |
| **ST207_2** | **2.86** | **+ 1.86 / - 1.24** | 112 | 1.80 | + 0.10 / - 0.10 | 0 | + 0.0 / - 0.0 | 30 | 0.1 | n.d | |
| **ST207_3** | **7.21** | **+ 0.00 / - 0.11** | 283 | 2.10 | + 0.00 / - 0.01 | 0 | + 0.0 / - 0.0 | 15 | 0.1 | 25.0 | 7.21 |
| **ST207_4** | **5.34** | **+ 2.79 / - 1.55** | 209 | 1.60 | + 0.10 / - 0.00 | 1.6 | + 0.0 / - 0.0 | 10 | 3 | 39.0 | 5.34 |
| **9/11/1930** | | | | | | | | | | | |
| **PST205_4** | **1.62** | **+ 0.62 / - 0.31** | 64 | 2.00 | + 0.05 / - 0.05 | 0.1 | + 0.0 / - 0.0 | 54 | 1 | 34.6 | 1.28 |
| **PST205_3** | **1.31** | **+ 1.55 / - 0.78** | 51 | 2.10 | + 0.10 / - 0.10 | 0 | + 0.0 / - 0.0 | 56 | 3 | 40.3 | 0.88 |
| **L1930** | **1.62** | **+ 4.17 / - 1.24** | 64 | 1.80 | + 0.50 / - 0.10 | 0.2 | + 0.0 / - 0.0 | 41 | 2 | n.d | |
| **4/5/2003 Paroxysm** | | | | | | | | | | | |
| **ST345_6A** | **2.86** | **+ 0.62 / - 0.47** | 112 | 1.90 | + 0.00 / - 0.10 | 3.2 | + 0.0 / - 0.0 | 34 | 1 | 29.0 | 2.68 |
| **ST345_16** | **6.90** | **+ 0.00 / - 0.35** | 270 | 2.60 | + 0.10 / - 0.00 | 0.4 | + 0.0 / - 0.0 | 26 | 10 | 48.0 | 6.90 |
| **3/15/2007 Paroxysm** | | | | | | | | | | | |
| **07PRXv2_2a** | **1.00** | **+ 0.31 / - 0.10** | 39 | 2.50 | + 0.00 / - 0.06 | 3.2 | + 0.0 / - 0.0 | 64 | 2 | n.d | |
| **07PRXV2_2b** | **0.50** | **+ 0.00 / - 0.06** | 20 | 2.30 | + 0.30 / - 0.00 | 0.1 | + 0.0 / - 0.0 | 128 | 12 | 23.5 | 0.39 |
| **07PRXv2_4** | **0.74** | **+ 0.38 / - 0.19** | 29 | 2.10 | + 0.00 / - 0.01 | 0 | + 0.0 / - 0.0 | 157 | 0.1 | n.d | |
| **07PRXv2_5** | **3.79** | **+ 0.00 / - 0.30** | 149 | 2.30 | + 0.10 / - 0.00 | 0.2 | + 0.0 / - 0.0 | 44 | 12 | n.d | |
| **11/8/2009 Major** | | | | | | | | | | | |
| **STN9_4** | **2.20** | **+ 0.00 / - 0.55** | 86 | 1.25 | + 0.05 / - 0.00 | 0 | + 0.0 / - 0.0 | 20 | 11 | 61.0 | 1.17 |
| **11/24/2009 Major** | | | | | | | | | | | |
| **STN8v2_1_2a** | **0.50** | **+ 1.40 / - 0.72** | 20 | 1.05 | + 0.00 / - 0.00 | 0.1 | + 0.0 / - 0.0 | 132 | 5 | n.d | |
| **STN8v2_1_2b** | **1.31** | **+ 0.47 / - 0.00** | 51 | 2.10 | + 0.00 / - 0.01 | 0.8 | + 0.0 / - 0.0 | 51 | 5 | n.d | |
| **7/3/2019 Paroxysm** | | | | | | | | | | | |
| **STGv2-3** | **3.48** | **+ 2.17 / - 1.86** | 137 | 2.63 | + 0.05 / - 0.00 | 0.4 | + 0.0 / - 0.0 | 38 | 35 | 34.9 | 3.31 |
| **STGv2_1** | **2.86** | **+ 0.31 / - 2.02** | 112 | 1.80 | + 0.10 / - 0.00 | 0.1 | + 0.0 / - 0.0 | 40 | 6 | 22.7 | 2.76 |
| **STGv2_5** | **0.90** | **+ 0.38 / - 0.23** | 35 | 1.85 | + 0.00 / - 0.00 | 0 | + 0.0 / - 0.0 | 111 | 0.1 | 21.4 | 0.76 |
| **STGv2_7** | **2.24** | **+ 3.89 / - 1.86** | 88 | 1.90 | + 0.20 / - 0.00 | 0.1 | + 0.0 / - 0.0 | 48 | 18 | 46.0 | 1.69 |
| **8/28/2019 Paroxysm** | | | | | | | | | | | |
| **SHE750v2_1** | **1.93** | **+ 3.25 / - 1.71** | 76 | 2.30 | + 0.20 / - 0.00 | 0.1 | + 0.0 / - 0.0 | 68 | 1 | n.d | |
| **SHE750_S_C** | **2.24** | **+ 0.62 / - 0.31** | 88 | 2.20 | + 0.00 / - 0.01 | 1.6 | + 0.0 / - 0.0 | 53 | 1 | n.d | |
| **SHE750v2_4** | **5.66** | **+ 0.00 / - 0.33** | 222 | 2.20 | + 0.00 / - 0.00 | 0.2 | + 0.0 / - 0.0 | 21 | 20 | 35.4 | 5.66 |

### 3.4.2 LP pyroclasts texture :

#### *3.4.2.1 Scanning electron microphotographs*

We acquired four SEM microphotographs at ×25 magnification and eight microphotographs at ×100 magnification, per sample. All SEM microphotographs are given in supplementary materials (Figure S3-5 to S3-10). Investigated tephra are all bubble rich and crystal poor, typical of LP products (Figure 3-4). Each sample exhibits heterogeneous bubble size and distribution as well as traces of bubble coalescence. Qualitative examination of SEM microphotographs indicates noticeable differences between major and paroxysmal bubble size distribution and overall density. Major eruptions (STN_8 and STN_9) are characterized by fewer and bigger bubbles than paroxysmal eruptions.

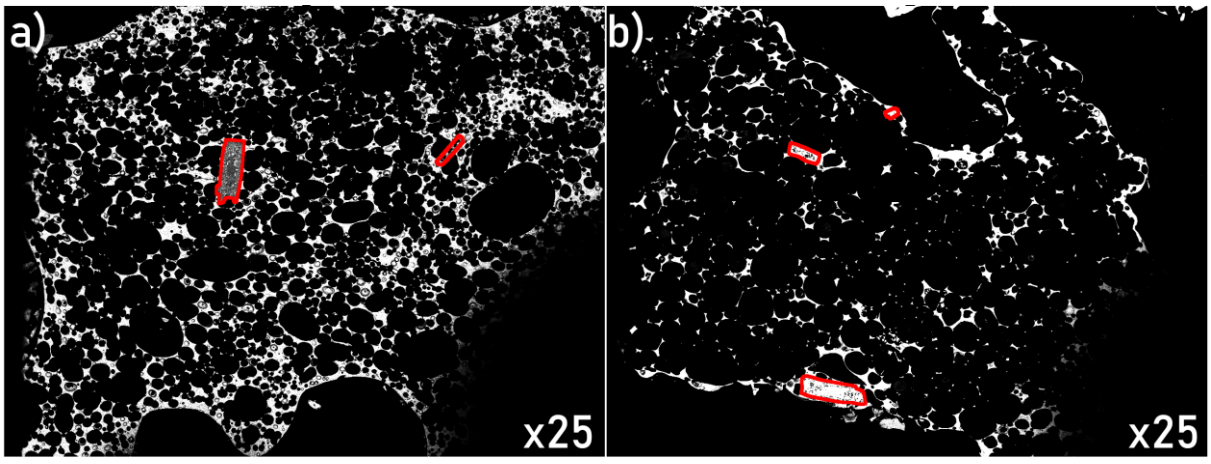


***Figure 3-4:*** *SEM microphotography of a) the L1930 sample (1930 paroxysm) and b) the STN8 sample (9th of November 2009). Vesicles are in black, glass in white and crystals are highlighted in red.*

#### *3.4.2.2 Decompression rate from Vesicle number density and Vesicularity*

All samples exhibit a majority of broadly spherical vesicles but also contain a few big and elongated bubbles sometimes surrounded by elongated smaller bubbles. Bubble size recorded are 4 to 1546 µm equally distributed between the different eruptions with only few variations in maximum recorded length (between 1046 and 1546 µm). Vesicularity ranges between 65-71% for paroxysms and 74-87% for major eruptions, which partially agree with Pioli et al. (2014), for the 2003 paroxysm and both major eruptions but not for the 2007 paroxysm where a higher vesicularity (within the ranges of 80%) is expected according to Pioli et al. (2014). This sample probably experienced HP mingling, which could explain the presence of several dendritic micro-crystals in the glass. The presence of isolated batches of LP-HP mingling is also reinforced by scarce matrix glass banding patterns only visible for paroxysms.

Bubble population distribution provides additional information about nucleation events during the ascent. For example, we can infer the number of nucleation event that took place during each studied eruptions (e.g., Polacci et al., 2003; Shea et al., 2010). A single nucleation event took place for the 24 November 2009 eruption, two for the 9$^{th}$ of November 2009 and August 2019 eruptions and three for the 15$^{th}$ century paroxysm, using the number of modes in the bubble size distribution histogram (Figure S3-3). The September 1930 and the 2007

paroxysms both resulted from either a single continuous or multiple successive nucleation events. The histogram of each of these eruptions display a mode corresponding to a small population of the biggest bubbles (with a diameter usually over 900 microns) which either corresponds to one early nucleation event happening before the final ascent or more likely bubble coalescence taking place during the ascent.

#### *3.4.2.3 Vesicle number density and decompression rate calculation*

Vesicle number density is calculated for each sample with the FOAMS software and automatically corrected for the sample vesicularity (i.e., $Nv_{corr}$; Shea et al., 2010). This vesicle number density is calculated around 11971 and 13125 $mm^{-3}$ for the 24 November and 8 November 2009 major eruptions respectively. Among the paroxysmal eruptions, the large-scale paroxysms are associated with the lowest $Nv_{corr}$ values (33635 and 50073 $mm^{-3}$ for 1930 and 15$^{th}$ century paroxysms, respectively) and both 2007 and August 2019 paroxysms are related to significantly higher $Nv_{corr}$ (75185 and 68946 $mm^{-3}$, respectively). We propose decompression rates calculations from bubble number density using the equations of Toramaru (2006) ranging from 1.57 to 1.88 MPa/s for the 24 and 8$^{th}$ of November 2009 major eruptions respectively, to 2.85, 3.43, 3.92, 4 MPa/s for the 1930, 15$^{th}$ century, 2007 and 2019 paroxysmal eruptions respectively (Table 3-3).

***Table 3-3:*** *Vesicle number density and related decompression rates calculated following Toramaru (2006). In detail, the decompression rates were calculated for T=1100°C (La Spina et al., 2015) and a partial volume of volatile element in the melt $V_m = 3e^{-29}$ $m^3$ (Toramaru, 2006). We calculated an average water diffusion coefficient from the equation of Freda et al. (2003), and determined the values of pressure and $H_2O$ content at saturation via the concentration plateaus in the embayments for each sample. Interfacial tension was set to 0.059 N/m, according to data from Le Gall and Pichavant (2016a, 2016b). $N_a$ and $N_v$ stand for the bubble density per surfacic or volumic unit, respectively and $N_{vcorr}$ stands for the bubble density per volumic unit of glass (corrected from bubble growth). $P_{sat}$ and $H_2O_{sat}$ are derived from embayment data.*

| | $N_a$ ($mm^{-2}$) | $N_v$ ($mm^{-3}$) | $N_{vcorr}$ ($mm^{-3}$) | dPdt (MPa/s) | Ascent rate (m/s) | $P_{sat}$ (MPa) | $H_2O_{sat}$ (wt.%) |
|---|---|---|---|---|---|---|---|
| **15th century Paroxysm** | 359 | 15355 | **50073** | **3.43** | 125 | 110 | 2.1 |
| **11/9/1930 Paroxysm** | 233 | 9971 | **33635** | **2.85** | 104 | 87 | 2.1 |
| **15/3/2007 Paroxysm** | 414 | 26128 | **75185** | **4.18** | 153 | 137 | 2.3 |
| **8/11/2009 Major** | 131 | 3427 | **13125** | **1.88** | 68 | 46 | 1.25 |
| **24/11/2009 Major** | 75 | 1579 | **11971** | **1.57** | 57 | 66 | 2.1 |
| **28/8/2019 Paroxysm** | 393 | 20221 | **68946** | **4.00** | 146 | 131 | 2.3 |

#### *3.4.2.4 Crystal texture analysis*

Combination of BSE microphotographs and microprobe analysis of 14 host crystals show noticeable variation of olivine composition (i.e., forsterite content; Fo) from the core to the rim. Details on the measurements and the BSE pictures are given in appendices (Figures S3-11). The olivines Fo content range around 68-86 for the 15$^{th}$ century, 82-83 for 1930, 71-86 for 2003, 70-86 for 2007, 70-74 for the 24 November 2009, 75-86 for July 2019 and 81-87 for August 2019. Eleven out of 14 olivines analyzed show a global reverse zonation pattern (i.e., higher Fo at the rim than at the core). Yet, 8 out of 14 crystals exhibit a 0.5 to 1.5 Fo decrease around 20 µm close to the rim. Few crystals display a complex (i.e., not concentric) core-to-rim Fo variation, that looks related to cracks (e.g., 07PRXv2_5) or occurrences of embayments and melt inclusions on some cases (e.g., SHE750_S, ST217_3 and STGv2_6). Except for STGv2_5, all 14 crystals analyzed show a large abundance of melt inclusions.

## 3.5 **Discussion**

### 3.5.1 Significance of different ascent rates:

#### *3.5.1.1 Comparison between embayment and bubble number density-derived decompression rates*

Both bubble number density (BND) speedometer and melt embayment modelling are methods relying on volatile exsolution and are therefore particularly sensitive to the last few km of ascent (e.g., Sparks, 1978; Dixon, 1997). They have been compared in silicic eruptions in previous studies which found that BND decompression rates are consistently higher than decompression rates from embayments by one to three orders of magnitude (e.g., Cassidy et al., 2018; Myers et al., 2021). Here, decompression rates from both methods agree within the same order of magnitude (Figure 3-5). The higher embayment-derived decompression rates, agree with the rates derived from vesicle number density on the same sample within a factor of two.

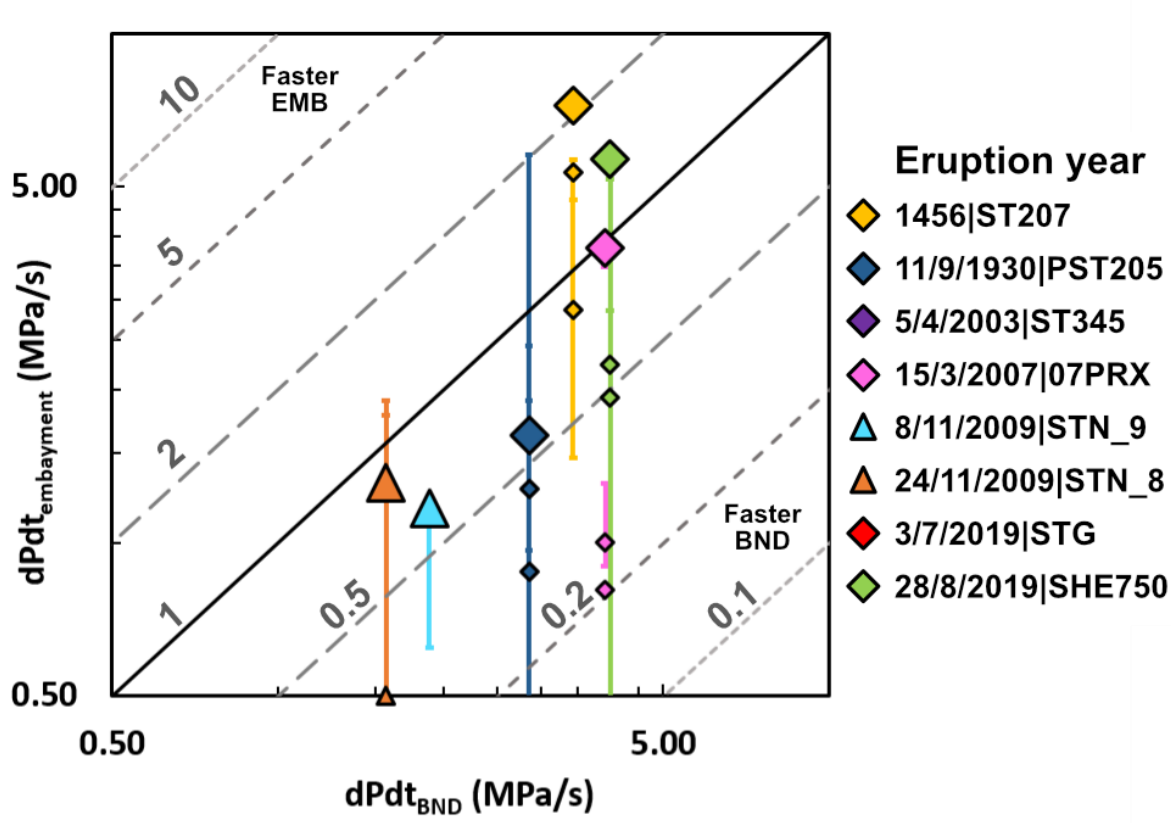


***Figure 3-5:*** *Comparison between bottleneck-corrected embayment-calculated and BND-calculated decompression rates. Triangles and diamonds are respectively for major and paroxysmal eruptions. The number associated with the seven parallel lines is the difference factor between the two decompression rates.*

Bubble number density results from this study provide decompression rates in agreement with the embayment modelling method, but range 1 to 2 order of magnitude higher than all past LP textural studies (e.g., Polacci et al., 2009; Andronico et al., 2021; Pichavant et al., 2022). This difference is partially explained by how 3D images are acquired. Vesicle number densities are one order of magnitude higher when converting 2D images to 3D images than when direct 3D images are acquired (Polacci et al., 2006, 2003; Shea et al., 2010). This is due to 2D image resolution being higher than 3D scans and thus decreasing the threshold of the minimal bubble size counted. In this study, the minimal bubble

size is around 4 µm while it is higher in other studies (e.g., 12 µm and over 12.5 µm respectively Pichavant et al. 2022; Polacci et al. 2009), despite vesicles smaller than 12 µm being observed (Pichavant et al., 2022). In the samples of this study, the 2D-proportion of bubbles ranging between 4 and 12 µm in size represents a significant one seventh to one sixth of the total number of vesicles measured in each sample (around 300 to 500 vesicles). The vesicularity found by Pichavant et al. (2022) is in good agreement with ours because the small bubbles between 4 and 12 µm have a negligible volume, but this results in a different BND. The last parameter contributing to the difference in BND estimates is the shape of the bubbles. A recent study on ash quantified the BND with a resolution down to 0.2 µm (Andronico et al., 2021). In this study, the ash fragments exhibit two types of vesicles: rounded, and sheared irregular-shaped, that the authors called type 1 and type 2 vesicles, respectively. Their hypothesis is that deformed vesicles are formed prior to spherical bubbles. Therefore, it is essential to consider solely type 1 vesicles for bubble number density calculations, as they are representative of the last ascent event. In addition, elongated bubbles provide stereological issues during the 3D conversion (Shea et al., 2010; Andronico et al., 2021). Only one third of the total vesicle number (Type 1 + 2) is therefore used for vesicle number density calculation prior to 3D conversion. In our study, the vast majority of vesicles are round and thus taken for the vesicle number density calculation. These three BND differences in the method of data acquisition may be responsible for

the one order of magnitude difference between our BND and that obtained in the literature.

### 3.5.2 Magma ascent rate and eruptive dynamics

Geophysical signals provide key insights into eruption monitoring and chronology prior to and during the eruption. Thermal imagery of the ejection of pyroclasts out of the vent at the summit crater during an eruption provides constrains over the very last step of magma ascent. Ballistics ejection speeds range from 90-130 m/s for both November 2009 major eruptions (L. Gurioli et al., 2013), from 90-160 m/s for both 2019 paroxysms (Giordano and De Astis, 2020), 150 m/s for the 2007 paroxysm (Andronico et al., 2013) and up to 200 m/s for the 2003 paroxysm (Rosi et al., 2006). Gas ejection rates were also constrained either with direct observations (e.g., 2003 and 2007 paroxysms) or recovered from ballistic dynamics using the equation of motion from Steinberg and Babenko (1978) (e.g., 2007 and both 2019 paroxysms; Ripepe and Harris, 2008; Giordano and De Astis, 2020, respectively). We calculated gas ejection rates for both 2009 major eruptions in a similar way using data from Gurioli et al. (2013) and obtained a range of 100-150 m/s for both events, while over 200 m/s was obtained for both 2019 paroxysms (Giordano and De Astis, 2020), 210 m/s for the 2007 paroxysm (Pistolesi et al., 2011; Andronico et al., 2013) and up to 320 m/s for the 2003 paroxysm (Rosi et al., 2006). The highest ascent rates determined by the

embayment method (46-283 m/s) are within the same range as these observations for each eruption.

Maximum ascent velocities from embayments correlate well ($R^2$=0.91, Pearson coefficient of 0.94) with maximum ballistic ejection velocities and very well with maximum gas ejection velocities ($R^2$=1.00, Pearson coefficient of 1.00), with the exception of the August 2019 paroxysm (Figure 3-6). Ballistics are consistently slowed down compared to the gas prior to ejection and the faster the ascent rate, the bigger the ballistic deceleration, in agreement with past studies (e.g., Steinberg and Babenko, 1978; Pistolesi et al., 2011). The mean ascent rate in the conduit (determined from embayments) is within the same order of magnitude as gas ejection rate for all eruptions, yet consistently slower, indicating some amount of magma acceleration near the surface. This velocity difference of ~60 m/s appears fairly constant between eruptions (figure 3-6).

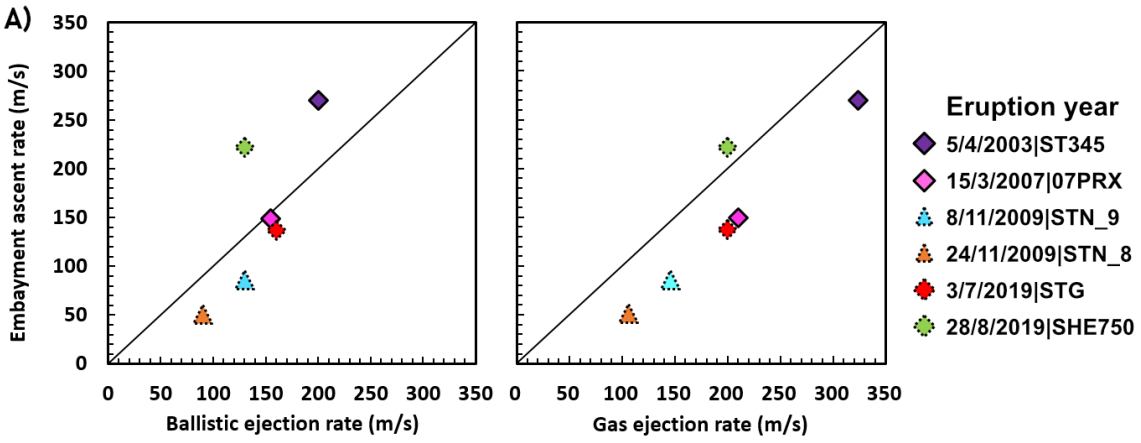


***Figure 3-6:*** *Comparison between conduit mean (i.e., maximum embayment determined) ascent rate and A) maximum ballistic ejection rate or B) maximum gas ejection rate. Major and paroxysmal eruptions are represented as triangles and diamonds respectively. In A), solid and dashed symbol contours represent direct observations and model calculations from deposits (Giordano and De Astis, 2020; L. Gurioli et al., 2013). The two symbols above the 1:1 line indicate that ballistics for these eruptions ascend in the conduit faster than they are ejected and thus a deceleration event prior to ejection out of the vent. Both parameters are well correlated ($R^2$=0.91). In B), solid*

*and dashed symbol contours represent direct observations and model calculations from ballistics ejection rate following the equation from Steinberg and Babenko (1978). Conduit ascent rate and gas ejection rate are strongly correlated ($R^2$=1) with a trend parallel to the 1:1 line, indicating proportionality prior to and after the fragmentation level, yet offset by a 60 m/s difference in velocity. In both cases, results for the 28 August 2019 paroxysm are noticeably off the trends.*

Intense vesiculation produces over pressurization of the magmatic conduit and leads to the deformation of the volcanic apparatus (e.g., Barth et al., 2019b). Ground deformation is proportional to the explosivity of an eruption yet follows a similar temporal evolution with each eruption (Ripepe et al., 2021). The ground tilt signal starts being noticeable around 5 to 10 minutes prior to eruption and ramps up noticeably in the last 30 to 150 s. These timescales are in very good agreement with our melt embayment modelling results.

### 3.5.3 Decompression rate and eruption parameters

During an eruption, the flow dynamic along conduit walls is not uniform and a heterogeneity in the ascent speed of individual batches of magma is expected (e.g., Gonnermann and Manga, 2007; Cassidy et al., 2018). Accordingly, the decompression rates we measured in several embayments from a single eruption vary widely, spanning over two orders of magnitude. The interesting parameter to extract is therefore the maximum decompression rate recorded for each eruption as this corresponds to the fastest the magma has ascended in a given eruption. Additionally, the energy output and eruptions dynamics of an eruption varies with time (e.g., Myers et al., 2021), starting low and increasing upon reaching a climax. To our knowledge, the tephra layers sampled for the 1456 and 1930 large scale

paroxysms are from the base of the deposit and thus likely not from the climax and most intense phase of the eruption. Data from the 1456 and 1930 large-scale paroxysms are likely not representative of the highest ascent rates for the whole eruptions and thus are not considered for the following discussions.

We compared our maximum decompression rates to recorded eruption parameters (Figure 3-7). A strong positive correlation appears between the maximum decompression rate and: (1) eruption magnitude ($R^2$=0.85 with a Pearson coefficient of 0.92), (2) eruption mass discharge rate ($R^2$=0.78 with a Pearson coefficient of 0.88) and (3) starting pressure ($R^2$=0.83 with a Pearson coefficient of 0.91). A weak correlation is apparent between the highest recorded decompression rates and plume height ($R^2$=0.48 with a Pearson coefficient of 0.69). We also looked at possible relations between melt embayment decompression rate and seismic data (i.e., ground tilt and seismic amplitude). Both resulted in an absence of clear correlation (see Figure S3-12).

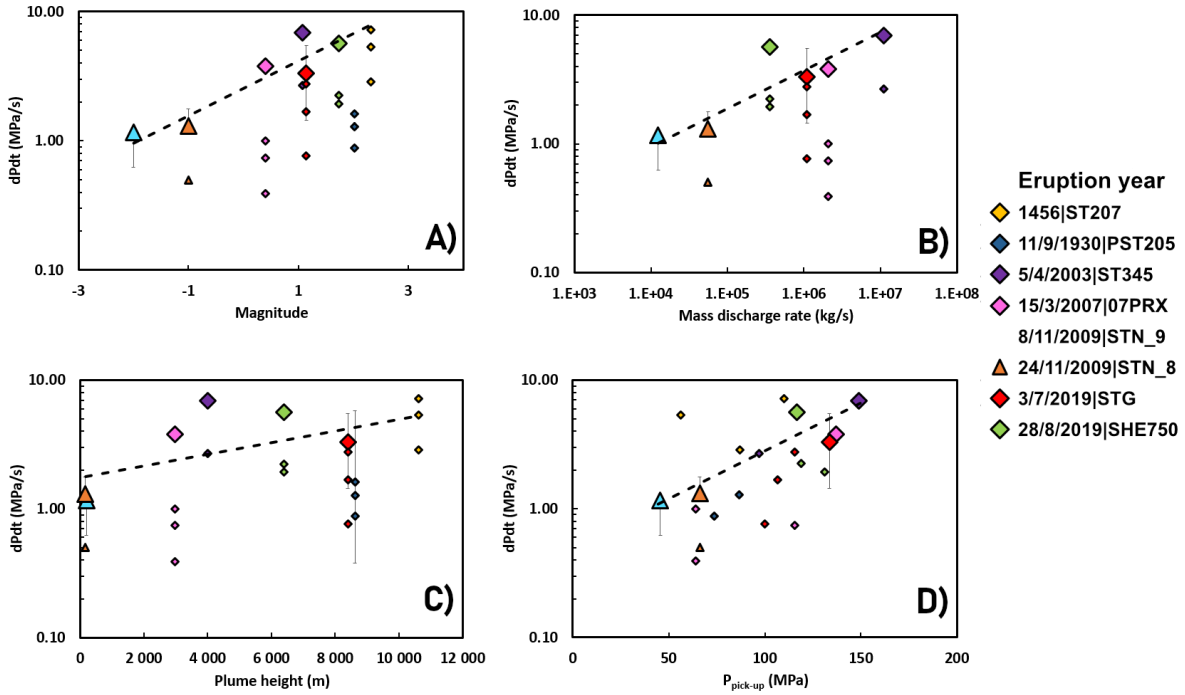


***Figure 3-7:*** *Comparison of bottleneck-corrected embayment-calculated decompression rates and eruption parameters. Triangles and diamonds are respectively for major and paroxysmal eruptions. The highest decompression rate for each major and small-scale paroxysm eruption is highlighted with a bigger symbol along with their associated 1σ error bars.*

Embayment-driven magma ascent rates are singularly high at Stromboli, even among others melt embayment modelling studies on mafic magma. Magma viscosity and volatile composition are both dynamics-related parameters that could explain such ascent rate differences. Stromboli magmas are Al-rich and Mg-depleted, which makes them more viscous than regular Hawaiian basalts and thus more likely to produce strong short-lived bursts rather than lava fountains. Yet, the magma viscosity and composition are quite similar to volcanoes such as Fuego and are not sufficient to explain the one order of magnitude ascent rate difference. We compared the embayment-determined ascent rates calculated for each mafic eruption with the maximum $H_2O$ and $CO_2$ content found in the melt inclusions,

the maximum $H_2O$ and $CO_2$ in the melt embayments and the $P_{pick\text{-}up}$ of these embayments (Fig. 3-8). A weak positive correlation appears between mafic embayment-determined ascent rates and: (1) melt inclusion maximum $H_2O$ ($R^2$=0.24), (2) melt inclusion maximum $CO_2$ content with the exception of the Aoba melt inclusions ($R^2$=0.39), (3) embayment $H_2O$ content ($R^2$=0.41) and (4) embayment $CO_2$ content ($R^2$=0.39). Embayment decompression rates show a strong positive correlation with the pressure at which embayments are picked-up by ascending magma ($R^2$=0.55). It is thus quite likely that the volatile content in the magma chamber, and more importantly the volatile content dissolved in the melt (and the related saturation pressure) when the magma starts ascending sufficiently enough to be recorded by melt embayments, play a major role on the fast ascent rate recorded at Stromboli.

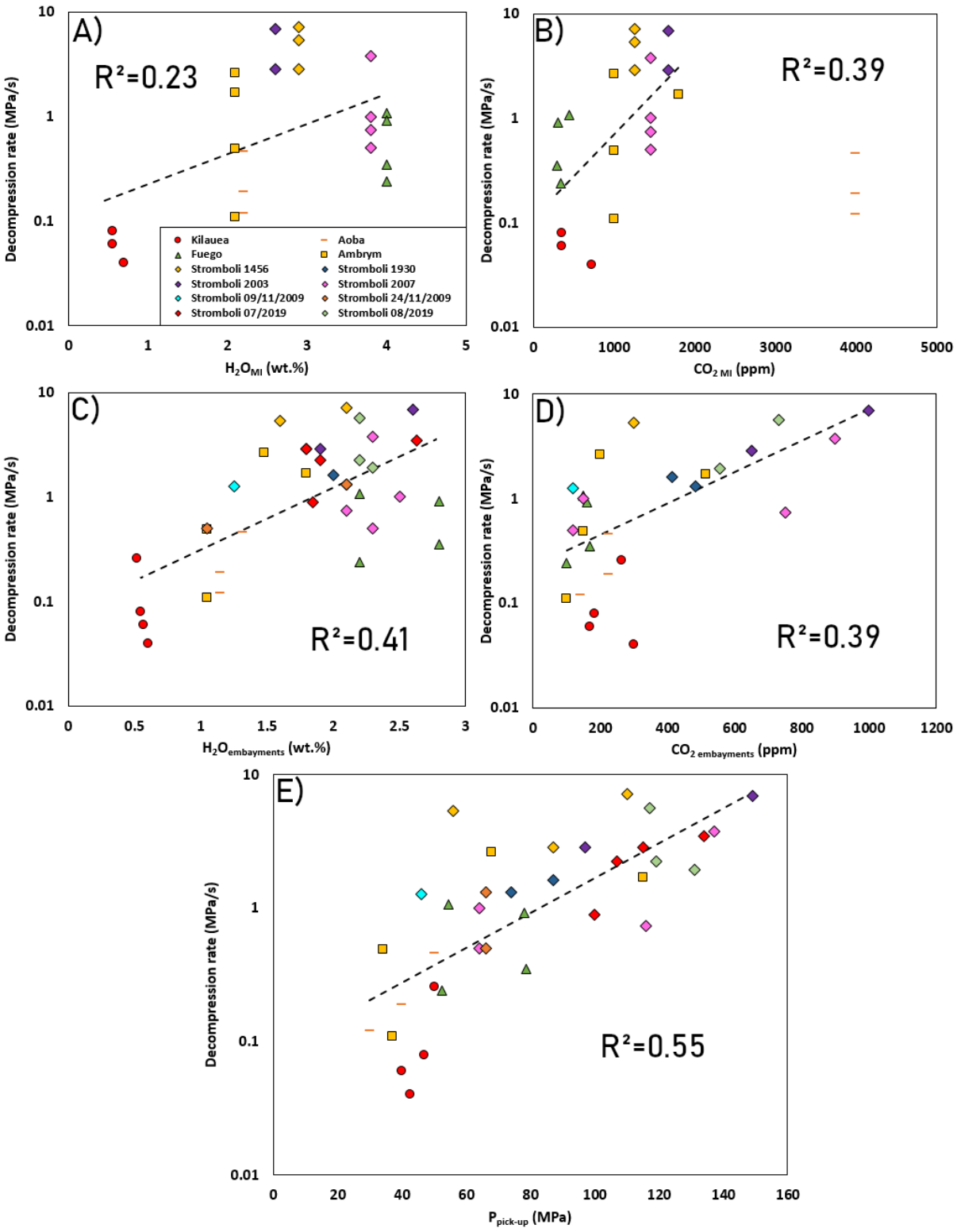


***Figure 3-8:*** *Comparison between embayment-determined magma decompression rate and melt inclusion A) maximum $H_2O$ concentration and B) maximum $CO_2$ concentration, melt embayment C) maximum $H_2O$ concentration and D) maximum $CO_2$ concentration, and E) embayment-determined $P_{pick\text{-}up}$ for several mafic magmas. Melt inclusions data of Kilauea, Aoba, Ambrym, Fuego and the 1456, 2003 and 2007 paroxysms come from Sides et al. (2014); Moussallam et al. (2019, 2021); Lloyd et al. (2014) and Métrich et al. (2010), respectively. Melt embayment data of Kilauea, Aoba, Ambrym, Fuego and Stromboli come from Ferguson et al. (2016);*

*Moussallam et al. (2019, 2021); Lloyd et al. (2014) and this study, respectively. $P_{pick\text{-}up}$ values are calculated from the model of Iacono-Marziano et al. (2012).*

We stress that the starting pressures data are more indicative of the minimal depth at which the ascent started (i.e., where the embayment-bearing crystal got picked up by the ascending flow) rather than the exact starting point at which the crystallization happened. For instance, Métrich et al. (2010) found embayments for the 2007 paroxysm with 2.5-3 wt.% $H_2O$ and 1300-1400 ppm $CO_2$, thus indicative of a higher starting pressure (~185 MPa) than recorded for the 2007 embayments in our study (149 MPa). This suggests that, for this eruption, magma started ascending from deeper than the depths recorded by embayments from our study, before driving the embayment-bearing crystals upward. Whether the embayment is formed at $P_{pick\text{-}up}$ or in a deeper part of the conduit and ascending slow enough to reset the different volatile diffusion profiles at $P_{pick\text{-}up}$ prior to the ascent is not known. A 150 µm embayment within these conditions would require around six hours to reset its $H_2O$ profile and around four days to reset the $CO_2$ profile, both of which are within the residence timeframe calculated by Métrich et al. (2021).

### 3.5.4 From major explosions to paroxysms: a model for magma ascent dynamics

Stromboli has been continuously active for the last 1400 years (Rosi et al., 2013) while exhibiting a variety of behavior with regular Strombolian activity

punctuated by intense paroxysmal eruptions (Rosi et al., 2006; Giudicepietro et al., 2020). Stromboli feeding system involves two magma chambers, a shallow one (2-4 km) and a deep one (7-10 km) (e.g., Aiuppa et al., 2010; Métrich et al., 2010). LP magma gradually transforms (by degassing and crystallization) into HP magma (Métrich et al., 2001) which ultimately feeds the Strombolian activity. Perturbations (i.e. magma recharge events from the lower crust) within the volatile-rich magma recharge events in the deep LP reservoir are thought to play a major role in triggering paroxysms (Métrich et al., 2021). Our results provide additional constraints on the magma dynamics of the last 7 km to the surface. We propose a very fast ascent phase at a speed up to 280 m/s from up to 5.8 km deep (Figure 3-9).

Starting from $P_{pick\text{-}up}$ (i.e., where the crystal is picked up by ascending magma, recorded by the concentration of volatile elements in the embayment plateau) onward, magma ascent becomes much faster. It must be fast enough to conserve the observed $H_2O$ diffusion gradients. As we have argued in the section of BND, a significant number of smaller bubbles should nucleate, while existing ones continue to grow by diffusion and decompression (Pichavant et al., 2022; this study). This rapid ascent cannot be recorded by methods such as the slow Fe-Mg diffusion at the crystal edge and impedes the formation of microlites in the matrix (e.g., Bertagnini et al., 2003; Métrich et al., 2001, 2010; Andronico et al., 2021; Pichavant et al., 2011, 2022). This stage lasts between 10 s and a few minutes with a notable acceleration near the surface. All of these observations indicate the

presence of a stage in which a very fast magma flow is recorded. Such a last-stage event is consistent with ground inflation because significant pressurization of the conduit follow this sudden ascent and vesiculation (e.g., Ripepe et al., 2021), despite not finding any clear correlation with neither tilt nor seismic amplitude.

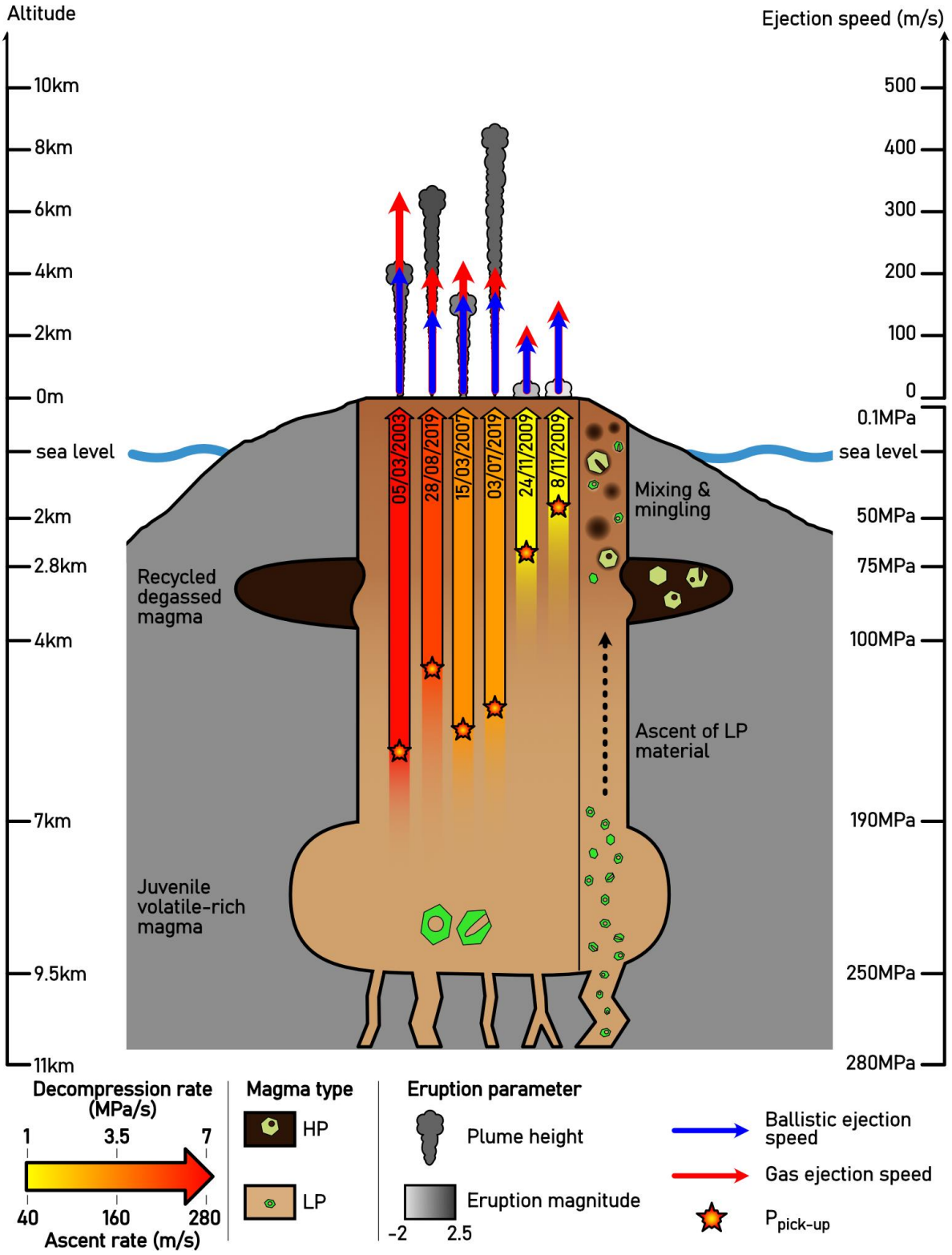


***Figure 3-9:*** *Schematic representation of the internal dynamics within Stromboli volcano for major and small-scale paroxysmal eruptions. The column at the utmost right is related to previous petrological studies including volatile-rich LP and volatile-poor HP magma generation from two separated magma chamber and their interaction (i.e., mixing and mingling). Large arrows in the conduit represent highest embayment-derived decompression rates calculated for each eruption from the fastest to the slowest ascent (left to right, respectively). The arrow are colored according to their decompression rate and their length indicates total vertical travel*

*distance recorded by embayments from $P_{pick\text{-}up}$ (indicated by the star) to the surface. Arrows are faded below $P_{pick\text{-}up}$ because the initiation pressure of magma ascent is not constrained with embayments. Here, $P_{pick\text{-}up}$ is representative solely of the values calculated with volatile concentrations within embayments from this study (i.e., where the crystal got picked-up by the ascending magma). Above the vent is represented the plume height. The shade of grey within the plumes indicates eruption magnitude. The length of blue and red arrows above the vent indicate maximum ballistic and gas ejection rates respectively.*

The transition from the start of the magma ascent to the rapid ascent recorded by embayments can be a part of continuous event or a discrete two-step event. Given that the window of the duration in which $H_2O$ is preserved in the inclusion while embayment is homogenized is short, we conclude the different speedometers captured a part of a single magma ascent event, rather than discrete two-step ascents with a ponding magma between the stages.

## 3.6 **Conclusion**

We investigated magma ascent rates at 8 of the latest Stromboli eruptions, with explosivity varying from major (2) to paroxysmal eruptions (6). Both melt embayment modelling and textural study agree in indicating that decompression rate over the last few km of ascent are high, with the highest ever recorded by the embayment method, and ranging between 0.39 to 7.21 MPa/s (20-283 m/s) for the 22 embayments. Maximum embayment-derived ascent rates correspond extremely well with bubble number density ascent rates, within a factor of two. The highest decompressions rates calculated for each eruption correlate well with eruption magnitude, mass eruption rate and depth of embayment storage, with a few notable outliers. Results from melt embayment modelling suggest that magmas rising from deeper ascend faster and lead to more volumic and intense

eruptions for major to small-scale paroxysmal events. Embayment-derived ascent rates correlate with gas and ballistic ejection rates, but are consistently ~60 m/s slower, indicating near-surface acceleration of the magma. We propose a fast magma ascent, recorded by embayments and bubble textures, lasting 10 s to 3 minutes and taking place, over at least the last 1.6-5.8 km of the conduit.

## 3.7 Acknowledgments

GG was supported by a PhD fellowship from the French Government “Ministère de l’Enseignement Supérieur, de la Recherche et de l’Innovation”. We sincerely thank Kenji Shimizu and Takayuki Ushikubo from the JAMSTEC Kochi institute (Japan) for providing SIMS advice and efficient sample preparation methods. Thorough guidance with the use of the SIMS from Etienne Deloule, Nordine Bouden and Johan Villeneuve (CRPG) were always appreciated. EPMA, BSE and RAMAN analysis greatly benefited from the expertise of Jean-Luc Devidal, Emmy Voyer and Federica Schiavi (LMV), respectively. Claire Fonquernie (LMV) is thanked for her help during sample preparation. We are grateful to Clément Petillot for the time spent sharing pointers about physics modelling and fluid mechanic. This is Laboratory of Excellence ClerVolc contribution number XX.

## 3.8 **Appendix**

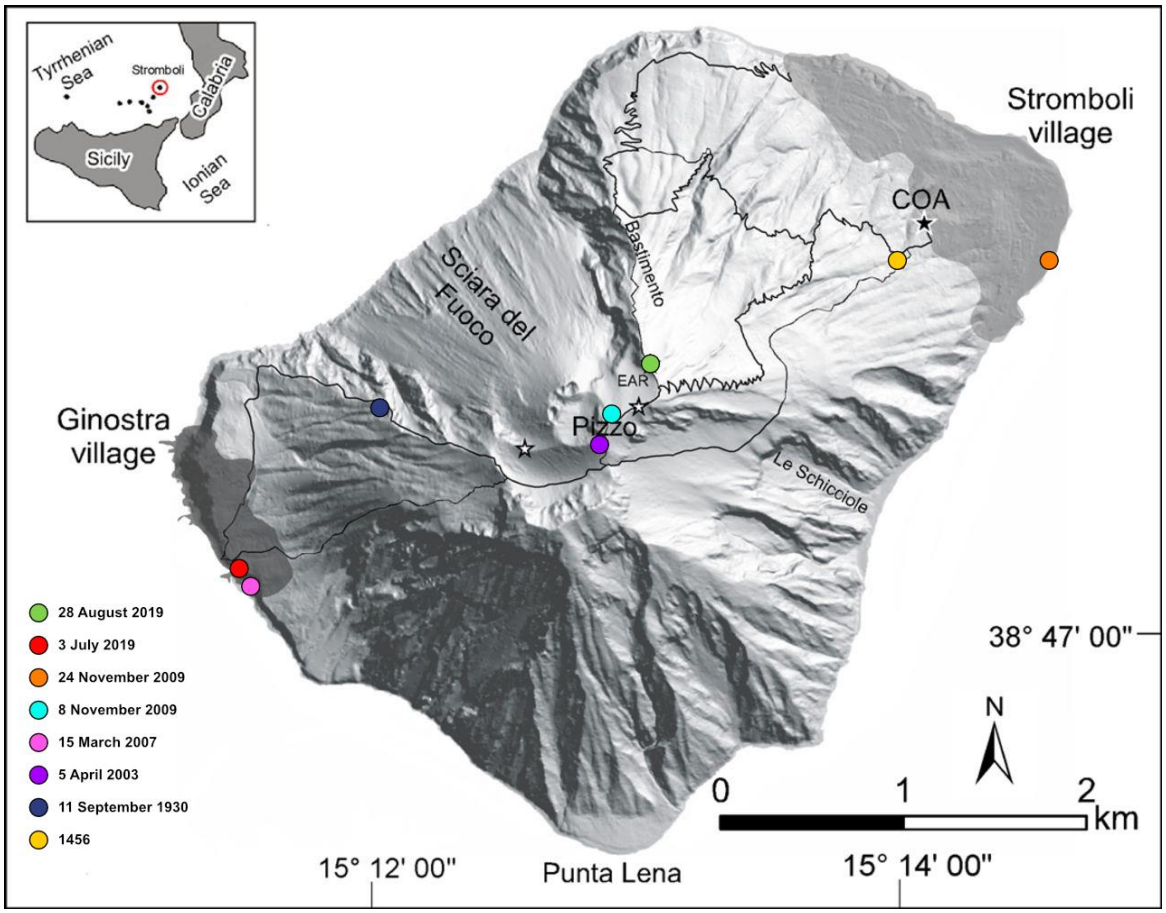


***Figure S3-1:*** *Shaded digital elevation model of Stromboli showing the tephras sampling sites. (Modified from Rosi et al., 2013)*

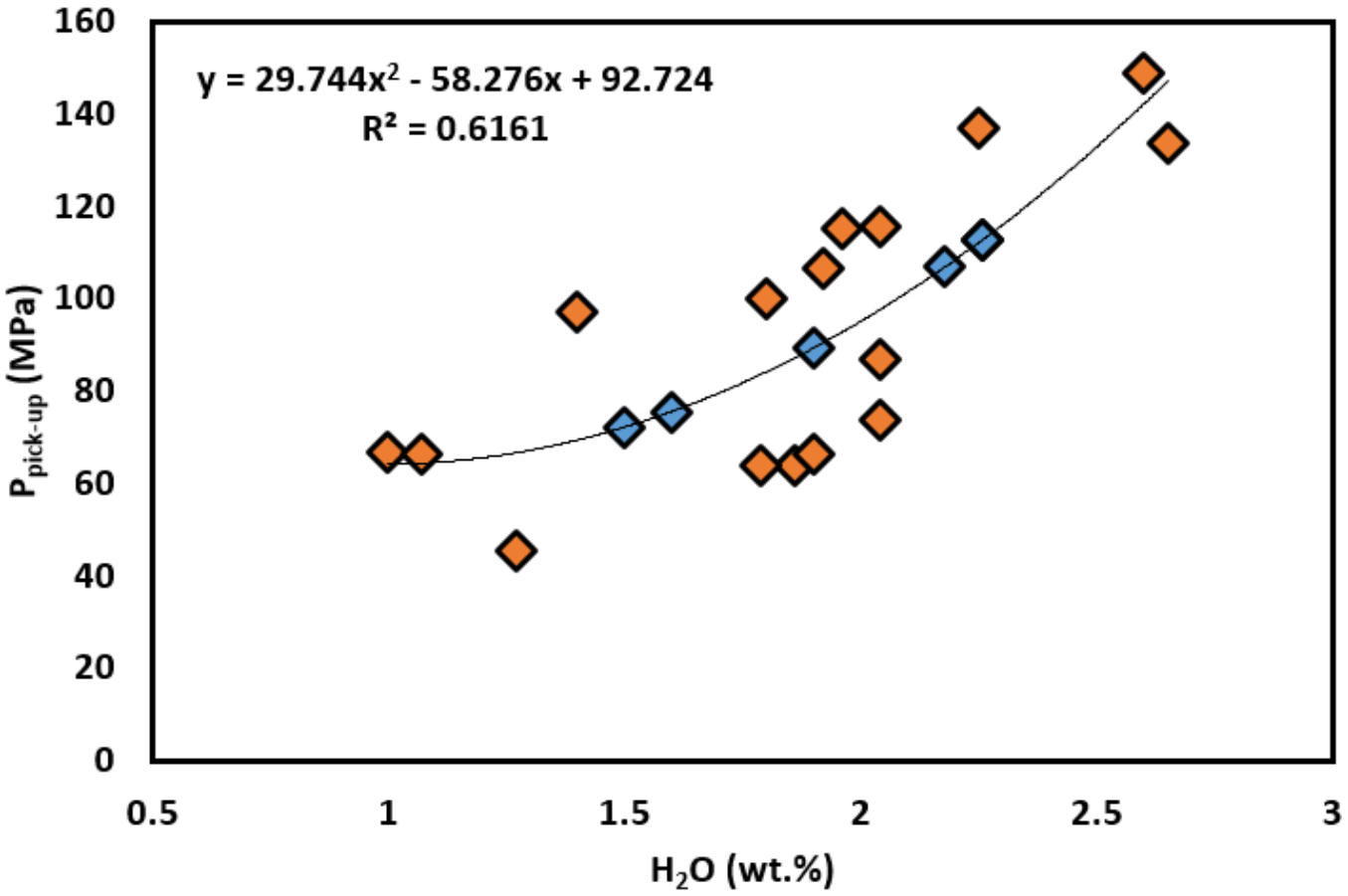


***Figure S3-2:*** *Embayments $P_{pick\text{-}up}$ vs $H_2O$ plateau concentration. The starting pressure is determined with the model from Iacono-Marziano et al., (2012), which uses both $CO_2$ and $H_2O$. The purpose of such relation is to propose an alternative for starting pressure determination for the few embayments with which we could not measure the $CO_2$ concentration (displayed in blue).*

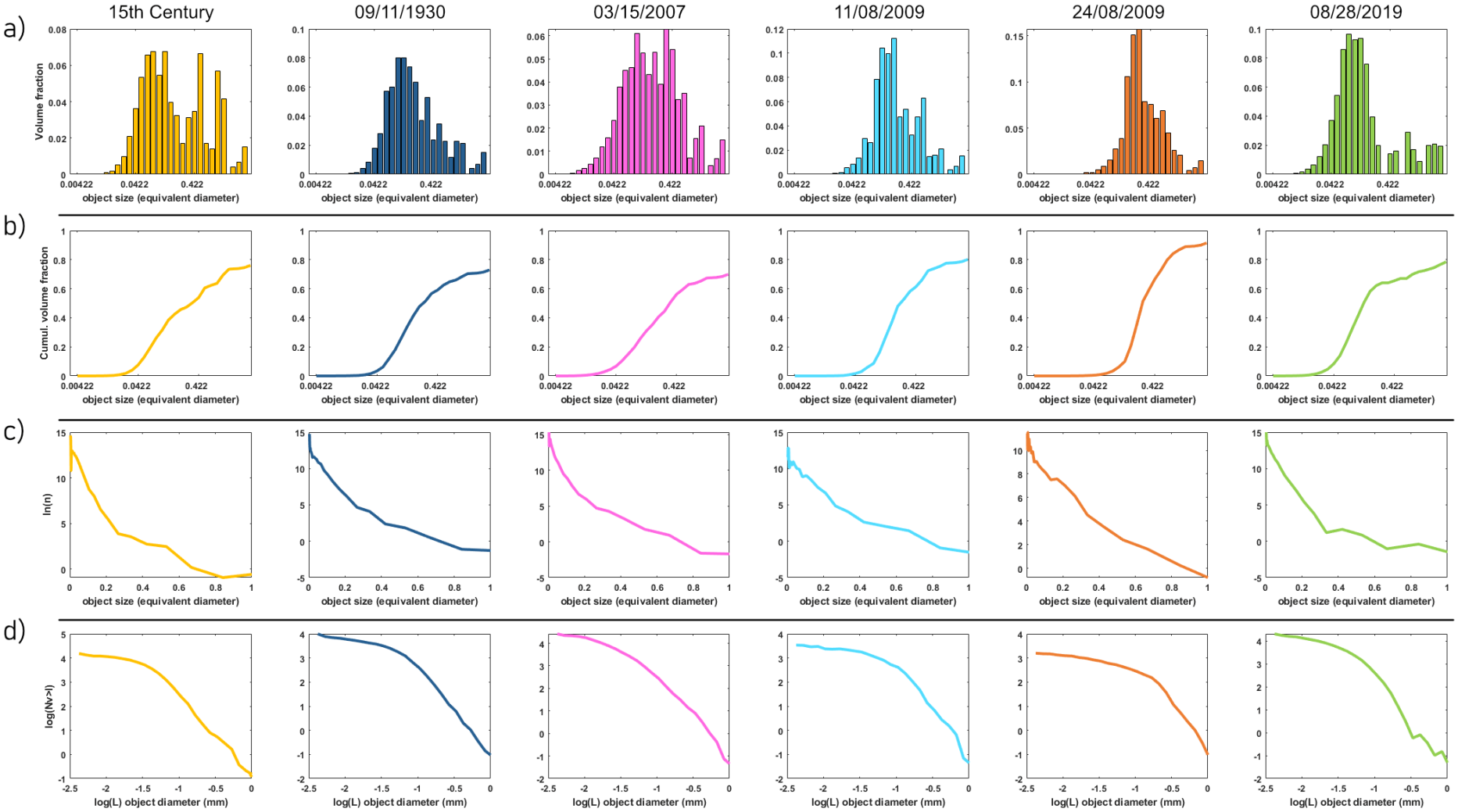


***Figure S3-3:*** *Multiple representation of the textural characteristics of the studied samples through size (L) and vesicle number density (Nv or n). These representations are associated with bubble nucleation and growth/coalescence as described in Shea et al. (2010). Each representation indicates more or less efficiently about the number of nucleation. (a) is the most straightforward to read as the number of modes indicates the number of nucleation events. (b) The shape of the curve also provide information about the number of nucleation events albeit not as precisely as (a). The (b) plots also indicate the presence of coalescence (mostly seen for the bigger bubble size). (c) Bubble growth rate can be calculated from the slope of the curve, different slopes being linked to different growth rates. These are challenging to quantify since the plots are hardly smooth enough to obtain a definite slope. Yet, except for the 15$^{th}$ century eruption, plots are quite rounded and thus more indicative of accelerating nucleation and growth. (d) The shape of the curve transition from a somewhat steep decrease to a straight and continuous decrease respectively for a single nucleation phase to continuous nucleation processes. All these representations provide slightly different results for the same sample and, since multiple vesiculation and degassing processes may happen at the same time, these representations should be interpreted with caution.*

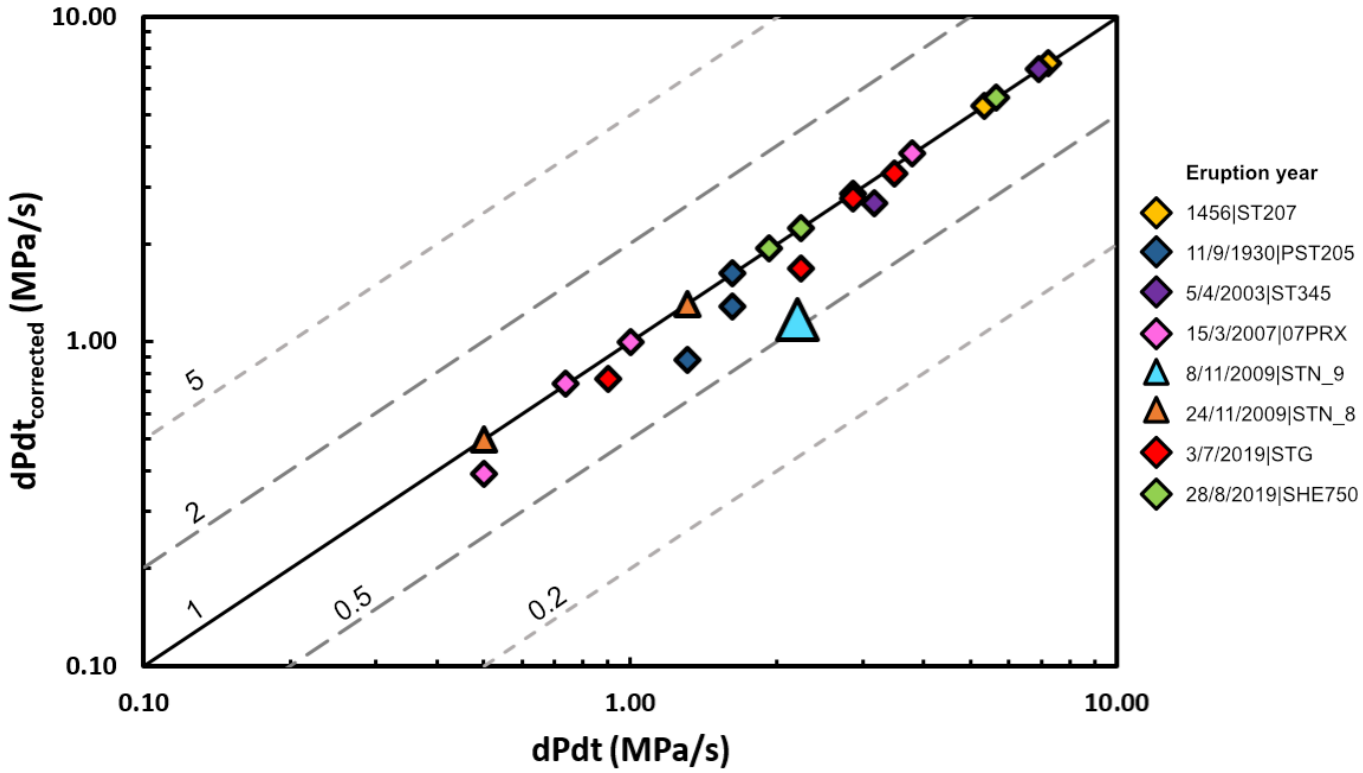


***Figure S3-4:*** *Bottleneck corrected decompression rate vs original decompression rate. Triangles and diamonds are respectively for major and paroxysmal eruptions. Only few embayments are impacted by the bottleneck correction (mostly STN9_4, the bigger light blue triangle). The number associated with the five parallel lines is the correction factor such as* $dPdt_{corrected}$ *= dPdt * Correction Factor.*

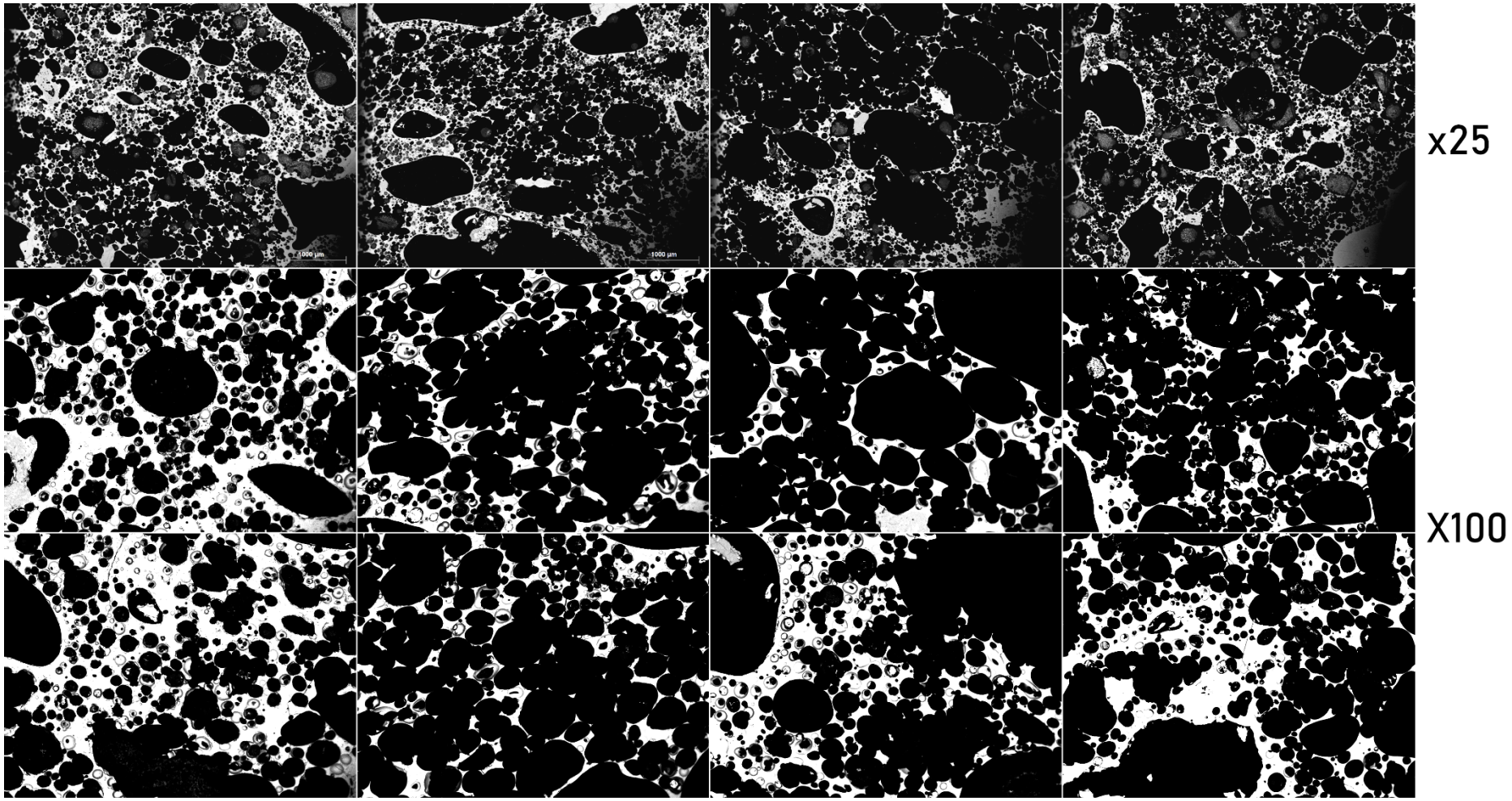


***Figure S3-5:*** *SEM microphotography of the PST217 sample (15th century paroxysm). Scale of the pictures follow the method described in Shea et al. (2010). Vesicles are in black and the glass is the bright interstitial area with crystals as darker polygonal areas.*

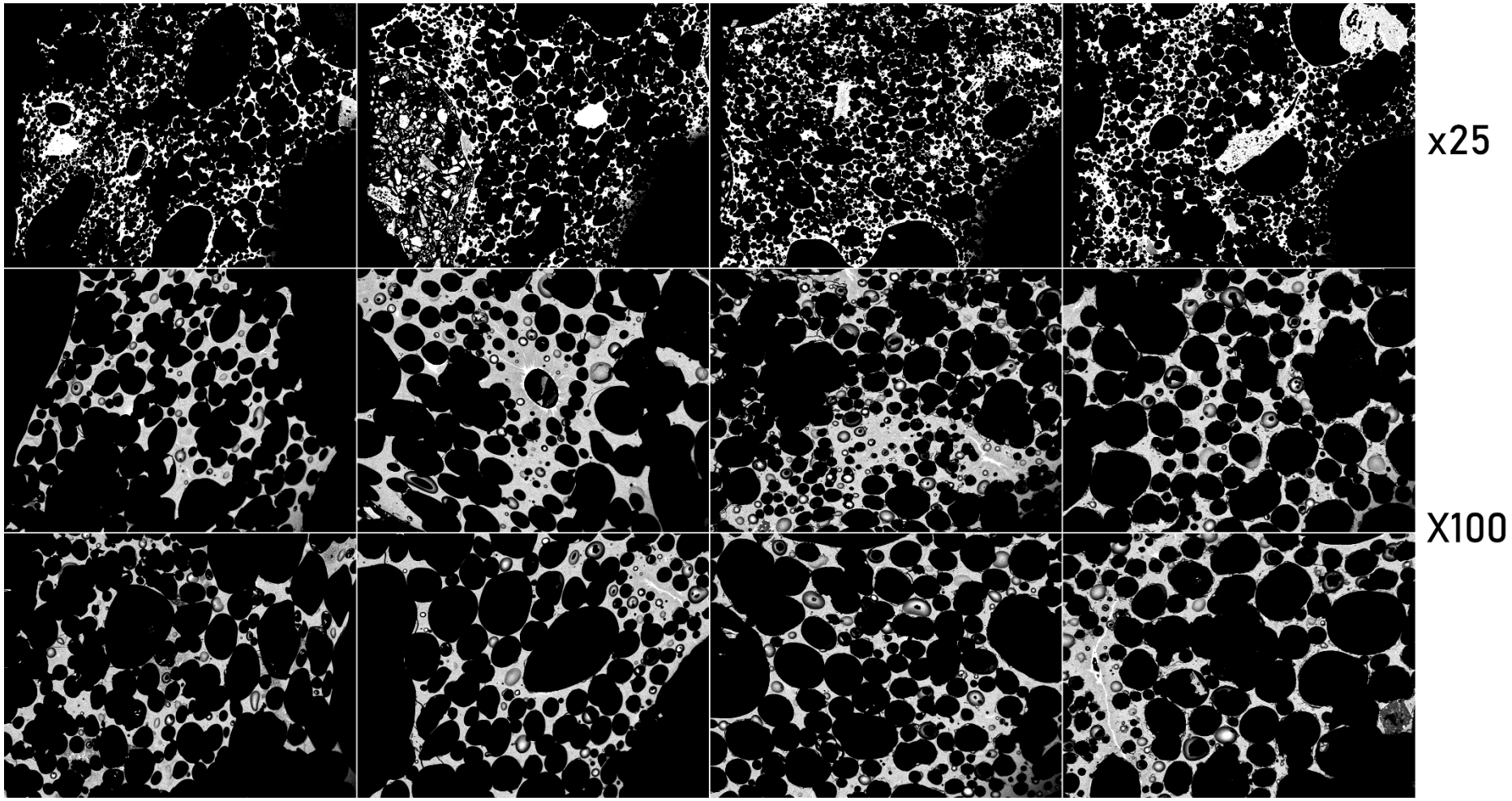


***Figure S3-6:*** *SEM microphotography of the L1930 sample (1930 paroxysm). Scale of the pictures follow the method described in Shea et al. (2010). Vesicles are in black and the glass is the bright interstitial area with crystals as darker polygonal areas.*

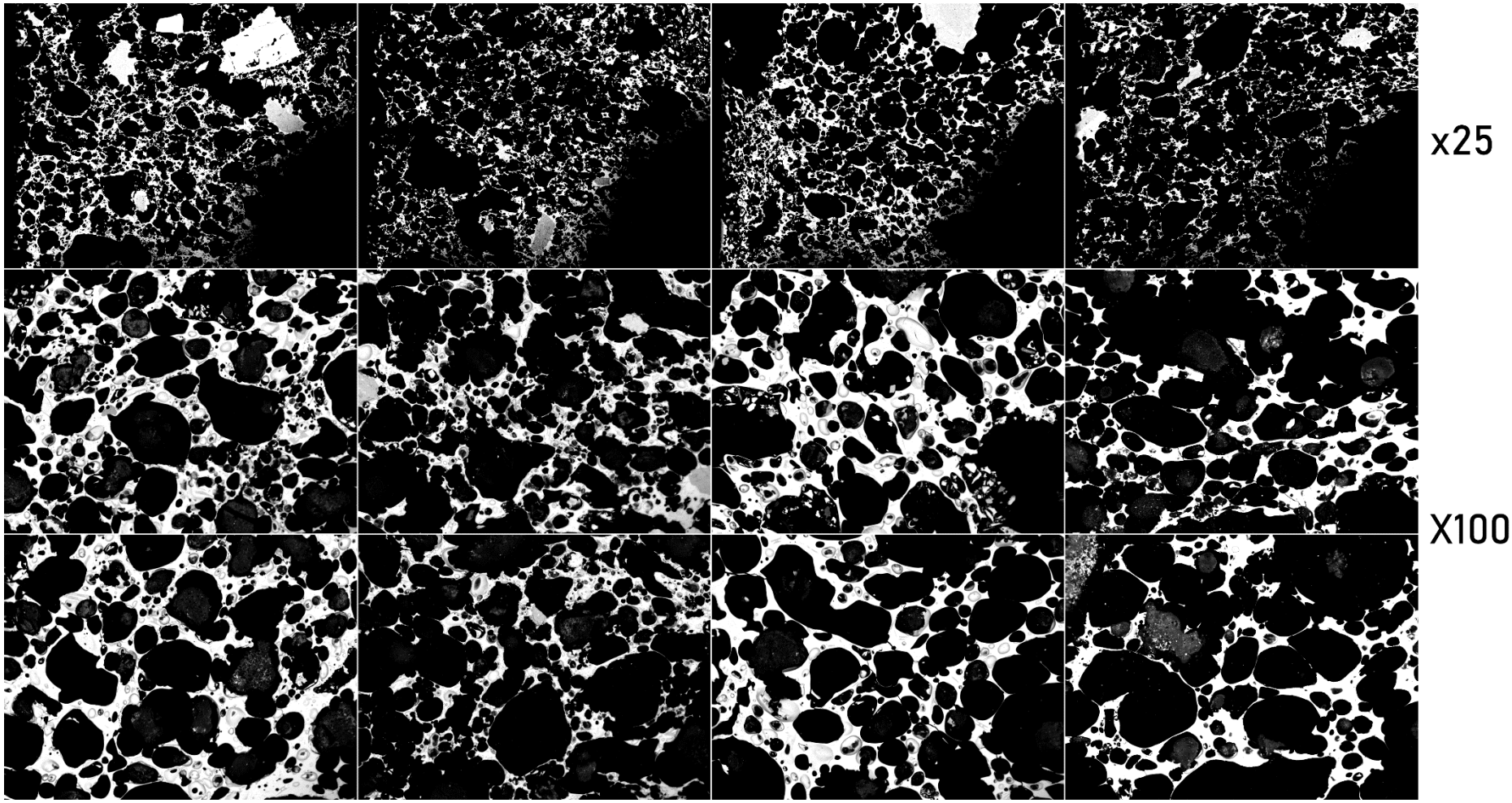


***Figure S3-7:*** *SEM microphotography of the 07PRX sample (2007 paroxysm). Scale of the pictures follow the method described in Shea et al. (2010). Vesicles are in black and the glass is the bright interstitial area with crystals as darker polygonal areas.*

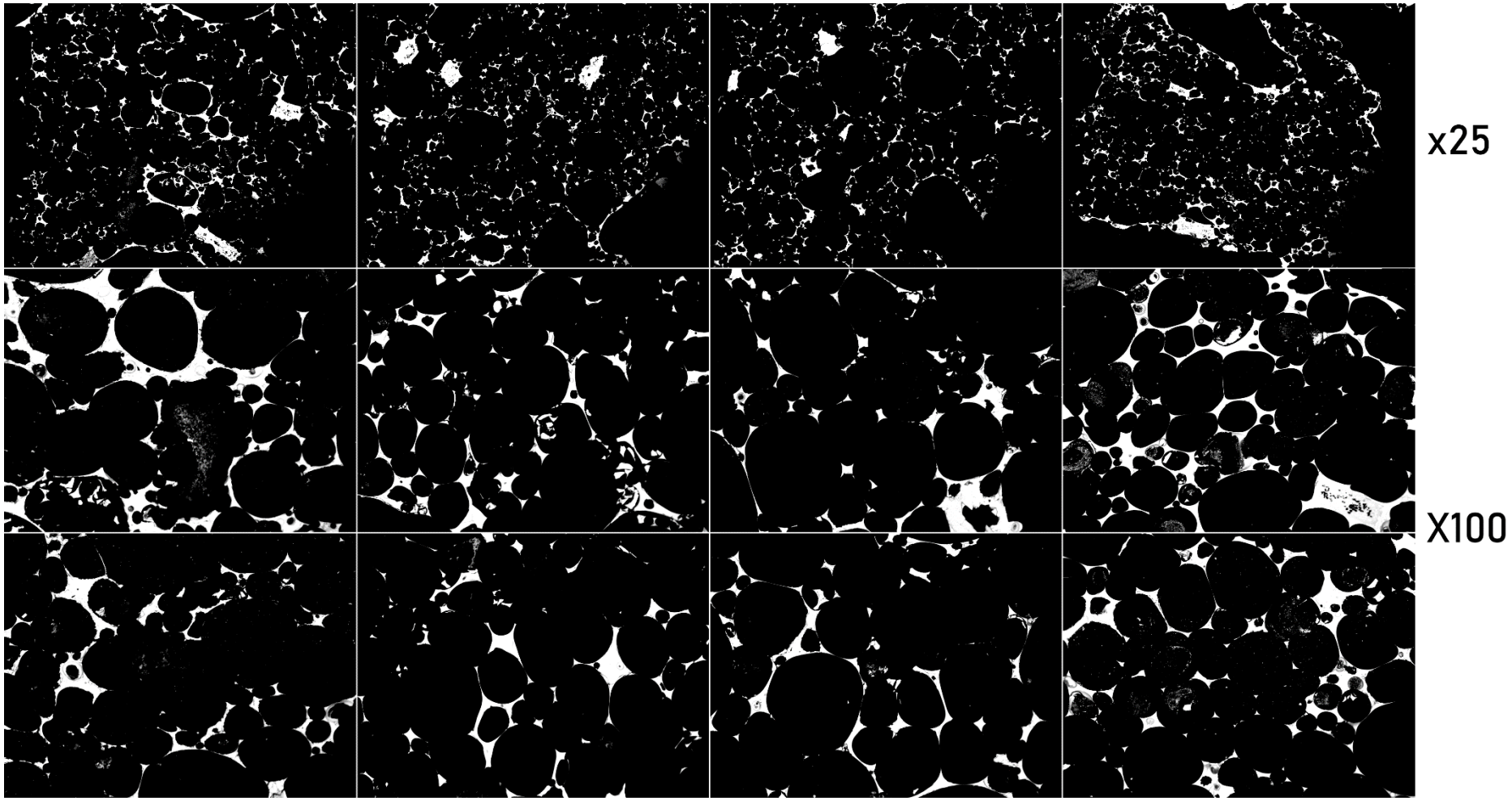


***Figure S3-8:*** *SEM microphotography of the STN8 sample (9th of November 2009 major). Scale of the pictures follow the method described in Shea et al. (2010). Vesicles are in black and the glass is the bright interstitial area with crystals as darker polygonal areas.*

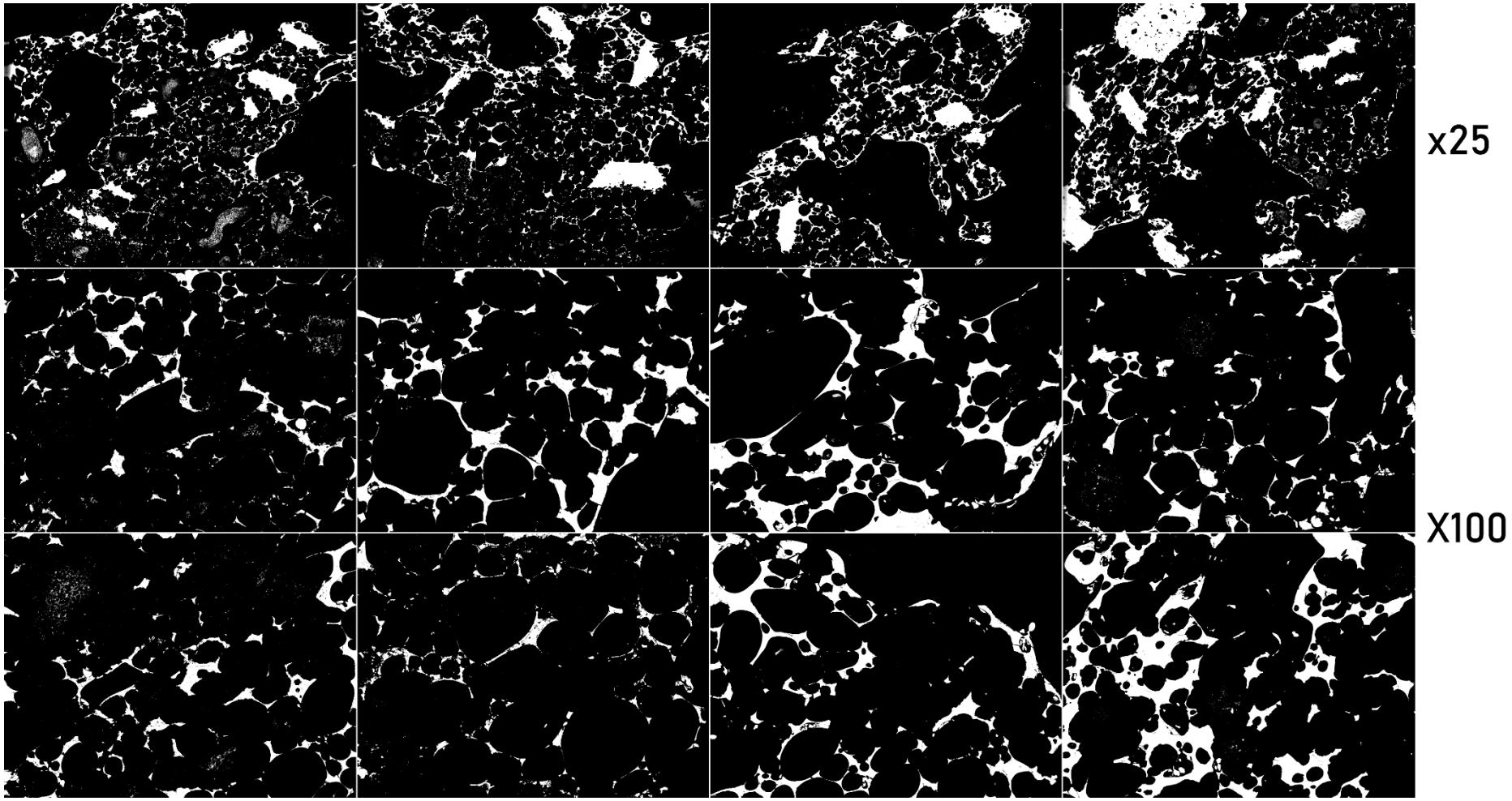


***Figure S3-9:*** *SEM microphotography of the STN9 sample (24th of November 2009 major). Scale of the pictures follow the method described in Shea et al. (2010). Vesicles are in black and the glass is the bright interstitial area with crystals as darker polygonal areas.*

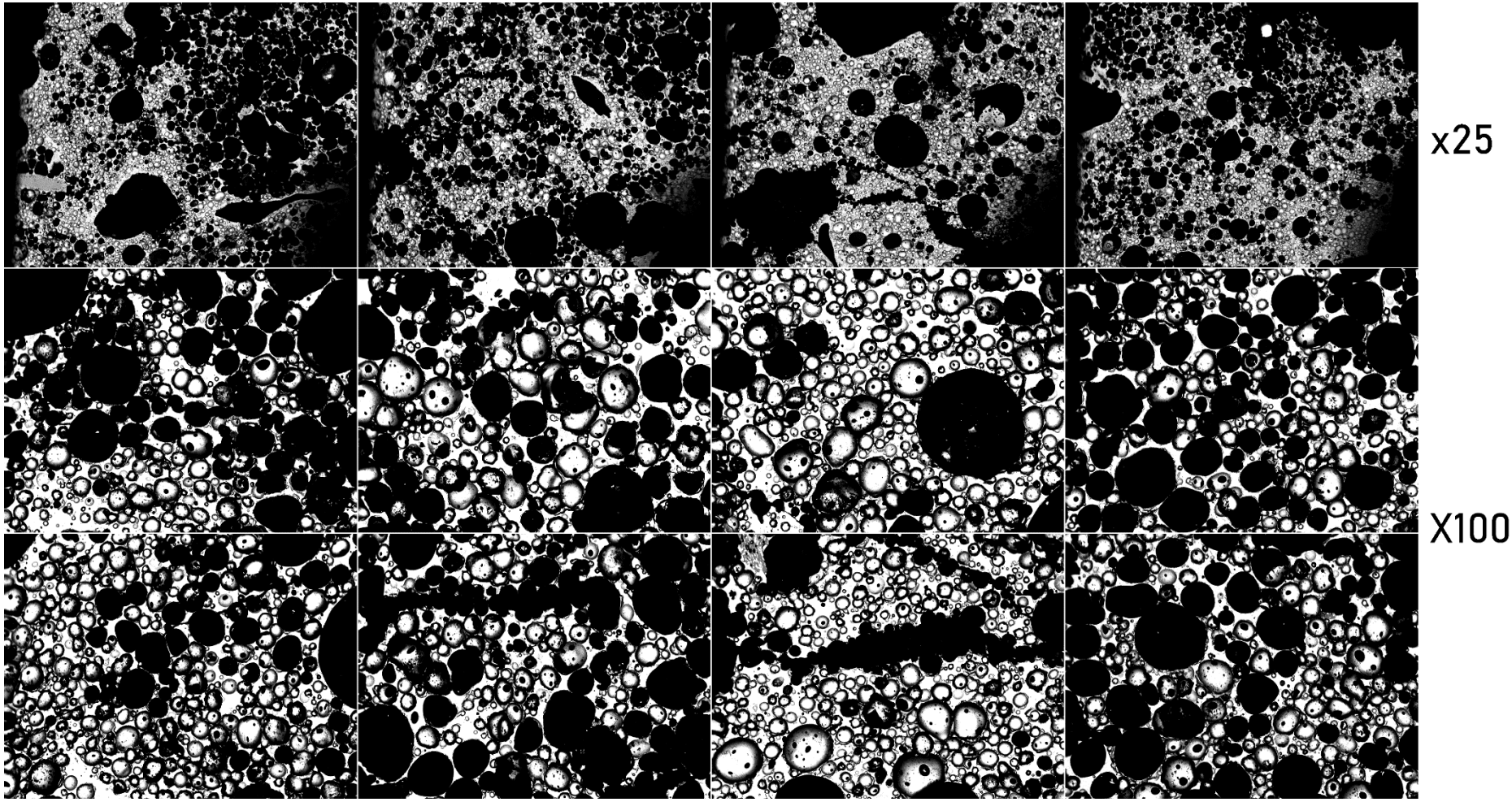


***Figure S3-10:*** *SEM microphotography of the L2019 sample (August 2019 paroxysmal). Scale of the pictures follow the method described in Shea et al. (2010). Vesicles are in black and the glass is the bright interstitial area with crystals as darker polygonal areas.*

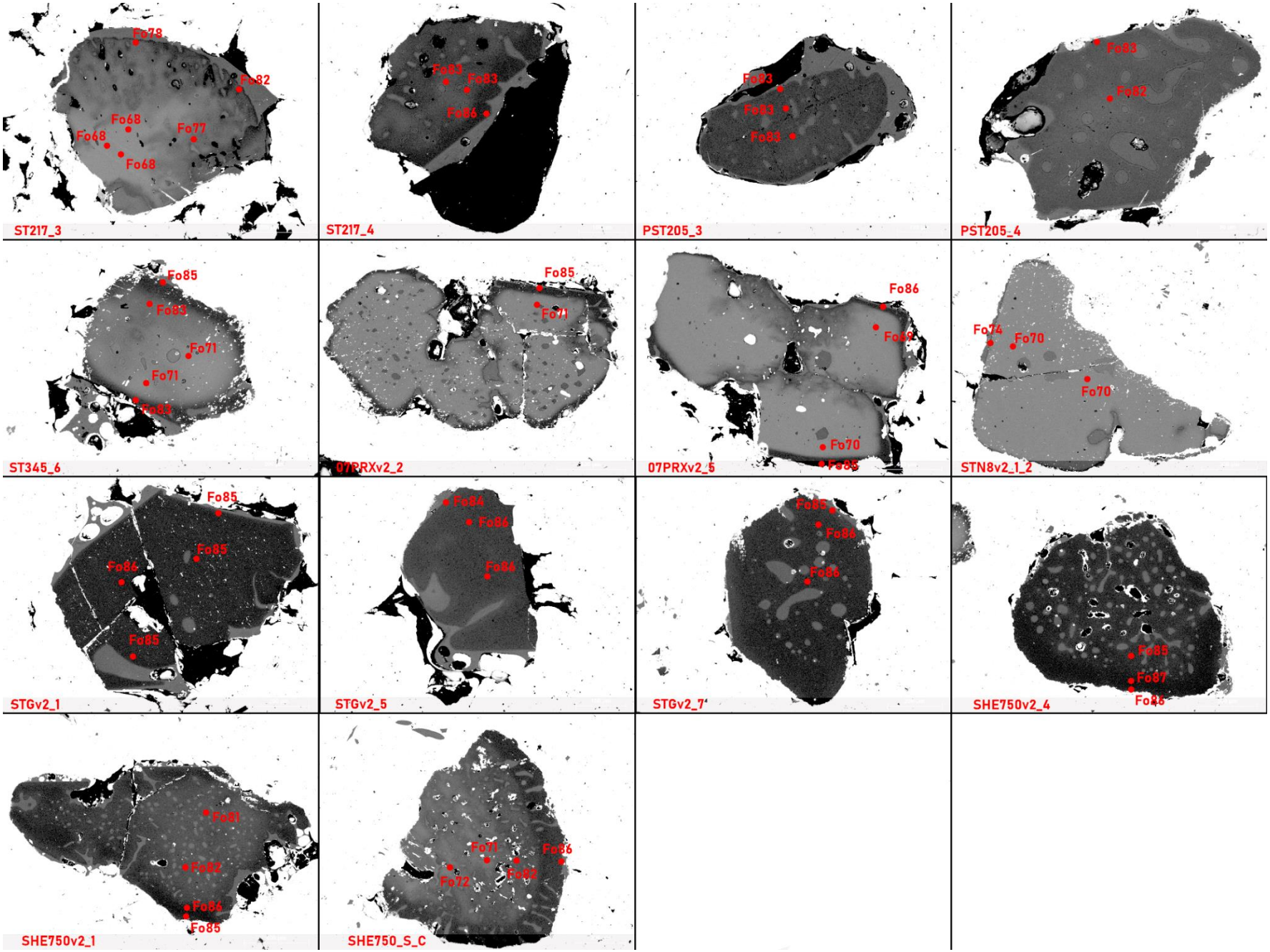


***Figure S3-11:*** *SEM pictures of embayment hosting crystals The contrast in these pictures is tuned up to underline the composition variations. Forsterite content Mg/(Mg+Fe)*100 from isolated microprobe analysis are represented in red.*

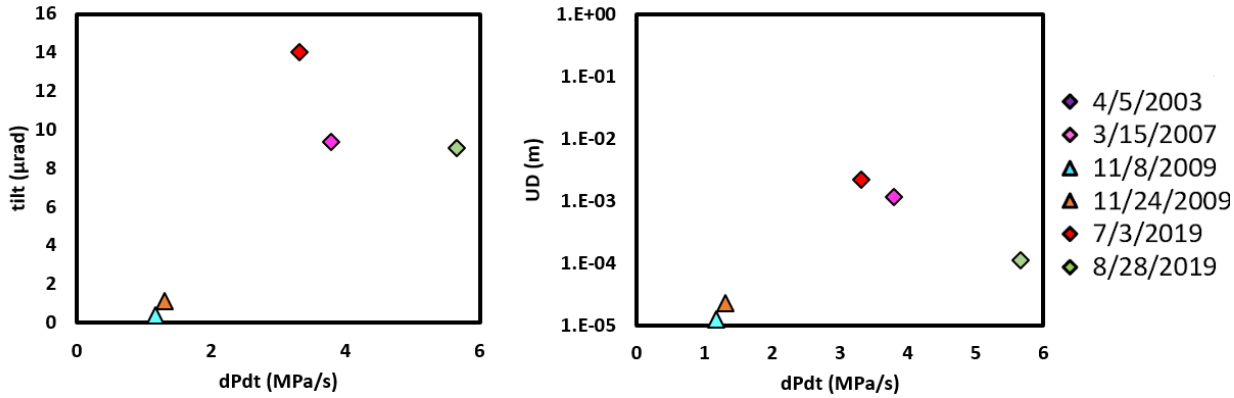


***Figure S3-12:*** *Embayment-driven maximum decompression rate vs surface tilt (left) and seismic amplitude (right). Triangles and diamond are for major and paroxysmal eruptions, respectively. No trend can be seen from either of these plots.*

**Table A1.1:** nanoSIMS calibration for the June 2021 session. Calibrations are made for $H_2O$,$CO_2$,S and Cl over $^{30}Si$ with associated error bars

| | Measured | | | | | Measured | | | | | Measured | | | | Measured | | | | |
|---|---|---|---|---|---|---|---|---|---|---|---|---|---|---|---|---|---|---|---|
| | **OH-/Si** | **err OH-/Si** | **H20 (wt.%)** | **err water content** | **H2O/SiO2** | **C-/Si** | **err C-/Si** | **CO2 (ppm)** | **CO2/SiO2** | **S-/Si** | **err S-/Si** | **S (ppm)** | **S/SiO2** | **Cl-/Si** | **err Cl-/Si** | **Cl(ppm)** | **Cl/SiO2** | **SiO2(wt.%)** |
| **B** | 2.76E-03 | 2.46E-04 | 0.03 | 0.0043 | 3.85E-04 | 1.34E-03 | 3.42E-04 | | | 3.19E-03 | 7.27E-04 | | | 6.35E-03 | 1.33E-03 | | | 78 |
| **STR11** | 4.64E-02 | 8.89E-04 | 0.79 | 0.21 | 1.57E-02 | 1.49E-03 | 8.97E-05 | 632 | 1.26E-03 | 2.47E-03 | 2.10E-04 | | | 1.08E-02 | 2.48E-04 | | | 50.2 |
| **Dr20** | 3.01E-02 | 7.65E-04 | 0.3988 | | 7.94E-03 | 2.66E-03 | 1.48E-04 | | | 5.67E-02 | 1.05E-03 | | | 7.05E-03 | 1.24E-04 | 302 | 6.02E-04 | 50.2 |
| **NIST612** | 1.05E-02 | 1.07E-05 | | | | 2.82E-04 | 2.84E-05 | | | 1.20E-02 | 1.14E-04 | 296 | 4.12E-04 | 6.72E-03 | 1.10E-03 | 50 | 6.95E-05 | 71.9 |
| **NIST610** | 4.53E-03 | 6.08E-04 | | | | 4.60E-04 | 1.03E-04 | | | 1.93E-02 | 7.23E-03 | 570 | 8.14E-04 | 1.15E-02 | 3.02E-04 | 500 | 7.14E-04 | 70 |
| **CLDR** | 1.28E-02 | 1.75E-04 | 0.16 | | 3.17E-03 | 1.35E-03 | 1.80E-04 | | | 4.92E-02 | 1.78E-04 | 956 | 1.90E-03 | 1.95E-03 | 3.58E-05 | | | 50.42 |
| **G1a** | 1.91E-01 | 1.48E-03 | 3.45 | | 7.48E-02 | 1.75E-03 | 3.56E-04 | | | 4.38E-03 | 7.72E-04 | | | 9.78E-03 | 1.94E-04 | | | 46.12 |
| **G1a** | 1.89E-01 | 1.43E-03 | 3.45 | | 7.48E-02 | 1.16E-03 | 9.57E-05 | | | 3.29E-03 | 1.32E-04 | | | 1.06E-02 | 4.95E-04 | | | 46.12 |
| **Gc2a** | 1.05E-02 | 5.37E-04 | 0.19 | | 3.96E-03 | 1.63E-03 | 3.39E-05 | 1291 | 2.69E-03 | 2.88E-03 | 9.69E-05 | | | 5.60E-03 | 5.83E-04 | | | 48 |
| **MRN_G1** | 7.30E-02 | 9.53E-04 | 1.8 | | 2.56E-02 | 2.95E-04 | 2.78E-05 | | | 2.27E-03 | 3.74E-05 | 62 | 8.83E-05 | 8.33E-02 | 1.24E-03 | | | 70.2 |
| **HW-G1** | 6.71E-02 | 5.13E-04 | 1.44 | | 3.11E-02 | 7.38E-04 | 6.52E-05 | 321 | 6.93E-04 | 7.00E-02 | 2.28E-04 | 1271 | 2.75E-03 | 9.43E-03 | 1.88E-04 | 243 | 5.25E-04 | 46.3 |
| **Suprasil** | 7.43E-04 | 1.94E-04 | 0.0001 | | 1.43E-06 | 2.13E-04 | 5.57E-05 | 2.00E+00 | 2.86E-06 | 1.22E-04 | 4.79E-06 | 5.00E-01 | 7.14E-07 | 2.50E-02 | 9.87E-04 | 1.00E+03 | 1.43E-03 | 70 |
| **Sommata M** | 0.036936 | 0.002753 | | | | 0.000275 | 9.5281E-06 | 133 | 0.00029231 | 0.14377 | 0.002594 | 2380 | 0.005231 | 0.16002 | 0.0086526 | 3416 | 0.007508 | 45.5 |

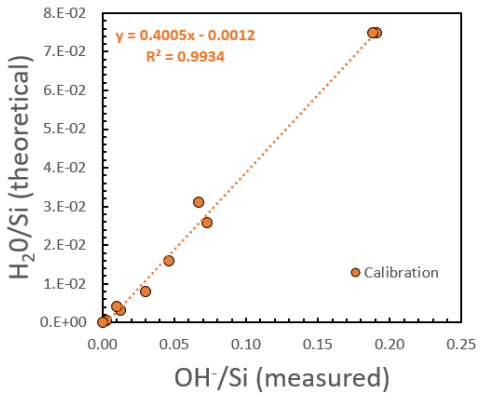


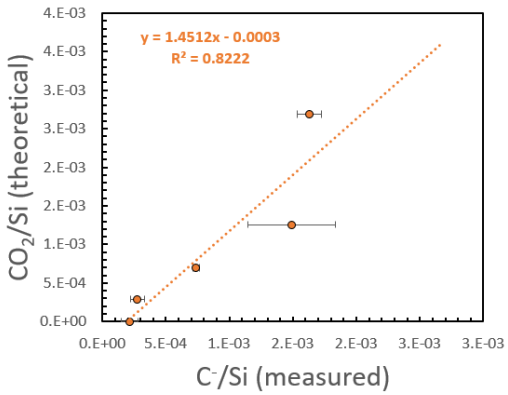


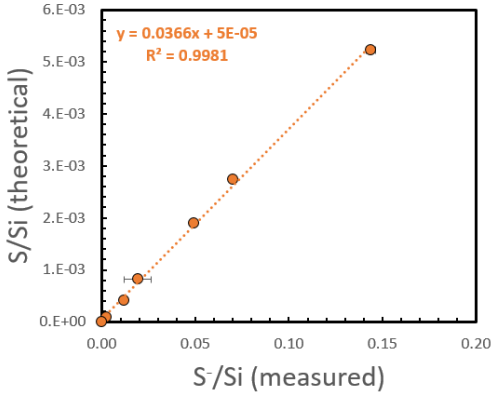


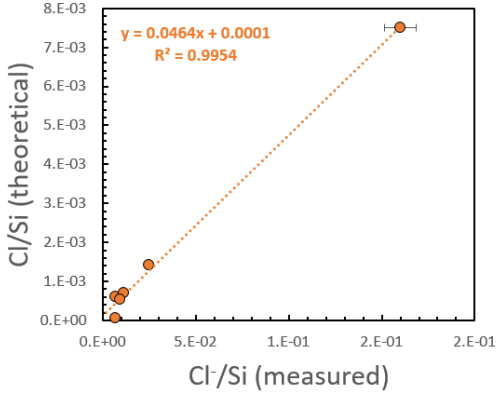

**Table A1.2**: nanoSIMS calibration for the February 2022 session. Calibrations are made for $H_2O$,$CO_2$,S and Cl over $^{30}Si$ with associated error bars

| | *Measured* | | | | | *Measured* | | | | *Measured* | | | | *Measured* | | | | |
|---|---|---|---|---|---|---|---|---|---|---|---|---|---|---|---|---|---|---|
| | ***OH-/Si*** | ***err OH-/Si*** | **H20 (wt.%)** | **err water co** | **H2O/SiO2** | ***C-/Si*** | ***err C-/Si*** | **CO2 (ppm)** | **CO2/SiO2** | ***S-/Si*** | ***err S-/Si*** | **S (ppm)** | **S/SiO2** | ***Cl-/Si*** | ***err Cl-/Si*** | **Cl(ppm)** | **Cl/SiO2** | **SiO2(wt.%)** |
| **Dr20** | *2.70E-02* | *3.18E-04* | 0.3988 | | 7.94E-03 | *3.41E-04* | *4.08E-05* | | | *5.23E-02* | *3.73E-04* | | | *6.72E-03* | *7.99E-05* | 302 | 6.02E-04 | 50.2 |
| **NIST610** | *1.53E-03* | *9.08E-04* | | | | *2.14E-04* | *3.24E-05* | | | *1.95E-02* | *7.71E-05* | 570 | 8.14E-04 | *1.05E-02* | *1.83E-04* | 500 | 7.14E-04 | 70 |
| **G1a** | *1.71E-01* | *1.02E-03* | 3.45 | | 7.48E-02 | *2.36E-04* | *4.88E-05* | 0 | 0.00E+00 | *1.25E-03* | *2.55E-05* | | | *8.52E-03* | *5.92E-04* | | | 46.12 |
| **B** | *1.10E-03* | *1.07E-05* | 0.03 | 0.0043 | 3.85E-04 | *7.68E-05* | *2.41E-05* | 0 | 0.00E+00 | *8.29E-05* | *4.55E-06* | | | *2.61E-03* | *4.66E-06* | | | 78 |
| **Gc2a** | *9.31E-03* | *9.51E-05* | 0.19 | | 3.96E-03 | *1.83E-03* | *5.09E-05* | 1291 | 2.69E-03 | *1.84E-03* | *3.90E-05* | | | *5.26E-03* | *2.26E-04* | | | 48 |
| **STR9** | *1.55E-02* | *8.02E-05* | 0.26 | 0.03 | 5.18E-03 | *6.69E-04* | *3.90E-05* | 5.56E+02 | 1.11E-03 | *5.20E-04* | *4.12E-05* | | | *7.18E-03* | *9.31E-05* | | | 50.2 |
| **STR10** | *1.59E-02* | *2.33E-04* | 0.27 | 0.03 | 5.38E-03 | *7.72E-04* | *2.15E-05* | 6.64E+02 | 1.32E-03 | *6.23E-04* | *3.79E-05* | | | *9.10E-03* | *5.53E-05* | | | 50.2 |
| **STR11** | *3.89E-02* | *4.08E-04* | 0.79 | 0.21 | 1.57E-02 | *8.53E-04* | *4.20E-05* | 632 | 1.26E-03 | *6.87E-04* | *1.64E-05* | | | *9.10E-03* | *4.26E-04* | | | 50.2 |
| **STR13** | *1.99E-01* | *1.16E-03* | 4.45 | 0.03 | 8.86E-02 | *9.21E-04* | *2.63E-05* | 8.64E+02 | 1.72E-03 | *6.83E-04* | *1.39E-05* | | | *9.24E-03* | *1.42E-04* | | | 50.2 |
| **Suprasil** | *5.15E-04* | *4.35E-05* | 0.0001 | | 1.43E-06 | | | | | *3.88E-04* | *6.52E-05* | 5.00E-01 | 7.14E-07 | *3.67E-02* | *1.10E-03* | 1.00E+03 | 1.43E-03 | 70 |
| **MRN_G1** | *6.56E-02* | *7.44E-04* | 1.8 | | 2.56E-02 | *3.24E-04* | *2.97E-05* | | | *2.19E-03* | *2.93E-05* | 62 | 8.83E-05 | *6.92E-02* | *5.24E-04* | | | 70.2 |
| **HW-G1** | *6.33E-02* | *3.36E-04* | 1.44 | | 3.11E-02 | | | | | *6.62E-02* | *7.96E-04* | 1271 | 2.75E-03 | *8.56E-03* | *9.76E-05* | 243 | 5.25E-04 | 46.3 |
| **Herasil** | *6.37E-04* | *1.20E-04* | 0 | | | *2.76E-04* | *3.52E-05* | | | *2.55E-04* | *3.24E-05* | | | *1.51E-04* | *3.80E-05* | | | |

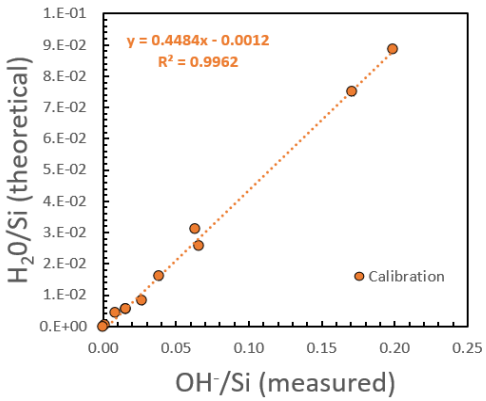


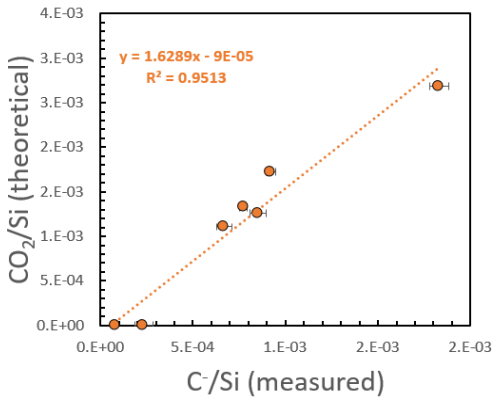


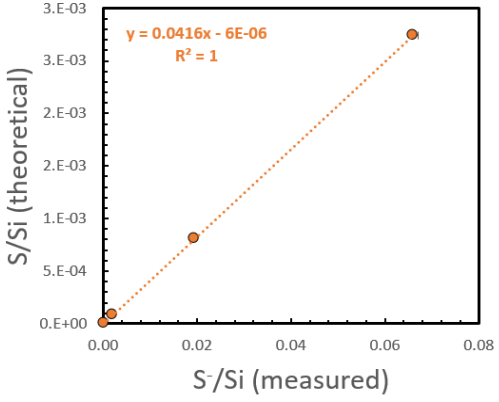


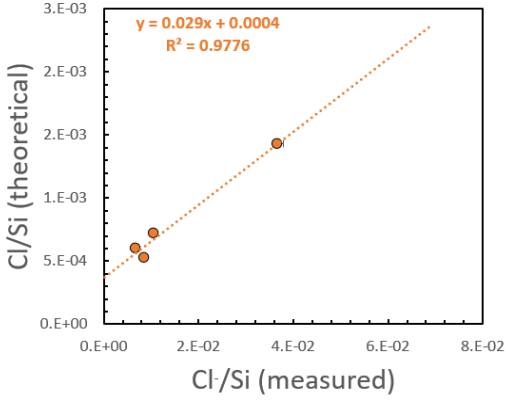

**Table A1.3:** nanoSIMS calibration for the May 2022 session. Calibrations are made for $H_2O$,$CO_2$,S and Cl over $^{30}Si$ with associated error bars

| | *Measured* | | | | | *Measured* | | | | *Measured* | | | | *Measured* | | | | |
|---|---|---|---|---|---|---|---|---|---|---|---|---|---|---|---|---|---|---|
| | ***OH-/Si*** | ***err OH-/Si*** | **H20 (wt.%)** | **err water co** | **H2O/SiO2** | ***C-/Si*** | ***err C-/Si*** | **CO2 (ppm)** | **CO2/SiO2** | ***S-/Si*** | ***err S-/Si*** | **S (ppm)** | **S/SiO2** | ***Cl-/Si*** | ***err Cl-/Si*** | **Cl(ppm)** | **Cl/SiO2** | **SiO2(wt.%)** |
| **NIST610** | 9.77E-04 | 5.79E-06 | | | | 1.26E-04 | 2.60E-05 | | | 2.20E-02 | 4.24E-05 | 570 | 8.14E-04 | 1.16E-02 | 7.18E-05 | 500 | 7.14E-04 | 70 |
| **B** | | | 0.03 | 0.0043 | 3.85E-04 | | | 0 | 0.00E+00 | | | | | | | | | 78 |
| **STR9** | 2.08E-02 | 2.33E-04 | 0.26 | 0.03 | 5.18E-03 | 6.85E-04 | 7.17E-06 | 556 | 1.11E-03 | 2.13E-01 | 5.37E-04 | | | 8.91E-03 | 5.20E-05 | | | 50.2 |
| **STR10** | | | 0.27 | 0.03 | 5.38E-03 | | | 664 | 1.32E-03 | | | | | | | | | 50.2 |
| **STR11** | 4.96E-02 | 3.12E-04 | 0.79 | 0.21 | 1.57E-02 | 8.63E-04 | 2.42E-05 | 632 | 1.26E-03 | 2.20E-01 | 9.00E-04 | | | 1.08E-02 | 5.64E-05 | | | 50.2 |
| **STR13** | 2.68E-01 | 1.33E-03 | 4.45 | 0.03 | 8.86E-02 | 1.01E-03 | 1.22E-05 | 864 | 1.72E-03 | 2.73E-01 | 9.67E-05 | | | 1.26E-02 | 4.50E-05 | | | 50.2 |
| **Suprasil** | 3.98E-04 | 2.86E-04 | 0.0001 | | 1.43E-06 | 1.34E-04 | 2.19E-05 | 2 | 2.86E-06 | 1.36E-04 | 2.06E-06 | 0.5 | 7.14E-07 | 4.71E-02 | 1.74E-04 | 1000 | 1.43E-03 | 70 |
| **MRN_G1** | 8.87E-02 | 5.16E-03 | 1.56 | | 2.22E-02 | 3.90E-04 | 1.17E-05 | | | 1.70E-04 | 2.31E-05 | 62 | 8.83E-05 | 9.16E-02 | 6.69E-04 | 2517 | | 70.2 |
| **HW-G1** | 7.49E-02 | 7.55E-04 | 1.44 | | 3.11E-02 | 9.17E-04 | 5.13E-05 | 321 | 6.93E-04 | 7.70E-02 | 5.69E-04 | 1271 | 2.75E-03 | 1.03E-02 | 4.20E-05 | 243 | 5.25E-04 | 46.3 |
| **519** | 1.12E-02 | 1.39E-04 | 0.17 | | 3.46E-03 | 4.23E-04 | 1.72E-05 | 165 | 3.36E-04 | 4.57E-02 | 3.69E-04 | 950 | 1.94E-03 | 1.95E-03 | 3.58E-05 | 45 | 9.17E-05 | 49.07 |
| **NS1** | 2.26E-02 | 6.43E-05 | 0.37 | | 7.40E-03 | 6.21E-03 | 3.54E-05 | 3150 | 6.30E-03 | 2.15E-03 | 3.11E-05 | | | 1.06E-03 | 3.52E-05 | | 0.00E+00 | 50 |

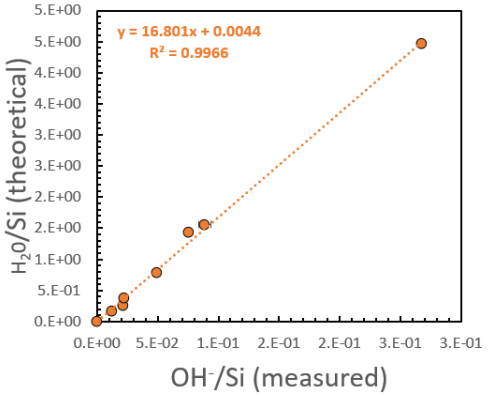


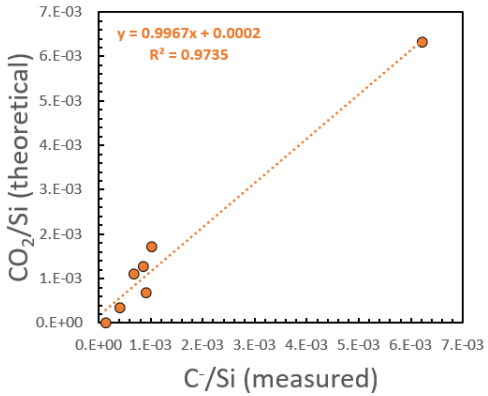


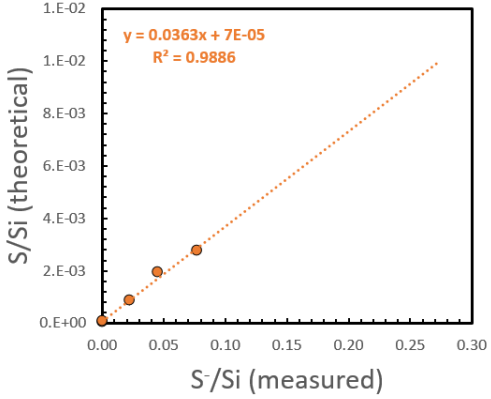


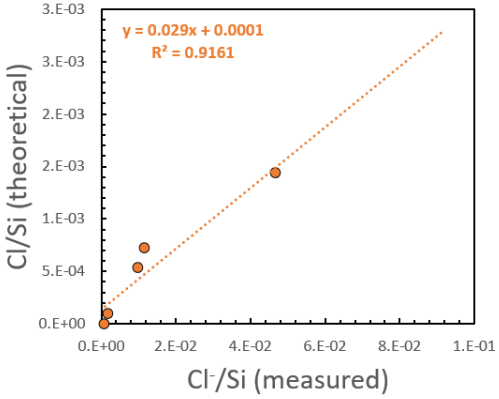

**Table A1.4:** SIMS calibration for the July 2020 session $H_2O$,$CO_2$,S,Cl and F over $^{28}Si$ (first row of plots) and $^{18}O$ (second row of plots). Standards are from shishkina et al., (2010) Jarosewich et al., (1980); Jochum et al., and (2000); Kamenetsky et al., (2000)

| Measured Name | 12C | 16.5 | 17O | 16O 1H | 18O | 19F | 27Al | 30Si | 32S | 35Cl | 12C /30Si Error | 16O 1H /30Si Error | 19F /30Si Error | 27Al /30S Error | 32S /30Si Error | 35Cl /30S Error | 30Si /18O Error | 17O /18O Error | 12C/18O | 16O 1H/18 | 19F/18O | 32S/18O | 35Cl/18O | Standards H2O | CO2 | F | S | Cl |
|---|---|---|---|---|---|---|---|---|---|---|---|---|---|---|---|---|---|---|---|---|---|---|---|---|---|---|---|---|
| **KL2G@1** | 434.02 | 4361.29 | 49463.85 | 23405 | 298870.2 | 24583.71 | 102979.2 | 364760.7 | 877.55 | 2542.93 | 0.001176 | 4.37221E-05 | 0.0643 | 0.001388 | 0.069631 | 0.003738 | 0.2756 | 0.009128 | 0.002479 | 0.000114819 | 0.007191 | 0.000348 | 1.224817 | 0.050521 | 0.169167 | 0.000544 | 0.00144 | 0.078756 | 0.085359 | 0.003036 | 0.008807 | 0.015 | 5.2 | 177 | 7.7 | 26 |
| **KL2G@2** | 440.35 | 5753.01 | 45282.67 | 17583.17 | 279432.4 | 22525.46 | 95058.61 | 283572.4 | 726.37 | 2002.95 | 0.00168 | 0.000174133 | 0.062711 | 0.002953 | 0.084471 | 0.006002 | 0.331344 | 0.017615 | 0.002713 | 0.00017754 | 0.007544 | 0.000603 | 1.010532 | 0.055184 | 0.165643 | 0.000616 | 0.001698 | 0.063371 | 0.085361 | 0.002742 | 0.007624 | 0.015 | 5.2 | 177 | 7.7 | 26 |
| **N72@1** | 1176.37 | 5172.22 | 55306.39 | 22249.65 | 312866.2 | 54781.15 | 153751.9 | 282173.1 | 662.15 | 1004.3.55 | 0.004325 | 0.000367308 | 0.080029 | 0.00355 | 0.200321 | 0.014268 | 0.562159 | 0.036595 | 0.002403 | 0.000148226 | 0.036542 | 0.002374 | 0.923314 | 0.051042 | 0.181701 | 0.000208 | 0.003933 | 0.073892 | 0.184959 | 0.002219 | 0.03374 | 0 | 0 | | | |
| **N72@2** | 607.95 | 5744.57 | 52185.41 | 18281.62 | 301570.6 | 45690.16 | 153556.8 | 254721.2 | 603.05 | 8604.65 | 0.002495 | 0.000265315 | 0.070318 | 0.002387 | 0.183854 | 0.01192 | 0.593475 | 0.037301 | 0.002418 | 0.000147029 | 0.034519 | 0.00218 | 0.867875 | 0.046154 | 0.176672 | 0.000456 | 0.002165 | 0.061028 | 0.153562 | 0.002099 | 0.029959 | 0 | 0 | | | |
| **M34@1** | 1380.08 | 5806.44 | 52848.48 | 1935675 | 308468.8 | 33545.75 | 137502.7 | 195122.8 | 1313.62 | 6757.4 | 0.006833 | 0.000506456 | 10.20859 | 0.666673 | 0.178415 | 0.012967 | 0.695104 | 0.042914 | 0.009649 | 0.000528945 | 0.03583 | 0.002483 | 0.647251 | 0.039143 | 0.174904 | 0.000601 | 0.004422 | 6.607517 | 0.115479 | 0.006245 | 0.023191 | 5.7 | 375 | | | |
| **M34@2** | 1173.95 | 5619.41 | 43707.74 | 1745335 | 232779.6 | 30706.57 | 131051.1 | 180421.5 | 1720.37 | 6333.48 | 0.006234 | 0.000446674 | 9.934142 | 0.679452 | 0.17531 | 0.012538 | 0.712068 | 0.040056 | 0.009755 | 0.000532309 | 0.03609 | 0.002299 | 0.630371 | 0.035189 | 0.173352 | 0.000565 | 0.003971 | 6.268156 | 0.110994 | 0.006155 | 0.022772 | 5.7 | 375 | | | |
| **M35@1** | 3708.85 | 5121.6 | 51336.89 | 1522826 | 300724.3 | 34371.55 | 133205.4 | 202400 | 1587.65 | 6625.07 | 0.017732 | 0.001246009 | 7.680212 | 0.483479 | 0.17477 | 0.012134 | 0.648994 | 0.030207 | 0.008004 | 0.000439721 | 0.033527 | 0.002076 | 0.688737 | 0.038836 | 0.173896 | 0.000463 | 0.012254 | 5.289646 | 0.120371 | 0.005513 | 0.023091 | 4.2 | 1019 | | | |
| **M35@2** | 2390.07 | 5532.22 | 47089.56 | 1240077 | 286397.4 | 29068.31 | 132476.3 | 179402.9 | 1397.4 | 5804.8 | 0.016168 | 0.00145147 | 7.123179 | 0.524622 | 0.16774 | 0.011966 | 0.727688 | 0.044923 | 0.008016 | 0.00050316 | 0.033382 | 0.002235 | 0.637175 | 0.037771 | 0.166765 | 0.000798 | 0.010302 | 4.538712 | 0.10688 | 0.005107 | 0.02127 | 4.2 | 1019 | | | |
| **M43@1** | 9444.52 | 5131.44 | 46877.03 | 880969.2 | 287707.6 | 30005.44 | 136907.9 | 198437.9 | 696.75 | 6477.32 | 0.049528 | 0.004750936 | 4.524861 | 0.296585 | 0.155397 | 0.011302 | 0.65108 | 0.029539 | 0.003601 | 0.000240302 | 0.033516 | 0.002302 | 0.707057 | 0.038461 | 0.166085 | 0.000478 | 0.035018 | 3.199335 | 0.110299 | 0.002546 | 0.023688 | 2.62 | 3172 | | | |
| **M43@2** | 10070.6 | 5423.94 | 47555.81 | 912609.3 | 295405.8 | 30663.19 | 140360.8 | 197612.8 | 687.6 | 6269.4 | 0.049245 | 0.003999963 | 4.702153 | 0.289605 | 0.159619 | 0.010747 | 0.698364 | 0.039587 | 0.003568 | 0.000226505 | 0.032623 | 0.002218 | 0.684204 | 0.035027 | 0.164244 | 0.001091 | 0.033694 | 3.217232 | 0.109212 | 0.002441 | 0.022321 | 2.62 | 3172 | | | |
| **M48@1** | 1316.87 | 5393.01 | 47638.14 | 334882.1 | 287530.8 | 32036.92 | 148182.6 | 225082.5 | 173.72 | 6102.37 | 0.005678 | 0.000392952 | 1.484101 | 0.067402 | 0.145907 | 0.009839 | 0.648229 | 0.038562 | 0.000735 | 8.1258E-05 | 0.027629 | 0.001573 | 0.803069 | 0.041127 | 0.169534 | 0.000321 | 0.00456 | 1.191836 | 0.117173 | 0.00059 | 0.022188 | 0.77 | 176 | | | |
| **M48@2** | 1488.95 | 5467.54 | 49868.65 | 368604 | 293212.9 | 35777.68 | 151880.7 | 241340.5 | 158.3 | 6716.25 | 0.005954 | 0.000427355 | 1.533621 | 0.075158 | 0.15316 | 0.010738 | 0.594349 | 0.032425 | 0.000638 | 5.85106E-05 | 0.028611 | 0.001804 | 0.842187 | 0.046213 | 0.173595 | 0.000647 | 0.005014 | 1.291596 | 0.128989 | 0.000537 | 0.024095 | 0.77 | 176 | | | |
| **40428@1** | 1398.4 | 5207.38 | 53465.78 | 460083.5 | 304299.4 | 353226 | 134386.2 | 246523.3 | 278069.8 | 144714.6 | 0.00549 | 0.000401 | 1.323071 | 0.0922 | 1.445284 | 0.0989 | 0.534276 | 0.0321 | 1.158642 | 0.0638 | 0.577197 | 0.0348 | 0.832123 | 0.0448 | 0.173102 | 0.000463 | 0.004568 | 1.600232 | 1.202654 | 0.964133 | 0.480239 | 0.85 | | 650 | 830 | 434 |
| **40428@2** | 1242.83 | 4926.13 | 51798.65 | 430054.5 | 301469.8 | 332842.2 | 132731.8 | 240086.1 | 266181.8 | 139264 | 0.00541 | 0.000587 | 1.850321 | 0.099 | 1.402083 | 0.100629 | 0.519946 | 0.025 | 1.140886 | 0.0657 | 0.572192 | 0.0364 | 0.816137 | 0.0431 | 0.175451 | 0.000348 | 0.004415 | 1.510115 | 1.144232 | 0.931119 | 0.466987 | 0.85 | | 650 | 830 | 434 |
| **47963@1** | 1288.92 | 5243.94 | 48550.07 | 531105.2 | 280948.1 | 503332.5 | 139062.9 | 214417.1 | 187828 | 343287.3 | 0.005802 | 0.000325936 | 2.862086 | 0.146822 | 2.407987 | 0.157902 | 0.639722 | 0.041438 | 0.897649 | 0.04810419 | 1.609851 | 0.094414 | 0.784665 | 0.044447 | 0.176294 | 0.000487 | 0.004553 | 2.245779 | 1.889463 | 0.704354 | 1.263194 | 1.45 | | 777 | 776 | 1356 |
| **47963@2** | 1577.08 | 5276.23 | 51594.49 | 657653 | 293226.2 | 564610.7 | 144933.1 | 231471.2 | 207571.5 | 373439.2 | 0.006562 | 0.000434569 | 2.965699 | 0.157032 | 2.364433 | 0.138504 | 0.591269 | 0.032536 | 0.922356 | 0.05073143 | 1.63073 | 0.093677 | 0.808627 | 0.045446 | 0.179034 | 0.000344 | 0.005307 | 2.398144 | 1.911944 | 0.745842 | 1.318652 | 1.45 | | 777 | 776 | 1356 |
| **VG2@1** | 1707.12 | 5837.38 | 49148.68 | 150524.1 | 290094.4 | 105339.3 | 107336.7 | 223162 | 367095.1 | 79404.06 | 0.00742 | 0.000517449 | 0.686853 | 0.030922 | 0.484025 | 0.029953 | 0.462752 | 0.025825 | 1.692903 | 0.08511164 | 0.335827 | 0.019844 | 0.790194 | 0.038516 | 0.173285 | 0.00043 | 0.005864 | 0.542747 | 0.382474 | 1.337722 | 0.265368 | 0.28 | 153 | 300 | 1424 | 298 |

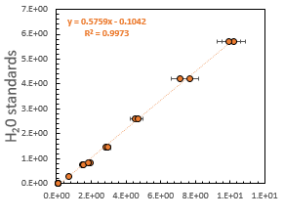


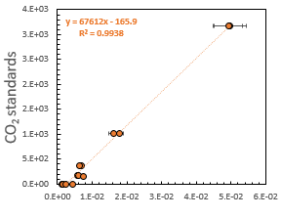


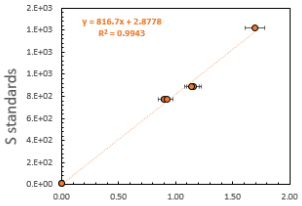


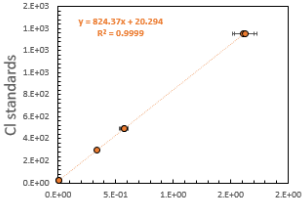


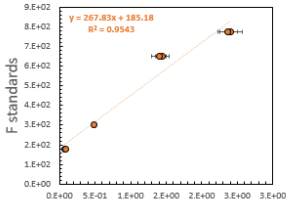


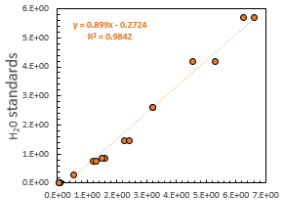


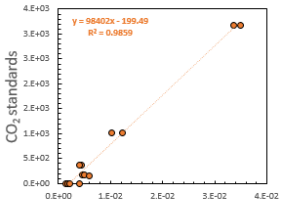


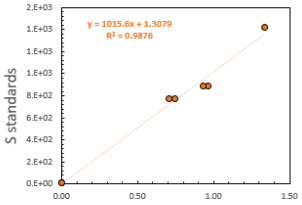


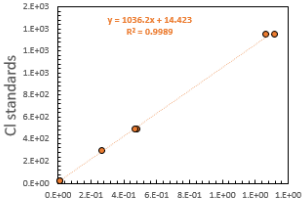


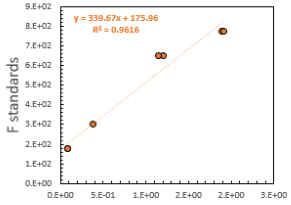

**Table A1.5:** Two raman calibration over two successive days (left and right being first and second day respectively). Calibrations are taken roughly each 3 hours. Calibrations for the first day display noticeable variations and discrepancies while the calibrations for the second day are more stable. The integral value is determined with linear baselines. Standards are a combination of synthetic glasses from Médard and Grove (2008) and melt inclusions from Stromboli and SWIR

| 10:00 AM | name | integral | average | OH area | Standard $H_2O$ (wt.%) |
|---|---|---|---|---|---|
| | Std_82_72-22_OH | 2197 | 3.086 | 4.06851852 | 0 |
| | SWIRB24_OH_pt | 20690 | 27 | 38.3148148 | 0.34 |
| | Std_STN8_8_OH_ | 124500 | 161.4 | 230.555556 | 1.35 |
| | Std_SHE750MI-O | 264800 | 343.4 | 490.37037 | 2.48 |
| 12:00 AM | | | | | |
| | Std_82_72-22_OH | 11030 | 14.28 | 20.4259259 | 0 |
| | SWIRB24_OH_pt | 44630 | 57.83 | 82.6481481 | 0.34 |
| | Std_STN8_8_OH_ | 166500 | 215.8 | 308.333333 | 1.35 |
| | Std_STN8_9_OH_ | 311800 | 404.4 | 577.407407 | 2.12 |
| | Std_SHE750MI-O | 334200 | 433.5 | 618.888889 | 2.48 |
| 3:00 PM | | | | | |
| | Std_82_72-22_OH | 7813 | 26.19 | 14.4685185 | 0 |
| | Std_SHE750MI-O | 403700 | 544.9 | 747.592593 | 2.48 |
| | Std_STN8_8_OH_ | 166600 | 225 | 308.518519 | 1.35 |
| | Std_STN8_9_OH_ | 319100 | 430.8 | 590.925926 | 2.12 |
| | SWIRB24_OH_pt | 42100 | 56.97 | 77.962963 | 0.34 |
| 7:00 PM | | | | | |
| | Std_82_72-22_OH | 1324 | 1.626 | 2.45185185 | 0 |
| | SWIRB24_OH_pt | 49070 | 63.61 | 90.8703704 | 0.34 |
| | Std_STN8_8_OH_ | 226500 | 293.7 | 419.444444 | 1.35 |
| | Std_STN8_9_OH_ | 464500 | 602.3 | 860.185185 | 2.12 |
| | Std_SHE750MI-O | 560000 | 726.3 | 1037.03704 | 2.48 |

| 10:00 AM | name | integral | average | OH area | Standard $H_2O$ (wt.%) |
|---|---|---|---|---|---|
| | 82_72_22_OH_pt (ba | 14720 | 21 | 27 | 0 |
| | SHE750MI_OH_pt (b | 305100 | 423 | 565 | 2.48 |
| | STN8_8_OH_pt (base | 118300 | 164 | 219 | 1.35 |
| | STN8_9_OH_pt (base | 219900 | 305 | 407 | 2.12 |
| | SWIRB24_OH_pt (ba | 35400 | 49 | 66 | 0.34 |
| 12:00 AM | | | | | |
| | 82_72_22_OH_pt1 (b | 20570 | 28 | 38 | 0 |
| | SHE750MI_OH_pt2 ( | 275700 | 372 | 511 | 2.48 |
| | STN8_8_OH_pt1 (bas | 94130 | 127 | 174 | 1.35 |
| | STN8_9_OH_pt2 (bas | 227000 | 306 | 420 | 2.12 |
| | SWIRB24_OH_pt1 (b | 32220 | 44 | 60 | 0.34 |
| 3:00 PM | | | | | |
| | SHE750MI_OH_pt3 ( | 332400 | 448 | 616 | 2.48 |
| | STN8_8_OH_pt2 (bas | 111600 | 150 | 207 | 1.35 |
| | STN8_9_OH_pt3 (bas | 226800 | 306 | 420 | 2.12 |
| | SWIRB24_OH_pt2 (b | 26320 | 36 | 49 | 0.34 |
| 7:00 PM | | | | | |
| | 82_72_22_OH_pt2 (b | 9898 | 13 | 18 | 0 |
| | SWIRB24_OH_pt2 (b | 19030 | 25 | 35 | 0.34 |
| | STN8_8_OH_pt3 (bas | 88780 | 115 | 164 | 1.35 |
| | SHE750MI_OH_pt4 ( | 269100 | 349 | 498 | 2.48 |

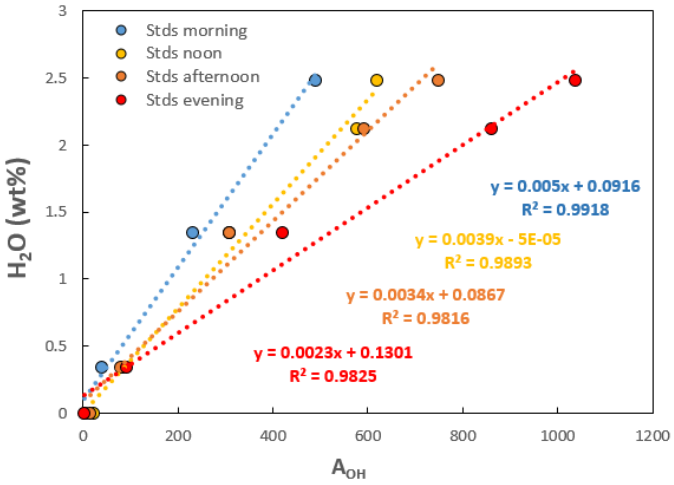


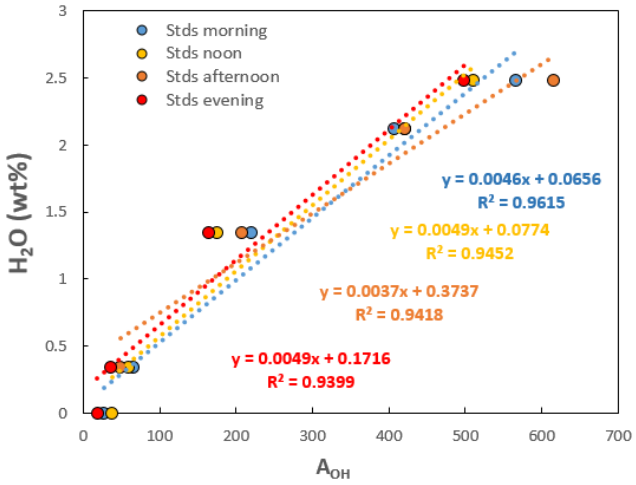

# 15th century - ST207_2

**Table A2.1a Measured profile**

| | | CO2 (ppm) | H2O (wt%) | S (ppm) | F (ppm) | Cl (ppm) | Length from the mouth (µm) | Comments | Analysis method |
|---|---|---|---|---|---|---|---|---|---|
| | | | | | | | | | Raman |
| ST207_2_pt | S2072 | | 0.40 | | | | 2 | | |
| ST207_2_pt1 | S2072 | | 0.49 | | | | 3 | | |
| ST207_2_pt2 | S2072 | | 0.67 | | | | 6 | | |
| ST207_2_pt3 | S2072 | | 0.82 | | | | 9 | | |
| ST207_2_pt4 | S2072 | | 0.96 | | | | 12 | | |
| ST207_2_pt5 | S2072 | | 1.11 | | | | 15 | | |
| ST207_2_pt6 | S2072 | | 1.32 | | | | 18 | | |
| ST207_2_pt7 | S2072 | | 1.29 | | | | 21 | | |
| ST207_2_pt8 | S2072 | | 1.40 | | | | 28 | | |
| ST207_2_pt9 | S2072 | | 1.49 | | | | 33 | | |
| ST207_2_pt10 | S2072 | | 1.52 | | | | 38 | | |
| ST207_2_pt11 | S2072 | | 1.52 | | | | 43 | | |
| ST207_2_pt12 | S2072 | | 1.61 | | | | 48 | | |
| ST207_2_ptEnd | S2072 | | 1.59 | | | | 53 | | |

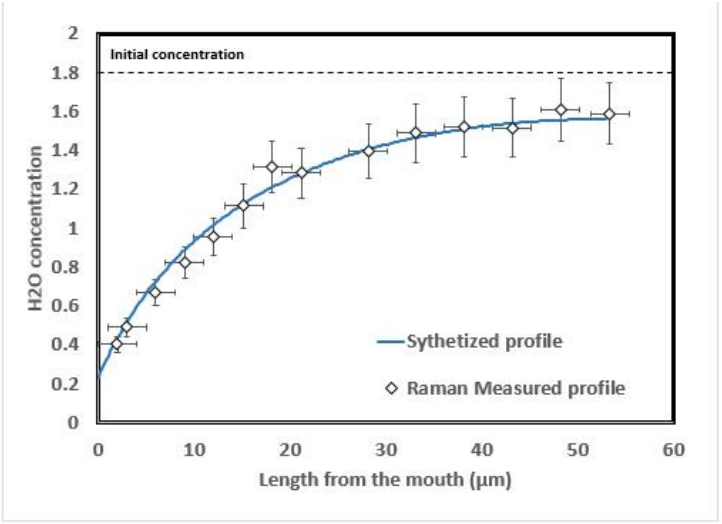


| | MPa/s | Approximate m/s |
|---|---|---|
| **Decompression rate** | **3.2** | **118** |

**Table A2.1c Size parameters**

| | |
|---|---|
| length (µm) | 52.0 |
| min width (µm) | 9.0 |
| max width (µm) | 19.0 |
| bottleneck ratio (%) | **53** |
| length/width | **2.7** |

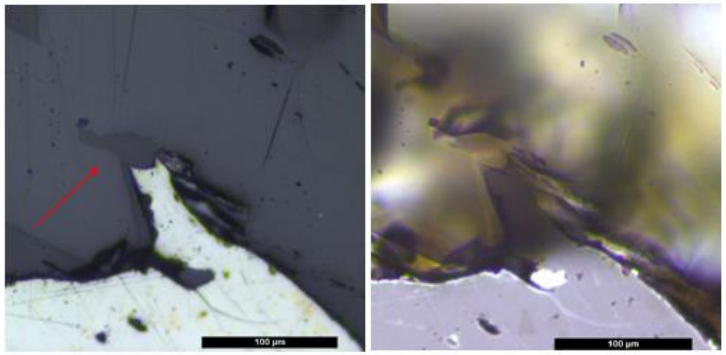

# 15th century - ST207_3

**Table A2.2a Measured profile**

| | | CO2 (ppm) | H2O (wt%) | S (ppm) | F (ppm) | Cl (ppm) | Length from the mouth (µm) | Comments | Analysis method |
|---|---|---|---|---|---|---|---|---|---|
| | | | | | | | | | Raman |
| ST207_3_pt | ST2073 | | 0.19 | | | | 0 | | |
| ST207_3_pt1 | ST2073 | | 0.32 | | | | 2 | | |
| ST207_3_pt2 | ST2073 | | 0.67 | | | | 4 | | |
| ST207_3_pt3 | ST2073 | | 0.94 | | | | 8 | | |
| ST207_3_pt4 | ST2073 | | 1.04 | | | | 10 | | |
| ST207_3_pt5 | ST2073 | | 1.28 | | | | 12 | | |
| ST207_3_pt6 | ST2073 | | 1.41 | | | | 14 | | |
| ST207_3_pt7 | ST2073 | | 1.63 | | | | 16 | | |
| ST207_3_pt8 | ST2073 | | 1.72 | | | | 20 | | |
| ST207_3_pt9 | ST2073 | | 1.80 | | | | 25 | | |
| ST207_3_pt10 | ST2073 | | 1.86 | | | | 33.5 | | |

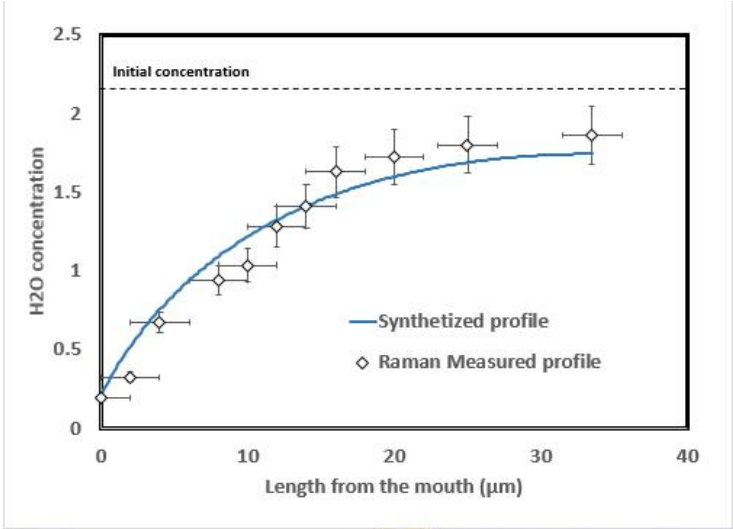


| | MPa/s | Approximate m/s |
|---|---|---|
| **Decompression rate** | **7.5** | **278** |

**Table A2.2c Size parameters**

| | |
|---|---|
| length (µm) | 34.0 |
| min width (µm) | 6.0 |
| max width (µm) | 8.0 |
| bottleneck ratio (%) | 25.0 |
| length/width | 4.3 |

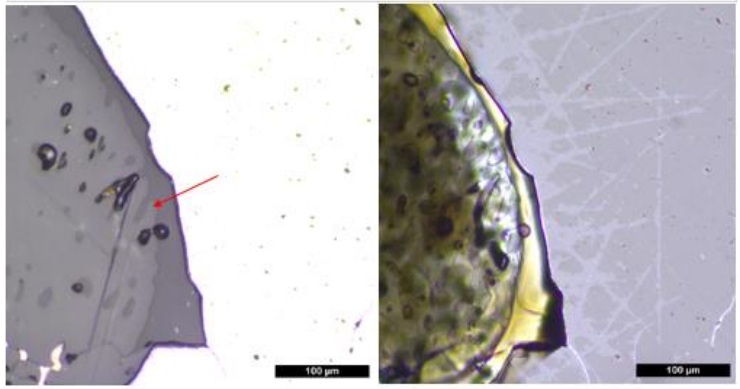

# 15th century - ST207_4

**Table A2.3a Measured profile**

| | CO2 (ppm) | H2O (wt%) | S (ppm) | F (ppm) | Cl (ppm) | Length from the mouth (µm) | Comments | Analysis method |
|---|---|---|---|---|---|---|---|---|
| ST207_4_pt | | 0.42 | | | | 0 | | Raman |
| ST207_4_pt1 | | 0.60 | | | | 3 | | |
| ST207_4_pt2 | | 0.82 | | | | 6 | | |
| ST207_4_pt3 | | 0.93 | | | | 9 | | |
| ST207_4_pt4 | | 1.12 | | | | 12 | | |
| ST207_4_pt5 | | 1.33 | | | | 15 | | |
| ST207_4_pt6 | | 1.46 | | | | 20 | | |
| ST207_4_pt7 | | 1.60 | | | | 25 | | |
| ST207_4_pt8 | | 1.33 | | | | 30 | | |
| ST207_4_pt9 | | 1.56 | | | | 36 | | |
| ST207_4_pt10 | | 1.62 | | | | 41 | | |
| ST207_4_pt11 | | 1.60 | | | | 51 | | |
| ST207_4_pt12 | | 1.58 | | | | 61 | | |
| ST207_4_pt13 | | 1.42 | | | | 71 | | |
| ST207_4_1 | 137 | 0.41 | 403 | | 1135 | 1 | | nanoSIMS |
| ST207_4_2 | 153 | 0.65 | 559 | | 1533 | 5 | | |
| ST207_4_3 | 219 | 0.88 | 664 | | 1600 | 10 | | |
| ST207_4_4 | 253 | 1.37 | 888 | | 1684 | 36 | | |
| ST207_4_5 | 303 | 1.48 | 1059 | | 1749 | 72 | | |

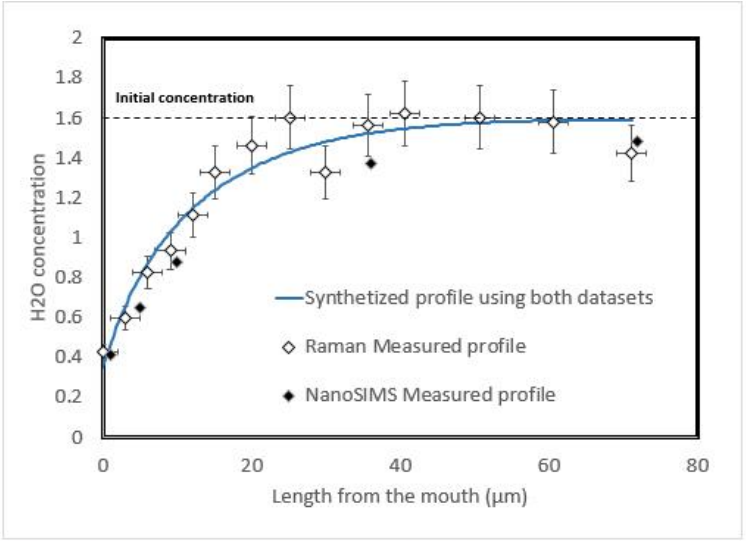


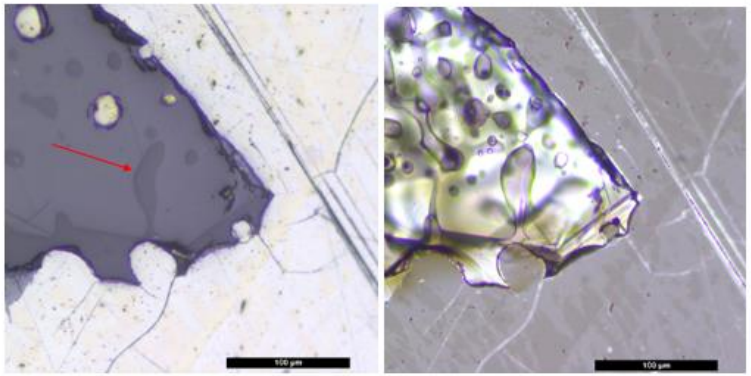

| | MPa/s | Approximate m/s |
|---|---|---|
| **Decompression rate** | **6.9** | **256** |

**Table A2.3c Size parameters**

| | |
|---|---|
| length (µm) | 77.9 |
| min width (µm) | 17.3 |
| max width (µm) | 28.4 |
| bottleneck ratio (%) | 39.0 |
| length/width | 2.7 |

# 11/09/1930 – PST205_3

**Table A2.4a Measured profile**

| | CO2 (ppm) | H2O (wt%) | S (ppm) | F (ppm) | Cl (ppm) | Length from the mouth (µm) | Comments | Analysis method |
|---|---|---|---|---|---|---|---|---|
| PST205_3_P2503 | 215.96803 | 0.58 | 729.32 | | 1351.37 | 1 | | nanoSIMS |
| PST205_3_P2503 | 257.90714 | 0.86 | 872.51 | | 1464.06 | 8 | | |
| PST205_3_P2503 | 288.39729 | 1.09 | 1021.2 | | 1573 | 15 | | |
| PST205_3_P2503 | 406.23081 | 1.47 | 1101.1 | | 1537 | 38 | | |
| PST205_3_P2503 | 415.1274 | 1.74 | 1119.2 | | 1536 | 60 | | |
| | | | | | | | | |
| PST205_v_1 | | | 763 | 945 | 1705 | 3 | | Microprobe |
| PST205_v_2 | | | 789 | 812 | 1685 | 6 | | |
| PST205_v_3 | | | 829 | 940 | 1682 | 9 | | |
| PST205_v_4 | | | 1012 | 759 | 1731 | 20 | | |
| PST205_v_5 | | | 1035 | 823 | 1739 | 25 | | |
| PST205_v_6 | | | 1025 | 931 | 1724 | 30 | | |
| PST205_v_7 | | | 1031 | 1039 | 1685 | 34 | | |
| PST205_v_8 | | | 1013 | 891 | 1679 | 39 | | |
| PST205_v_9 | | | 1074 | 922 | 1713 | 45 | | |
| PST205_v_10 | | | 1037 | 906 | 1719 | 50 | | |
| PST205_v_11 | | | 1043 | 805 | 1731 | 55 | | |
| PST205_v_12 | | | 1072 | 977 | 1764 | 61 | | |
| PST205_v_13 | | | 1110 | 890 | 1755 | 66 | | |

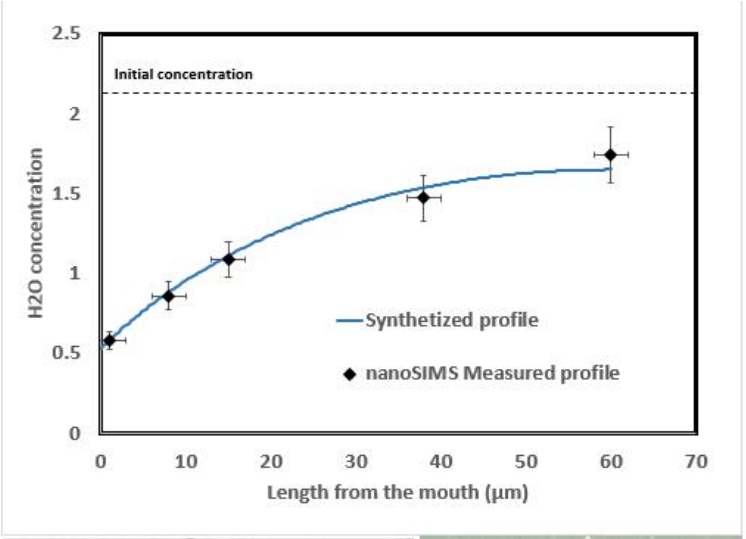


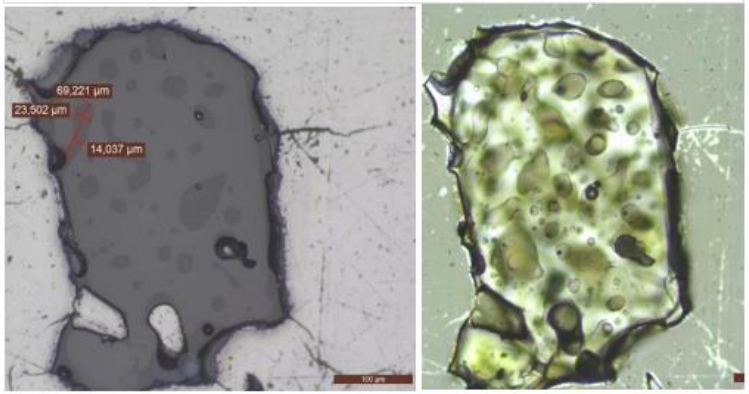


| | MPa/s | Approximate m/s |
|---|---|---|
| **Decompression rate** | **1.3** | **49** |

**Table A2.4c Size parameters**

| | |
|---|---|
| length (µm) | 69.2 |
| min width (µm) | 14.0 |
| max width (µm) | 23.5 |
| bottleneck ratio (%) | 40.3 |
| length/width | 2.9 |

# 11/09/1930 – PST205_4

**Table A2.5a Measured profile**

| | CO2 (ppm) | H2O (wt%) | S (ppm) | F (ppm) | Cl (ppm) | Length from the mouth (µm) | Comments | Analysis method |
|---|---|---|---|---|---|---|---|---|
| PST205_4_P2504 | | 0.43 | | | | 3 | | Raman |
| PST205_4_P2504 | | 0.64 | | | | 7 | | |
| PST205_4_P2504 | | 0.78 | | | | 11 | | |
| PST205_4_P2504 | | 1.04 | | | | 14 | | |
| PST205_4_P2504 | | 1.11 | | | | 17 | | |
| PST205_4_P2504 | | 1.18 | | | | 20 | | |
| PST205_4_P2504 | | 1.16 | | | | 24 | | |
| PST205_4_P2504 | | 1.34 | | | | 28 | | |
| PST205_4_P2504 | | 1.19 | | | | 31 | | |
| PST205_4_P2504 | | 1.30 | | | | 33 | | |
| PST205_4_P2504 | | 1.28 | | | | 36 | | |
| PST205_4_P2504 | | 1.34 | | | | 39 | | |
| PST205_4_P2504 | | 1.37 | | | | 42 | | |
| PST205_4_P2504 | | 2.04 | | | | inf | Measurement take | |
| | 484 | 1.99 | 1160 | | 1676 | inf | Measurement take | nanoSIMS |
| | | | | | | | | Microprobe |
| PST205_4_v_1 | | | 385 | 890 | 1336 | 5 | | |
| PST205_4_v_2 | | | 682 | 964 | 1410 | 10 | | |
| PST205_4_v_3 | | | 950 | 779 | 1643 | 15 | | |
| PST205_4_v_4 | | | 967 | 849 | 1686 | 20 | | |
| PST205_4_v_5 | | | 1001 | 746 | 1795 | 24 | | |
| PST205_4_v_6 | | | 1014 | 781 | 1753 | 29 | | |
| PST205_4_v_7 | | | 1030 | 812 | 1725 | 35 | | |
| PST205_4_v_8 | | | 1037 | 1019 | 1756 | 41 | | |
| PST205_4_v_9 | | | 1065 | 913 | 1773 | 47 | | |

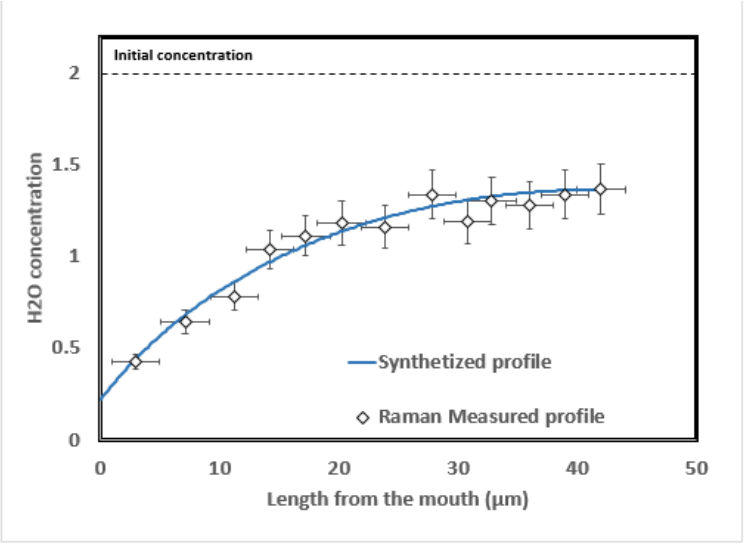


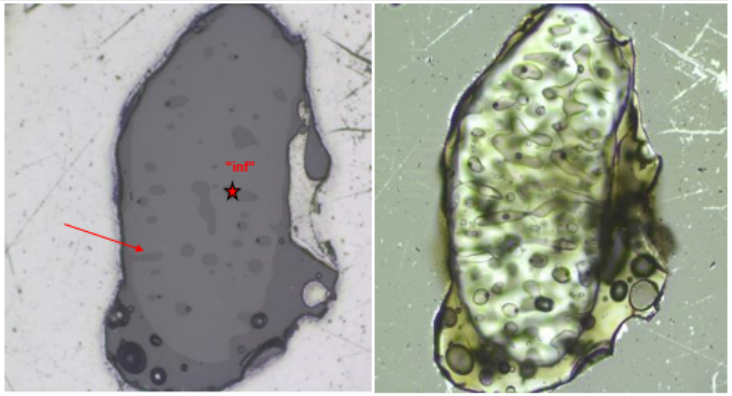


| | MPa/s | Approximate m/s |
|---|---|---|
| **Decompression rate** | **1.9** | **71** |

**Table A2.5c Size parameters**

| | |
|---|---|
| length (µm) | 62.0 |
| min width (µm) | 8.5 |
| max width (µm) | 13.0 |
| bottleneck ratio (%) | 34.6 |
| length/width | 4.8 |

# 11/09/1930 – L1930

**Table A2.6a Measured profile**

| | | CO2 (ppm) | H2O (wt%) | S (ppm) | F (ppm) | Cl (ppm) | Length from the mouth (µm) | Comments | Analysis method |
|---|---|---|---|---|---|---|---|---|---|
| | | | | | | | | | Raman |
| L1930_pt1 | L1930 | | 0.53 | | | | 3 | | |
| L1930_pt2 | L1930 | | 0.62 | | | | 6 | | |
| L1930_pt3 | L1930 | | 0.73 | | | | 9 | | |
| L1930_pt4 | L1930 | | 0.93 | | | | 12 | | |
| L1930_pt5 | L1930 | | 0.83 | | | | 15 | | |
| L1930_pt6 | L1930 | | 0.99 | | | | 20 | | |
| L1930_pt7 | L1930 | | 1.02 | | | | 25 | | |
| L1930_pt9 | L1930 | | 0.88 | | | | 35 | | |

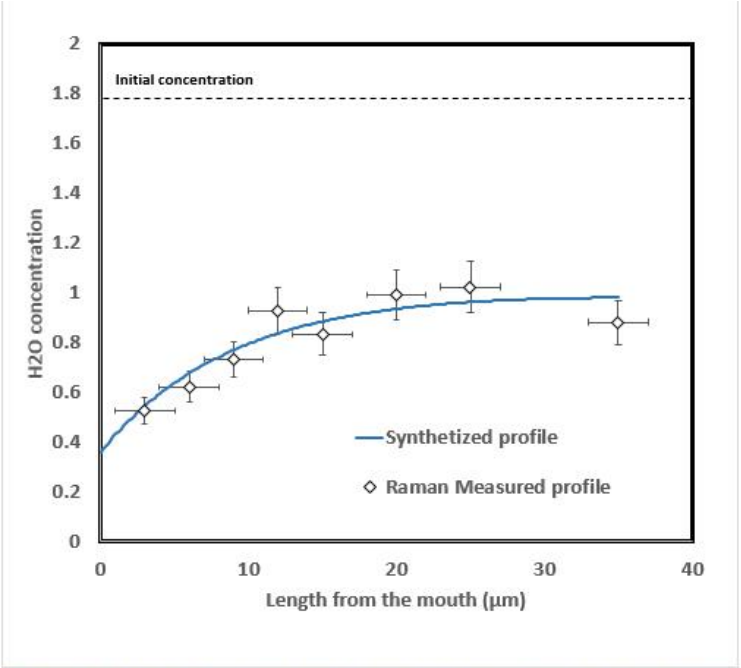


| | MPa/s | Approximate m/s |
|---|---|---|
| **Decompression rate** | **1.6** | **60** |

**Table A2.6c Size parameters**

| | |
|---|---|
| length (µm) | 74.0 |
| min width (µm) | 19.4 |
| max width (µm) | 22.4 |
| bottleneck ratio (%) | 13.3 |
| length/width | 3.3 |

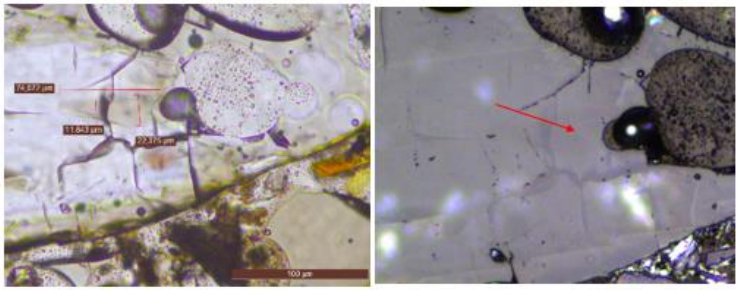

# 05/04/2003 – ST345_6

**Table A2.7a Measured profile**

| | CO2 (ppm) | H2O (wt%) | S (ppm) | F (ppm) | Cl (ppm) | Length from the mouth (µm) | Comments | Analysis method |
|---|---|---|---|---|---|---|---|---|
| S3456A | 614 | 0.85 | 1440 | | 1328 | 16 | | nSIMS 2021 |
| S3456A | | 1.56 | 1543 | | 1440 | 40 | CO2 overshoot | |
| S3456A | | 1.74 | 1475 | | 1392 | 46 | CO2 overshoot | |
| S3456A | 650 | 1.67 | 1468 | | 1341 | 50 | | |
| S3456A | 642 | 1.68 | 1440 | | 1314 | 56 | | |
| S3456A | 680 | 1.69 | 1440 | | 1334 | 62 | | |
| S3456A | 653 | 1.66 | 1545 | | 1435 | 68 | | |
| S3456A | | | | | | | | |
| S3456A | | | | | | | | |
| S3456A | 540 | 0.58 | 1276 | | 876 | 5 | | nSIMS 2022 |
| S3456A | 602 | 0.71 | 1245 | | 871 | 12 | | |
| S3456A | 571 | 0.73 | 1094 | | 908 | 17 | | |
| S3456A | 543 | 1.37 | 1371 | | 965 | 41 | | |
| S3456A | 550 | 1.39 | 1372 | | 939 | 47 | | |

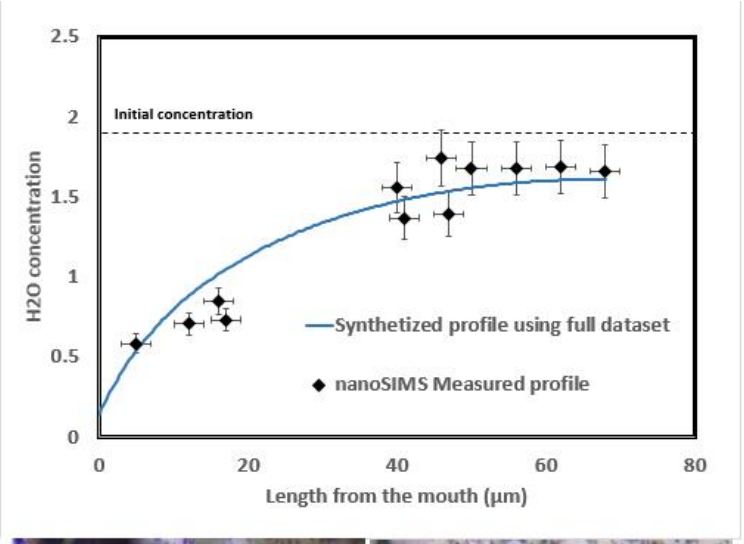


| | MPa/s | Approximate m/s |
|---|---|---|
| **Decompression rate** | **3.2** | **118** |

**Table A2.7c Size parameters**

| | |
|---|---|
| length (µm) | 68 |
| min width (µm) | 12 |
| max width (µm) | 17 |
| bottleneck ratio (%) | 29 |
| length/width | 4 |

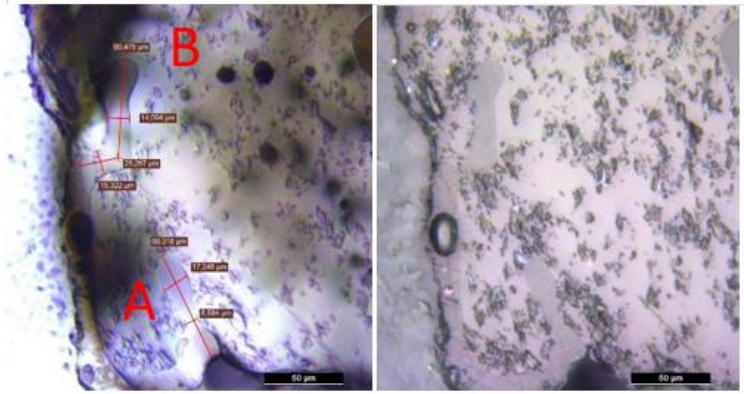

# 05/04/2003 – ST345_16

**Table A2.8a Measured profile**

| | CO2 (ppm) | H2O (wt%) | S (ppm) | F (ppm) | Cl (ppm) | Length from the mouth (µm) | Comments | Analysis method |
|---|---|---|---|---|---|---|---|---|
| | | | | | | | | nSIMS 2022 |
| 20220203_ S34516 | 1010 | 1.87 | 1168 | | 763 | 13 | | |
| 20220203_ S34516 | 908 | 1.93 | 1348 | | 835 | 17 | | |
| 20220203_ S34516 | 881 | 2.38 | 1205 | | 764 | 47 | | |
| 20220203_ S34516 | 895 | 2.50 | 1238 | | 771 | 53 | | |
| 20220203_ S34516 | 997 | 2.70 | 1308 | | 807 | 87 | | |
| 20220203_ S34516 | 948 | 2.64 | 1264 | | 780 | 91 | | |
| 20220203_ S34516 | 964 | 2.63 | 1234 | | 773 | 95 | | |
| 20220203_ S34516 | 949 | 2.58 | 1233 | | 775 | 100 | | |
| 20220203_ S34516 | 895 | 2.63 | 1347 | | 834 | 104 | | |
| | | | | | | | | Raman |
| ST345_16_pt2 | | 1.15 | | | | 3 | | |
| ST345_16_pt3 | | 1.57 | | | | 6 | | |
| ST345_16_pt4 | | 1.53 | | | | 9 | | |
| ST345_16_pt5 | | 1.55 | | | | 12 | | |
| ST345_16_pt6 | | 1.76 | | | | 15 | | |

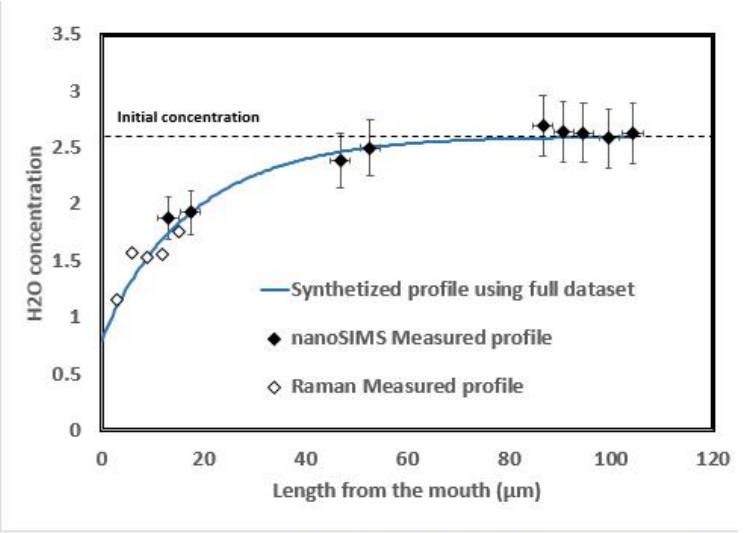


| | MPa/s | Approximate m/s |
|---|---|---|
| **Decompression rate** | **6.9** | **256** |

**Table A2.8c Size parameters**

| | |
|---|---|
| length (µm) | 121.0 |
| min width (µm) | 10.4 |
| max width (µm) | 20.0 |
| bottleneck ratio (%) | 48.0 |
| length/width | 6.1 |

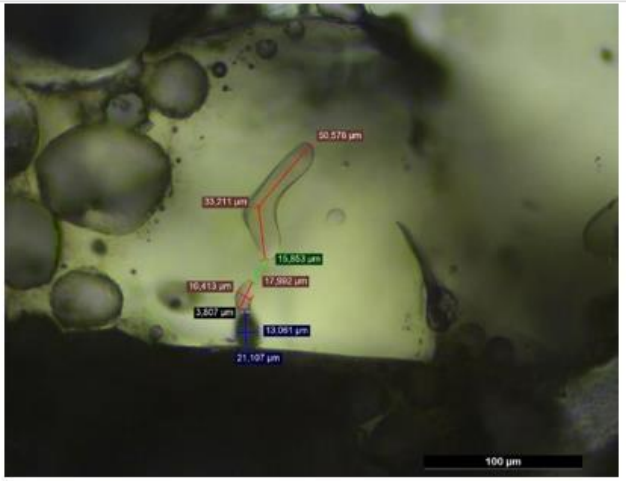


Green section is overpolished

# 15/3/2007 – 07PRXv2_2

**Table A2.9a Measured profile**

| | CO2 (ppm) | H2O (wt%) | S (ppm) | F (ppm) | Cl (ppm) | Length from the mouth (µm) | Comments | Analysis method |
|---|---|---|---|---|---|---|---|---|
| 07PRXV2_ 7PV2A | | 0.69 | | | | 5 | | Raman |
| 07PRXV2_ 7PV2A | | 0.79 | | | | 10 | | |
| 07PRXV2_ 7PV2A | | 0.86 | | | | 15 | | |
| 07PRXV2_ 7PV2A | | 0.88 | | | | 20 | | |
| 07PRXV2_ 7PV2A | | 1.01 | | | | 25 | | |
| 07PRXV2_ 7PV2A | | 1.09 | | | | 30 | | |
| 07PRXV2_ 7PV2A | | 1.33 | | | | 40 | | |
| An.2021-01 7PV2A | | 1.35 | | | | 45 | | |
| 07PRXV2_ 7PV2A | | 1.47 | | | | 50 | | |
| An.2021-01 7PV2A | | 1.60 | | | | 55 | | |
| An.2021-01 7PV2A | | 1.66 | | | | 60 | | |
| 07PRXV2_ 7PV2A | | 1.86 | | | | 70 | | |
| 07PRXV2_ 7PV2A | | 1.81 | | | | 75 | | |
| 07PRXV2_ 7PV2A | | 1.86 | | | | 85 | | |
| | | | | | | | | |
| 20220203_ 7PV2B | 146 | 1.18 | 705 | | 710 | 11 | | nSIMS2022 |
| 20220203_ 7PV2B | 126 | 1.30 | 659 | | 678 | 18 | | |
| 20220203_ 7PV2B | 120 | 1.36 | 637 | | 672 | 24 | | |
| 20220203_ 7PV2B | 54 | 1.43 | 637 | | 697 | 32 | | |
| 20220203_ 7PV2B | 80 | 1.46 | 610 | | 702 | 39 | | |
| 20220203_ 7PV2B | 52 | 1.51 | 593 | | 692 | 44 | | |
| 20220203_ 7PV2B | 64 | 1.52 | 577 | | 690 | 46 | | |
| 20220203_ 7PV2B | 63 | 1.58 | 577 | | 698 | 52 | | |
| 20220203_ 7PV2B | 67 | 1.62 | 544 | | 703 | 55 | | |
| 20220203_ 7PV2B | 74 | 1.65 | 549 | | 716 | 61 | | |
| 20220203_ 7PV2B | 53 | 1.67 | 528 | | 699 | 64 | | |
| 20220203_ 7PV2B | 38 | 1.70 | 530 | | 706 | 70 | | |
| 20220203_ 7PV2B | 41 | 1.74 | 524 | | 710 | 75 | | |
| 20220203_ 7PV2B | 33 | 1.75 | 512 | | 698 | 80 | | |
| 20220203_ 7PV2B | 35 | 1.77 | 517 | | 697 | 86 | | |
| 20220203_ 7PV2B | 4 | 1.79 | 522 | | 706 | 91 | | |

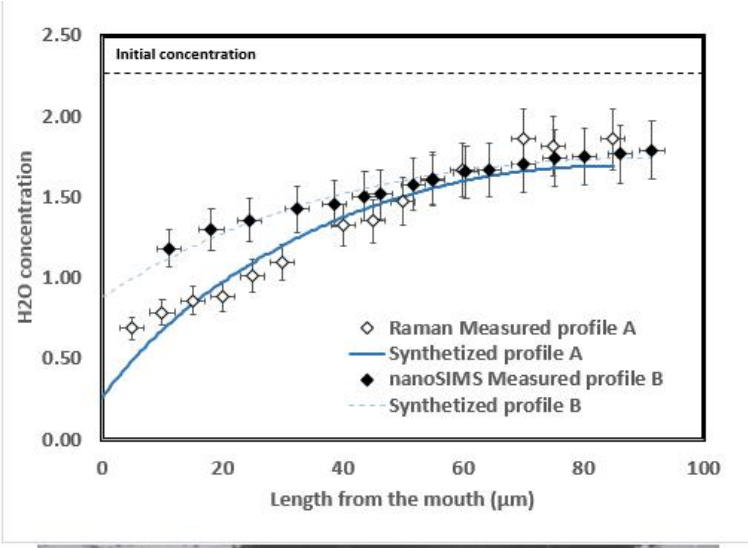


| | MPa/s | Approximate m/s |
|---|---|---|
| **Decompression rate A** | **1** | **37** |
| **Decompression rate B** | **0.5** | **19** |

| **Table A2.9c Size param** | **Embayment A** | **Embayment B** |
|---|---|---|
| length (µm) | 91.0 | 112.0 |
| min width (µm) | 19.0 | 39.0 |
| max width (µm) | 30.0 | 51.0 |
| bottleneck ratio (%) | 36.7 | 23.5 |
| length/width | 3.0 | 2.2 |

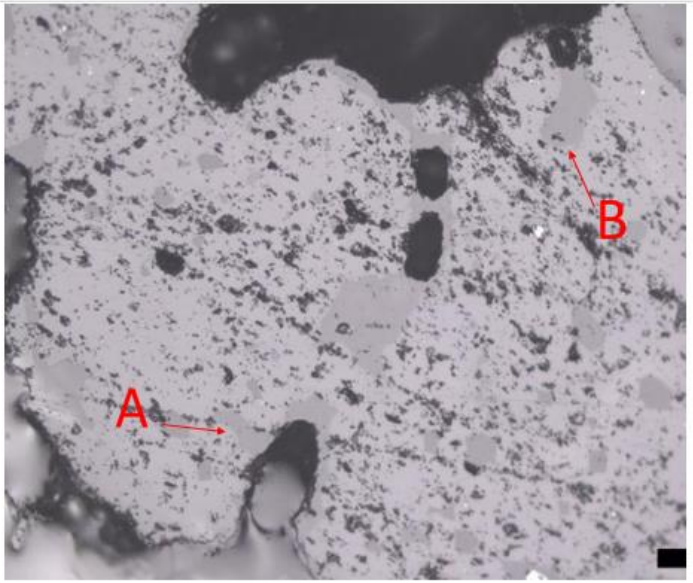

# 15/3/2007 – 07PRXv2_4

**Table A2.10a Measured profile**

| | CO2 (ppm) | H2O (wt%) | S (ppm) | F (ppm) | Cl (ppm) | Length from the mouth (µm) | Comments | Analysis method nSIMS 2021 |
|---|---|---|---|---|---|---|---|---|
| 20210624_ 7PV4 | | 0.36 | 680 | | 705 | 5 | | |
| 20210624_ 7PV4 | 109 | 0.52 | 600 | | 644 | 11 | | |
| 20210624_ 7PV4 | 154 | 0.65 | 638 | | 539 | 18 | | |
| 20210624_ 7PV4 | 236 | 0.76 | 711 | | 753 | 24 | | |
| 20210625_ 7PV4 | 904 | 1.18 | 1055 | | 892 | 40 | | |
| 20210625_ 7PV4 | 661 | 1.10 | 1031 | | 733 | 48 | | |
| 20210625_ 7PV4 | 871 | 1.61 | 1098 | | 787 | 56 | | |
| 20210625_ 7PV4 | 574 | 1.84 | 1107 | | 688 | 64 | | |
| 20210625_ 7PV4 | 697 | 1.94 | 1163 | | 707 | 72 | | |
| 20210625_ 7PV4 | 700 | 1.98 | 1146 | | 618 | 80 | | |
| 20210625_ 7PV4 | 713 | 2.01 | 1188 | | 709 | 88 | | |
| 20210625_ 7PV4 | 706 | 2.01 | 1164 | | 634 | 96 | | |
| 20210625_ 7PV4 | 747 | 2.04 | 1191 | | 672 | 104 | | |
| 20210625_ 7PV4 | 766 | 2.04 | 1177 | | 613 | 113 | | |

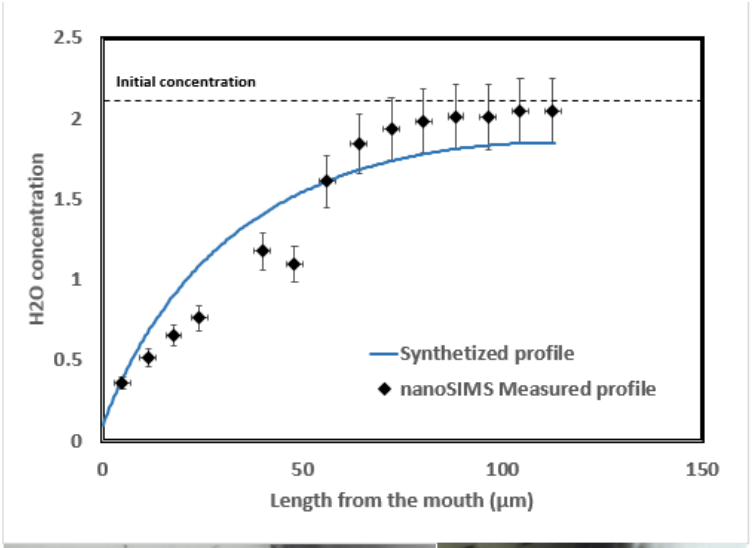


| | MPa/s | Approximate m/s |
|---|---|---|
| **Decompression rate** | **0.8** | **30** |

**Table A2.10c Size parameters**

| | |
|---|---|
| length (µm) | 150.0 |
| min width (µm) | 19.0 |
| max width (µm) | 36.0 |
| bottleneck ratio (%) | 47.2 |
| length/width | 4.2 |

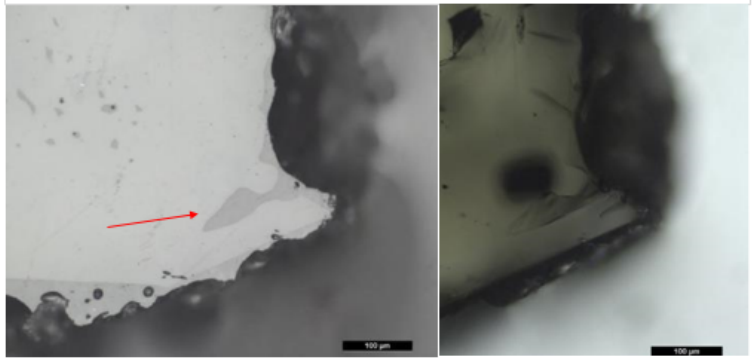

# 15/3/2007 – 07PRXv2_5

**Table A2.11a Measured profile**

| | CO2 (ppm) | H2O (wt%) | S (ppm) | F (ppm) | Cl (ppm) | Length from the mouth (µm) | Comments | Analysis method |
|---|---|---|---|---|---|---|---|---|
| | | | | | | | | nSIMS 2022 |
| 20220202_ 7PV5 | 808 | 1.13 | 1369 | | 905 | 5 | | |
| 20220202_ 7PV5 | 755 | 1.39 | 1302 | | 847 | 9 | | |
| 20220202_ 7PV5 | 786 | 1.59 | 1312 | | 846 | 16 | | |
| 20220202_ 7PV5 | 761 | 1.73 | 1334 | | 858 | 22 | | |
| 20220202_ 7PV5 | 807 | 1.86 | 1338 | | 854 | 29 | | |
| 20220202_ 7PV5 | 793 | 1.94 | 1352 | | 862 | 36 | | |
| 20220202_ 7PV5 | 916 | 2.03 | 1371 | | 865 | 42 | | |
| 20220202_ 7PV5 | 837 | 2.07 | 1386 | | 866 | 48 | | |
| 20220202_ 7PV5 | 884 | 2.08 | 1369 | | 856 | 56 | | |
| 20220202_ 7PV5 | 798 | 2.12 | 1347 | | 857 | 62 | | |
| 20220202_ 7PV5 | 790 | 2.11 | 1345 | | 839 | 69 | | |
| 20220202_ 7PV5 | 829 | 2.13 | 1377 | | 852 | 75 | | |
| 20220202_ 7PV5 | 952 | 2.17 | 1377 | | 863 | 81 | | |
| 20220202_ 7PV5 | 873 | 2.19 | 1376 | | 868 | 88 | | |
| 20220202_ 7PV5 | 921 | 2.21 | 1426 | | 865 | 94 | | |
| 20220202_ 7PV5 | 812 | 2.25 | 1440 | | 877 | 101 | | |
| | | | | | | | | Raman |
| 07_24_m | | 0.97 | | | | 0 | | |
| 07_24_1 | | 1.18 | | | | 3 | | |
| 07_24_2 | | 1.31 | | | | 6 | | |
| 07_24_3 | | 1.45 | | | | 9 | | |
| 07_24_4 | | 1.48 | | | | 12 | | |
| 07_24_5 | | 1.61 | | | | 15 | | |
| 07_24_6 | | 1.81 | | | | 20 | | |
| 07_24_7 | | 1.92 | | | | 30 | | |
| 07_24_8 | | 2.07 | | | | 40 | | |
| 07_24_9 | | 2.03 | | | | 50 | | |
| 07_24_10 | | 2.24 | | | | 75 | | |
| 07_24_11 | | 2.22 | | | | 94 | | |

| | MPa/s | Approximate m/s |
|---|---|---|
| **Decompression rate** | **3.8** | **141** |

**Table A2.11c Size parameters**

| | |
|---|---|
| length (µm) | 110.0 |
| min width (µm) | 21.0 |
| max width (µm) | 50.0 |
| bottleneck ratio (%) | 58.0 |
| length/width | 2.2 |

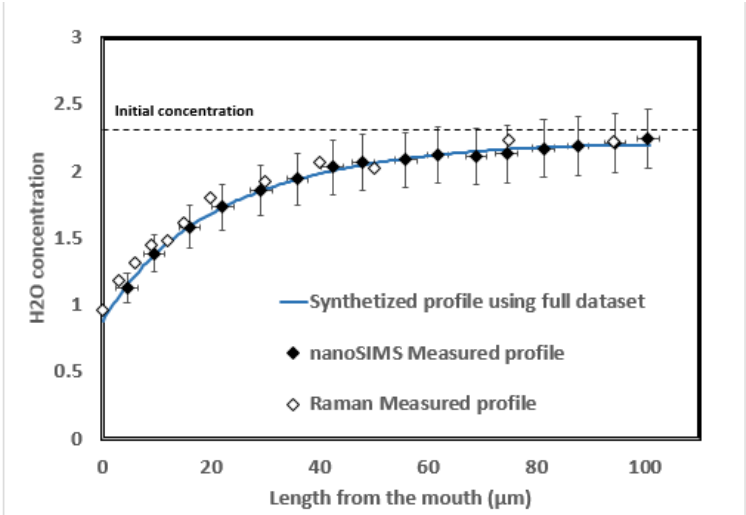


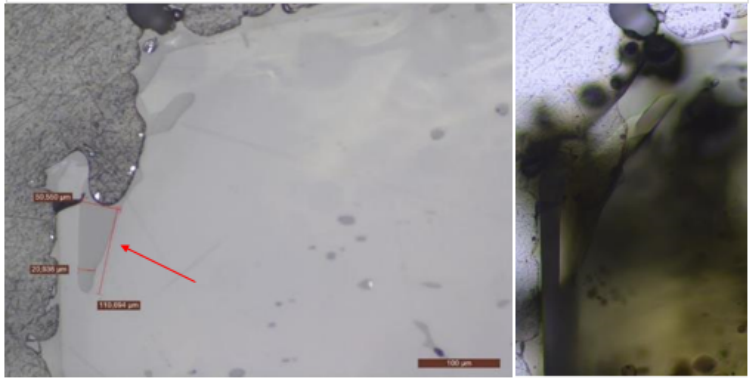

# 08/11/2009 – STN9_4

**Table A2.12a Measured profile**

| | CO2 (ppm) | H2O (wt%) | S (ppm) | F (ppm) | Cl (ppm) | Length from the mouth (µm) | Comments | Analysis method |
|---|---|---|---|---|---|---|---|---|
| STN9_4enc ST94 | 676 | 0.92 | 454 | 654 | 1445 | 5 | | SIMS2020 |
| STN9_4enc ST94 | 850 | 1.12 | 463 | 673 | 1477 | 25 | | |
| STN9_4enc ST94 | 785 | 1.17 | 516 | 636 | 1435 | 44 | | |
| STN9_4enc ST94 | 445 | 1.21 | 536 | 642 | 1461 | 60 | | |
| STN9_4enc ST94 | 395 | 1.23 | 485 | 665 | 1460 | 74 | | |
| STN9_4enc ST94 | 121 | 1.27 | 456 | 580 | 1257 | 91 | | |
| ST94_m | | 0.63 | | | | 0 | | Raman |
| ST94_1 | | 0.75 | | | | 3 | | |
| ST94_2 | | 0.85 | | | | 6 | | |
| ST94_3 | | 0.97 | | | | 9 | | |
| ST94_4 | | 1.01 | | | | 12 | | |
| ST94_5 | | 1.01 | | | | 15 | | |
| ST94_6 | | 1.15 | | | | 20 | | |
| ST94_7 | | 1.19 | | | | 40 | | |
| ST94_8 | | 1.26 | | | | 50 | | |
| ST94_9 | | 1.37 | | | | 60 | | |

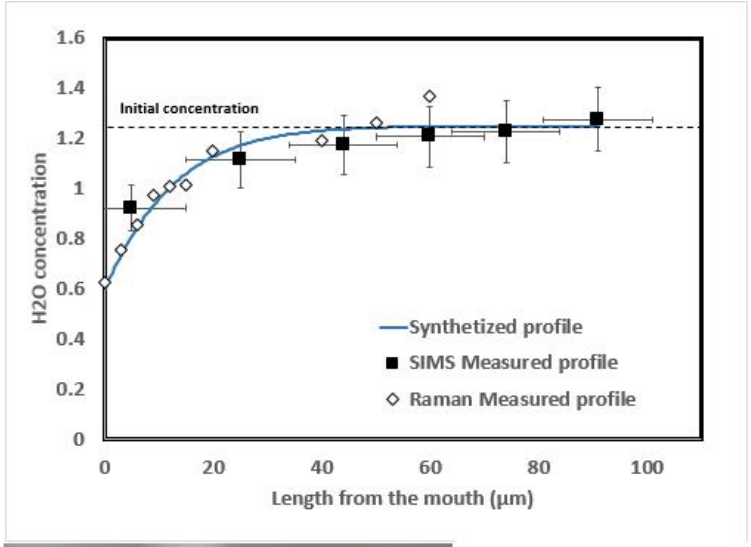


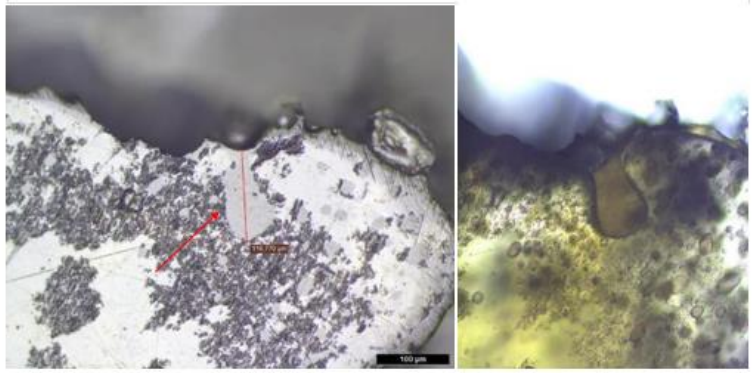

| | MPa/s | Approximate m/s |
|---|---|---|
| **Decompression rate** | **2.2** | **82** |

**Table A2.12c Size parameters**

| | | |
|---|---|---|
| length (µm) | 117.0 | |
| min width (µm) | 26.0 | |
| max width (µm) | 66.6 | |
| bottleneck ratio (%) | 61.0 | Major bottleneck |
| length/width | 1.8 | |

# 24/11/2009 – STN8v2_1

**Table A2.13a Measured profile**

| | CO2 (ppm) | H2O (wt%) | S (ppm) | F (ppm) | Cl (ppm) | Length from the mouth (µm) | Comments | Analysis method |
|---|---|---|---|---|---|---|---|---|
| | | | | | | | | Raman |
| STN8v2_1_ ST8V2a | | 0.60 | | | | 0 | | |
| STN8v2_1_ ST8V2a | | 0.73 | | | | 5 | | |
| STN8v2_1_ ST8V2a | | 0.76 | | | | 10 | | |
| STN8v2_1_ ST8V2a | | 0.83 | | | | 15 | | |
| STN8v2_1_ ST8V2a | | 0.83 | | | | 20 | | |
| STN8v2_1_ ST8V2a | | 0.86 | | | | 25 | | |
| STN8v2_1_ ST8V2a | | 0.93 | | | | 30 | | |
| STN8v2_1_ ST8V2a | | 0.95 | | | | 35 | | |
| STN8v2_1_ ST8V2a | | 0.92 | | | | 40 | | |
| STN8v2_1_ ST8V2a | | 0.94 | | | | 45 | | |
| STN8v2_1_ ST8V2a | | 0.99 | | | | 50 | | |
| STN8v2_1_ ST8V2a | | 1.03 | | | | 60 | | |
| STN8v2_1_ ST8V2a | | 1.07 | | | | 70 | | |
| STN8v2_1_ ST8v2b | | 0.71 | | | | 0 | | nSIMS2022 |
| STN8v2_1_ ST8v2b | | 0.84 | | | | 5 | | |
| STN8v2_1_ ST8v2b | | 0.94 | | | | 10 | | |
| STN8v2_1_ ST8v2b | | 0.91 | | | | 15 | | |
| STN8v2_1_ ST8v2b | | 1.02 | | | | 20 | | |
| STN8v2_1_ ST8v2b | | 1.16 | | | | 25 | | |
| STN8v2_1_ ST8v2b | | 1.30 | | | | 30 | | |
| STN8v2_1_ ST8v2b | | 1.37 | | | | 35 | | |
| STN8v2_1_ ST8v2b | | 1.58 | | | | 40 | | |
| STN8v2_1_ ST8v2b | | 1.54 | | | | 45 | | |
| STN8v2_1_ ST8v2b | | 1.61 | | | | 50 | | |
| STN8v2_1_ ST8v2b | | 1.60 | | | | 55 | | |
| STN8v2_1_ ST8v2b | | 1.75 | | | | 60 | | |
| STN8v2_1_ ST8v2b | | 1.79 | | | | 65 | | |
| STN8v2_1_ ST8v2b | | 1.91 | | | | 70 | | |
| STN8v2_1_ ST8v2b | | 1.91 | | | | 75 | | |
| STN8v2_1_ ST8v2b | | 1.91 | | | | 80 | | |
| STN8v2_1_ ST8v2b | | 1.90 | | | | 85 | | |

| | MPa/s | Approximate m/s |
|---|---|---|
| **Decompression rate A** | **0.5** | **19** |
| **Decompression rate B** | **1.3** | **49** |

| **Table A2.13c Size parameters** | **Embayment A** | **Embayment B** |
|---|---|---|
| length | 124.0 | 75.0 |
| min width | 52.0 | 15.0 |
| max width | 59.0 | 23.0 |
| bottleneck ratio (%) | 11.9 | 34.8 |
| length/width | 2.1 | 3.3 |

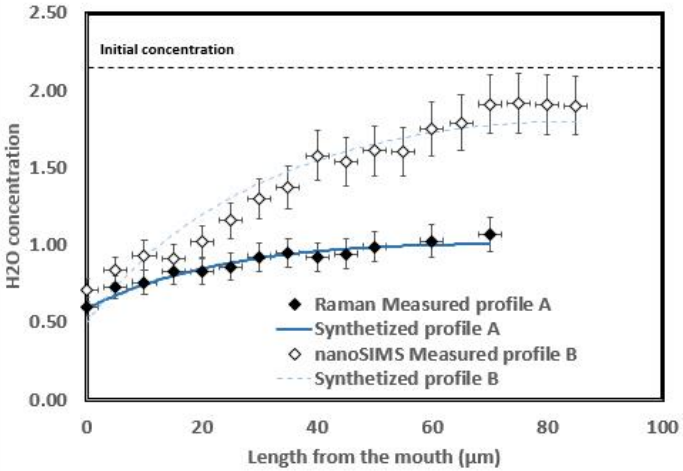


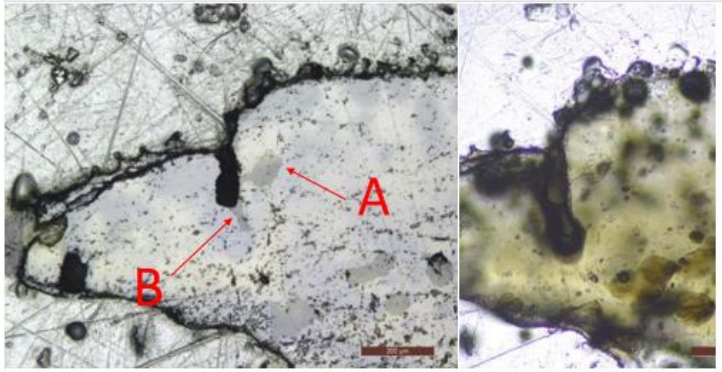

# 03/07/2019 – STGv2_1

**Table A2.14a Measured profile**

| | CO2 (ppm) | H2O (wt%) | S (ppm) | F (ppm) | Cl (ppm) | Length from the mouth (µm) | Comments | Analysis method |
|---|---|---|---|---|---|---|---|---|
| 20220201_S STG1 | n.d | 0.77 | 1414 | | 1656 | 3 | CO2 overshoot | nSIMS 2022 |
| 20220201_S STG1 | 562 | 1.17 | 936 | | 914 | 9 | | |
| 20220201_S STG1 | 218 | 1.43 | 914 | | 859 | 14 | | |
| 20220201_S STG1 | 251 | 1.47 | 921 | | 862 | 20 | | |
| 20220201_S STG1 | 268 | 1.46 | 902 | | 840 | 25 | | |
| 20220202_S STG1 | 414 | 1.49 | 972 | | 921 | 38 | | |
| 20220202_S STG1 | 274 | 1.52 | 957 | | 944 | 60 | | |
| 20220202_S STG1 | 222 | 1.66 | 910 | | 941 | 82 | | |
| 20220202_S STG1 | 285 | 1.89 | 1008 | | 949 | 104 | | |
| 20220202_S STG1 | 164 | 1.70 | 625 | | 682 | 124 | | |
| 20220202_S STG1 | 160 | 1.86 | 762 | | 885 | 138 | | |
| 20220202_S STG1 | 155 | 1.95 | 802 | | 993 | 152 | | |
| 20220202_S STG1 | 457 | 1.96 | 660 | | 928 | 173 | | |

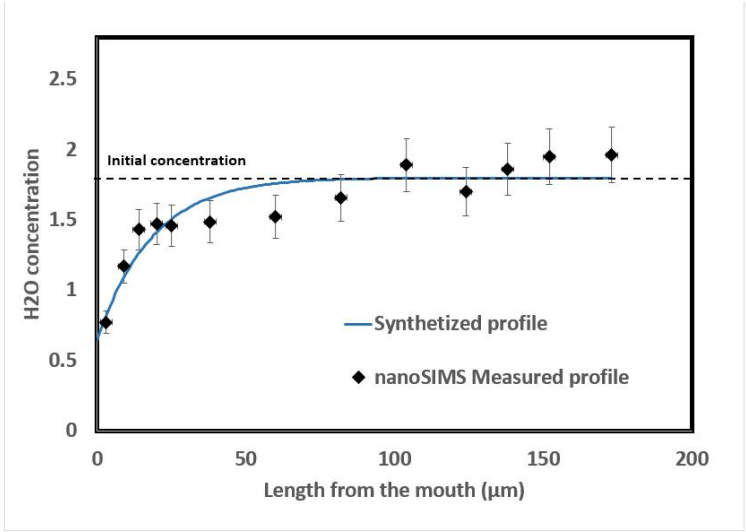


| | MPa/s | Approximate m/s |
|---|---|---|
| **Decompression rate** | **2.9** | **106** |

**Table A2.14c Size parameters**

| | |
|---|---|
| length (µm) | 190.0 |
| min width (µm) | 66.5 |
| max width (µm) | 86.0 |
| bottleneck ratio (%) | 22.7 |
| length/width | 2.2 |

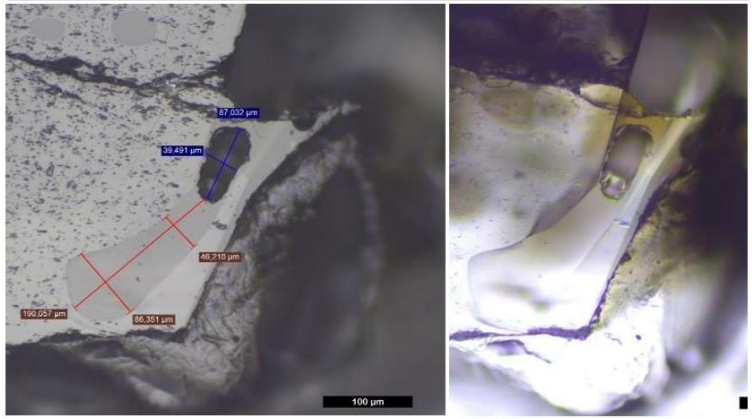

# 03/07/2019 – STGv2_3

**Table A2.15a Measured profile**

| | CO2 (ppm) | H2O (wt%) | S (ppm) | F (ppm) | Cl (ppm) | Length from the mouth (µm) | Comments | Analysis method nSIMS 2022 |
|---|---|---|---|---|---|---|---|---|
| 20210624_ STG3 | | 2.01 | 626 | | 1191 | 10 | | |
| 20210623_ STG3 | 216 | 2.10 | 615 | | 1151 | 17 | | |
| 20210623_ STG3 | 243 | 2.19 | 622 | | 1136 | 21 | | |
| 20210623_ STG3 | 221 | 2.25 | 657 | | 1149 | 27 | | |
| 20210623_ STG3 | 240 | 2.32 | 678 | | 1128 | 31 | | |
| 20210623_ STG3 | n.d | 2.48 | 730 | | 1237 | 36 | unstable CO2 signals | |
| 20210623_ STG3 | 288 | 2.39 | 751 | | 1130 | 40 | | |
| 20210623_ STG3 | 312 | 2.42 | 837 | | 1176 | 46 | | |
| 20210623_ STG3 | n.d | 2.50 | 875 | | 1160 | 51 | unstable CO2 signals | |
| 20210623_ STG3 | 391 | 2.47 | 941 | | 1189 | 56 | | |
| 20210623_ STG3 | 430 | 2.50 | 962 | | 1157 | 61 | | |
| 20210623_ STG3 | 454 | 2.53 | 1031 | | 1195 | 66 | | |
| 20210623_ STG3 | 401 | 2.57 | 1057 | | 1177 | 70 | | |
| 20210623_ STG3 | 418 | 2.56 | 1088 | | 1188 | 76 | | |
| 20210623_ STG3 | 434 | 2.54 | 1081 | | 1164 | 80 | | |
| 20210623_ STG3 | 436 | 2.58 | 1145 | | 1217 | 86 | | |
| 20210623_ STG3 | 474 | 2.59 | 1132 | | 1194 | 89 | | |
| 20210623_ STG3 | 465 | 2.60 | 1162 | | 1219 | 95 | | |
| 20210623_ STG3 | 448 | 2.61 | 1157 | | 1180 | 100 | | |
| 20210623_ STG3 | 470 | 2.62 | 1187 | | 1224 | 105 | | |
| 20210623_ STG3 | 454 | 2.65 | 1184 | | 1193 | 110 | | |
| 20210623_ STG3 | 449 | 2.64 | 1191 | | 1218 | 115 | | |
| 20210623_ STG3 | 474 | 2.61 | 1188 | | 1180 | 120 | | |

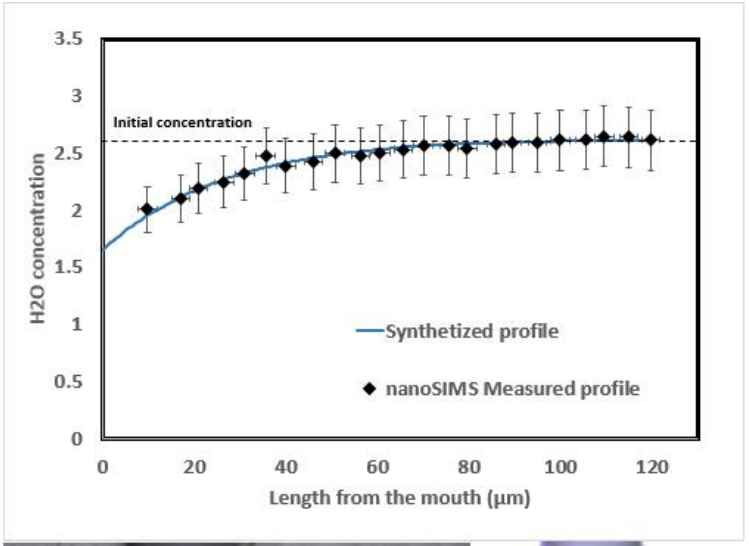


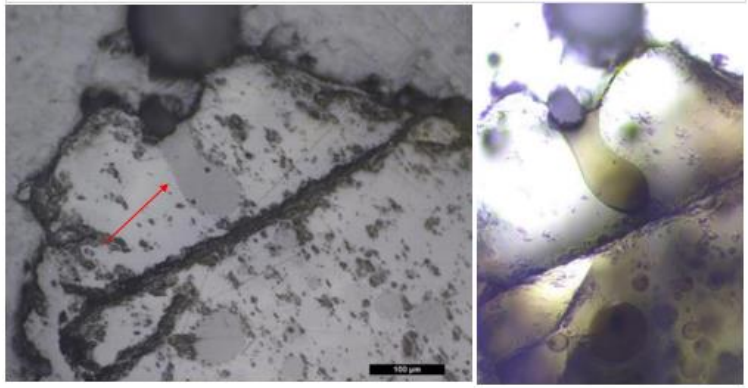

| | MPa/s | Approximate m/s |
|---|---|---|
| **Decompression rate** | **3.5** | **129** |

**Table A2.15c Size parameters**

| | |
|---|---|
| length (µm) | 132.0 |
| min width (µm) | 41.0 |
| max width (µm) | 63.0 |
| bottleneck ratio (%) | 34.9 |
| length/width | 2.1 |

# 03/07/2019 – STGv2_5

**Table A2.16a Measured profile**

| | CO2 (ppm) | H2O (wt%) | S (ppm) | F (ppm) | Cl (ppm) | Length from the mouth (µm) | Comments | Analysis method |
|---|---|---|---|---|---|---|---|---|
| 20220203_ STG5 | 71 | 0.31 | 751 | | 606 | 6 | CO2 overshoot | nSIMS 2022 |
| 20220203_ STG5 | 487 | 0.57 | 992 | | 723 | 10 | | |
| 20220203_ STG5 | 308 | 0.57 | 875 | | 653 | 15 | | |
| 20220204_ STG5 | 429 | 0.78 | 997 | | 732 | 17 | | |
| 20220204_ STG5 | 457 | 0.93 | 977 | | 719 | 22 | | |
| 20220203_ STG5 | 555 | 1.56 | 1130 | | 782 | 57 | | |
| 20220203_ STG5 | 558 | 1.65 | 1094 | | 753 | 62 | | |
| 20220203_ STG5 | 562 | 1.70 | 1088 | | 744 | 68 | | |
| 20220203_ STG5 | 567 | 1.73 | 1070 | | 729 | 74 | | |
| 20220203_ STG5 | 559 | 1.74 | 1079 | | 728 | 79 | | |
| 20220203_ STG5 | 593 | 1.80 | 1100 | | 740 | 84 | | |
| 20220203_ STG5 | 666 | 1.80 | 1070 | | 730 | 91 | | |
| 20220203_ STG5 | 558 | 1.82 | 1082 | | 738 | 96 | | |
| 20220203_ STG5 | 678 | 1.83 | 1083 | | 730 | 101 | | |
| 20220203_ STG5 | 672 | 1.81 | 1100 | | 725 | 106 | | |
| 20220203_ STG5 | 827 | 1.85 | 1098 | | 744 | 111 | | |
| 20220203_ STG5 | 684 | 1.80 | 1091 | | 731 | 117 | | |
| 20220203_ STG5 | 656 | 1.80 | 1088 | | 735 | 123 | | |

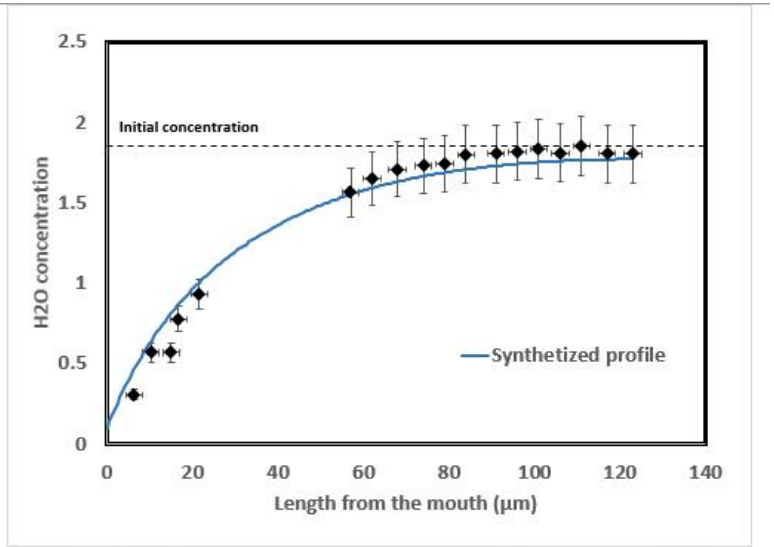


| | MPa/s | Approximate m/s |
|---|---|---|
| **Decompression rate** | **0.9** | **33** |

**Table A2.16c Size parameters**

| | | |
|---|---|---|
| length (µm) | 137.0 | |
| min width (µm) | 11.0 | overpolishing (not 2.8µm) |
| max width (µm) | 14.0 | |
| bottleneck ratio (%) | 21.4 | |
| length/width | 9.8 | |

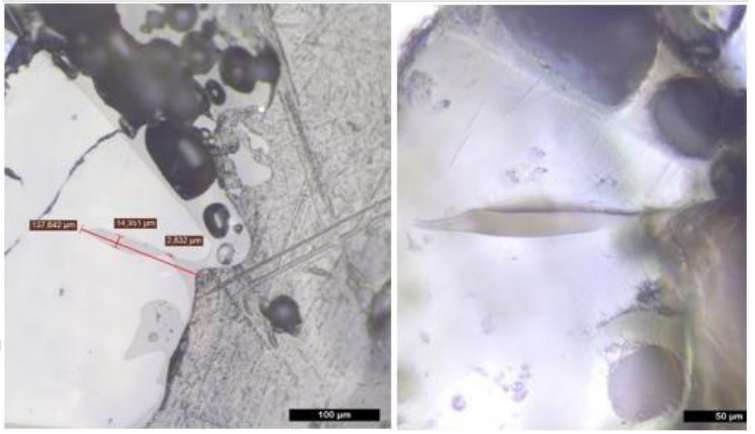

# 03/07/2019 – STGv2_7

**Table A2.17a Measured profile**

| | CO2 (ppm) | H2O (wt%) | S (ppm) | F (ppm) | Cl (ppm) | Length from the mouth (µm) | Comments | Analysis method nanoSIMS |
|---|---|---|---|---|---|---|---|---|
| STG2_7_pi STG7 | 699 | 1.26 | 1257 | | 1362 | 1 | | |
| STG2_7_pi STG7 | 678 | 1.52 | 1230 | | 1303 | 8 | | |
| STG2_7_pi STG7 | 654 | 1.61 | 1191 | | 1232 | 15 | | |
| STG2_7_pi STG7 | 679 | 1.65 | 1114 | | 1121 | 22 | | |
| STG2_7_pi STG7 | 638 | 1.69 | 1128 | | 1135 | 29 | | |
| STG2_7_pi STG7 | 617 | 1.72 | 1130 | | 1144 | 36 | | |
| STG2_7_pi STG7 | 635 | 1.79 | 1184 | | 1205 | 43 | | |
| STG2_7_pi STG7 | 661 | 1.87 | 1241 | | 1298 | 50 | | |
| STG2_7_pi STG7 | 694 | 1.92 | 1336 | | 1473 | 58 | | |

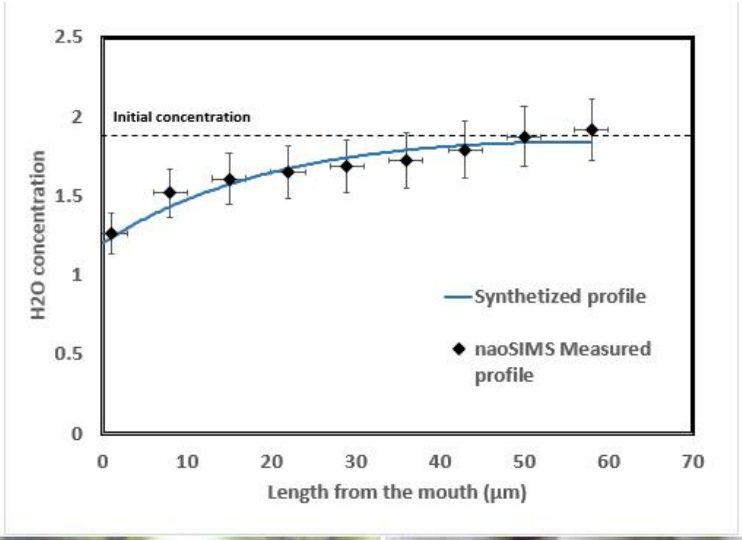


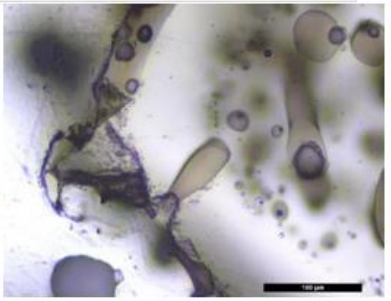

| | MPa/s | Approximate m/s |
|---|---|---|
| **Decompression rate** | 2.2 | 83 |

**Table A2.17c Size parameters**

| | |
|---|---|
| length (µm) | 78.0 |
| min width (µm) | 16.3 |
| max width (µm) | 30.1 |
| bottleneck ratio (%) | 46.0 |
| length/width | 2.6 |

# 28/08/2019 – SHE750v2_1

**Table A2.18a Measured profile**

| | CO2 (ppm) | H2O (wt%) | S (ppm) | F (ppm) | Cl (ppm) | Length from the mouth (µm) | Comments | Analysis method |
|---|---|---|---|---|---|---|---|---|
| 20220202_S7501 | 857 | 1.11 | 1127 | | 976 | 0 | CO2 overshoot | nSIMS 2022 |
| 20220202_S7501 | 898 | 1.23 | 1131 | | 998 | 0 | | |
| 20220201_S7501 | 407 | 1.93 | 1293 | | 1031 | 25 | | |
| 20220201_S7501 | 314 | 1.85 | 1307 | | 1036 | 24 | | |
| 20220201_S7501 | 329 | 1.88 | 1324 | | 1016 | 28 | | |
| 20220201_S7501 | 437 | 1.91 | 1311 | | 980 | 33 | | |
| 20220201_S7501 | 506 | 1.92 | 1296 | | 943 | 37 | | |
| 20220201_S7501 | 548 | 2.11 | 1379 | | 954 | 67 | | |
| 20220201_S7501 | 581 | 2.20 | 1300 | | 899 | 74 | | |
| 20220201_S7501 | 596 | 2.25 | 1287 | | 883 | 78 | | |
| 20220201_S7501 | 585 | 2.26 | 1240 | | 857 | 85 | | |
| 20220201_S7501 | 604 | 2.26 | 1270 | | 876 | 88 | | |
| 20220201_S7501 | 556 | 2.21 | 1275 | | 867 | 95 | | |
| SHE750v2_1_Interior | | 1.71 | | | | 15 | | Raman |
| SHE750v2_1_GI01 | | 1.26 | | | | 0 | | |
| SHE750v2_1_GI02 | | 1.25 | | | | 0 | | |
| SHE750v2_1_GI03 | | 1.26 | | | | 0 | | |

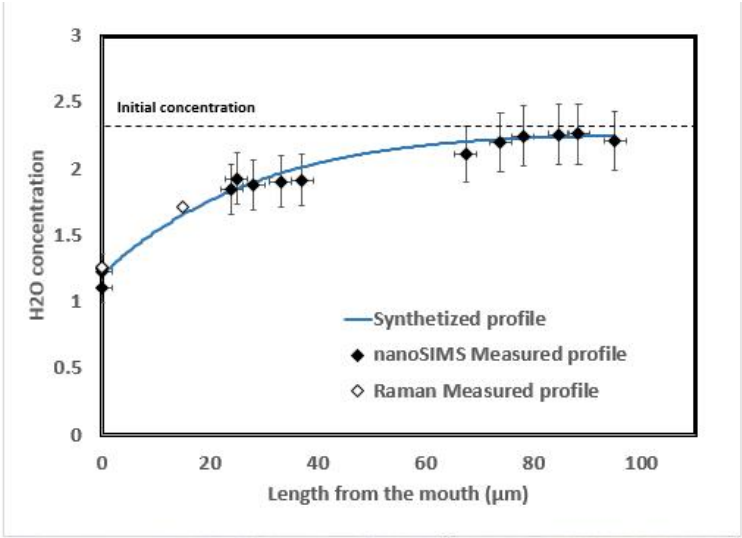


| | MPa/s | Approximate m/s |
|---|---|---|
| **Decompression rate** | **1.9** | **72** |

**Table A2.18c Size parameters**

| | |
|---|---|
| length (µm) | 100.0 |
| min width (µm) | 14.0 |
| max width (µm) | 24.0 |
| bottleneck ratio (%) | 41.7 |
| length/width | 4.2 |

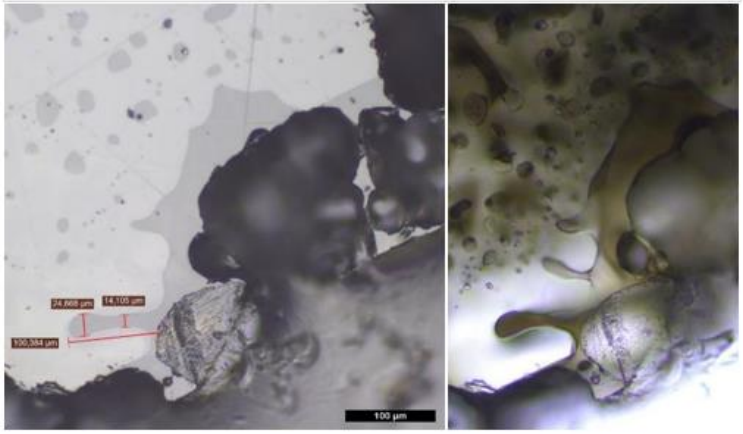

# 28/08/2019 – SHE750_S_C

**Table A2.19a Measured profile**

| | $CO_2$ (ppm) | $H_2O$ (wt%) | S (ppm) | F (ppm) | Cl (ppm) | Length from the mouth (µm) | Comments | Analysis method |
|---|---|---|---|---|---|---|---|---|
| **SHE750_**: S750C | | 0.35 | | | | 1 | | **Raman** |
| SHE750_S. S750C | | 0.46 | | | | 6 | | |
| SHE750_S. S750C | | 0.60 | | | | 11 | | |
| SHE750_S. S750C | | 0.57 | | | | 16 | | |
| SHE750_S. S750C | | 0.85 | | | | 21 | | |
| SHE750_S. S750C | | 0.95 | | | | 26 | | |
| SHE750_S. S750C | | 1.21 | | | | 31 | | |
| SHE750_S. S750C | | 1.63 | | | | 41 | | |
| SHE750_S. S750C | | 1.91 | | | | 51 | | |
| SHE750_S. S750C | | 2.07 | | | | 61 | | |
| SHE750_S. S750C | | 2.16 | | | | 71 | | |
| SHE750_S. S750C | | 2.06 | | | | 81 | | |
| SHE750_S. S750C | | 2.16 | | | | 86 | | |
| SHE750_S. S750C | | 2.10 | | | | 97 | | |
| SHE750_S. S750C | | 2.18 | | | | 110 | | |
| SHE750_S. S750C | | 2.15 | | | | 123 | | |
| | | | | | | | | |
| SHE750_S_m | | 1.38 | | | | 35 | | **SIMS 2020** |
| SHE750_S_1 | | 2.10 | | | | 52 | | |
| SHE750_S_2 | | 2.29 | | | | 70 | | |

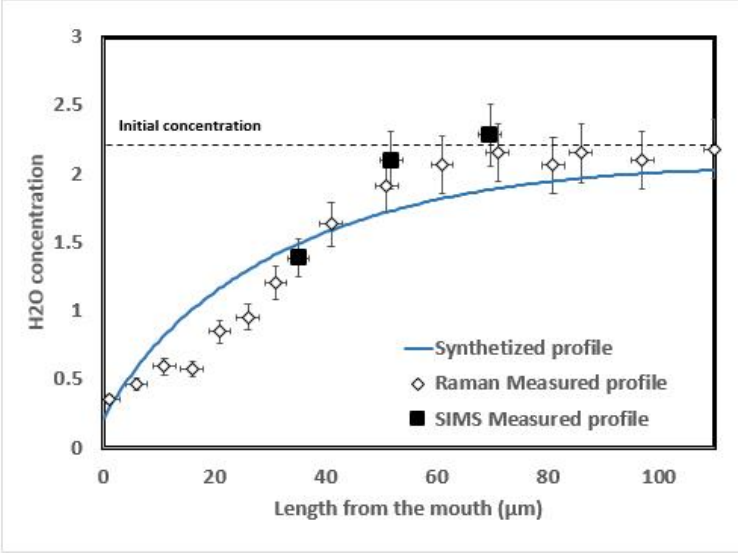


| | MPa/s | Approximate m/s |
|---|---|---|
| **Decompression rate** | **1.3** | **49** |

**Table A2.19c Size parameters**

| | |
|---|---|
| length (µm) | 130.0 |
| min width (µm) | 15.0 |
| max width (µm) | 26.0 |
| bottleneck ratio (%) | 42.3 |
| length/width | 5.0 |

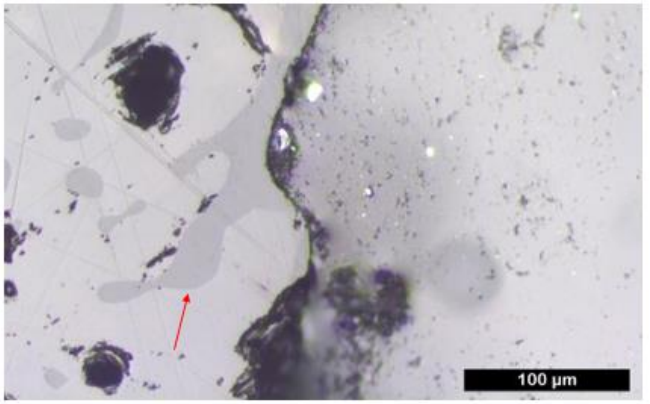

# 28/08/2019 – SHE750v2_4

**Table A2.20a Measured profile**

| | CO2 (ppm) | H2O (wt%) | S (ppm) | F (ppm) | Cl (ppm) | Length from the mouth (µm) | Comments | Analysis method |
|---|---|---|---|---|---|---|---|---|
| | | | | | | | | nSIMS |
| SHE750v2_4 S7v4 | 447 | 1.31 | 1221 | | 1489 | 1 | | |
| SHE750v2_4 S7v4 | 570 | 1.62 | 1273 | | 1515 | 7 | | |
| SHE750v2_4 S7v4 | 551 | 1.76 | 1274 | | 1490 | 12 | | |
| SHE750v2_4 S7v4 | 602 | 1.92 | 1285 | | 1467 | 18 | | |
| SHE750v2_4 S7v4 | 642 | 2.18 | 1332 | | 1470 | 43 | | |
| SHE750v2_4 S7v4 | 650 | 2.20 | 1388 | | 1538 | 62 | | |
| SHE750v2_4 S7v4 | 732 | 2.24 | 1380 | | 1510 | 94 | | |

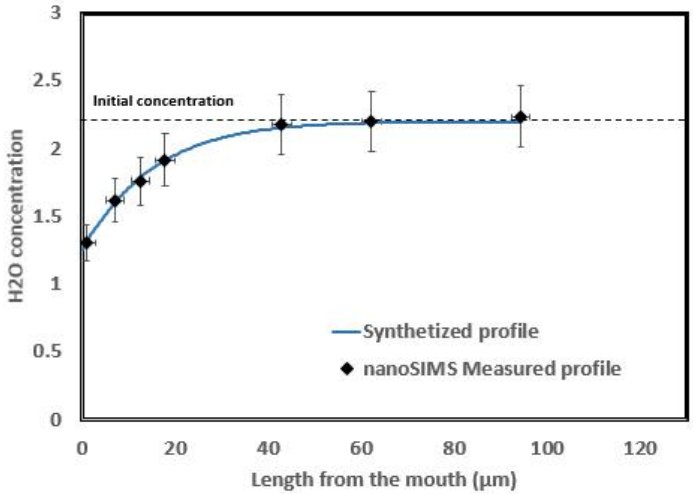


| | MPa/s | Approximate m/s |
|---|---|---|
| **Decompression rate** | **5.7** | **210** |

**Table A2.20c Size parameters**

| | |
|---|---|
| length (µm) | 112.7 |
| min width (µm) | 13.8 |
| max width (µm) | 21.4 |
| bottleneck ratio (%) | 35.4 |
| length/width | 5.3 |

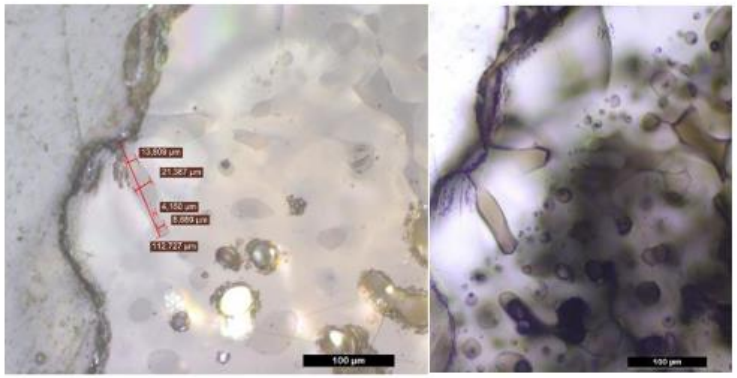

**Table A3.1**: Summary of the EMBER input parameters. The tested pre-existing volatile content ($M_0$) range for 0-3.2 wt.% for each embayment

| | dP/dt min (MPa/s) | dP/dt max (MPa/s) | Step | $C^{o}_{H2O}$ min (wt%) | $C^{o}_{H2O}$ max (wt%) | Step | $P_{pick\text{-}up}$ (MPa) | $P_{end}$ (MPa) |
|---|---|---|---|---|---|---|---|---|
| **15th century Paroxysmal** | | | | | | | | |
| **ST207_2** | 0.1 | 10 | 10 | 1.6 | 1.8 | 3 | 87 | 0.1-10 |
| **ST207_3** | 0.1 | 10 | 10 | 1.8 | 2.2 | 5 | 110 | 0.1-10 |
| **ST207_4** | 0.1 | 10 | 10 | 1.6 | 1.8 | 3 | 56 | 0.1-10 |
| **11/9/1930 Paroxysmal** | | | | | | | | |
| **PST205_4** | 0.1 | 10 | 10 | 2 | 2.1 | 3 | 87 | 0.1-10 |
| **PST205_3** | 0.1 | 10 | 20 | 1.7 | 2.1 | 5 | 74 | 0.1-10 |
| **L1930** | 0.1 | 10 | 10 | 1 | 2 | 11 | 67 | 0.1-10 |
| **5/4/2003 Paroxysmal** | | | | | | | | |
| **ST345_6A** | 0.1 | 10 | 10 | 1.7 | 1.9 | 3 | 97 | 0.1-10 |
| **ST345_16** | 0.1 | 10 | 10 | 2.6 | 2.8 | 3 | 149 | 0.1-10 |
| **15/3/2007 Paroxysmal** | | | | | | | | |
| **07PRXv2_2a** | 0.1 | 10 | 10 | 2 | 2.5 | 6 | 64 | 0.1-10 |
| **07PRXV2_2b** | 0.1 | 10 | 10 | 2 | 2.5 | 6 | 64 | 5-15 |
| **07PRXv2_4** | 0.1 | 1 | 40 | 2 | 2.1 | 3 | 116 | 0.1-10 |
| **07PRXv2_5** | 0.1 | 10 | 10 | 2.2 | 2.4 | 3 | 137 | 5-15 |
| **8/11/2009 Major** | | | | | | | | |
| **STN9_4** | 0.1 | 10 | 20 | 1.25 | 1.35 | 3 | 46 | 0.1-10 |
| **24/11/2009 Major** | | | | | | | | |
| **STN8v2_1_2a** | 0.1 | 10 | 10 | 1.05 | 2 | 3 | 66 | 0.1-10 |
| **STN8v2_1_2b** | 0.1 | 10 | 10 | 2 | 2.1 | 2 | 66 | 0.1-10 |
| **3/7/2019 Paroxysm** | | | | | | | | |
| **STGv2-3** | 0.1 | 10 | 10 | 2.6 | 2.65 | 3 | 134 | 20-40 |
| **STGv2_1** | 0.1 | 10 | 10 | 1.8 | 2.2 | 5 | 115 | 0.1-10 |
| **STGv2_5** | 0.1 | 10 | 10 | 1.75 | 1.85 | 3 | 100 | 0.1-10 |
| **STGv2_7** | 0.1 | 10 | 10 | 1.9 | 2.1 | 3 | 107 | 10-30 |
| **28/8/2019 Paroxysm** | | | | | | | | |
| **SHE750v2_1** | 0.1 | 10 | 10 | 2.2 | 2.4 | 3 | 131 | 0.1-10 |
| **SHE750_S_C** | 0.1 | 10 | 10 | 2.1 | 2.2 | 3 | 119 | 0.1-10 |
| **SHE750v2_4** | 0.1 | 10 | 10 | 1.8 | 2.2 | 3 | 117 | 10-30 |

**Table A3.2**: Summary of the embayment characteristics. The embayments labelled as "no bottleneck" are trapezoidal-shaped with a large base near the outlet bubble and gradually thinner farther in the interior. Except for PST205_3, ST345_16 and SHE750_S_C, all embayments are straight. The subscript n indicates the absence of the outlet bubble.

| | Eruption date | Eruption type | Length (µm) | Maximal width (µm) | Minimal width (µm) | Length/width ratio | Bottleneck % |
|---|---|---|---|---|---|---|---|
| **ST207_2** | 15th century | Paroxysm | 52 | 19 | 9 | 2.7 | no bottleneck |
| **ST207_3$_n$** | 15th century | Paroxysm | 34 | 8 | 6 | 4.3 | 25 |
| **ST207_4** | 15th century | Paroxysm | 78 | 28 | 17 | 2.7 | 39 |
| **PST205_3** | 9/11/1930 | Paroxysm | 69 | 24 | 14 | 2.9 | 40 |
| **PST205_4$_n$** | 9/11/1930 | Paroxysm | 62 | 13 | 9 | 4.8 | 35 |
| **L1930** | 9/11/1930 | Paroxysm | 74 | 22 | 19 | 3.3 | no bottleneck |
| **ST345_6A** | 4/5/2003 | Paroxysm | 68 | 17 | 12 | 4.0 | 29 |
| **ST345_16** | 4/5/2003 | Paroxysm | 121 | 20 | 10 | 6.1 | 48 |
| **07PRXv2_2a** | 3/15/2007 | Paroxysm | 91 | 30 | 19 | 3.0 | 37 |
| **07PRXV2_2b** | 3/15/2007 | Paroxysm | 112 | 51 | 39 | 2.2 | 24 |
| **07PRXv2_4** | 3/15/2007 | Paroxysm | 150 | 36 | 19 | 4.2 | 47 |
| **07PRXv2_5** | 3/15/2007 | Paroxysm | 110 | 50 | 21 | 2.2 | no bottleneck |
| **STN9_4** | 11/8/2009 | Major | 117 | 67 | 26 | 1.8 | 61 |
| **STN8v2_1_2a** | 11/24/2009 | Major | 124 | 59 | 52 | 2.1 | 12 |
| **STN8v2_1_2b** | 11/24/2009 | Major | 75 | 23 | 15 | 3.3 | 35 |
| **STGv2_1** | 7/3/2019 | Paroxysm | 190 | 86 | 67 | 2.2 | 23 |
| **STGv2_3** | 7/3/2019 | Paroxysm | 132 | 63 | 41 | 2.1 | 35 |
| **STGv2_5** | 7/3/2019 | Paroxysm | 137 | 14 | 11 | 9.8 | 21 |
| **STGv2_7** | 7/3/2019 | Paroxysm | 78 | 30 | 16 | 2.6 | 46 |
| **SHE750v2_1** | 8/28/2019 | Paroxysm | 100 | 24 | 14 | 4.2 | 42 |
| **SHE750_S_C$_n$** | 8/28/2019 | Paroxysm | 130 | 26 | 15 | 5.0 | 42 |
| **SHE750v2_4** | 8/28/2019 | Paroxysm | 113 | 21 | 14 | 5.3 | 36 |

*n - missing outlet bubble*

**Table A3.3**: Major composition of studied embayments. Mid, e and m indicate that the measurement have been achieved in the middle of the interior, at the end and near the outlet bubble respectively. Certain embayments (mostly .from the 15th century and 1930 paroxysms) could not be directly analyzed.

| | ST345 | | | 07PRX2 | | | | | | | | | | STN9 | |
|---|---|---|---|---|---|---|---|---|---|---|---|---|---|---|---|
| **Sample name** | **6_m** | **6_e** | **6 glass** | **2A_m** | **2A_e** | **2B_m** | **2B_e** | **3_m** | **3_e** | **4 m** | **4_e** | **5_m** | **5_e** | **4_m** | **4_e** |
| **$SiO_2$** | 47.94 | 48.55 | 50.30 | 50.33 | 48.92 | 48.52 | 48.80 | 48.93 | 48.82 | 49.20 | 49.05 | 47.86 | 48.10 | 49.62 | 49.42 |
| **$TiO_2$** | 1.02 | 1.00 | 0.97 | 0.97 | 0.98 | 0.93 | 0.91 | 0.99 | 1.00 | 0.92 | 1.00 | 0.92 | 0.95 | 1.18 | 1.06 |
| **$Al_2O_3$** | 18.93 | 18.60 | 19.19 | 18.49 | 18.75 | 18.57 | 18.44 | 18.37 | 18.83 | 19.24 | 18.33 | 18.03 | 18.01 | 17.20 | 17.90 |
| **FeO** | 8.51 | 7.95 | 7.91 | 7.79 | 8.24 | 8.09 | 7.83 | 8.46 | 8.16 | 8.05 | 7.87 | 8.41 | 7.96 | 8.81 | 8.54 |
| **MnO** | 0.25 | 0.16 | 0.16 | 0.15 | 0.16 | 0.13 | 0.17 | 0.17 | 0.16 | 0.15 | 0.15 | 0.10 | 0.17 | 0.16 | 0.12 |
| **MgO** | 4.51 | 4.23 | 4.51 | 5.10 | 4.22 | 4.54 | 4.60 | 5.17 | 3.75 | 4.03 | 3.78 | 4.97 | 4.58 | 5.00 | 4.48 |
| **CaO** | 12.71 | 12.55 | 10.76 | 11.66 | 12.40 | 12.18 | 11.81 | 12.28 | 12.89 | 12.91 | 12.80 | 12.82 | 12.08 | 11.06 | 10.93 |
| **$Na_2O$** | 2.91 | 2.70 | 2.92 | 2.45 | 2.54 | 2.81 | 2.60 | 2.35 | 2.62 | 2.77 | 2.61 | 2.45 | 2.53 | 2.77 | 2.87 |
| **$K_2O$** | 1.94 | 1.81 | 2.62 | 1.82 | 1.83 | 1.99 | 1.90 | 1.77 | 1.84 | 1.97 | 1.84 | 1.80 | 1.88 | 2.30 | 2.40 |
| **$P_2O_5$** | 0.53 | 0.66 | 0.61 | 0.62 | 0.55 | 0.54 | 0.43 | 0.64 | 0.58 | 0.63 | 0.67 | 0.52 | 0.52 | 0.48 | 0.67 |
| **Total** | 99.26 | 98.21 | 99.94 | 99.38 | 98.59 | 98.28 | 97.50 | 99.14 | 98.65 | 99.87 | 98.09 | 97.90 | 96.79 | 98.57 | 98.38 |

| | STN8_1 | | | | STG2 | | | | | | | SHE750v2 | | | | |
|---|---|---|---|---|---|---|---|---|---|---|---|---|---|---|---|---|
| **Sample name** | **2A_m** | **2A_e** | **2B_m** | **2B_e** | **1_m** | **1_e** | **3_m** | **3_e** | **5_m** | **5_e** | **7_mid** | **S_C_mid** | **1_m** | **1_e** | **4_m** | **4_e** |
| **$SiO_2$** | 50.77 | 49.54 | 49.86 | 50.41 | 49.02 | 49.52 | 49.85 | 48.99 | 49.08 | 48.63 | 48.76 | 48.28 | 49.73 | 49.10 | 48.70 | 48.86 |
| **$TiO_2$** | 1.06 | 1.08 | 1.16 | 1.08 | 0.91 | 0.93 | 0.93 | 0.94 | 1.03 | 1.00 | 0.92 | 0.96 | 0.94 | 0.92 | 0.95 | 0.96 |
| **$Al_2O_3$** | 18.19 | 17.40 | 17.76 | 17.79 | 18.32 | 18.59 | 18.38 | 17.97 | 18.98 | 18.46 | 17.88 | 18.51 | 18.50 | 18.25 | 18.62 | 18.19 |
| **FeO** | 8.02 | 8.70 | 8.77 | 8.58 | 8.22 | 7.54 | 7.55 | 7.75 | 7.98 | 8.30 | 7.70 | 7.80 | 7.56 | 7.80 | 7.85 | 8.22 |
| **MnO** | 0.17 | 0.21 | 0.14 | 0.22 | 0.17 | 0.20 | 0.16 | 0.18 | 0.21 | 0.15 | 0.12 | 0.18 | 0.20 | 0.22 | 0.16 | 0.13 |
| **MgO** | 4.33 | 4.78 | 4.62 | 4.38 | 4.72 | 4.59 | 4.57 | 4.85 | 4.22 | 4.17 | 4.46 | 4.56 | 4.62 | 4.48 | 4.48 | 4.64 |
| **CaO** | 10.97 | 11.24 | 11.38 | 11.62 | 11.82 | 11.14 | 11.07 | 11.22 | 11.58 | 12.03 | 11.42 | 11.83 | 11.37 | 11.61 | 11.83 | 11.72 |
| **$Na_2O$** | 2.87 | 2.69 | 2.67 | 2.59 | 2.81 | 2.77 | 2.86 | 2.45 | 2.69 | 3.11 | 2.73 | 2.62 | 2.79 | 2.64 | 2.64 | 2.65 |
| **$K_2O$** | 2.35 | 2.02 | 2.17 | 2.09 | 2.03 | 2.08 | 2.13 | 1.90 | 2.13 | 2.01 | 1.92 | 1.95 | 1.98 | 1.96 | 1.94 | 1.80 |
| **$P_2O_5$** | 0.84 | 0.71 | 0.82 | 0.81 | 0.61 | 0.47 | 0.53 | 0.59 | 0.69 | 0.66 | 0.56 | 0.51 | 0.57 | 0.59 | 0.58 | 0.57 |
| **Total** | 99.57 | 98.37 | 99.34 | 99.57 | 98.62 | 97.83 | 98.02 | 96.84 | 98.59 | 98.51 | 96.48 | 97.18 | 98.27 | 97.56 | 97.76 | 97.72 |

# CHAPITRE 4

# Développement d'une relation empirique entre vitesse d'émission, débit massique et taille du conduit pour les éruptions normales à paroxysmales au Stromboli

La mesure du débit massique de matériel volcanique (Mass Discharge Rate ; MDR) produit pendant une éruption explosive est un objectif central et un défi pour la volcanologie moderne. Suite à la mise en avant de relations entre MDR et vitesse maximale d'éjection de gaz à l'évent (par le biais de la vitesse de remontée du magma ; voir chapitre 3), nous proposons une relation empirique qui peut être utilisée comme un outil de prédiction en temps réel pour dériver le MDR pendant un événement en cours, si la vitesse d'éjection des gaz ($G_v$) est mesurée. Pour établir cette relation, nous avons utilisé vingt-neuf mesures de MDR et de $G_v$ pour des événements normaux, majeurs et paroxysmaux à Stromboli (Italie), ainsi que dix estimations basées sur la littérature de MDR et de $G_v$ pour des panaches à Stromboli, Fuego, Mt. St. Helens et Pinatubo. Pour Stromboli uniquement, nous trouvons deux tendances suite à un classement statistique décroissant. La première corrélation a une forte pente, est linéaire, a un faible $R^2$ (0.36), et s'applique aux émissions à dominante balistique (les éruptions Stromboliennes plus petites). Cette corrélation n'est visible que pour un des deux évents étudiés et dépends potentiellement de paramètres éruptifs superficiels. La seconde est une relation de loi de puissance avec un $R^2$ de 0,93, où le $MDR = 10^{(0.013G_v+3.107)}$ kg/s et s'applique aux panaches de cendres montant par convection. Plus généralement et grâce à l'ajout de certaines données de la littérature sur les éruptions de 1980 et 1991 pour le Mt. St. Helens et le Pinatubo, respectivement, cette relation devient $MDR = 10^{(0.0124G_v+3.1533)}$ kg/s et acquiert une portée plus globale. En combinant ces relations avec l'équation de conservation de la masse (MDR = $G_v$

□ *A*, □□étant la densité du panache et *A* étant la surface de la section transversale de l'évent), on peut également déduire le rayon de l'évent. Notre modèle permet donc une évaluation simultanée du rayon du conduit supérieur et du débit massique de produit éruptif à l'évent à partir d'une mesure indépendante de la vitesse d'éjection des gaz. Il peut être appliqué aux éruptions en cours ou passées si une estimation de la vitesse d'éjection maximale du gaz est disponible. En considérant le rôle prépondérant du MDR pour la modélisation numérique des panaches volcaniques, cette méthode empirique rapide et directe permet d'obtenir le MDR à partir des réseaux de surveillance par caméra thermique et appliquée pour assister le suivi en temps réel des panaches volcaniques.

*Type of Paper: Short Scientific Communication*

# An empirical relation between velocity, mass discharge rate and vent area for normal through paroxysmal eruptions at Stromboli

**Guillaume Georgeais[1], Andrew J. L. Harris[1], Yves Moussallam[2,3], Kenneth T. Koga[4], Estelle F. Rose-Koga[4]**

[1] *Université Clermont Auvergne, CNRS, IRD, OPGC, Laboratoire Magmas et Volcans, F-63000 Clermont-Ferrand, France*

[2] *Lamont-Doherty Earth Observatory, Columbia University, New York, NY 10027, USA*

[3] *Department of Earth and Planetary Sciences, American Museum of Natural History, New York, NY 10024, USA*

[4] *Institut des Sciences de la Terre d'Orléans (ISTO), UO/CNRS/BRGM, 1A rue de la Férollerie, 45071, Orléans, France*

✉ **Guillaume.Georgeais.pro@gmail.com**

Submitted to *Bulletin of Volcanology*

## 4.1 Abstract

Measuring Mass Discharge Rate (MDR) during an explosive eruption is a central goal of, and challenge for, modern volcanology. Based on published and new data for normal through paroxysmal explosions at Stromboli (Italy), we propose an empirical relation that can be used as a real-time predictive tool to derive MDR during an ongoing event by measuring at-vent gas jet velocity ($G_v$). We find two trends in both cross-correlation and rank order statistics among sixty-five simultaneous measurements of MDR and $G_v$ for normal, major and paroxysmal events. One of the trends defines a power law relation, $MDR = 10^{(0.015G_v+2.434)}$ kg/s, with an $R^2$ of 0.81, and applies to ash plumes ascending by convection. Combining this relation with the conservation of mass equation allows at-vent plume density and/or vent area to be derived (MDR = $G_v$ □ $A$, □ being plume density and $A$ being vent cross-sectional area). We find that while a vent radius of 2 m and plume density of 0.35 kg/m$^3$ fits with normal activity, a 290 x 2.5 m vent area likely feeds a 10 kg/m$^3$ jet during paroxysms. Initial tests on available data shows promise in extending the correlation between MDR and $G_v$ beyond Stromboli and/or to events with higher MDR (>$10^7$ kg/s). However, the exact relation will depend on magma composition, temperature and volatile content, as well as conduit radius and vent overpressure.

**Keywords:** Thermal imagery, Eruption intensity, Volcano Monitoring, Stromboli, Mt. St. Helens, Pinatubo

## 4.2 Acknowledgments

GG was supported by a PhD fellowship from the French Government “Ministère de l’Enseignement Supérieur, de la Recherche et de l’Innovation”. This is contribution no. 601 of the ClerVolc program of the International Research Center for Disaster Sciences and Sustainable Development of the University of Clermont Auvergne.

## 4.3 Funding

GG acknowledges support from the laboratory of excellence ClerVolc for funding this project.

**Conflicts of interest/Competing interests**

The authors declare no conflicts nor competing interest

## 4.4 Introduction

Can we predict the intensity of a volcanic eruption at its onset? Answering this question is one of the biggest challenges currently faced by volcanology (e.g., Sparks, 2003; Poland et al. 2020; Poland and Anderson, 2020). While the likely onset of an eruption can be assessed using precursory signals such as tremor migration, at-vent gas measurements and/or ground deformation (e.g., Chouet and Matoza, 2013; Belousov et al. 2015; Aiuppa et al. 2017), predicting the potential intensity or magnitude of the ensuing explosive event remains elusive. The hazard posed by an explosive eruption is associated with its intensity and magnitude, with the largest eruptions being those associated with the greatest number of fatalities (e.g., Simkin and Siebert, 1994; Pyle, 1998; Baxter et al. 2003). Likewise, the greater the intensity, the greater the disruption to human activity and the environment (e.g., Chester et al. 2000; Self, 2006; Cardwell et al. 2020). Furthermore, intensity can combine with wind direction and speed to determine final plume height and position (Slawson and Csanady, 1967), as well as cloud drift direction. Such meteorological effects can potentially magnify the impacts of smaller events as was shown by global disruption to airline activities during Iceland's 2010 Eyjafjallajökull eruption (e.g., Neal and Guffanti, 2011; Harris et al. 2012; Weber et al. 2012).

Mass Discharge Rate (MDR; mass flux in kg/s) is commonly used to assess the hazard associated with an explosive eruption, especially through the VEI or Volcanic Explosivity Index (Newhall and Self, 1982). Time-averaged MDR is usually calculated from the total erupted mass divided by eruption duration (e.g., Mason et al. 2004; Bryan et al. 2010; Pyle,

2015). Peak MDR can be calculated from maximum plume height as MDR is proportional to plume height to the power of four for Vulcanian-to-Plinian eruptions (Wilson et al. 1978). Geophysical signals, such as seismicity and Doppler radar (e.g., Brodsky et al., 1999; Freret-Lorgeril et al., 2018; Maki et al., 2021), can also be used. However, such approaches suffer either from time lags between measurement and processing, and while very few active volcanoes are monitored by radar others lack seismic coverage.

We propose an alternative for deriving MDR to contribute to real-time monitoring. Our solution is based on thermal or visible video and uses an empirical relation between MDR and gas jet velocity derived from data for explosive events at Stromboli (Italy). At Stromboli, the plumbing system (e.g., Bertagnini et al. 1999, 2013; Métrich et al. 2005, 2010, 2021), explosion source mechanisms (e.g., Chouet et al. 1999; Ripepe and Gordeev 1999; Ripepe et al. 2001) and emission dynamics (e.g., Patrick et al. 2007; Scharff et al. 2008; Gurioli et al. 2013) have been intensively studied and are closely monitored (e.g., Ripepe et al. 2007; Pioli and Harris 2019; Giudicepietro et al. 2020). The wealth of data means that Stromboli is the best place to test relations between a variety of eruption source term and plume ascent parameters, such as explosion depth, emission velocity, gas jet velocity and MDR (e.g., Ripepe et al. 2002; Delle Donne and Ripepe 2012; Harris et al. 2012b; Bombrun et al. 2015). We thus use Stromboli to explore an empirical relation between at-vent gas velocity and MDR using published and new datasets for which the two parameters can be simultaneously derived.

**Table 4-1** Data set for ballistic ($B_v$) and gas ($G_v$) velocities and mass discharge rate (MDR) for normal, major, and paroxysmal eruptions at Stromboli. $B_v$ and $G_v$ re-calculated using Equation (8) of Harris et al. (2012) are given in bold.

| Date of eruption | Eruption type | Data type | Method | Bv (m/s) | Direct Gv independent measurement (m/s) | Literature derived Gv calculated (m/s) | Max derived Gv re-calculated (m/s) | Max derived Bv re-calculated (m/s) | Max Mass discharge rate (kg/s) | Ref. |
|---|---|---|---|---|---|---|---|---|---|---|
| **4/5/2003** | **Parox** | Radiometer | Waveform analysis | 200 | 310 | | **297** | | 1.10E+07 | Rosi et al. (2006) |
| **4/5/2003** | **Parox** | Radiometer - Seismic | Waveform delay time | 185 | | 324 | **276** | | | Ripepe and Harris (2008) |
| **3/15/2007** | **Parox** | thermal video | Particle tracking | 155 | 210 | | **234** | | 2.20E+06 | Andronico et al. (2013), Pistolesi et al. (2012) |
| **11/8/2009** | **Major** | Bomb mapping | ballistic model | 130 | n.d | | **199** | | 1.20E+04 | Gurioli et al. (2013), Pioli et al. (2014) |
| **11/24/2009** | **Major** | Bomb mapping | ballistic model | 90 | n.d | | **142** | | 5.50E+04 | Gurioli et al. (2013), Pioli et al. (2014) |
| **7/3/2019** | **Parox** | Bomb mapping | ballistic model | 160 | n.d | 200 | **241** | | 1.40E+06 | Giordano and De Astis (2021) |
| **8/28/2019** | **Parox** | Bomb mapping | ballistic model | 130 | n.d | 200 | **199** | | 3.60E+05 | Giordano and De Astis (2021) |
| **6/27/2004** | Normal | thermal video | Gas cloud and particle tracking | 129 | 213 | | **197** | | | Harris et al. (2012) |
| **6/2/2010** | Normal | thermal video | Gas cloud and particle tracking | | 8-48 | | | **23** | | Harris et al. (2013) |
| **6/8/2010** | Normal | thermal video | Gas cloud and particle tracking | | 8-35 | | | **14** | | Harris et al. (2013) |
| **6/2004** | Normal | thermal video | Particle tracking | 3-101 | | | **158** | | | Patrick et al. (2007) |
| **9/27/1991** | Normal | acoustic sounder | Waveform analysis | 20-80 | | | **128** | | | Weill et al. (1992) |
| **9/1971** | Normal | high speed camera | Particle tracking | 2-72 | 94-112 | | **117** | | | Chouet et al. (1974) |
| **4/2000** | Normal | doppler radar | Waveform analysis | 44-70 | | | **114** | | | Hort et al. (2003) |
| **9/1994** | Normal | thermal video | Particle tracking | 35-45 | 40-105 | | **79** | | | Ripepe et al. (2001) |
| **1/29/1988 to 9/8/1989** | Normal | thermal video | Particle tracking | 16-22 | 70 | | **46** | | | Ripepe et al. (1993) |
| **10/1/1996** | Normal | doppler radar | Waveform analysis | 7-13 | | | **34** | | | Hort and Seyfried (1998) |
| **27/9/2012 to 18/5/2014** | Normal | thermal video | Gas cloud and particle tracking | | | 240 | | | 1.30E+03 | Bombrun et al. (2015) |
| **26/5/2013 to 26/5/2016** | Normal | Visible light and thermal video | Gas cloud and particle tracking | | | 112 | | | 5.25E+04 | Tournigand et al. (2017) |

## 4.5 Method

In terms of increasing magnitude, persistent explosive activity at Stromboli can be divided into normal (10–$10^4$ kg), major ($10^5$–$10^7$ kg), and paroxysmal (>$10^8$ kg) events (e.g., Barberi et al. 1993; Rosi et al. 2006; Harris and Ripepe 2007; Gurioli et al. 2013; Leduc et al. 2015). We examined 65 eruptive events (59 normal, 2 major and 4 paroxysmal) for which suitable data were available (Table 4-1). Mass discharge rate for normal eruptions was obtained using video recorded by a thermal camera during 2 and 8 June 2010. At-vent MDR for each of the 21 recorded events was obtained by dividing the total mass emitted during each eruption by eruption duration. For this dataset the mass of each eruption has already been calculated by Harris et al. (2013), but the duration has not. Thus, to obtain duration we considered the time between the first appearance of the plume and the last bomb to exit the vent as representing the start and the end of the eruption, respectively. Videos used were recorded at 30 frames per second, and in the compressed data 10 frames were equivalent to one second of recording. The uncertainty is five frames (0.5 s), so that (considering the same uncertainty for the start and end of the event) error on duration is ±1 second. We also quantified the MDR for normal explosive activity at Stromboli during October 2012 and May 2014 using thermal infrared video and following the same procedure as above. The mass, exit velocity and duration of these 31 eruptions have already been calculated by Bombrun et al. (2015), and we again used the durations to convert to MDR. In addition, we included MDR and gas ejection velocities for transient ash-dominated normal eruptions at Stromboli as derived from thermal and visible imagery by Tournigand et al. (2017).

Mass discharge rates for major and paroxysmal eruptions at Stromboli were taken from the literature as follows:

- For the 8 and 24 November 2009 major eruptions, we used the MDR given by Gurioli et al. (2013);

- For the 2003 and 2007 paroxysms, we used the MDR of Rosi et al. (2006) and Pistolesi et al. (2011), respectively;
- MDR for both 2019 paroxysms (July and August) were calculated from maximum plume height by Giordano and De Astis (2020) following the equation of Mastin et al. (2009).

Velocities for each of the normal explosions considered here are given by Harris et al. (2013) and Bombrun et al. (2015), and for the major and paroxysmal events by the same references as given above for MDR. These values are all ballistic velocities ($B_v$), which we convert to gas jet velocities ($G_v$) using equation (8) of Harris et al. (2012b):

$$G_v = 1.41 \times B_v + 15.3 \quad (1)$$

This relation is set for normal explosions at Stromboli and correlates well with directly measured gas ejection velocities (Fig. 4-1). Literature data usually provide a range of gas ejection rates due to longer-lasting events showing variations in velocity (Pioli and Harris, 2019) therefore we prioritized the highest value recorded for each eruption which is usually recorded at the onset of the eruption (Harris et al. 2013). The literature-derived data base is given in Table 4-1, and our calculated MDR data are given in Table 4-2.

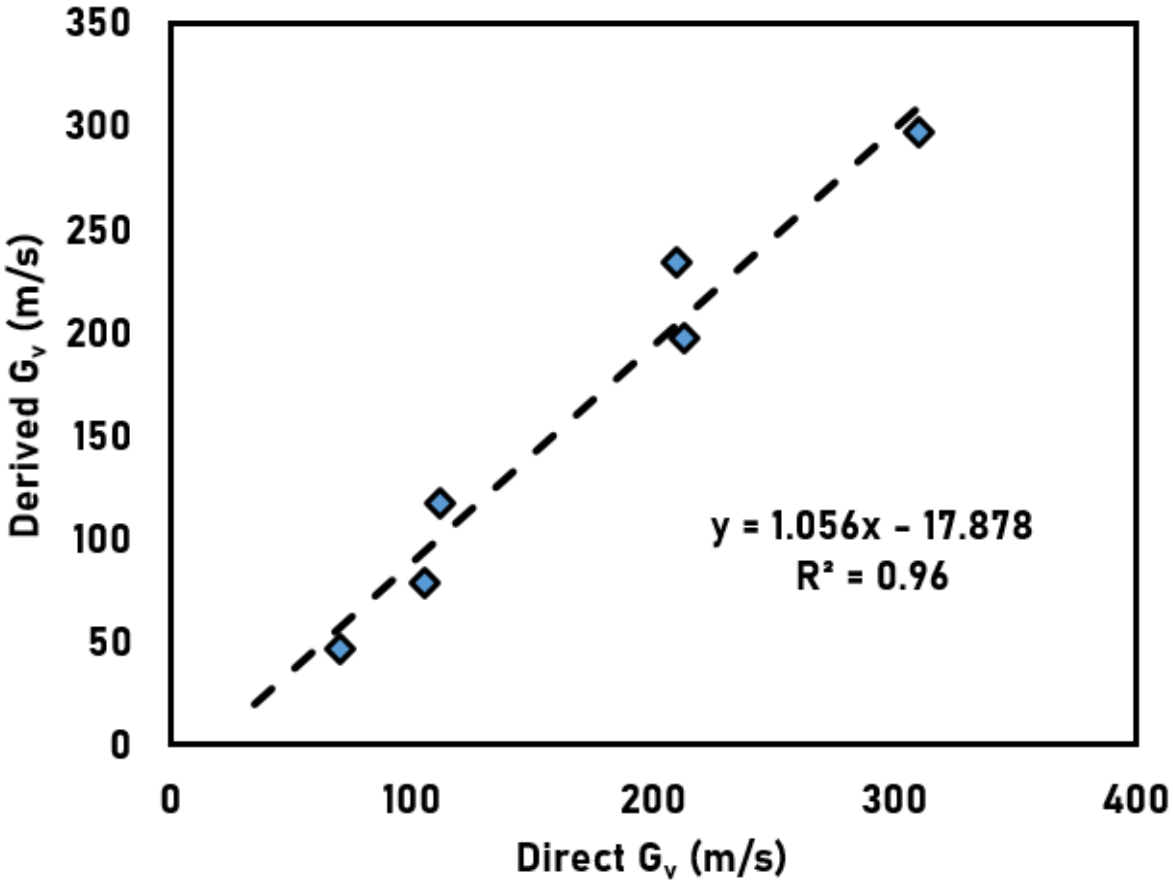


**Fig. 4-1** Comparison between max gas velocity ($G_v$), as derived from ballistic ejection velocity, and directly measured maximum gas velocities for major to paroxysmal eruptions at Stromboli. See Table 4-1 for data and sources.

## 4.6 **Results**

The 21 normal explosions at Stromboli recorded by Harris et al. (2013) lasted between 3 and 28 seconds, giving MDRs ranging from 32 to 800 kg/s (Table 4-2). Eruptions from vent NE1 lasted longer (average of 18 s) than eruptions from NE2 (average of 6 s). This leads to a wider range of MDR values for events at NE2 than NE1 (Fig. 4-2a). In Figure 4-2a, data from Bombrun et al. (2015) fall in a cluster of low MDR and high gas velocities (150–250 m/s, MDR $< 10^4$ kg/s), and data from Tournigand et al. (2017) have high MDR with low gas velocities

(<150 m/s, MDR ≥ $10^4$ kg/s). MDR for these normal explosions show correlations with gas velocity with an $R^2$ of between 0.5 and 0.83 depending on the data set used (Fig. 4-2a).

MDR for the major and paroxysmal events range between $10^4$ and $10^7$ kg/s, with gas jet velocities in the range 142–297 m/s (Table 4-1). The relation between MDR and gas velocity for the six major and paroxysmal explosion shows a positive, linear correlation with an $R^2$ of 0.79.

Eruption magnitudes have been shown to have a power-law dependence (Pyle, 1998). This can be expressed as a rank order plot, as obtained by sorting the values of a dataset from the highest to the lowest (Sornette et al. 1996). This method can be used to constrain whether the dataset is homogeneous (cf. Schneider and Barbera, 1998) within a single volcanic system. The rank order plot for our Stromboli data shows two trends representing two different populations (Fig. 4-3). These two populations are apparent in the rank order statistics for both gas velocity and MDR and involve a first group of low gas velocity and MDR, and a second group of high gas velocity and MDR. We thus define two main populations and treat them separately. The first involves ballistic-dominated normal emissions (Fig. 4-2a). The second includes all major and paroxysmal events, plus one ash-dominated normal eruption, this population being ash-rich emissions involving convective ascent dynamics (Fig. 4-2b)

**Table 4-2** Mass and duration data obtained from thermal video for normal explosions at Stromboli's NE1 and NE2 vents (derived MDR in bold).

| Crater | Date | Time | Maximum Velocity* | Total Mass* | | Duration | MDR | $Log_{10}$(MDR) |
|---|---|---|---|---|---|---|---|---|
| | (dd/mm/yy) | (hh:mm:ss) | (m $s^{-1}$) | (x $10^3$ kg) | | (s) | (kg/s) | (kg/s) |
| NE1 | 2/6/2010 | 11:35:23 | 16.6 | 1.1 | 1.4 | 18.6 | **67** | 1.83 |
| NE1 | 2/6/2010 | 11:57:51 | 39.5 | 3.5 | 3.8 | 22.9 | **160** | 2.20 |
| NE1 | 2/6/2010 | 12:22:35 | 8.3 | 2.7 | 3 | 18.2 | **156** | 2.19 |
| NE1 | 2/6/2010 | 14:08:51 | 39.5 | 1.7 | 1.8 | 19.0 | **92** | 1.96 |
| NE1 | 2/6/2010 | 14:38:43 | 47.8 | 1.7 | 1.9 | 16.4 | **110** | 2.04 |
| NE1 | 2/6/2010 | 14:59:53 | 37.4 | 3.3 | 3.7 | 28.1 | **125** | 2.10 |
| NE1 | 2/6/2010 | 15:48:05 | 43.6 | 1.1 | 1.2 | 27.2 | **42** | 1.63 |
| NE1 | 2/6/2010 | 16:08:17 | 33.3 | 0.9 | 1 | 9.4 | **101** | 2.00 |
| NE1 | 2/6/2010 | 16:12:11 | 47.8 | 1.3 | 1.4 | 6.6 | **204** | 2.31 |
| NE1 | 8/6/2010 | 13:50:46 | 33.3 | 1.3 | 1.4 | 10.2 | **132** | 2.12 |
| Average | | | 34.7 | 1.9 | 2.1 | 17.7 | 119 | 2.0 |
| NE2 | 8/6/2010 | 12:43:43 | 22.9 | 2.3 | 2.6 | 5.0 | **489** | 2.69 |
| NE2 | 8/6/2010 | 13:29:57 | 29.1 | 0.4 | 0.5 | 5.2 | **86** | 1.94 |
| NE2 | 8/6/2010 | 14:03:17 | 20.8 | 0.32 | 0.35 | 3.4 | **99** | 1.99 |
| NE2 | 8/6/2010 | 14:05:23 | 35.3 | 1.9 | 2.1 | 5.2 | **385** | 2.59 |
| NE2 | 8/6/2010 | 14:20:28 | 27 | 1.1 | 1.2 | 4.8 | **239** | 2.38 |
| NE2 | 8/6/2010 | 15:08:56 | 29.1 | 1.1 | 1.2 | 4.6 | **250** | 2.40 |
| NE2 | 8/6/2010 | 15:19:10 | 33.3 | 1.3 | 1.4 | 5.0 | **270** | 2.43 |
| NE2 | 8/6/2010 | 16:32:13 | 33.3 | 3.8 | 4.2 | 5.0 | **799** | 2.90 |
| NE2 | 8/6/2010 | 17:00:32 | 8.3 | 0.09 | 0.1 | 3.0 | **32** | 1.50 |
| NE2 | 8/6/2010 | 18:03:52 | 24.9 | 0.56 | 0.63 | 18.6 | **32** | 1.50 |
| NE2 | 8/6/2010 | 18:20:31 | 27 | 0.13 | 0.15 | 4.2 | **33** | 1.52 |
| Average | | | 26.5 | 1.2 | 1.3 | 5.8 | 247 | 2.2 |

** data from Harris et al. (2013)*

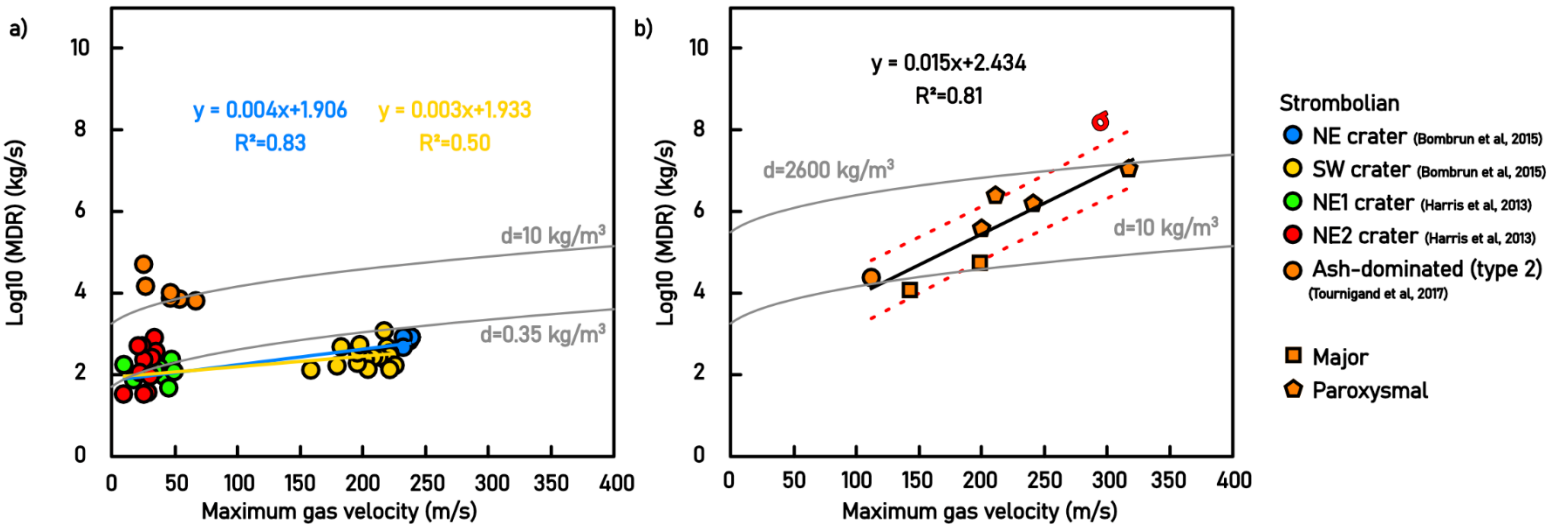


**Fig. 4-2** Relationships between MDR and maximum gas velocity for (a) normal, and (b) major and paroxysmal eruptions at Stromboli. Gray line gives fit obtained from Equation (4); red dashed lines represent the σ uncertainty envelope. The yellow trend is the fit to the data of Bombrun et al. (2015) and NE1 data of Harris et al. (2013), and the blue trend considers all NE crater data.

## 4.7 Discussion

The two trends apparent for Stromboli in the cross-correlation (Fig. 4-2a and b) and rank order plot (Fig. 4-3) result from the different plume types considered and differences in their associated ascent dynamics. Normal explosions at Stromboli are associated with slug flow in the conduit (Gonnermann and Manga, 2012) and are characterized by very low levels of fragmentation to produce bomb-dominated plumes with particles that follow ballistic trajectories (e.g., Chouet et al. 1974; Patrick et al. 2007; Gurioli et al. 2013). In contrast, major and paroxysmal events involve rapid ascent of magma coupled with a gas phase from depths of 7–10 km and are characterized by higher degrees of fragmentation (e.g., Bertagnini et al. 1999; Métrich et al. 2005, 2010, 2021; Pioli et al. 2014). The result is an ash-dominated plume whose

ascent is dominated by convection (cf. Wilson and Self 1980; Rosi et al. 2006; Harris et al. 2008).

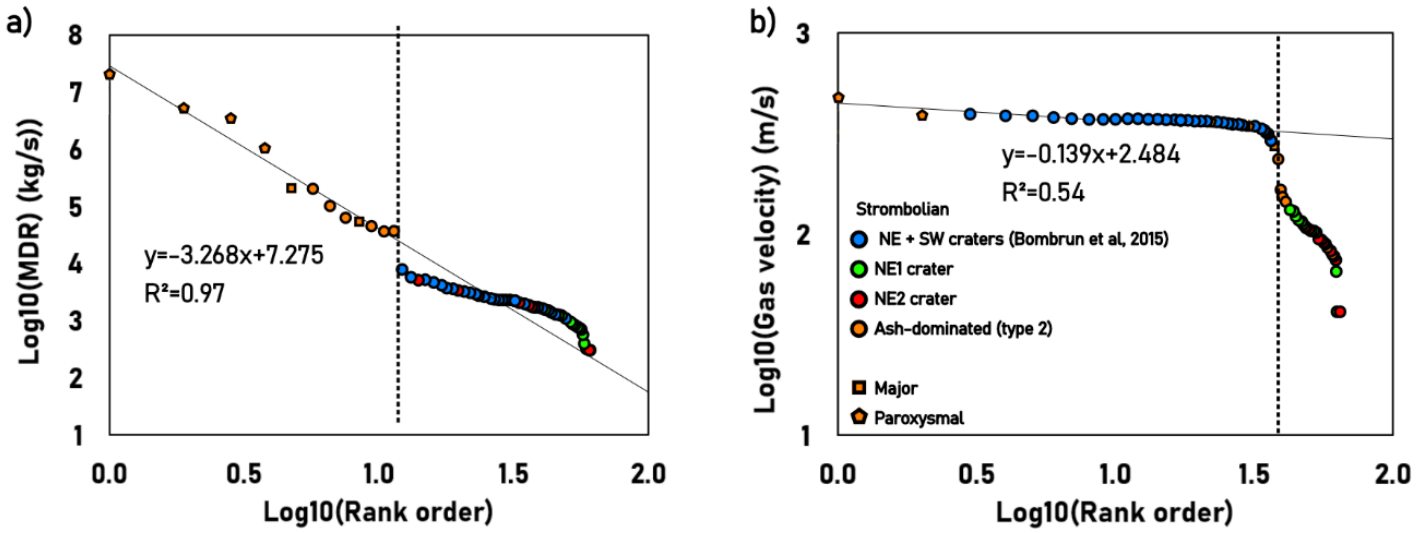


**Fig. 4-3** Rank order representation of Stromboli's normal, major and paroxysmal eruptions in terms of a) the mass discharge rate and b) the maximum gas ejection rate. Both MDR rank order and $G_v$ rank order analyses display a gap between a higher and lower group. The dashed line marks the separation between the higher ranked group composed of paroxysmal, major and ash-dominated emissions, and the lower ranked group of ballistic-dominated normal events.

Cross-correlation using data for ballistic-dominated normal explosions at Stromboli gives a relation between MDR and maximum gas velocity ($G_v$ in m/s) of (Fig. 4-2a, yellow regression line):

$$MDR = 10^{(0.003G_v+1.933)} \qquad R^2 = 0.50 \quad (2a)$$

Considering only a single vent improves the correlation. For instance, the relation for the NE crater vent 1 (NE1; Fig. 4-2a, blue regression line) is:

$$MDR = 10^{(0.004G_v+1.906)} \qquad R^2 = 0.83 \quad (2b)$$

These two relations are consistent with differences in vent size, gas/particle ratio, crater geometry, overpressure and volatile content between craters and events (Harris et al. 2013). The cross-correlation for ash-dominated normal, major and paroxysmal events gives

$$MDR = 10^{(0.015G_v+2.434)} \qquad R^2 = 0.81 \quad (3)$$

This is the black regression line of Figure 4-2b.

### 4.7.1 The next largest event at Stromboli?

Application of maximum likelihood statistics to our rank order plots (cf. Sornette et al. 1996; Pyle 1998) can indicate the most probable MDR and gas velocity for the hypothetical next largest eruption not recorded in our data (i.e., an event larger than the 2003 paroxysm). On this basis, an eruption at Stromboli larger than the 2003 paroxysm would have an MDR of 2.19 × $10^7$ kg/s and a gas ejection velocity of 338 m/s. Our current data set for Stromboli is missing at least two paroxysms, i.e., those of 1456 and 1930. Both have been described as being larger than the 2003 paroxysm (e.g., Rosi et al. 2006; Bertagnini et al. 2011; Métrich et al. 2021), but both lack an assessment of MDR and $G_v$. We thus propose that the MDR and $G_v$ calculated for the next largest eruption in our dataset are possibly representative of the 1456 and 1930 larger-scale paroxysms.

### 4.7.2 At-vent mass balance and vent size during normal and paroxysmal activity

MDR is related to gas velocity through magma density ($\rho$) and conduit cross sectional area, *A*:

$$MDR \approx \rho G_v A \quad (4)$$

Given a conduit radius which is the same as the typical vent size at Stromboli, i.e., 2 m (Harris et al. 2012b), we find that the normal ballistic-dominated events fit with a cloud density of 0.35

kg/m$^3$. This corresponds to the density of steam at 650 K (Harris et al. 2013). Instead, ash-dominated normal events fit with 10 kg/m$^3$ (Fig. 4-2a). Note, that these values are for at-vent conditions and are hence in the gas-thrust region of the jet before entrainment of air.

The lower and higher limits of the data set for major and paroxysmal eruptions can only be reproduced with a cloud density of 10 and 2600 kg/m$^3$, respectively (Fig. 4-2b). The latter density is close to the dense-rock value of basaltic magma, and does not provide a realistic plume density. For paroxysmal eruptions the conduit radius likely exceeds 2 m, where conduit erosion during high-energy events, as suggested by Macedonio et al. (1994), would cause the vent to become widened during a higher energy events. Using the MDR and $G_v$ for the July 2019 paroxysm (Table 4-1), with a cloud density of 10 kg/m$^3$, gives a circular vent radius of ~13 m. A 290 m long and 2.5 m wide source also provides a fit for the paroxysmal events. This would represent an eruption from the entire length of a SW-NE trending dyke underlying the crater terrace, and is consistent with emission from all three active craters during a paroxysm (Harris et al. 2008). It is also consistent with collapse of the crater terrace following paroxysms to create a continuous trench in place of the typical three-crater system that characterizes Stromboli's crater terrace during sustained periods of normal activity (cf. Harris and Ripepe, 2007) and the ejection of meter-sized blocks of the "shattered the shallow subvolcanic system" (Renzulli et al. 2009).

We calculate the at-vent mass fraction of pyroclasts ($f$) within the plume using a simple mixture model:

$$\rho \approx f \times \rho_{pyroclast} + (1 - f) \times \rho_{gas} \quad (5)$$

A pyroclast density ($\rho_{pyroclast}$) of ~800 kg/m$^3$, calculated using an average pyroclast vesicularity of 70 % following Pichavant et al. (2022), a gas density ($\rho_{gas}$) of 0.35 kg/m$^3$ (Harris et al. 2013), and a plume density of 10 kg/m$^3$ results in a mixture of ~1 % pyroclasts and ~99 %

gas. This is consistent with Wilson and Self (1980) who estimated dense particle weight fractions of less than 2 % in Vulcanian eruption clouds produced by Fuego's 1978 eruption (Guatemala).

### 4.7.3 Towards a global predictive model for eruption intensity?

At-vent gas and particle velocities vary as a function of vent geometry, over-pressure, magma temperature, volatile content, particle size and gas density (e.g., Steinberg and Babenko 1976; Woods and Bower 1995; Harris et al. 2012b). By restricting our consideration to a single system, we limit the variation in volatile content, temperature, crater/vent geometry, pressure, ash/gas ratio, and gas density. Velocity of ballistic particles is also related to particle size, the drag coefficient, and the velocity of the gas cloud to which the particles are coupled (cf. Harris et al. 2012b). Thus, considering an empirical fit to gas velocity simplifies the problem (Fig. 4-4). Our results indicate that, if eruption types and styles are considered separately according to their dynamics, and measurements of mass eruption rate, gas velocity and particle velocity are available, then an empirical relation relating the three can be derived.

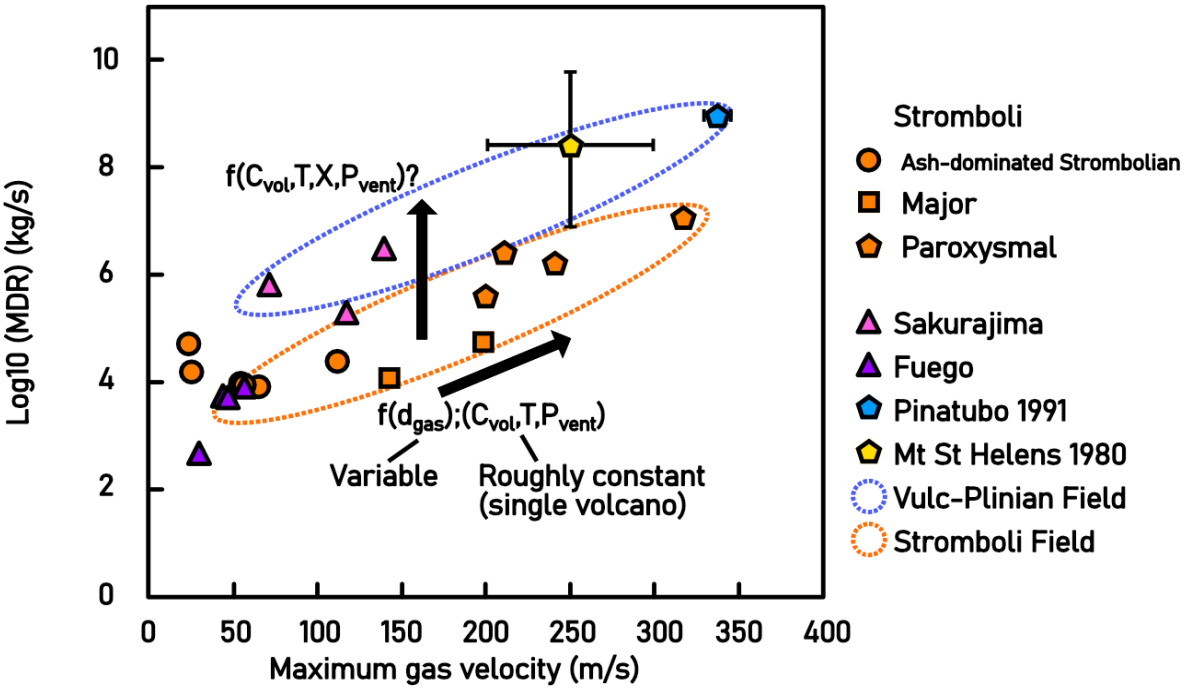

**Fig. 4-4** MDR and $G_v$ relations. Orange field is that defined by the data for ash-dominated emissions at Stromboli, where the positive, linear increase as a function of gas density ($d_{gas}$), volatile content ($C_{vol}$), conduit size and vent overpressure ($P_{vent}$), magma temperature (T) and silica content (X). The blue "Vulcanian-Plinian" field falls on a similar trend but is at a level two orders of magnitude higher than the "Strombolian" trend. Sakurajima, Mt. St. Helens and Pinatubo data fall within this field, all three being volcanoes associated with higher magma volatile content ($C_{vol}$), silica content (X), conduit size and vent pressure ($P_{vent}$) than Stromboli.

We assess whether this can be extended to other, higher magnitude systems by considering:

- Pinatubo 1991 (VEI = 6; Bluth et al. 1992);
- Mt. St. Helens 1980 (VEI = 5; Tilling et al. 1990);
- Fuego 2012 (VEI ≤ 2; Smithsonian Institution Global Volcanism Program and Venzke 2022);
- Sakurajima 2013 (VEI ≤ 3; Smithsonian Institution Global Volcanism Program and Venzke 2022).

For Fuego and Sakurajima we take the MDR and $G_v$ as derived from thermal and visible imagery by Tournigand et al. (2017). For Pinatubo, an MDR ranging between $6.8 \times 10^8$ and $10^9$ kg/s has been calculated from granulometry (Koyaguchi and Ohno 2001) and satellite data (Koyaguchi and Tokuno 1993). Estimates of the MDR at Mt. St. Helens range from $1–8 \times 10^7$ kg/s (Pyle, 2015) to $2–6 \times 10^9$ kg/s (Brodsky et al. 1999). In both cases, we use the full range. For Pinatubo we calculate gas velocity using the freely decompressing jet model of Woods and Bower (1995):

$$G_v = 1.85 \times (n_0 RT)^{1/2} \quad (6)$$

Here $n_0$ is the melt volatile concentration (6.4–7 wt %, Rutherford and Devine, 1996), $R$ is the vapor-gas constant (461.5 J/kg K), and T is the magma temperature (1073 K). For the 18 May 1980 eruption of Mt. St. Helens we use the range of velocities given by Carey and Sigurdsson (1985) and Woods and Bower (1995), i.e., 200–300 m/s. As for Stromboli, we use velocity values as close as possible to the conduit-to-crater-exit interface, where the at-surface decompression of the volcanic jet has the least impact (Woods and Bower, 1995), and where vent-leaving values can be compared between cases.

MDR values for Sakurajima, Pinatubo, and Mt. St. Helens are one-to-three orders of magnitude higher than those for Stromboli and Fuego at similar gas velocities (Fig. 4-4). However, the relationship between gas velocity and MDR remains linear and positive. This is consistent with the decompressing jet model of Woods and Bower (1995) for the emission dynamics of gas-particle mixtures, where variations in magma volatile content, over-pressure, vent geometry, and magma temperature account for the differences observed between each system (Fig. 4-4).

## 4.8 Conclusion

The empirical relationship established in this study provides a means of predicting MDR within an order of magnitude at the onset of an explosive event using the initial gas jet velocity as a measurement parameter. This means that, if a real-time measurement of gas velocity are available, then MDR can be empirically derived with known uncertainty for two event types: ballistic and convective emissions. Our derived relationship specifically applies to explosive events at Stromboli with VEI ranging from zero to three.

Extending the analysis to available data from other systems and events with higher VEI suggest applicability of our approach to other systems. Our argument is for a database with simultaneous measurements of MDR and at-vent velocities for a variety of systems, allowing extension of this analysis. Given the importance of MDR as a key source term in forward

modeling (cf. Bonadonna et al. 2011), such a fast and straightforward empirical approach that allows MDR estimation through real-time provision of vent-leaving particle velocities from video camera-based monitoring networks shows promise.

# CHAPITRE 5

# DISCUSSION ET PERSPECTIVES

## 5.1 Vers une relation globale entre vitesse d'ascension et explosivité des magmas pour les basaltes ?

L'essentiel du travail réalisé au cours de cette thèse a eu pour but d'étudier à différentes échelles les relations entre vitesse d'ascension et explosivité des magmas. Il m'a permis d'établir successivement une base de données comparable des vitesses d'ascension des magmas déterminées via la méthode des embayments, de mettre une avant une possible relation entre vitesse d'ascension maximale et magnitude des magmas basaltiques, d'établir cette relation et d'autres avec l'intensité et la pression de début d'ascension pour le Stromboli et d'articuler certaines de ces relations en un modèle prédictif empirique et instantané du débit massique d'une éruption à partir de l'imagerie thermique. Chaque nouvelle étude effectuée sur les embayments a cependant le potentiel d'enrichir un peu plus notre base de données et, de ce fait, contribuer au renforcement d'un regard critique envers la tendance globale entre vitesse d'ascension des magma et magnitude de l'éruption pour des magmas basaltiques (déterminée au chapitre 2). Nous avons donc intégré les données obtenues pour le Stromboli dans la base de données afin d'observer comment ont évolué les tendances globales entre vitesse d'ascension et magnitude, intensité et hauteur du panache (Fig. 5-1).

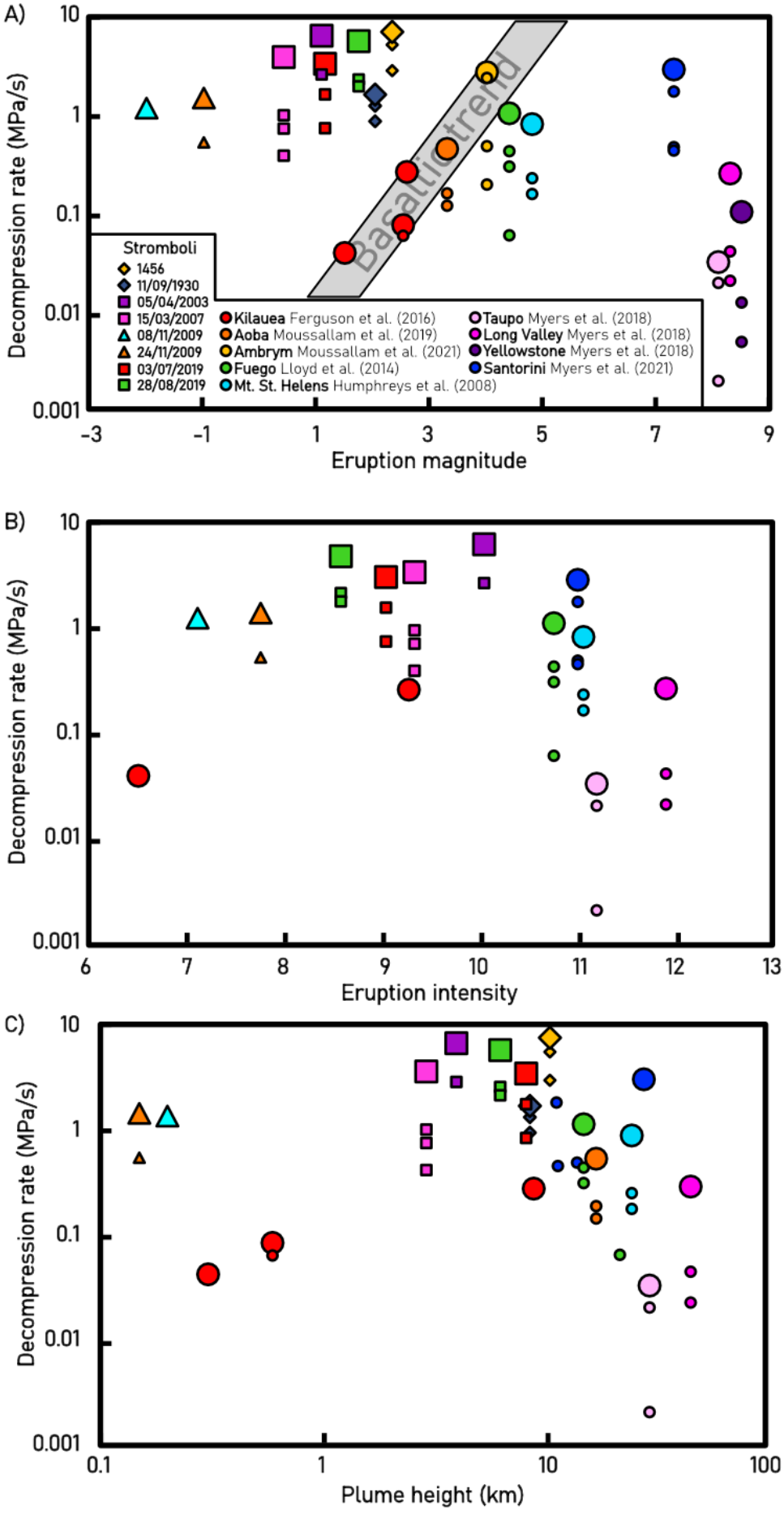
A)
Decompression rate (MPa/s)
10
1
0.1
0.01
0.001
-3
-1
1
3
5
7
9
Eruption magnitude
Basaltic trend
Stromboli
1456
11/09/1930
05/04/2003
15/03/2007
08/11/2009
24/11/2009
03/07/2019
28/08/2019
Kilauea Ferguson et al. (2016)
Aoba Moussallam et al. (2019)
Ambrym Moussallam et al. (2021)
Fuego Lloyd et al. (2014)
Mt. St. Helens Humphreys et al. (2008)
Taupo Myers et al. (2018)
Long Valley Myers et al. (2018)
Yellowstone Myers et al. (2018)
Santorini Myers et al. (2021)
B)
Decompression rate (MPa/s)
10
1
0.1
0.01
0.001
6
7
8
9
10
11
12
13
Eruption intensity
C)
Decompression rate (MPa/s)
10
1
0.1
0.01
0.001
0.1
1
10
100
Plume height (km)

***Figure 5-1 :*** *Comparaison entre les vitesses de décompression déterminées via la méthode des embayments et A) la magnitude des éruptions, B) l'intensité des éruptions et C) la hauteur du panache. Les données mises en avant dans le chapitre 2 sont représentées avec des cercles, celles décrites dans le chapitre 3 sont représentées par des triangles, carrés ou losange selon s'il s'agit respectivement d'une éruption majeure, paroxysmale ou paroxysmale de grande ampleur du Stromboli. La vitesse maximale déterminée pour chaque éruption est mise en avant avec un symbole plus gros. La relation entre vitesse maximale de décompression et magnitude d'une éruption visible pour les magmas basaltiques et décrite au chapitre 2 est représenté en gris. Les vitesses de décompression pour le Stromboli sont au-dessus (plus élevées) que n'importe quelle tendance potentielle pour les basaltes dans les trois cas.*

Les données de vitesse de décompression pour le Stromboli sont systématiquement plus hautes que celles contenues dans la base de donnée, à magnitude, intensité et hauteur de panache égaux. Ainsi, les données du Stromboli sont toujours supérieures aux tendances décrites dans le chapitre 2. La prise en compte des données de Stromboli modifie donc considérablement les tendances. Le $R^2$ de la corrélation entre vitesse de décompression et magnitude décrite dans le chapitre 2 (concernant uniquement les magmas basaltiques) passe de 0.87 à 0.02, celle avec la hauteur du panache passe de 0.89 à 0.12 et celle avec l'intensité, même si elle n'est composée que de trois points à l'origine, passe de 0.99 à 0.28. A l'inverse des conclusions énoncées à la fin du chapitre 2, il semble maintenant assez improbable qu'il existe une potentielle relation entre vitesse de décompression et magnitude, intensité et hauteur du panache pour les magmas basaltiques. Il est cependant encore trop tôt pour totalement réfuter cette possibilité. En effet, nous avons vu dans les chapitres 2 et 3 que les résultats de la méthode des embayments sont dépendant du trajet effectué par chaque cristal et constituent donc plus une gamme qu'une valeur moyenne. Cela est partiellement dû au fait que le magma qui remonte ne suit pas forcément la même dynamique tout au long du conduit et des différences dans les divers groupes de magma

impliqués sont attendues (Gonnermann and Manga, 2007; Cassidy et al., 2018). C'est pourquoi nous considérons toujours les vitesses de décompression les plus élevées comme représentatives d'une éruption. Il n'est pas impossible que les études précédentes (Lloyd et al., 2014; Ferguson et al., 2016; Moussallam et al., 2019, 2021) n'aient pas trouvé et mesuré les embayments associés aux vitesses d'ascension les plus élevées. La multiplication des études qui effectuent des mesures de vitesse d'ascension sur l'ensemble des unités d'un dépôt (similaires à Myers et al., 2021) permettrait de mieux contraindre le pic de dynamisme au cours d'une éruption longue et donc les niveaux à échantillonner en priorité pour obtenir les embayments associés aux vitesses d'ascension les plus rapides.

Il est aussi parfaitement possible que l'action d'autres paramètres (composition chimiques, teneurs en éléments volatils, viscosité, fo2) entraine des différences fondamentales dans la vitesse de remontée pour certains volcans et pas pour d'autres. On est, de ce fait, en droit de se demander à quel point le contexte volcanique joue sur les dynamiques éruptives. Par exemple, un contexte de point chaud produit des magmas relativement pauvres en éléments volatils (Dixon, 1997; Hilton et al., 2000; Ferguson et al., 2016) et, selon nos observations du chapitre 3 (Fig. 3-6), produirait, de ce fait , une force de flottaison et une vitesse d'ascension théoriquement plus faibles que pour des magmas d'arc. Cette différence concerne principalement les faibles vitesses d'ascension obtenues pour le Kilauea, qui est un volcan de point chaud, mais n'est pas suffisant pour expliquer les différences de vitesse entre les différents volcans d'arc.

Etendre la comparaison à l'ensemble des paramètres étudiés (vitesse de décompression, magnitude, débit massique, hauteur du panache, pression de début de remontée et vitesse d'éjection de balistiques et de gaz) pour Stromboli et à l'échelle globale renforce les observations précédentes (Figure 5-2). A l'échelle globale, je n'observe aucune relation forte excepté entre la magnitude, le débit massique et la hauteur du panache ($R^2 > 0.7$), trois paramètres constitutifs de l'index d'explosivité volcanique (Newhall and Self, 1982). Les différentes corrélations sont en général bien plus prometteuses à l'échelle du Stromboli, non seulement pour la vitesse de décompression mais aussi entre la pression de début de remontée et la magnitude ou encore le débit massique. L'ensemble de ces relations renforcent l'idée que la simplification d'un problème complexe comme une éruption volcanique à travers l'étude d'un unique volcan permettrait de mieux en contraindre la structure dynamique puis de l'étendre à d'autres systèmes et contextes.

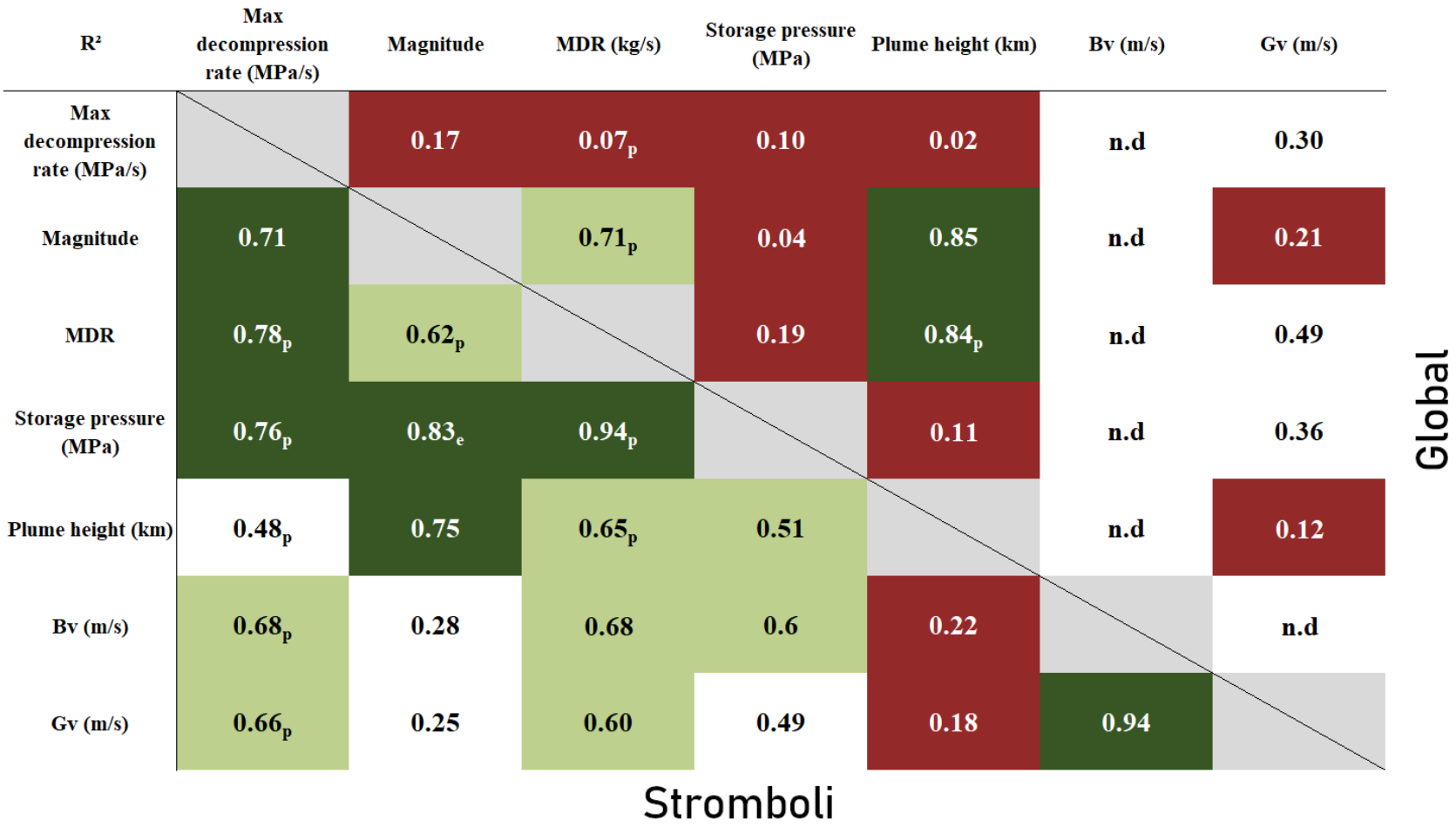


**Figure 5-2 :** Synthèse des $R^2$ des courbes de tendance linéaire entre les différents paramètres étudiés (vitesse de décompression, magnitude, débit massique, hauteur du panache, pression de début de remontée et vitesse d'éjection de balistiques et de gaz) pour Stromboli et à l'échelle globale. Les indices p et e sont indicatifs d'une relation selon une loi de puissance ou exponentielle, respectivement.

## 5.2 Perspectives

La méthode des embayments est récente et gagne graduellement en popularité au fur et à mesure que de nouvelles études viennent la développer et la complexifier. Que ce soit pour la méthode en elle-même ou la détermination de systématiques dans la dynamique magmatique, il existe de nombreux axes de développements potentiels suite à ce travail de thèse. La polyvalence d'application de la méthode des embayments et sa capacité à être utilisée pour des systèmes rhyolitiques, intermédiaires et basaltiques rendent sa caractérisation plus longue et compliquée. Des études récentes (deGraffenried and Shea, 2021; Ruefer et al., 2021; Befus et al., 2023) se concentrent sur la caractérisation de la forme 3D des embayments et de son impact potentiel sur les vitesses de remontée. Le problème principal est que l'ensemble de ces caractérisations, cruciales pour le bon emploi de la méthode, n'ont été réalisées que sur des magmas rhyolitiques. Il me semble donc nécessaire d'aussi caractériser plus en détail l'impact de la forme des embayments pour des magmas basaltiques et intermédiaires. De façon similaire à l'étude de deGraffenried and Shea, (2021), cet axe de recherche pourrait reprendre les variations de forme simples et en quantifier l'impact pour une gamme de magma basaltiques à intermédiaires en comparant les résultats 3D et 1D. Ce phénomène n'est pas simple et dépends non seulement de la forme 3D mais aussi de la vitesse

réelle de remontée de magma (deGraffenried and Shea, 2021), ce qui renforce d'autant plus la nécessité d'une caractérisation précise pour tous types de magma.

La méthode des embayments repose principalement sur une base théorique de l'exsolution des espèces volatiles avec la décompression et leur diffusion le long des embayments. Des limites théoriques ont été établies dans les études de Liu et al. (2007) et Myers et al. (2018, 2021) pour les magmas siliciques (vitesse de décompression inférieure à 0.25 MPa/s) car la perte par diffusion d'$H_2O$ le long des embayments ne seraient alors plus enregistrée. Il existe cependant plusieurs occurrences d'embayments enregistrant des vitesses supérieures à 0.25 MPa/s dans la littérature sur les systèmes siliciques (jusqu'à 1.6 MPa/s pour le Mt. St. Helens et jusqu'à 0.9 MPa/s pour le Santorin ; Humphreys et al., 2008, Myers et al., 2021, respectivement). Il semble donc important de préciser si une telle limite existe et, si oui, dans quel cas elle se manifeste pour l'ensemble des compositions basaltiques à rhyolitiques. Il serait possible de vérifier ce genre de paramètre expérimentalement via l'utilisation d'un piston cylindre ou d'un autoclave pour décomprimer des échantillons à vitesse connue et les comparer avec le signal enregistré. De plus, cela permettrait de tester et calibrer le comportement des différents éléments volatils ($H_2O$, $CO_2$ et S) et les limites d'enregistrement relative à chacun d'entre eux. Des études expérimentales de décompression pour des embayments issus de magmas rhyolitiques commencent à apparaître avec des résultats prometteurs (Hosseini et al., 2023) mais sur une faible gamme de vitesses de décompression. La modélisation prédictive selon différentes vitesses,

conditions aux frontières et longueur des embayments permettrait de mieux contraindre ces limites théoriques ainsi que leur sensibilité aux différents paramètres. Finalement, plutôt qu'une limite théorique de vitesse d'ascension, il me semble plus juste de déterminer une durée de remontée limite en dessous de laquelle le profil de diffusion ne varie plus significativement et le modèle ne détermine plus avec précision la vitesse de remontée. En effet, cette durée est spécifique au profil de diffusion alors que la détermination de la vitesse de décompression est dépendante du profil de dégazage et des pressions de début et de fin de remontée (pour une même durée, une plus grande distance implique une plus grande vitesse).

Enfin, un axe de recherche potentiel découlant de cette étude ferait écho à la discussion développée précédemment. Il serait sans doute judicieux de mesurer l'impact du contexte géologique (magma d'arc, point chaud) sur les vitesses mesurables grâce aux embayments. En comparant des volcans de contexte similaire, il serait peut-être possible de déterminer des relations entre vitesse de remontée du magma et d'autres paramètres éruptifs. Cela pourrait se faire de façon similaire à l'étude développée au cours du chapitre 3. Le Stromboli dispose en général d'une plus grande quantité d'éléments volatils sous forme dissoute et sous forme gazeuse comparé aux autres volcans d'arc basaltiques étudiés avec les embayments, responsable en grande partie des fortes vitesses d'ascension mesurées au Stromboli. Une étude plus approfondie de l'impact des différents paramètres (composition chimiques, teneurs en éléments volatils, viscosité, fo2,

taille du conduit) sur la relation magnitude/vitesse de décompression permettrait de déterminer si cette relation est spécifique à chaque volcan séparément ou applicables aux volcans avec des paramètres « similaires ».

En détail, l'étude de plusieurs éruptions plus ou moins violentes d'un unique volcan issu d'un contexte géologique différent, autre que le Stromboli, permettrait de nuancer d'avantage les conclusions développées au chapitre 3, tout en complétant d'avantage la base de données. Ce genre de développement nécessite cependant une plus grande quantité d'études, ce qui constitue une raison supplémentaire pour lesquelles le logiciel EMBER est gratuit, polyvalent, à la disposition de tous et le plus simple d'utilisation possible.

# CHAPITRE 6

# CONCLUSIONS

Cette thèse a permis de mettre en avant des relations et des systématiques permettant potentiellement d'expliquer et d'aider à caractériser certaines dynamiques magmatiques.

Il est possible d'effectuer les conclusions suivantes :

1) Pour le volcan Stromboli, et en particulier les éruptions majeures et paroxysmales de faible ampleur, il existe une relation entre vitesse de décompression du magma et la magnitude, l'intensité de l'éruption et la profondeur du début de l'accélération du magma. Il n'existe pas de relation précise avec la hauteur du panache, potentiellement à cause des effets atmosphériques non négligeables dans certains cas. Il est possible qu'il existe des relations spécifiques pour chaque volcan ou chaque système séparément mais il est encore trop tôt pour pouvoir l'affirmer.
2) Il n'existe actuellement pas de relation globale précise et significative entre vitesse de décompression du magma et la magnitude, l'intensité ou la hauteur du panache de chaque éruption. Il n'est pas impossible que des relations existent que ce soit à l'échelle globale ou en considérant les différents types de magma ou de contexte volcanique séparément, mais de telles relations sont, à ce jour, hautement improbables en l'absence de davantage de données.
3) La prise en compte conjuguée des corrélations entre vitesse de décompression et intensité de l'éruption, et la vitesse d'éjection des gaz à

l'évent permet de retrouver la relation théorique entre intensité et vitesse d'éjection des gaz pour le Stromboli. Ces relations sont dépendantes des types d'éruption considérées (émettant des balistiques ou un panache de cendres). Cette relation, associée à la mesure du conduit, permet par extension d'obtenir aussi une estimation de la densité du panache.

4) Les vitesses d'ascension obtenues pour le Stromboli sont en moyenne très élevées. Cela est possiblement dû à la forte teneur en éléments volatils du magma, comme mis en avant par les relations entre vitesse de décompression et pression enregistrée par les embayments, source d'une transition en profondeur entre un système dégazage ouvert vers un système fermé. La teneur en éléments volatils sous forme gazeuse dans le magma est une source additionnelle non négligeable entrainant le magma vers la surface. La quantification précise de cette quantité de gaz ainsi que son impact restent cependant à déterminer. La transition d'un système de dégazage ouvert vers un système de dégazage fermé entraine l'accélération du magma et le début de l'enregistrement de l'ascension par les embayments.
5) A l'instar de la méthode texturale des densités de vésicules, les embayments sont particulièrement sensibles aux derniers kilomètres de remontée où les volatiles dégazent significativement. Cette sensibilité est potentiellement à l'origine de la relation observée entre la vitesse de décompression moyenne dans le conduit et vitesse d'éjection des gaz pour le Stromboli. Continuer à

appliquer et développer cette méthode des embayments apparait donc comme une méthode pertinente pour l'étude des dynamiques magmatiques sur les derniers kilomètres de remontée.

La méthode des embayments, bien qu'efficace, nécessite malgré tout une grande rigueur de préparation, nécessaire pour potentiellement trouver le maximum d'échantillons pertinents, malgré leur rareté. Les embayments exploitables comme géochronomètres proviennent exclusivement de téphras et nécessitent d'être parfaitement vitreux. L'un des critères essentiels mis en avant est principalement la forme des embayments. En observant la distance moyenne sur laquelle les profils de diffusion varient, il semble raisonnable de sélectionner en priorité les embayments de plus de 100 µm de long. Ils doivent être le plus droit possible. Dans le cas où ils présentent un goulot d'étranglement, celui-ci doit être inférieur à 40% du diamètre maximal. Une règle simple est de sélectionner des embayments au moins deux fois plus longs que large de façon à pouvoir le considérer suffisamment tubulaire pour négliger tout potentiel mouvement advectif du liquide silicaté. Il est essentiel de sélectionner un embayment qui ne présente pas de bulles à l'intérieur mais une bulle à leur embouchure, bien que la présence et l'effet exact d'une telle bulle soient encore peu contraints. Quand bien même le développement graduel de la méthode devrait permettre d'assouplir ces règles une fois les processus mieux connus, les critères de sélection méthodiques et rigoureux des échantillons restent à ce jour les meilleurs alliés de toute personne souhaitant étudier les embayments.

# BIBLIOGRAPHIE


Aiuppa, A., Bertagnini, A., Métrich, N., Moretti, R., Di Muro, A., Liuzzo, M., Tamburello, G., 2010. A model of degassing for Stromboli volcano. Earth and Planetary Science Letters 295, 195–204. https://doi.org/10.1016/j.epsl.2010.03.040

Aiuppa, A., Bitetto, M., Francofonte, V., Velasquez, G., Parra, C.B., Giudice, G., Liuzzo, M., Moretti, R., Moussallam, Y., Peters, N., Tamburello, G., Valderrama, Oscar.A., Curtis, A., 2017. A CO2-gas precursor to the March 2015 Villarrica volcano eruption. Geochemistry, Geophysics, Geosystems 18, 2120–2132. https://doi.org/10.1002/2017GC006892

Aki, K., Koyanagi, R., 1981. Deep volcanic tremor and magma ascent mechanism under Kilauea, Hawaii. Journal of Geophysical Research 86, 7095. https://doi.org/10.1029/JB086iB08p07095

Anderson, A.T., 1991. Hourglass inclusions: Theory and application to the Bishop Rhyolitic Tuff. American Mineralogist 76, 530–547.

Andrews, B.J., 2014. Magmatic storage conditions, decompression rate, and incipient caldera collapse of the 1902 eruption of Santa Maria Volcano, Guatemala. Journal of Volcanology and Geothermal Research 282, 103–114. https://doi.org/10.1016/j.jvolgeores.2014.06.009

Andronico, D., Del Bello, E., D'Oriano, C., Landi, P., Pardini, F., Scarlato, P., de' Michieli Vitturi, M., Taddeucci, J., Cristaldi, A., Ciancitto, F., Pennacchia, F., Ricci, T., Valentini, F., 2021. Uncovering the eruptive patterns of the 2019 double paroxysm eruption crisis of Stromboli volcano. Nat Commun 12, 4213. https://doi.org/10.1038/s41467-021-24420-1

Andronico, D., Taddeucci, J., Cristaldi, A., Miraglia, L., Scarlato, P., Gaeta, M., 2013. The 15 March 2007 paroxysm of Stromboli: video-image analysis, and textural and compositional features of the erupted deposit. Bull Volcanol 75, 733. https://doi.org/10.1007/s00445-013-0733-2

Bagdassakov, N., Dorfman, A., Dingwell, D., 2000. Effect of alkalis, phosphorus, and water on the surface tension of haplogranite melt. American Mineralogist 85, 33–40. https://doi.org/10.2138/am-2000-0105

Barth, A., Edmonds, M., Woods, A., 2019a. Valve-like dynamics of gas flow through a packed crystal mush and cyclic strombolian explosions. Sci Rep 9, 821. https://doi.org/10.1038/s41598-018-37013-8

Barth, A., Newcombe, M., Plank, T., Gonnermann, H., Hajimirza, S., Soto, G., Saballos, A., 2019b. Magma decompression rate correlates with explosivity at basaltic volcanoes – constraints from water diffusion in olivine 67.

Baxter, P., Allard, P., Halbwachs, M., Komorowski, J., Andrew, W., Ancia, A., 2003. Human health and vulnerability in the Nyiragongo volcano eruption and humanitarian crisis at Goma, Democratic Republic of Congo. Acta Vulcanologica, 14(1/2), 109.

Befus, K.S., Ruefer, A.C., Allison, C.M., Thompson, J.O., 2023. Quartz-hosted inclusions and embayments reveal storage, fluxing, and ascent of the Mesa Falls Tuff, Yellowstone. Earth and Planetary Science Letters 601, 117909. https://doi.org/10.1016/j.epsl.2022.117909

Behrens, H., Zhang, Y., 2001. Ar diffusion in hydrous silicic melts: Implications for volatile diffusion mechanisms and fractionation. Earth and Planetary Science Letters 192, 363–376. https://doi.org/10.1016/S0012-821X(01)00458-7

Belousov, A., Belousova, M., Edwards, B., Volynets, A., Melnikov, D., 2015. Overview of the precursors and dynamics of the 2012–13 basaltic fissure eruption of Tolbachik Volcano, Kamchatka, Russia. Journal of Volcanology and Geothermal Research, SI: 2012-13 Tolbachik eruption 307, 22–37. https://doi.org/10.1016/j.jvolgeores.2015.06.013

Bertagnini, A., Coltelli, M., Landi, P., Pompilio, M., Rosi, M., 1999. Violent explosions yield new insights into dynamics of Stromboli volcano. Eos, Transactions American Geophysical Union 80, 633–636. https://doi.org/10.1029/99EO00415

Bertagnini, A., Di Roberto, A., Pompilio, M., 2011. Paroxysmal activity at Stromboli: lessons from the past. Bull Volcanol 73, 1229–1243. https://doi.org/10.1007/s00445-011-0470-3

Bertagnini, A., Méltrich, N., Francalanci, L., Landi, P., Tommasini, S., Conticelli, S., 2013. Volcanology and Magma Geochemistry of the Present-Day Activity: Constraints on the Feeding System, in: Calvari, S., Inguaggiato, S., Puglisi, G., Ripepe, M., Rosi, M. (Eds.), Geophysical Monograph Series. American Geophysical Union, Washington, D. C., pp. 19–37. https://doi.org/10.1029/182GM04

Bertagnini, A., Metrich, N., Francalanci, L., Landi, P., Tommasini, S., Conticelli, S., 2008. Volcanology and magma geochemistry of the present-day activity: constraints on the feeding system. American Geophysical Union.

Bertagnini, A., Métrich, N., Landi, P., Rosi, M., 2003. Stromboli volcano (Aeolian Archipelago, Italy): An open window on the deep-feeding system of a steady state basaltic volcano: DEEP-FEEDING SYSTEM OF STROMBOLI. J. Geophys. Res. 108. https://doi.org/10.1029/2002JB002146

Bevilacqua, A., Bertagnini, A., Pompilio, M., Landi, P., Del Carlo, P., Di Roberto, A., Aspinall, W., Neri, A., 2020. Major explosions and paroxysms at Stromboli (Italy): a new historical catalog and temporal models of occurrence with uncertainty quantification. Sci Rep 10, 17357. https://doi.org/10.1038/s41598-020-74301-8

Bluth, G.J.S., Doiron, S.D., Schnetzler, C.C., Krueger, A.J., Walter, L.S., 1992. Global tracking of the $SO_2$ clouds from the June, 1991 Mount Pinatubo eruptions. Geophys. Res. Lett. 19, 151–154. https://doi.org/10.1029/91GL02792

Bombrun, M., Harris, A., Gurioli, L., Battaglia, J., Barra, V., 2015. Anatomy of a Strombolian eruption: Inferences from particle data recorded with thermal video. Journal of Geophysical Research: Solid Earth 120, 2367–2387. https://doi.org/10.1002/2014JB011556

Bonadonna, C., 2005. Probabilistic modeling of tephra dispersal: Hazard assessment of a multiphase rhyolitic eruption at Tarawera, New Zealand. J. Geophys. Res. 110, B03203. https://doi.org/10.1029/2003JB002896

Bonadonna, C., Cioni, R., Costa, A., Druitt, T., Phillips, J., Pioli, L., Andronico, D., Harris, A., Scollo, S., Bachmann, O., Bagheri, G., Biass, S., Brogi, F., Cashman, K., Dominguez, L., Dürig, T., Galland, O., Giordano, G., Gudmundsson, M., Hort, M., Höskuldsson, A., Houghton, B., Komorowski, J.C., Küppers, U., Lacanna, G., Pennec, J.L.L., Macedonio, G., Manga, M., Manzella, I., Vitturi, M. de' M., Neri, A., Pistolesi, M., Polacci, M., Ripepe, M., Rossi, E., Scheu, B., Sulpizio, R., Tripoli, B., Valade, S., Valentine, G., Vidal, C., Wallenstein, N., 2016. MeMoVolc report on classification and dynamics of volcanic explosive eruptions. Bulletin of Volcanology 78.

Bonadonna, C., Genco, R., Gouhier, M., Pistolesi, M., Cioni, R., Alfano, F., Hoskuldsson, A., Ripepe, M., 2011. Tephra sedimentation during the 2010 Eyjafjallajökull eruption (Iceland) from deposit, radar, and satellite observations. Journal of Geophysical Research: Solid Earth 116. https://doi.org/10.1029/2011JB008462

Brennen, C.E., 2005. Fundamentals of Multiphase Flow. Cambridge University Press.

Brodsky, E.E., Kanamori, H., Sturtevant, B., 1999. A seismically constrained mass discharge rate for the initiation of the May 18, 1980 Mount St. Helens eruption. J. Geophys. Res. 104, 29387–29400. https://doi.org/10.1029/1999JB900308

Browne, B., Gardner, J., 2006. The influence of magma ascent path on the texture, mineralogy, and formation of hornblende reaction rims. Earth and Planetary Science Letters 246, 161–176. https://doi.org/10.1016/j.epsl.2006.05.006

Browne, B., Szramek, L., 2015. Rates of Magma Ascent and Storage, in: The Encyclopedia of Volcanoes. Elsevier, pp. 203–214. https://doi.org/10.1016/B978-0-12-385938-9.00009-2

Bryan, S.E., Peate, I.U., Peate, D.W., Self, S., Jerram, D.A., Mawby, M.R., Marsh, J.S. (Goonie), Miller, J.A., 2010. The largest volcanic eruptions on Earth. Earth-Science Reviews 102, 207–229. https://doi.org/10.1016/j.earscirev.2010.07.001

Calvari, S., Spampinato, L., Bonaccorso, A., Oppenheimer, C., Rivalta, E., Boschi, E., 2011. Lava effusion — A slow fuse for paroxysms at Stromboli volcano? Earth and Planetary Science Letters 301, 317–323. https://doi.org/10.1016/j.epsl.2010.11.015

Cannavò, F., Camacho, A.G., González, P.J., Mattia, M., Puglisi, G., Fernández, J., 2015. Real Time Tracking of Magmatic Intrusions by means of Ground Deformation Modeling during Volcanic Crises. Sci Rep 5, 10970. https://doi.org/10.1038/srep10970

Cardwell, R.J., McDonald, G.W., Wotherspoon, L.M., 2020. Simulation of post-volcanic eruption time variant land use and economic impacts in the Auckland region of New Zealand. Bull Volcanol 82, 64. https://doi.org/10.1007/s00445-020-01400-9

Carey, S., Sigurdsson, H., 1985. The May 18, 1980 eruption of Mount St. Helens: 2. Modeling of dynamics of the Plinian Phase. Journal of Geophysical Research: Solid Earth 90, 2948–2958. https://doi.org/10.1029/JB090iB04p02948

Cassidy, M., Cole, Paul.D., Hicks, K.E., Varley, N.R., Peters, N., Lerner, A.H., 2015. Rapid and slow: Varying magma ascent rates as a mechanism for Vulcanian explosions. Earth and Planetary Science Letters 420, 73–84. https://doi.org/10.1016/j.epsl.2015.03.025

Cassidy, M., Manga, M., Cashman, K., Bachmann, O., 2018. Controls on explosive-effusive volcanic eruption styles. Nature Communications 9, 2839. https://doi.org/10.1038/s41467-018-05293-3

Castro, J.M., Dingwell, D.B., 2009. Rapid ascent of rhyolitic magma at Chaitén volcano, Chile. Nature 461, 780–783. https://doi.org/10.1038/nature08458

Castro, J.M., Gardner, J.E., 2008. Did magma ascent rate control the explosive-effusive transition at the Inyo volcanic chain, California. Geol 36, 279. https://doi.org/10.1130/G24453A.1

Chester, D., R, D., Duncan, A., Guest, J., 2000. The increasing exposure of cities to the effects of volcanic eruptions: A global survey. Global Environmental Change Part B: Environmental Hazards 2, 89–103. https://doi.org/10.1016/S1464-2867(01)00004-3

Chouet, B., Hamisevicz, N., McGetchin, T.R., 1974. Photoballistics of volcanic jet activity at Stromboli, Italy. Journal of Geophysical Research (1896-1977) 79, 4961–4976. https://doi.org/10.1029/JB079i032p04961

Chouet, B., Saccorotti, G., Dawson, P., Martini, M., Scarpa, R., De Luca, G., Milana, G., Cattaneo, M., 1999. Broadband measurements of the sources of explosions at Stromboli Volcano, Italy. Geophysical Research Letters 26, 1937–1940. https://doi.org/10.1029/1999GL900400

Chouet, B.A., Matoza, R.S., 2013. A multi-decadal view of seismic methods for detecting precursors of magma movement and eruption. Journal of Volcanology and Geothermal Research 252, 108–175. https://doi.org/10.1016/j.jvolgeores.2012.11.013

Costa, F., Shea, T., Ubide, T., 2020a. Diffusion chronometry and the timescales of magmatic processes. Nat Rev Earth Environ 1, 201–214. https://doi.org/10.1038/s43017-020-0038-x

Couch, S., 2003. The Kinetics of Degassing-Induced Crystallization at Soufriere Hills Volcano, Montserrat. Journal of Petrology 44, 1477–1502. https://doi.org/10.1093/petrology/44.8.1477

deGraffenried, R., Shea, T., 2020. Modeling diffusion in 1D within melt embayments: correcting for 3D geometry. Presented at the AGU Fall Meeting 2020, AGU.

deGraffenried, R.L., Shea, T., 2021. Using Volatile Element Concentration Profiles in Crystal-Hosted Melt Embayments to Estimate Magma Decompression Rate: Assumptions and Inherited Errors. Geochem Geophys Geosyst 22. https://doi.org/10.1029/2021GC009672

Delle Donne, D., Ripepe, M., 2012. High-frame rate thermal imagery of Strombolian explosions: Implications for explosive and infrasonic source dynamics. Journal of Geophysical Research: Solid Earth 117. https://doi.org/10.1029/2011JB008987

Demouchy, S., Mackwell, S., 2006. Mechanisms of hydrogen incorporation and diffusion in iron-bearing olivine. Phys Chem Minerals 33, 347–355. https://doi.org/10.1007/s00269-006-0081-2

Dixon, J.E., 1997. Degassing of alkalic basalts. American Mineralogist 82, 368–378. https://doi.org/10.2138/am-1997-3-415

Dobran, F., 1992. Nonequilibrium flow in volcanic conduits and application to the eruptions of Mt. St. Helens on May 18, 1980, and Vesuvius in AD 79. Journal of Volcanology and Geothermal Research 49, 285–311. https://doi.org/10.1016/0377-0273(92)90019-A

Endo, E.T., Murray, T., 1991. Real-time Seismic Amplitude Measurement (RSAM): a volcano monitoring and prediction tool. Bull Volcanol 53, 533–545. https://doi.org/10.1007/BF00298154

Faure, F., Schiano, P., 2005. Experimental investigation of equilibration conditions during forsterite growth and melt inclusion formation. Earth and Planetary Science Letters 236, 882–898. https://doi.org/10.1016/j.epsl.2005.04.050

Ferguson, D.J., Gonnermann, H.M., Ruprecht, P., Plank, T., Hauri, E.H., Houghton, B.F., Swanson, D.A., 2016. Magma decompression rates during explosive eruptions of Kīlauea volcano, Hawaii, recorded by melt embayments. Bulletin of Volcanology 78, 71. https://doi.org/10.1007/s00445-016-1064-x

Freda, C., Baker, D.R., Romano, C., Scarlato, P., 2003. Water diffusion in natural potassic melts. Geological Society, London, Special Publications 213, 53–62. https://doi.org/10.1144/GSL.SP.2003.213.01.04

Freda, C., Baker, D.R., Scarlato, P., 2005. Sulfur diffusion in basaltic melts. Geochimica et Cosmochimica Acta 69, 5061–5069. https://doi.org/10.1016/j.gca.2005.02.002

Freret-Lorgeril, V., Donnadieu, F., Scollo, S., Provost, A., Fréville, P., Guéhenneux, Y., Hervier, C., Prestifilippo, M., Coltelli, M., 2018. Mass Eruption Rates of Tephra Plumes During the 2011–2015 Lava Fountain Paroxysms at Mt. Etna From Doppler Radar Retrievals. Front. Earth Sci. 6, 73. https://doi.org/10.3389/feart.2018.00073

Gardner, J.E., Sigurdsson, H., Carey, S.N., 1991. Eruption dynamics and magma withdrawal during the Plinian Phase of the Bishop Tuff Eruption, Long Valley Caldera. J. Geophys. Res. 96, 8097. https://doi.org/10.1029/91JB00257

Georgeais, G., Koga, K.T., Moussallam, Y., Rose-Koga, E.F., 2021. Magma decompression rate calculations with EMBER: A user-friendly software to model diffusion of $H_2O$, $CO_2$ and S in melt embayments. Geochem Geophys Geosyst. https://doi.org/10.1029/2020GC009542

Geschwind, C.-H., Rutherford, M.J., 1995. Crystallization of microlites during magma ascent: the fluid mechanics of 1980–1986 eruptions at Mount St Helens. Bulletin of Volcanology 57, 356–370. https://doi.org/10.1007/BF00301293

Giordano, G., De Astis, G., 2020. The summer 2019 basaltic Vulcanian eruptions (paroxysms) of Stromboli. Bull Volcanol 83, 1. https://doi.org/10.1007/s00445-020-01423-2

Girona, T., Costa, F., 2013. DIPRA: A user-friendly program to model multi-element diffusion in olivine with applications to timescales of magmatic processes. Geochemistry, Geophysics, Geosystems 14, 422–431. https://doi.org/10.1029/2012GC004427

Giudicepietro, F., López, C., Macedonio, G., Alparone, S., Bianco, F., Calvari, S., De Cesare, W., Delle Donne, D., Di Lieto, B., Esposito, A.M., Orazi, M., Peluso, R., Privitera, E., Romano, P., Scarpato, G., Tramelli, A., 2020a. Geophysical precursors of the July-August 2019 paroxysmal eruptive phase and their implications for Stromboli volcano (Italy) monitoring. Scientific Reports 10, 10296. https://doi.org/10.1038/s41598-020-67220-1

Global Volcanism Program, Venzke, E., 2022. Volcanoes of the World, v.5.

Gonnermann, H., Manga, M., 2012. Dynamics of magma ascent in the volcanic conduit Chapter 4 Overview. https://doi.org/10.1017/cbo9781139021562.004

Gonnermann, H.M., Manga, M., 2007. The Fluid Mechanics Inside a Volcano. Annual Review of Fluid Mechanics 39, 321–356. https://doi.org/10.1146/annurev.fluid.39.050905.110207

Gurioli, L, Colo, L., Bollasina, A.J., Harris, A.J.L., Whittington, A., Ripepe, M., 2013. Dynamics of Strombolian explosions: Inferences from field and laboratory studies of erupted bombs from Stromboli volcano. Journal of Geophysical Research 27.

Gurioli, L., Harris, A.J.L., Colò, L., Bernard, J., Favalli, M., Ripepe, M., Andronico, D., 2013. Classification, landing distribution, and associated flight parameters for a bomb field emplaced during a single major explosion at Stromboli, Italy. Geology 41, 559–562. https://doi.org/10.1130/G33967.1

Harris, A.J.L., Delle Donne, D., Dehn, J., Ripepe, M., Worden, A.K., 2013. Volcanic plume and bomb field masses from thermal infrared camera imagery. Earth and Planetary Science Letters 365, 77–85. https://doi.org/10.1016/j.epsl.2013.01.004

Harris, Andrew J. L., Gurioli, L., Hughes, E.E., Lagreulet, S., 2012. Impact of the Eyjafjallajökull ash cloud: A newspaper perspective. Journal of Geophysical Research: Solid Earth 117. https://doi.org/10.1029/2011JB008735

Harris, Andrew J. L., Ripepe, M., Calvari, S., Lodato, L., Spampinato, L., 2013. The 5 April 2003 Explosion of Stromboli: Timing of Eruption Dynamics Using Thermal Data, in: Calvari, S., Inguaggiato, S., Puglisi, G., Ripepe, M., Rosi, M. (Eds.), Geophysical Monograph Series. American Geophysical Union, Washington, D. C., pp. 305–316. https://doi.org/10.1029/182GM25

Harris, Andrew J.L., Ripepe, M., Hughes, E.A., 2012. Detailed analysis of particle launch velocities, size distributions and gas densities during normal explosions at Stromboli. Journal of Volcanology and Geothermal Research 231–232, 109–131. https://doi.org/10.1016/j.jvolgeores.2012.02.012

Hauri, E., Wang, J., Dixon, J.E., King, P.L., Mandeville, C., Newman, S., 2002. SIMS analysis of volatiles in silicate glasses: 1. Calibration, matrix effects and comparisons with FTIR. Chemical Geology, Melt Inclusions at the Millennium: Toward a Deeper Understanding of Magmatic Processes 183, 99–114. https://doi.org/10.1016/S0009-2541(01)00375-8

Hilton, D.R., Thirlwall, M.F., Taylor, R.N., Murton, B.J., Nichols, A., 2000. Controls on magmatic degassing along the Reykjanes Ridge with implications for the helium paradox. Earth and Planetary Science Letters 183, 43–50. https://doi.org/10.1016/S0012-821X(00)00253-3

Hosseini, B., Myers, M.L., Watkins, J.M., Harris, M.A., 2023. Are We Recording? Putting Embayment Speedometry to the Test Using High Pressure-Temperature Decompression Experiments. Geochemistry, Geophysics, Geosystems 24, e2022GC010770. https://doi.org/10.1029/2022GC010770

Humphreys, M.C.S., Menand, T., Blundy, J.D., Klimm, K., 2008. Magma ascent rates in explosive eruptions: Constraints from H2O diffusion in melt inclusions. Earth and Planetary Science Letters 270, 25–40. https://doi.org/10.1016/j.epsl.2008.02.041

Iacono-Marziano, G., Morizet, Y., Le Trong, E., Gaillard, F., 2012. New experimental data and semi-empirical parameterization of H2O–CO2 solubility in mafic melts. Geochimica et Cosmochimica Acta 97, 1–23. https://doi.org/10.1016/j.gca.2012.08.035

Jarosewich, E., Nelen, J. a., Norberg, J.A., 1980. Reference Samples for Electron Microprobe Analysis*. Geostandards Newsletter 4, 43–47. https://doi.org/10.1111/j.1751-908X.1980.tb00273.x

Jochum, K.P., Dingwell, D.B., Rocholl, A., Stoll, B., Hofmann, A.W., Becker, S., Besmehn, A., Bessette, D., Dietze, H.-J., Dulski, P., Erzinger, J., Hellebrand, E., Hoppe, P., Horn, I., Janssens, K., Jenner, G. a., Klein, M., McDonough, W. f., Maetz, M., Mezger, K., Müker, C., Nikogosian, I. k., Pickhardt, C., Raczek, I., Rhede, D., Seufert, H. m., Simakin, S. g., Sobolev, A. v., Spettel, B., Straub, S., Vincze, L., Wallianos, A., Weckwerth, G., Weyer, S., Wolf, D., Zimmer, M., 2000. The Preparation and Preliminary Characterisation of Eight Geological MPI-DING Reference Glasses for In-Situ Microanalysis. Geostandards Newsletter 24, 87–133. https://doi.org/10.1111/j.1751-908X.2000.tb00590.x

Johnston, E., R.S.J., S., Phillips, J., Carey, S., 2014. Revised Estimates for the Volume of the Late Bronze Age Minoan Eruption, Santorini, Greece. Journal of the Geological Society 171. https://doi.org/10.1144/jgs2013-113

KAMENETSKY, V.S., EVERARD, J.L., CRAWFORD, A.J., VARNE, R., EGGINS, S.M., LANYON, R., 2000. Enriched End-member of Primitive MORB Melts: Petrology and Geochemistry of Glasses from Macquarie Island (SW Pacific). Journal of Petrology 41, 411–430. https://doi.org/10.1093/petrology/41.3.411

Kelfoun, K., 2017. A two-layer depth-averaged model for both the dilute and the concentrated parts of pyroclastic currents: A Model For Pyroclastic Currents. J. Geophys. Res. Solid Earth 122, 4293–4311. https://doi.org/10.1002/2017JB014013

Kelfoun, K., Vargas, S.V., 2016. VolcFlow capabilities and potential development for the simulation of lava flows. SP 426, 337–343. https://doi.org/10.1144/SP426.8

Klein, F.W., Koyanagi, R.Y., Nakata, J.S., Tanigawa, W.R., 1987. The seismicity of Kilauea's magma system. US Geol. Surv. Prof. Pap 1350, 1019–1185.

Klügel, A., 1998. Reactions between mantle xenoliths and host magma beneath La Palma (Canary Islands): constraints on magma ascent rates and crustal reservoirs. Contributions to Mineralogy and Petrology 131, 237–257. https://doi.org/10.1007/s004100050391

Klügel, A., Hansteen, T.H., Schmincke, H.-U., 1997. Rates of magma ascent and depths of magma reservoirs beneath La Palma (Canary Islands). Terra Nova 9, 117–121. https://doi.org/10.1046/j.1365-3121.1997.d01-15.x

Kohlstedt, D.L., Mackwell, S.J., 1998. Diffusion of hydrogen and intrinsic point defects in olivine. Zeitschrift fur physikalische chemie 207, 147–162.

Koyaguchi, T., 2005. An analytical study for 1-dimensional steady flow in volcanic conduits. Journal of Volcanology and Geothermal Research, Volcanic Eruption Mechanisms 143, 29–52. https://doi.org/10.1016/j.jvolgeores.2004.09.009

Koyaguchi, T., Ohno, M., 2001. Reconstruction of eruption column dynamics on the basis of grain size of tephra fall deposits: 2. Application to the Pinatubo 1991 eruption. Journal of Geophysical Research: Solid Earth 106, 6513–6533. https://doi.org/10.1029/2000JB900427

Koyaguchi, T., Tokuno, M., 1993. Origin of the giant eruption cloud of Pinatubo, June 15, 1991. Journal of Volcanology and Geothermal Research 55, 85–96. https://doi.org/10.1016/0377-0273(93)90091-5

La Felice, S., Landi, P., 2011. The 2009 paroxysmal explosions at Stromboli (Italy): magma mixing and eruption dynamics. Bull Volcanol 73, 1147–1154. https://doi.org/10.1007/s00445-011-0502-z

La Spina, G., Burton, M., de' Michieli Vitturi, M., 2015. Temperature evolution during magma ascent in basaltic effusive eruptions: A numerical application to Stromboli volcano. Earth and Planetary Science Letters 426, 89–100. https://doi.org/10.1016/j.epsl.2015.06.015

Le Gall, N., Pichavant, M., 2016a. Homogeneous bubble nucleation in H2O- and H2O-CO2-bearing basaltic melts: Results of high temperature decompression experiments. Journal of Volcanology and Geothermal Research 327, 604–621. https://doi.org/10.1016/j.jvolgeores.2016.10.004

Le Gall, N., Pichavant, M., 2016b. Experimental simulation of bubble nucleation and magma ascent in basaltic systems: Implications for Stromboli volcano. American Mineralogist 101, 1967–1985. https://doi.org/10.2138/am-2016-5639

Le Voyer, M., Asimow, P.D., Mosenfelder, J.L., Guan, Y., Wallace, P.J., Schiano, P., Stolper, E.M., Eiler, J.M., 2014. Zonation of H2O and F Concentrations around Melt Inclusions in Olivines. Journal of Petrology 55, 685–707. https://doi.org/10.1093/petrology/egu003

Leduc, L., Gurioli, L., Harris, A., Colò, L., Rose-Koga, E.F., 2015. Types and mechanisms of strombolian explosions: characterization of a gas-dominated explosion at Stromboli. Bull Volcanol 77, 8. https://doi.org/10.1007/s00445-014-0888-5

Lister, J.R., Kerr, R.C., 1991. Fluid-mechanical models of crack propagation and their application to magma transport in dykes. J. Geophys. Res. 96, 10049. https://doi.org/10.1029/91JB00600

Liu, Y., Anderson, A.T., Wilson, C.J.N., 2007. Melt pockets in phenocrysts and decompression rates of silicic magmas before fragmentation. Journal of Geophysical Research 112, B06204. https://doi.org/10.1029/2006JB004500

Lloyd, A.S., Ruprecht, P., Hauri, E.H., Rose, W., Gonnermann, H.M., Plank, T., 2014. NanoSIMS results from olivine-hosted melt embayments: Magma ascent rate during explosive basaltic eruptions. Journal of Volcanology and Geothermal Research 283, 1–18. https://doi.org/10.1016/j.jvolgeores.2014.06.002

Lyons, J.J., Waite, G.P., Ichihara, M., Lees, J.M., 2012. Tilt prior to explosions and the effect of topography on ultra-long-period seismic records at Fuego volcano, Guatemala: TILT AND THE EFFECT OF TOPOGRAPHY. Geophys. Res. Lett. 39, n/a-n/a. https://doi.org/10.1029/2012GL051184

MacDonald, G.A., 1973. G. A. MacDonald 1972. Volcanoes. A discussion of volcanoes, volcanic products, and volcanic phenomena. xii + 510 pp., 120 figs, 144 pls. 15 tables. Prentice-Hall, International, New Jersey. Price £8.50. Geol. Mag. 110, 87–88. https://doi.org/10.1017/S0016756800047476

Macedonio, G., Costa, A., Longo, A., 2005. A computer model for volcanic ash fallout and assessment of subsequent hazard. Computers & Geosciences 31, 837–845. https://doi.org/10.1016/j.cageo.2005.01.013

Mackwell, S.J., Kohlstedt, D.L., 1990. Diffusion of hydrogen in olivine: Implications for water in the mantle. J. Geophys. Res. 95, 5079. https://doi.org/10.1029/JB095iB04p05079

Maki, M., Kim, Y., Kobori, T., Hirano, K., Lee, D.-I., Iguchi, M., 2021. Analyses of three-dimensional weather radar data from volcanic eruption clouds. Journal of Volcanology and Geothermal Research 412, 107178. https://doi.org/10.1016/j.jvolgeores.2021.107178

Manga, M., Castro, J., Cashman, K.V., Loewenberg, M., 1998. Rheology of bubble-bearing magmas. Journal of Volcanology and Geothermal Research 87, 15–28. https://doi.org/10.1016/S0377-0273(98)00091-2

Martel, C., Iacono-Marziano, G., 2015. Timescales of bubble coalescence, outgassing, and foam collapse in decompressed rhyolitic melts. Earth and Planetary Science Letters 412, 173–185. https://doi.org/10.1016/j.epsl.2014.12.010

Martel, C., Pichavant, M., Bourdier, J.-L., Traineau, H., Holtz, F., Scaillet, B., 1998. Magma storage conditions and control of eruption regime in silicic volcanoes: experimental evidence from Mt. Pelée. Earth and Planetary Science Letters 156, 89–99. https://doi.org/10.1016/S0012-821X(98)00003-X

Mason, B.G., Pyle, D.M., Oppenheimer, C., 2004. The size and frequency of the largest explosive eruptions on Earth. Bull Volcanol 66, 735–748. https://doi.org/10.1007/s00445-004-0355-9

Mastin, L., Van Eaton, A., Lowenstern, J., 2014. Modeling ash fall distribution from a Yellowstone supereruption. Geochemistry, Geophysics, Geosystems 15. https://doi.org/10.1002/2014GC005469

Mastin, L.G., 2005. The controlling effect of viscous dissipation on magma flow in silicic conduits. Journal of Volcanology and Geothermal Research 143, 17–28. https://doi.org/10.1016/j.jvolgeores.2004.09.008

Mastin, L.G., Guffanti, M., Servranckx, R., Webley, P., Barsotti, S., Dean, K., Durant, A., Ewert, J.W., Neri, A., Rose, W.I., Schneider, D., Siebert, L., Stunder, B., Swanson, G., Tupper, A., Volentik, A., Waythomas, C.F., 2009. A multidisciplinary effort to assign realistic source parameters to models of volcanic ash-cloud transport and dispersion during eruptions. Journal of Volcanology and Geothermal Research, Improved Prediction and Tracking of Volcanic Ash Clouds 186, 10–21. https://doi.org/10.1016/j.jvolgeores.2009.01.008

Médard, E., Grove, T.L., 2008. The effect of H2O on the olivine liquidus of basaltic melts: experiments and thermodynamic models. Contrib Mineral Petrol 155, 417–432. https://doi.org/10.1007/s00410-007-0250-4

Mercalli, G., 1907. I Vulcani Attivi della Terra Morfologia—Dinamismo—Prodotti Distribuzione Geografica-Cause. Nature 76, 291–291. https://doi.org/10.1038/076291a0

Métrich, N, Bertagnini, A., Di Muro, A., 2010. Conditions of Magma Storage, Degassing and Ascent at Stromboli: New Insights into the Volcano Plumbing System with Inferences on the Eruptive Dynamics. Journal of Petrology 51, 603–626. https://doi.org/10.1093/petrology/egp083
Métrich, N., Bertagnini, A., Landi, P., Rosi, M., 2001. Crystallization Driven by Decompression and Water Loss at Stromboli Volcano (Aeolian Islands, Italy). Journal of Petrology 42, 1471–1490. https://doi.org/10.1093/petrology/42.8.1471
Métrich, N., Bertagnini, A., Landi, P., Rosi, M., Belhadj, O., 2005. Triggering mechanism at the origin of paroxysms at Stromboli (Aeolian Archipelago, Italy): The 5 April 2003 eruption. Geophysical Research Letters 32. https://doi.org/10.1029/2004GL022257
Métrich, N., Bertagnini, A., Pistolesi, M., 2021. Paroxysms at Stromboli Volcano (Italy): Source, Genesis and Dynamics. Front. Earth Sci. 9. https://doi.org/10.3389/feart.2021.593339
Misiti, V., Vetere, F., Mangiacapra, A., Behrens, H., Cavallo, A., Scarlato, P., Dingwell, D.B., 2009. Viscosity of high-K basalt from the 5th April 2003 Stromboli paroxysmal explosion. Chemical Geology 260, 278–285. https://doi.org/10.1016/j.chemgeo.2008.12.023
Mourtada-Bonnefoi, C., Laporte, D., 2004. Mourtada-Bonnefoi, C. C. & Laporte, D. Kinetics of bubble nucleation in a rhyolitic melt: an experimental study of the effect of ascent rate. Earth Planet. Sci. Lett. 218, 521-537. Earth and Planetary Science Letters 218, 521–537. https://doi.org/10.1016/S0012-821X(03)00684-8
Moussallam, Y., Médard, E., Georgeais, G., Rose-Koga, E.F., Koga, K.T., Pelletier, B., Bani, P., Shreve, T.L., Grandin, R., Boichu, M., Tari, D., Peters, N., 2021a. How to turn off a lava lake? A petrological investigation of the 2018 intra-caldera and submarine eruptions of Ambrym volcano. Bull Volcanol 83, 36. https://doi.org/10.1007/s00445-021-01455-2
Moussallam, Y., Rose-Koga, E.F., Koga, K.T., Médard, E., Bani, P., Devidal, J.-L., Tari, D., 2019. Fast ascent rate during the 2017–2018 Plinian eruption of Ambae (Aoba) volcano: a petrological investigation. Contrib Mineral Petrol 174, 90. https://doi.org/10.1007/s00410-019-1625-z
Myers, M.L., Druitt, T.H., Schiavi, F., Gurioli, L., Flaherty, T., 2021. Evolution of magma decompression and discharge during a Plinian event (Late Bronze-Age eruption, Santorini) from multiple eruption-intensity proxies. Bull Volcanol 83, 18. https://doi.org/10.1007/s00445-021-01438-3
Myers, M.L., Wallace, P.J., Wilson, C.J.N., Watkins, J.M., Liu, Y., 2018. Ascent rates of rhyolitic magma at the onset of three caldera-forming eruptions. American Mineralogist 103, 952–965. https://doi.org/10.2138/am-2018-6225
Neal, C., Guffanti, M., 2011. Airborne Volcanic Ash--A Global Threat to Aviation [WWW Document]. URL https://pubs.usgs.gov/fs/2010/3116/ (accessed 10.18.22).
Neal, C.A., Brantley, S.R., Antolik, L., Babb, J.L., Burgess, M., Calles, K., Cappos, M., Chang, J.C., Conway, S., Desmither, L., Dotray, P., Elias, T., Fukunaga, P., Fuke, S., Johanson, I.A., Kamibayashi, K., Kauahikaua, J., Lee, R.L., Pekalib, S., Miklius, A., Million, W., Moniz, C.J., Nadeau, P.A., Okubo, P., Parcheta, C., Patrick, M.R., Shiro, B., Swanson, D.A., Tollett, W., Trusdell, F., Younger, E.F., Zoeller, M.H., Montgomery-Brown, E.K., Anderson, K.R., Poland, M.P., Ball, J.L., Bard, J., Coombs, M., Dietterich, H.R., Kern, C., Thelen, W.A., Cervelli, P.F., Orr, T., Houghton, B.F., Gansecki, C., Hazlett, R., Lundgren, P., Diefenbach, A.K., Lerner, A.H., Waite, G., Kelly, P., Clor, L., Werner, C., Mulliken, K., Fisher, G., Damby, D., 2019. The 2018 rift eruption and summit collapse of Kīlauea Volcano. Science 363, 367–374. https://doi.org/10.1126/science.aav7046
Newcombe, M.E., Plank, T., Barth, A., Asimow, P.D., Hauri, E., 2020. Water-in-olivine magma ascent chronometry: Every crystal is a clock. Journal of Volcanology and Geothermal Research 398, 106872. https://doi.org/10.1016/j.jvolgeores.2020.106872
Newhall, C.G., Self, S., 1982. The volcanic explosivity index (VEI) an estimate of explosive magnitude for historical volcanism. J. Geophys. Res. 87, 1231. https://doi.org/10.1029/JC087iC02p01231
Newman, S., Lowenstern, J.B., 2002. VolatileCalc: a silicate melt–H2O–CO2 solution model written in Visual Basic for excel. Computers & Geosciences 28, 597–604. https://doi.org/10.1016/S0098-3004(01)00081-4

Ni, H., Zhang, L., 2018. A general model of water diffusivity in calc-alkaline silicate melts and glasses. Chemical Geology 478, 60–68. https://doi.org/10.1016/j.chemgeo.2017.10.010
Nishimura, T., 2006. Ground deformation due to magma ascent with and without degassing. Geophys. Res. Lett. 33, L23309. https://doi.org/10.1029/2006GL028101
Nowak, M., Behrens, H., 1997. An experimental investigation on diffusion of water in haplogranitic melts. Contrib Mineral Petrol 126, 365–376. https://doi.org/10.1007/s004100050256
Nowak, M., Schreen, D., Spickenbom, K., 2004. Argon and CO2 on the race track in silicate melts: A tool for the development of a CO2 speciation and diffusion model. Geochimica et Cosmochimica Acta 68, 5127–5138. https://doi.org/10.1016/j.gca.2004.06.002
Papale, P., Dobran, F., 1993. Modeling of the ascent of magma during the plinian eruption of Vesuvius in A.D. 79. Journal of Volcanology and Geothermal Research, Mount Vesuvius 58, 101–132. https://doi.org/10.1016/0377-0273(93)90104-Y
Patrick, M.R., Harris, A.J.L., Ripepe, M., Dehn, J., Rothery, D.A., Calvari, S., 2007. Strombolian explosive styles and source conditions: insights from thermal (FLIR) video. Bull Volcanol 69, 769–784. https://doi.org/10.1007/s00445-006-0107-0
Pichavant, M., Di Carlo, I., Pompilio, M., Le Gall, N., 2022. Timescales and mechanisms of paroxysm initiation at Stromboli volcano, Aeolian Islands, Italy. Bull Volcanol 84, 36. https://doi.org/10.1007/s00445-022-01545-9
Pichavant, M., Di Carlo, I., Rotolo, S.G., Scaillet, B., Burgisser, A., Le Gall, N., Martel, C., 2013. Generation of CO2-rich melts during basalt magma ascent and degassing. Contributions to Mineralogy and Petrology 166, 545–561. https://doi.org/10.1007/s00410-013-0890-5
Pichavant, M., Pompilio, M., D'Oriano, C., Carlo, I.D., 2011. Petrography, mineralogy and geochemistry of a primitive pumice from Stromboli: implications for the deep feeding system. European Journal of Mineralogy 23, 499–517. https://doi.org/10.1127/0935-1221/2011/0023-2109
Pioli, L., Harris, A.J.L., 2019. Real-Time Geophysical Monitoring of Particle Size Distribution During Volcanic Explosions at Stromboli Volcano (Italy). Frontiers in Earth Science 7.
Pioli, L., Pistolesi, M., Rosi, M., 2014. Transient explosions at open-vent volcanoes: The case of Stromboli (Italy). Geology 42, 863–866. https://doi.org/10.1130/G35844.1
Pistolesi, M., Delle Donne, D., Pioli, L., Rosi, M., Ripepe, M., 2011. The 15 March 2007 explosive crisis at Stromboli volcano, Italy: Assessing physical parameters through a multidisciplinary approach. J. Geophys. Res. 116, B12206. https://doi.org/10.1029/2011JB008527
Polacci, M., Baker, D., Mancini, L., Tromba, G., Zanini, F., 2006. Three-dimensional investigation of volcanic textures by X-ray microtomography and implications for conduit processes. Geophysical Research Letters - GEOPHYS RES LETT 33. https://doi.org/10.1029/2006GL026241
Polacci, M., Baker, D.R., Mancini, L., Favretto, S., Hill, R.J., 2009. Vesiculation in magmas from Stromboli and implications for normal Strombolian activity and paroxysmal explosions in basaltic systems. Journal of Geophysical Research: Solid Earth 114. https://doi.org/10.1029/2008JB005672
Polacci, M., Papale, P., Rosi, M., 2001. Textural heterogeneities in pumices from the climactic eruption of Mount Pinatubo, 15 June 1991, and implications for magma ascent dynamics. Bull Volcanol 63, 83–97. https://doi.org/10.1007/s004450000123
Polacci, M., Pioli, L., Rosi, M., 2003. The Plinian phase of the Campanian Ignimbrite eruption (Phlegrean Fields, Italy): Evidence from density measurements and textural characterization of pumice. Bulletin of Volcanology 65, 418–432. https://doi.org/10.1007/s00445-002-0268-4
Poland, M.P., Anderson, K.R., 2020. Partly Cloudy With a Chance of Lava Flows: Forecasting Volcanic Eruptions in the Twenty-First Century. Journal of Geophysical Research: Solid Earth 125, e2018JB016974. https://doi.org/10.1029/2018JB016974
Poland, M.P., Lopez, T., Wright, R., Pavolonis, M.J., 2020. Forecasting, Detecting, and Tracking Volcanic Eruptions from Space. Remote Sens Earth Syst Sci 3, 55–94. https://doi.org/10.1007/s41976-020-00034-x

Prousevitch, A.A., Sahagian, D.L., Anderson, A.T., 1993. Dynamics of diffusive bubble growth in magmas: Isothermal case. J. Geophys. Res. 98, 22283–22307. https://doi.org/10.1029/93JB02027

Proussevitch, A.A., Sahagian, D.L., 1998. Dynamics and energetics of bubble growth in magmas: Analytical formulation and numerical modeling. Journal of Geophysical Research: Solid Earth 103, 18223–18251. https://doi.org/10.1029/98JB00906

Pyle, D.M., 2015. Sizes of Volcanic Eruptions, in: The Encyclopedia of Volcanoes. Elsevier, pp. 257–264. https://doi.org/10.1016/B978-0-12-385938-9.00013-4

Pyle, D.M., 1998. Forecasting sizes and repose times of future extreme volcanic events. Geology 26, 367–370. https://doi.org/10.1130/0091-7613(1998)026<0367:FSARTO>2.3.CO;2

Ripepe, M., Ciliberto, S., Della Schiava, M., 2001. Time constraints for modeling source dynamics of volcanic explosions at Stromboli. Journal of Geophysical Research: Solid Earth 106, 8713–8727. https://doi.org/10.1029/2000JB900374

Ripepe, M., Gordeev, E., 1999. Gas bubble dynamics model for shallow volcanic tremor at Stromboli. Journal of Geophysical Research: Solid Earth 104, 10639–10654. https://doi.org/10.1029/98JB02734

Ripepe, M., Harris, A.J.L., 2008. Dynamics of the 5 April 2003 explosive paroxysm observed at Stromboli by a near-vent thermal, seismic and infrasonic array: EXPLOSIVE PAROXYSM AT STROMBOLI IN 2003. Geophys. Res. Lett. 35, n/a-n/a. https://doi.org/10.1029/2007GL032533

Ripepe, M., Harris, A.J.L., Carniel, R., 2002. Thermal, seismic and infrasonic evidences of variable degassing rates at Stromboli volcano. Journal of Volcanology and Geothermal Research 118, 285–297. https://doi.org/10.1016/S0377-0273(02)00298-6

Ripepe, M., Lacanna, G., Pistolesi, M., Silengo, M.C., Aiuppa, A., Laiolo, M., Massimetti, F., Innocenti, L., Della Schiava, M., Bitetto, M., La Monica, F.P., Nishimura, T., Rosi, M., Mangione, D., Ricciardi, A., Genco, R., Coppola, D., Marchetti, E., Delle Donne, D., 2021. Ground deformation reveals the scale-invariant conduit dynamics driving explosive basaltic eruptions. Nat Commun 12, 1683. https://doi.org/10.1038/s41467-021-21722-2

Ripepe, M., Marchetti, E., Ulivieri, G., 2007. Infrasonic monitoring at Stromboli volcano during the 2003 effusive eruption: Insights on the explosive and degassing process of an open conduit system. Journal of Geophysical Research: Solid Earth 112. https://doi.org/10.1029/2006JB004613

Rose-Koga, E.F., Koga, K.T., Devidal, J.-L., Shimizu, N., Voyer, M.L., Dalou, C., Döbeli, M., 2020. In-situ measurements of magmatic volatile elements, F, S, and Cl, by electron microprobe, secondary ion mass spectrometry, and heavy ion elastic recoil detection analysis. American Mineralogist 105, 616–626. https://doi.org/10.2138/am-2020-7221

Rosi, M., Bertagnini, A., Harris, A.J.L., Pioli, L., Pistolesi, M., Ripepe, M., 2006. A case history of paroxysmal explosion at Stromboli: Timing and dynamics of the April 5, 2003 event. Earth and Planetary Science Letters 243, 594–606. https://doi.org/10.1016/j.epsl.2006.01.035

Rosi, M., Pistolesi, M., Bertagnini, A., Landi, P., Pompilio, M., Di Roberto, A., 2013. Chapter 14 Stromboli volcano, Aeolian Islands (Italy): present eruptive activity and hazards. Geological Society, London, Memoirs 37, 473–490. https://doi.org/10.1144/M37.14

Ruefer, A.C., Befus, K.S., Thompson, J.O., Andrews, B.J., 2021. Implications of Multiple Disequilibrium Textures in Quartz-Hosted Embayments. Frontiers in Earth Science 9.

Rust, A.C., Manga, M., Cashman, K.V., 2003. Determining flow type, shear rate and shear stress in magmas from bubble shapes and orientations. Journal of Volcanology and Geothermal Research 122, 111–132. https://doi.org/10.1016/S0377-0273(02)00487-0

Rutherford, M.J., 2008. Magma Ascent Rates. Reviews in Mineralogy and Geochemistry 69, 241–271. https://doi.org/10.2138/rmg.2008.69.7

Rutherford, M.J., Devine, J.D., 1996. Preeruption Pressure-Temperature Conditions and Volatiles in the 1991 Dacitic Magma of Mount Pinatubo [WWW Document]. URL https://pubs.usgs.gov/pinatubo/ruth/ (accessed 10.27.22).

Rutherford, M.J., Gardner, J.E., Sigurdsson, H., 2000. Rates of magma ascent. Encyclopedia of volcanoes 207–217.
Rutherford, M.J., Hill, P.M., 1993. Magma ascent rates from amphibole breakdown: An experimental study applied to the 1980–1986 Mount St. Helens eruptions. Journal of Geophysical Research: Solid Earth 98, 19667–19685. https://doi.org/10.1029/93JB01613
Rutherford, M.J., Sigurdsson, H., Carey, S., Davis, A., 1985. The May 18, 1980, eruption of Mount St. Helens: 1. Melt composition and experimental phase equilibria. Journal of Geophysical Research: Solid Earth 90, 2929–2947. https://doi.org/10.1029/JB090iB04p02929
Scandone, R., Malone, S.D., 1985. Magma supply, magma discharge and readjustment of the feeding system of mount St. Helens during 1980. Journal of Volcanology and Geothermal Research 23, 239–262. https://doi.org/10.1016/0377-0273(85)90036-8
Scharff, L., Hort, M., Harris, A.J.L., Ripepe, M., Lees, J.M., Seyfried, R., 2008. Eruption dynamics of the SW crater of Stromboli volcano, Italy — An interdisciplinary approach. Journal of Volcanology and Geothermal Research 176, 565–570. https://doi.org/10.1016/j.jvolgeores.2008.05.008
Schiavi, F., Bolfan-Casanova, N., Withers, A.C., Médard, E., Laumonier, M., Laporte, D., Flaherty, T., Gómez-Ulla, A., 2018. Water quantification in silicate glasses by Raman spectroscopy: Correcting for the effects of confocality, density and ferric iron. Chemical Geology 483, 312–331. https://doi.org/10.1016/j.chemgeo.2018.02.036
Schilling, S.P., 1998. LAHARZ; GIS programs for automated mapping of lahar-inundation hazard zones. U.S. Geological Survey ; Information Services. https://doi.org/10.3133/ofr98638
Schneider, H., Barbera, F., 1998. 18 Application of order statistics to sampling plans for inspection by variables, in: Handbook of Statistics. Elsevier, pp. 497–511. https://doi.org/10.1016/S0169-7161(98)17020-7
Self, S., 2006. The effects and consequences of very large explosive volcanic eruptions. Phil. Trans. R. Soc. A. 364, 2073–2097. https://doi.org/10.1098/rsta.2006.1814
Shea, T., 2017. Bubble nucleation in magmas: A dominantly heterogeneous process? Journal of Volcanology and Geothermal Research 343, 155–170. https://doi.org/10.1016/j.jvolgeores.2017.06.025
Shea, T., Houghton, B.F., Gurioli, L., Cashman, K.V., Hammer, J.E., Hobden, B.J., 2010. Textural studies of vesicles in volcanic rocks: An integrated methodology. Journal of Volcanology and Geothermal Research 190, 271–289. https://doi.org/10.1016/j.jvolgeores.2009.12.003
Shimizu, K., Saal, A.E., Hauri, E.H., Perfit, M.R., Hékinian, R., 2019. Evaluating the roles of melt-rock interaction and partial degassing on the CO2/Ba ratios of MORB: Implications for the CO2 budget in the Earth's depleted upper mantle. Geochimica et Cosmochimica Acta 260, 29–48. https://doi.org/10.1016/j.gca.2019.06.013
Shimozuru, D., 1968. Discussion on the energy partition of volcanic eruption. Bull Volcanol 32, 383–394. https://doi.org/10.1007/BF02599777
Shishkina, T.A., Botcharnikov, R.E., Holtz, F., Almeev, R.R., Portnyagin, M.V., 2010. Solubility of H2O- and CO2-bearing fluids in tholeiitic basalts at pressures up to 500MPa. Chemical Geology 277, 115–125. https://doi.org/10.1016/j.chemgeo.2010.07.014
Shreve, T., Grandin, R., Boichu, M., Garaebiti, E., Moussallam, Y., Ballu, V., Delgado, F., Leclerc, F., Vallée, M., Henriot, N., Cevuard, S., Tari, D., Lebellegard, P., Pelletier, B., 2019. From prodigious volcanic degassing to caldera subsidence and quiescence at Ambrym (Vanuatu): the influence of regional tectonics. Scientific Reports 9, 18868. https://doi.org/10.1038/s41598-019-55141-7
Sides, I.R., Edmonds, M., Maclennan, J., Swanson, D.A., Houghton, B.F., 2014. Eruption style at Kīlauea Volcano in Hawai'i linked to primary melt composition. Nature Geoscience 7, 464.
Simkin, T., Siebert, L., 1994. Volcanoes of the world (2nd edition). Tucson, Geoscience Press, p. 349.
Sornette, D., Knopoff, L., Kagan, Y.Y., Vanneste, C., 1996. Rank-ordering statistics of extreme events: Application to the distribution of large earthquakes. Journal of Geophysical Research: Solid Earth 101, 13883–13893. https://doi.org/10.1029/96JB00177

Sparks, R.S.J., 2003. Forecasting volcanic eruptions. Earth and Planetary Science Letters 210, 1–15. https://doi.org/10.1016/S0012-821X(03)00124-9
Sparks, R.S.J., 1978. The dynamics of bubble formation and growth in magmas: A review and analysis. Journal of Volcanology and Geothermal Research 3, 1–37. https://doi.org/10.1016/0377-0273(78)90002-1
Sparks, R.S.J., Baker, L., Brown, R., Field, M., Schumacher, J., Stripp, G., L. Walters, A., 2006. Dynamical constraints on kimberlite volcanism. Journal of Volcanology and Geothermal Research 155, 18–48. https://doi.org/10.1016/j.jvolgeores.2006.02.010
Sparks, R.S.J., Bursik, M.I., Carey, S.N., Gilbert, J., Glaze, L.S., Sigurdsson, H., Woods, A., 1997. Volcanic Plumes. Wiley, Chichester.
Spera, F.J., 1984. Carbon dioxide in petrogenesis III: role of volatiles in the ascent of alkaline magma with special reference to xenolith-bearing mafic lavas. Contributions to Mineralogy and Petrology 88, 217–232. https://doi.org/10.1007/BF00380167
Stein, D., Spera, F., 2002. Shear viscosity of rhyolite-vapor emulsions at magmatic temperatures by concentric cylinder rheometry. Journal of Volcanology and Geothermal Research 113, 243–258. https://doi.org/10.1016/S0377-0273(01)00260-8
Steinberg, G.S., Babenko, J.I., 1978. Experimental velocity and density determination of volcanic gases during eruption. Journal of Volcanology and Geothermal Research 3, 89–98. https://doi.org/10.1016/0377-0273(78)90005-7
Suzuki, T., 1983. A theoretical model for the dispersion of tephra., in: Arc Volcanism, Physics and Tectonics. Terra Scientific Publishing 95–113.
Szramek, L.A., 2016. Mafic Plinian eruptions: Is fast ascent required?: Is Fast Ascent Required? J. Geophys. Res. Solid Earth 121, 7119–7136. https://doi.org/10.1002/2016JB013208
Tilling, R.I., Topinka, L.J., Swanson, D.A., 1990. Eruptions of Mount St. Helens: Past, Present, and Future. U.S. Department of the Interior, Geological Survey.
Toramaru, A., 2006. BND (bubble number density) decompression rate meter for explosive volcanic eruptions. Journal of Volcanology and Geothermal Research 154, 303–316. https://doi.org/10.1016/j.jvolgeores.2006.03.027
Toramaru, A., 1995. Numerical study of nucleation and growth of bubbles in viscous magmas. Journal of Geophysical Research: Solid Earth 100, 1913–1931. https://doi.org/10.1029/94JB02775
Toramaru, A., 1989. Vesiculation process and bubble size distributions in ascending magmas with constant velocities. J. Geophys. Res. 94, 17523. https://doi.org/10.1029/JB094iB12p17523
Tournigand, P.-Y., Taddeucci, J., Gaudin, D., Peña Fernández, J.J., Del Bello, E., Scarlato, P., Kueppers, U., Sesterhenn, J., Yokoo, A., 2017. The Initial Development of Transient Volcanic Plumes as a Function of Source Conditions. Journal of Geophysical Research: Solid Earth 122, 9784–9803. https://doi.org/10.1002/2017JB014907
Tryggvason, E., 1994. Surface deformation at the Krafla volcano, North Iceland, 1982–1992. Bulletin of Volcanology 56, 98–107. https://doi.org/10.1007/BF00304105
Van Eaton, A., Herzog, M., Wilson, C., Mcgregor, J., 2012. Ascent dynamics of large phreatomagmatic eruption clouds: The role of microphysics. Journal of Geophysical Research (Solid Earth) 117, 3203. https://doi.org/10.1029/2011JB008892
Vergniolle, S., Jaupart, C., 1986. Separated two-phase flow and basaltic eruptions. Journal of Geophysical Research: Solid Earth 91, 12842–12860. https://doi.org/10.1029/JB091iB12p12842
Weber, K., Eliasson, J., Vogel, A., Fischer, C., Pohl, T., van Haren, G., Meier, M., Grobéty, B., Dahmann, D., 2012. Airborne in-situ investigations of the Eyjafjallajökull volcanic ash plume on Iceland and over north-western Germany with light aircrafts and optical particle counters. Atmospheric Environment, Volcanic ash over Europe during the eruption of Eyjafjallajöekull on Iceland, April-May 2010 48, 9–21. https://doi.org/10.1016/j.atmosenv.2011.10.030
Wiesner, M.G., Wetzel, A., Catane, S.G., Listanco, E.L., Mirabueno, H.T., 2004. Grain size, areal thickness distribution and controls on sedimentation of the 1991 Mount Pinatubo tephra

layer in the South China Sea. Bull Volcanol 66, 226–242. https://doi.org/10.1007/s00445-003-0306-x
Wilson, L., Head, J.W., 1981. Ascent and eruption of basaltic magma on the Earth and Moon. J. Geophys. Res. 86, 2971–3001. https://doi.org/10.1029/JB086iB04p02971
Wilson, L., Self, S., 1980. Volcanic explosion clouds: Density, temperature, and particle content estimates from cloud motion. Journal of Geophysical Research: Solid Earth 85, 2567–2572. https://doi.org/10.1029/JB085iB05p02567
Wilson, L., Sparks, R.S.J., Huang, T.C., Watkins, N.D., 1978. The control of volcanic column heights by eruption energetics and dynamics. Journal of Geophysical Research: Solid Earth 83, 1829–1836. https://doi.org/10.1029/JB083iB04p01829
Wilson, L., Sparks, R.S.J., Walker, G.P.L., 1980. Explosive volcanic eruptions -- IV. The control of magma properties and conduit geometry on eruption column behaviour. Geophysical Journal International 63, 117–148. https://doi.org/10.1111/j.1365-246X.1980.tb02613.x
Witham, F., Blundy, J., Kohn, S.C., Lesne, P., Dixon, J., Churakov, S.V., Botcharnikov, R., 2012. SolEx: A model for mixed COHSCl-volatile solubilities and exsolved gas compositions in basalt. Computers & Geosciences 45, 87–97. https://doi.org/10.1016/j.cageo.2011.09.021
Woods, A.W., Bower, S.M., 1995. The decompression of volcanic jets in a crater during explosive volcanic eruptions. Earth and Planetary Science Letters 131, 189–205. https://doi.org/10.1016/0012-821X(95)00012-2
Woods, A.W., Wohletz, K., 1991. Dimensions and dynamics of co-ignimbrite eruption columns. Nature 350, 225–227. https://doi.org/10.1038/350225a0
Zhang, Y., Behrens, H., 2000. H2O diffusion in rhyolitic melts and glasses. Chemical Geology 169, 243–262. https://doi.org/10.1016/S0009-2541(99)00231-4
Zhang, Y., Ni, H., Chen, Y., 2010. Diffusion Data in Silicate Melts. Reviews in Mineralogy and Geochemistry 72, 311–408. https://doi.org/10.2138/rmg.2010.72.8
Zhang, Y., Xu, Z., Zhu, M., Wang, H., 2007. Silicate melt properties and volcanic eruptions: SILICATE MELT PROPERTIES. Rev. Geophys. 45. https://doi.org/10.1029/2006RG000216